

## Structural steel joints under M-N - from advanced modelling to design recommendations

**Auteur :** Archambeau, Loïc

**Promoteur(s) :** Demonceau, Jean-François

**Faculté :** Faculté des Sciences appliquées

**Diplôme :** Master en ingénieur civil des constructions, à finalité spécialisée en "civil engineering"

**Année académique :** 2024-2025

**URI/URL :** <http://hdl.handle.net/2268.2/23283>

---

### Avertissement à l'attention des usagers :

Tous les documents placés en accès ouvert sur le site le site MatheO sont protégés par le droit d'auteur. Conformément aux principes énoncés par la "Budapest Open Access Initiative"(BOAI, 2002), l'utilisateur du site peut lire, télécharger, copier, transmettre, imprimer, chercher ou faire un lien vers le texte intégral de ces documents, les disséquer pour les indexer, s'en servir de données pour un logiciel, ou s'en servir à toute autre fin légale (ou prévue par la réglementation relative au droit d'auteur). Toute utilisation du document à des fins commerciales est strictement interdite.

Par ailleurs, l'utilisateur s'engage à respecter les droits moraux de l'auteur, principalement le droit à l'intégrité de l'oeuvre et le droit de paternité et ce dans toute utilisation que l'utilisateur entreprend. Ainsi, à titre d'exemple, lorsqu'il reproduira un document par extrait ou dans son intégralité, l'utilisateur citera de manière complète les sources telles que mentionnées ci-dessus. Toute utilisation non explicitement autorisée ci-avant (telle que par exemple, la modification du document ou son résumé) nécessite l'autorisation préalable et expresse des auteurs ou de leurs ayants droit.

---



UNIVERSITY OF LIÈGE  
FACULTY OF APPLIED SCIENCES

---

# **Structural steel joints under M-N - from advanced modelling to design recommendations**

---

Master thesis carried out by  
**Loïc Archambeau**  
in view to obtain the master's degree of Civil Engineer

**Promotor :**

Pr. Dr Ir Demonceau J.-F.

**Jury members :**

Ir Golea T.  
Pr. Dr Ir Duchêne L.  
Dr Ir Weynand K.

Academic year 2024-2025

# Acknowledgments

First and foremost, I would like to express my heartfelt and deepest gratitude to my research supervisor, Prof. Jean-François Demonceau, for giving me the opportunity to carry out this thesis under his guidance. Your expertise, availability, and teaching skills were invaluable factors in the success of this study. Your trust and genuine goodwill have been essential in helping me grow in confidence throughout this journey. Thank you for sharing your passion for research with me.

Then, I would like to express my deep thanks to Ir Tudor Golea, who also accompanied me all along the realisation of this work. Your advice, support, and experience were truly valuable and significantly improved the quality of this thesis. Our discussions have always been insightful and have greatly contributed to my progress.

I also express my sincere gratitude to the other members of my thesis committee, Prof. Laurent Duchêne and Dr Klaus Weynand, for generously giving their time and for their valuable contribution to the evaluation of this thesis. I am deeply grateful to Dr. Weynand for the opportunity to make full use of the COP software. Without a doubt, it was indeed an invaluable tool in the successful completion of this thesis.

Last but not least, I would like to warmly thank my friends, and even more so my family, for their unwavering support over the past months. Your presence on my side was truly a landmark during the many moments of questioning that I faced, helping me grow and push my limits a little more each day. Thank you for always believing in me, even when I doubted myself. None of this would have been possible without you.

# Summary

**Title : Structural steel joints under M-N - from advanced modelling to design recommendations**

This Master thesis focusses on the characterisation and design of structural steel joints subjected to bending and axial forces (M-N).

A brief state-of-the-art review is first carried out to highlight the most relevant analytical and numerical models currently available. Then, based on various joint configurations found in the literature, a comprehensive set of analyses is performed. These include comparisons with commercial software, validation of the analytical model using experimental data, parametric studies on various geometrical and mechanical properties, and validation of an innovative finite element through detailed local numerical models.

Subsequently, building on all the knowledge acquired, a review is conducted on the M-N interaction criteria recommended in both current and upcoming versions of the European standard. As the main objective of this work, three new criteria have been fully developed to address the identified issues while keeping in mind practical implementation aspects. Finally, to support potential integration into a future version of the standard, the complete derivation procedures for these design recommendations are clearly defined and extensively illustrated through multiple practical application examples.



# Résumé

## **Titre : Assemblages structurels en acier soumis à M-N – de la modélisation avancée aux recommandations de conception**

Ce mémoire de Master se concentre sur la caractérisation et la conception des assemblages en acier structurel soumis à des efforts de flexion et des efforts axiaux (M-N).

Une brève revue de l'état de l'art est d'abord réalisée afin de mettre en évidence les modèles analytiques et numériques les plus pertinents actuellement disponibles. Ensuite, sur base de plusieurs configurations d'assemblages issues de la littérature, de multiples analyses sont effectuées. Celles-ci incluent des comparaisons avec un logiciel commercial, la validation du modèle analytique à l'aide de données expérimentales, des études paramétriques sur diverses propriétés géométriques et mécaniques, ainsi que la validation d'un élément fini innovant au moyen de modèles numériques locaux détaillés.

Par la suite, en s'appuyant sur l'ensemble des connaissances acquises, une évaluation approfondie est menée sur les critères d'interaction M-N recommandés dans les versions actuelle et à venir de la norme européenne. En tant qu'objectif principal de ce travail, trois nouveaux critères sont entièrement développés afin de répondre aux lacunes identifiées, tout en gardant à l'esprit les aspects liés à leur mise en œuvre. Enfin, afin de faciliter une éventuelle intégration dans une future version de la norme, les procédures complètes de calcul de ces recommandations sont clairement exposées et richement illustrées au travers d'exemples d'application.

# Nomenclature

$\beta$	The transformat. parameter converting the web panel resistance into an equivalent "beam force"
$\gamma_{M0}$	The partial safety factor for resistance of cross-sections whatever the class is
$\gamma_{M1}$	The partial safety factor for resistance of members to instability assessed by member checks
$\gamma_{M2}$	The partial factor for resistance of cross-sections in tension to fracture
$\epsilon$	A coefficient depending on $f_y$
$\bar{\lambda}_p$	The plate slenderness
$\rho$	The reduction factor for plate buckling
$a_p$	The throat thickness of the weld between the beam flange and the end-plate
$A_s$	The tensile stress area of the bolt in the threaded part
$A_{vc}$	The shear area of the column
$d_c$	The clear depth of the column web
$E$	The Young modulus of the steel
$f_{y,fc}$	The design yield strength of the column flange
$f_{y,wb}$	The design yield strength of the beam web
$f_{y,wc}$	The design yield strength of the column web
$f_{ub}$	The ultimate tensile strength of the bolt
$F_{c,fb,Rd}$	The design compression resistance of the combined beam flange and web
$F_{c,wc,Rd}$	The design resistance of the column web in transverse compression
$F_{t,Rd}$	The design tension resistance of a bolt
$F_{t,wc,Rd}$	The design resistance of the column web in transverse tension
$F_{T,i,Rd}$	The design tension resistance of a T-stub flange for mode $i$
$F_{wp,Rd}$	The "beam-force" resistance of the column web panel
$h_b$	The depth of the beam
$h_i$	The lever arm of the joint row $i$
$h_w$	The thickness of a washer
$k_2$	A coefficient depending on the bolt type
$k_b$	The height of the bolt head
$l_{eff,cp}$	The circular pattern effective length
$l_{eff,i}$	The effective length of mode $i$
$l_{eff,nc}$	The non-circular pattern effective length
$L_b$	The bolt elongation length
$m_n$	The height of the nut
$M_{c,Rd}$	The design moment resistance of the beam cross-section, as defined in EN 1993-1-1 2005 [6]
$M_{pl,i,Rd}$	The design plastic moment resistant of equivalent T-stub flanges for mode $i$
$n$	The total number of rows in the joint

---

$r_c$	The fillet radius of the column
$s_p$	The total dispersion length at $45^\circ$ through the end-plate (at least $t_{ep}$ and up to $2t_{ep}$ )
$t_{ep}$	The thickness of the end-plate
$t_{fb}$	The thickness of the beam flange
$t_{fc}$	The thickness of the column flange
$t_{wc}$	The thickness of the column web
$V_{wp,Rd}$	The design plastic shear resistance of the column web panel

BFC	Beam flange and web in compression
BT	Bolts in tension
BWT	Beam web in tension
CFB	Column flange in transverse bending
CWC	Column web in transverse compression
CWS	Column web panel in shear
CWT	Column web in transverse tension
EPB	End-plate in bending

In this work, the English numerical convention is adopted, where a period (.) is used as the decimal separator and a comma (,) is used to separate thousands.

# Contents

<b>1</b>	<b>Introduction</b>	<b>1</b>
<b>2</b>	<b>State-of-the-art</b>	<b>3</b>
2.1	Standard model . . . . .	3
2.2	Analytical model . . . . .	5
2.3	Numerical model . . . . .	5
<b>3</b>	<b>Advanced models</b>	<b>7</b>
3.1	Objectives . . . . .	7
3.2	Methodology . . . . .	8
3.2.1	Component method . . . . .	9
3.2.2	Cerfontaine model . . . . .	22
3.2.3	Python implementation . . . . .	26
3.2.4	COP software . . . . .	26
3.2.5	Parametric analysis . . . . .	27
3.2.6	FINELG software . . . . .	27
3.2.7	Finite element modelling . . . . .	28
3.3	Database . . . . .	31
3.3.1	FAILNOMORE joint configurations . . . . .	31
3.3.2	Coimbra joint configurations . . . . .	35
3.3.3	Cerfontaine thesis example . . . . .	38
3.4	Results and discussions . . . . .	40
3.4.1	FAILNOMORE joint configurations . . . . .	40
3.4.2	Coimbra joint configurations . . . . .	50
3.4.3	Parametric analysis . . . . .	57
3.4.4	Local finite element analysis . . . . .	62
<b>4</b>	<b>M-N design recommendations</b>	<b>66</b>
4.1	Objectives . . . . .	66
4.2	Interaction criteria according to standards . . . . .	66
4.3	Proposed new interaction criteria . . . . .	68
4.3.1	Six-point criterion . . . . .	68
4.3.2	Eight-point criterion without "non-interaction" thresholds . . . . .	70
4.3.3	Eight-point criterion with "non-interaction" thresholds . . . . .	71
4.4	Application examples . . . . .	73
<b>5</b>	<b>Conclusions</b>	<b>79</b>

<b>A</b>	<b>FAILNOMORE joint configurations</b>	<b>83</b>
A.1	Configuration A1 . . . . .	83
A.1.1	Component characterisation - 3. . . . .	83
A.1.2	Row/Group characterisation - 4. . . . .	91
A.1.3	Row lever arms calculation - 5. . . . .	92
A.1.4	Resistances $F_{Rd}^+$ & $F_{Rd}^-$ of each row - 6. . . . .	92
A.1.5	Characteristic M-N resistance points - 7. . . . .	92
A.1.6	Ductile resistance interaction curve - 8. . . . .	94
A.2	Configuration A2 . . . . .	95
A.3	Configuration B1 . . . . .	97
A.4	Configuration B3 . . . . .	99
A.5	Configuration C2 . . . . .	102
A.6	Configuration C3 . . . . .	105
<b>B</b>	<b>Coimbra joint configurations</b>	<b>108</b>
B.1	Flush end-plate configuration . . . . .	108
B.2	Extended end-plate configuration . . . . .	111
B.3	Geometrical properties measured in laboratory . . . . .	114
<b>C</b>	<b>Parametric Analysis</b>	<b>119</b>

# List of Figures

1.1	Examples of structural steel joints under M-N . . . . .	1
1.2	EN 1993-1-8:2005 - Current M-N interaction criterion proposed [19] . . . . .	2
2.1	Active components of a typical joint under pure hogging bending moment [30] . . . . .	4
2.2	Mechanical model of a typical extended end-plate beam-to-column joint [21] . . . . .	5
2.3	New mechanical model of a typical single-sided joint with an extended end-plate [22] . . . . .	6
3.1	Methodology steps to analytically design ductile joints under M-N . . . . .	8
3.2	Component characterisation - Elastic perfectly plastic behaviour law $F - \Delta$ . . . . .	9
3.3	Dimensions of an equivalent T-stub flange [7] . . . . .	14
3.4	Effective lengths for an unstiffened column flange in a bolted connection [28] . . . . .	15
3.5	Design resistance $F_{T,Rd}$ of a T-stub flange [7] . . . . .	16
3.6	Schemes of the geometric dimensions for bolt-rows close to a stiffener [28] . . . . .	18
3.7	Effective lengths for a stiffened column flange in a bolted connection [28] . . . . .	19
3.8	Effective lengths for an extended end-plate [28] . . . . .	19
3.9	Illustration of the lever arms of a typical beam-to-column joint . . . . .	22
3.10	Hogging bending moment - $n + 1$ distributions of internal forces of the joint from Figure 3.9	24
3.11	Sagging bending moment - $n + 1$ distributions of internal forces of the joint from Figure 3.9	25
3.12	Characteristic M-N resistance points of the joint from Figure 3.9 . . . . .	25
3.13	Ductile resistance interaction curve of the joint from Figure 3.9 . . . . .	26
3.14	Local numerical studies - FAILNOMORE joints configurations numerical models . . . . .	28
3.15	Local numerical studies - Behaviour laws associated to the different elements . . . . .	29
3.16	FAILNOMORE - Joint configuration A1 - Technical drawing . . . . .	32
3.17	FAILNOMORE - Joint configuration A2 - Technical drawing . . . . .	33
3.18	FAILNOMORE - Joint configuration B1 - Technical drawing . . . . .	33
3.19	FAILNOMORE - Joint configuration B3 - Technical drawing . . . . .	34
3.20	FAILNOMORE - Joint configuration C2 - Technical drawing . . . . .	34
3.21	FAILNOMORE - Joint configuration C3 - Technical drawing . . . . .	35
3.22	Coimbra - Flush end-plate joint configuration - Technical drawing . . . . .	36
3.23	Coimbra - Extended end-plate joint configuration - Technical drawing . . . . .	37
3.24	Cerfontaine thesis example - Technical drawing . . . . .	39
3.25	FAILNOMORE - Joint configurations A1 & A2 - Ductile resistance interaction curves - 8. . . . .	48
3.26	FAILNOMORE - Joint configurations B1 & B3 - Ductile resistance interaction curves - 8. . . . .	49
3.27	FAILNOMORE - Joint configurations C2 & C3 - Ductile resistance interaction curves - 8. . . . .	49
3.28	Coimbra - Flush end-plate configuration - Ductile curves and experimental results . . . . .	54
3.29	Coimbra - Extended end-plate configuration - Ductile curves and experimental results . . . . .	55
3.30	Coimbra - Flush end-plate configuration - Mean end-plate thickness ( $t_{ep} = 15.38$ mm) . . . . .	56
3.31	Coimbra - Extended end-plate configuration - Mean end-plate thickness ( $t_{ep} = 15.58$ mm) . . . . .	56
3.32	Parametric analysis - Cerfontaine example - Variation of the column steel grade . . . . .	58
3.33	Parametric analysis - Configuration C2 - Variation of the beam steel grade . . . . .	58

3.34	Parametric analysis - Cerfontaine example - Variation of the end-plate steel grade . . . . .	59
3.35	Parametric analysis - Configuration C2 - Variation of the bolts steel grade . . . . .	59
3.36	Parametric analysis - Configuration A1 - Increase of the end-plate thickness . . . . .	60
3.37	Parametric analysis - Cerfontaine example - Decrease of the end-plate thickness . . . . .	61
3.38	Parametric analysis - Configuration C2 - Decrease of the column flange thickness . . . . .	61
3.39	Parametric analysis - Configuration A1 - Variation of the transformation parameter $\beta$ . . .	62
3.40	Local numerical studies - Configuration C2 - $M - \phi$ curves - Hogging bending moment . .	65
3.41	Local numerical studies - Configuration C2 - $M - \phi$ curves - Sagging bending moment . .	65
4.1	FAILNOMORE - Joint configuration A1 - M-N interaction criteria according to standards .	67
4.2	FAILNOMORE - Joint configuration A1 - Six-point criterion . . . . .	69
4.3	FAILNOMORE - Joint configuration A1 - Eight-point criterion without non-interact. thresh- olds . . . . .	70
4.4	FAILNOMORE - Joint configuration A1 - Eight-point criterion with non-interact. thresholds	72
4.5	FAILNOMORE - Joint configuration A2 - New M-N interaction criteria . . . . .	73
4.6	FAILNOMORE - Joint configuration B1 - New M-N interaction criteria . . . . .	74
4.7	FAILNOMORE - Joint configuration B3 - New M-N interaction criteria . . . . .	75
4.8	FAILNOMORE - Joint configuration C2 - New M-N interaction criteria . . . . .	76
4.9	FAILNOMORE - Joint configuration C3 - New M-N interaction criteria . . . . .	77
4.10	Cerfontaine example - New M-N interaction criteria . . . . .	78
A.1	FAILNOMORE - Joint configurations A1 - Technical drawing . . . . .	83
A.2	FAILNOMORE - Configuration A1 - Hogging bending moment - $n + 1$ distributions of int. forces . . . . .	92
A.3	FAILNOMORE - Configuration A1 - Sagging bending moment - $n + 1$ distributions of int. forces . . . . .	93
A.4	FAILNOMORE - Joint configuration A1 - Ductile resistance interaction curve - 8. . . . .	94
A.5	FAILNOMORE - Joint configuration A2 - Technical drawing . . . . .	95
A.6	FAILNOMORE - Joint configuration A2 - Ductile resistance interaction curve - 8. . . . .	96
A.7	FAILNOMORE - Joint configuration B1 - Technical drawing . . . . .	97
A.8	FAILNOMORE - Joint configuration B1 - Ductile resistance interaction curve - 8. . . . .	99
A.9	FAILNOMORE - Joint configurations B3 - Technical drawing . . . . .	99
A.10	FAILNOMORE - Joint configuration B3 - Ductile resistance interaction curve - 8. . . . .	101
A.11	FAILNOMORE - Joint configuration C2 - Technical drawing . . . . .	102
A.12	FAILNOMORE - Joint configuration C2 - Ductile resistance interaction curve - 8. . . . .	104
A.13	FAILNOMORE - Joint configurations C3 - Technical drawing . . . . .	105
A.14	FAILNOMORE - Joint configuration C3 - Ductile resistance interaction curve - 8. . . . .	107
B.1	Coimbra - Flush end-plate joint configuration - Technical drawing . . . . .	108
B.2	Coimbra - Flush end-plate configuration - Four ductile resistance interaction curves - 8. . .	110
B.3	Coimbra - Extended end-plate joint configuration - Technical drawing . . . . .	111
B.4	Coimbra - Extended end-plate configuration - Four ductile resistance interaction curves - 8.	113
B.5	Coimbra - End-plate and beam dimensions measured in laboratory [15] . . . . .	114
B.6	Coimbra - Column dimensions measured in laboratory [15] . . . . .	114
B.7	Coimbra - FE tests - Actual end-plate and beam geometrical properties [15] . . . . .	115
B.8	Coimbra - FE tests - Actual column geometrical properties [15] . . . . .	116
B.9	Coimbra - EE tests - Actual end-plate and beam geometrical properties [15] . . . . .	117
B.10	Coimbra - EE tests - Actual column geometrical properties [15] . . . . .	118
C.1	Parametric analysis - Variation of the column steel grades . . . . .	120

C.2	Parametric analysis - Variation of the beam steel grades . . . . .	121
C.3	Parametric analysis - Variation of the end-plate steel grades . . . . .	122
C.4	Parametric analysis - Variation of the bolts steel grades . . . . .	123
C.5	Parametric analysis - Increase of the end-plate thickness . . . . .	124
C.6	Parametric analysis - Decrease of the end-plate thickness . . . . .	125
C.7	Parametric analysis - Decrease of the column flange thickness . . . . .	126
C.8	Parametric analysis - Variation of the transformation parameter $\beta$ . . . . .	127



# List of Tables

2.1	Names and abbreviations of the relevant components . . . . .	4
3.1	FAILNOMORE - Names and connected profiles of the different joint configurations [16] . .	31
3.2	FAILNOMORE - Steel sections relevant geometrical properties [2] . . . . .	31
3.3	FAILNOMORE - Bolts geometrical & mechanical properties [1] . . . . .	32
3.4	Coimbra - Steel sections theoretical geometrical properties [2] . . . . .	35
3.5	Coimbra - Bolts theoretical geometrical & mechanical properties [1] . . . . .	36
3.6	Coimbra - Mean steel mechanical properties and standard deviations [13] & [15] . . . . .	37
3.7	Coimbra - Minimum and maximum steel mechanical properties measured in laboratory [15]	38
3.8	Coimbra - Flush end-plate configuration - Experimental results [13] . . . . .	38
3.9	Coimbra - Extended end-plate configuration - Experimental results [15] . . . . .	38
3.10	Cerfontaine example - Steel sections geometrical properties [2] . . . . .	39
3.11	Cerfontaine example - Bolts geometrical & mechanical properties [1] . . . . .	39
3.12	FAILNOMORE - Configuration A1 - Components properties - Individual rows - 3. . . . .	40
3.13	FAILNOMORE - Configuration A1 - Components properties - Group of rows - 3. . . . .	41
3.14	FAILNOMORE - Configuration A1 - Row/Group resistances - 4. . . . .	41
3.15	FAILNOMORE - Configuration A1 - Levers arms and $F_{i,Rd}^+$ & $F_{i,Rd}^-$ resistance values - 5. & 6. .	41
3.16	FAILNOMORE - Configuration A1 - Characteristic M-N resistance points - 7. . . . .	41
3.17	FAILNOMORE - Configuration A1 - COP - Characteristic M-N resistance points . . . . .	42
3.18	FAILNOMORE - Configuration B1 - Components properties - Individual rows - 3. . . . .	43
3.19	FAILNOMORE - Configuration B1 - Components properties - Group of rows - 3. . . . .	43
3.20	FAILNOMORE - Configuration B1 - Row/Group resistances - 4. . . . .	44
3.21	FAILNOMORE - Configuration B1 - Lever arms and $F_{i,Rd}^+$ & $F_{i,Rd}^-$ resistance values - 5. & 6. .	44
3.22	FAILNOMORE - Configuration B1 - Characteristic M-N resistance points - 7. . . . .	44
3.23	FAILNOMORE - Configuration B1 - COP - Characteristic M-N resistance points . . . . .	44
3.24	FAILNOMORE - Configuration C2 - Components properties - Individual rows - 3. . . . .	45
3.25	FAILNOMORE - Configuration C2 - Components properties - Group of rows - 3. . . . .	46
3.26	FAILNOMORE - Configuration C2 - Row/Group resistances - 4. . . . .	47
3.27	FAILNOMORE - Configuration C2 - Lever arms and $F_{i,Rd}^+$ & $F_{i,Rd}^-$ resistance values - 5. & 6. .	47
3.28	FAILNOMORE - Configuration C2 - Characteristic M-N resistance points - 7. . . . .	47
3.29	FAILNOMORE - Configuration C2 - COP - Characteristic M-N resistance points . . . . .	47
3.30	Coimbra - Flush end-plate configuration - Components properties - Individual rows - 3. . .	50
3.31	Coimbra - Flush end-plate configuration - Components properties - Group of rows - 3. . .	50
3.32	Coimbra - Flush end-plate configuration - Row/Group resistances - 4. . . . .	50
3.33	Coimbra - Flush end-plate config. - Lever arms and $F_{i,Rd}^+$ & $F_{i,Rd}^-$ resistance values - 5. & 6. .	51
3.34	Coimbra - Flush end-plate configuration - Theoretical - Characteristic M-N resistance points - 7. . . . .	51
3.35	Coimbra - Flush end-plate configuration - Minimum - Characteristic M-N resistance points - 7. . . . .	51

3.36	Coimbra - Flush end-plate configuration - Mean - Characteristic M-N resistance points - 7.	51
3.37	Coimbra - Flush end-plate configuration - Maximum - Characteristic M-N resistance points - 7. . . . .	51
3.38	Coimbra - Extended end-plate configuration - Components properties - Individual rows - 3.	52
3.39	Coimbra - Extended end-plate configuration - Components properties - Group of rows - 3.	52
3.40	Coimbra - Extended end-plate configuration - Row/Group resistances - 4. . . . .	52
3.41	Coimbra - Extended end-plate config. - Lever arms and $F_{i,Rd}^+$ & $F_{i,Rd}^-$ resistance values - 5. & 6.	53
3.42	Coimbra - Extended end-plate config. - Theoretical - Characteristic M-N resistance points - 7.	53
3.43	Coimbra - Extended end-plate config. - Minimum - Characteristic M-N resistance points - 7.	53
3.44	Coimbra - Extended end-plate config. - Mean - Characteristic M-N resistance points - 7. . .	53
3.45	Coimbra - Extended end-plate config. - Maximum - Characteristic M-N resistance points - 7.	54
3.46	Local numerical studies - Configuration A1 - Characteristic M-N resistance points . . . . .	63
3.47	Local numerical studies - Configuration B1 - Characteristic M-N resistance points . . . . .	64
3.48	Local numerical studies - Configuration C2 - Characteristic M-N resistance points . . . . .	64
4.1	FAILNOMORE - Joint configuration A1 - Threshold values . . . . .	67
4.2	FAILNOMORE - Joint configuration A1 - Horizontal gap - "Non-interaction" thresholds . .	71
4.3	FAILNOMORE - Joint configuration A1 - Horizontal gap - Maximum bending moment . .	71
4.4	FAILNOMORE - Joint configuration A2 - Threshold values . . . . .	73
4.5	FAILNOMORE - Joint configuration A2 - Horizontal gap - "Non-interaction" thresholds . .	73
4.6	FAILNOMORE - Joint configuration A2 - Horizontal gap - Maximum bending moment . .	73
4.7	FAILNOMORE - Joint configuration B1 - Threshold values . . . . .	74
4.8	FAILNOMORE - Joint configuration B1 - Horizontal gap - "Non-interaction" thresholds . .	74
4.9	FAILNOMORE - Joint configuration B1 - Horizontal gap - Maximum bending moment . .	74
4.10	FAILNOMORE - Joint configuration B3 - Threshold values . . . . .	75
4.11	FAILNOMORE - Joint configuration B3 - Horizontal gap - "Non-interaction" thresholds . .	75
4.12	FAILNOMORE - Joint configuration B3 - Horizontal gap - Maximum bending moment . .	75
4.13	FAILNOMORE - Joint configuration C2 - Threshold values . . . . .	76
4.14	FAILNOMORE - Joint configuration C2 - Horizontal gap - "Non-interaction" thresholds . .	76
4.15	FAILNOMORE - Joint configuration C2 - Horizontal gap - Maximum bending moment . .	76
4.16	FAILNOMORE - Joint configuration C3 - Threshold values . . . . .	77
4.17	FAILNOMORE - Joint configuration C3 - Horizontal gap - "Non-interaction" thresholds . .	77
4.18	FAILNOMORE - Joint configuration C3 - Horizontal gap - Maximum bending moment . .	77
A.1	FAILNOMORE - Configuration A1 - Components properties - Individual rows - 3. . . . .	91
A.2	FAILNOMORE - Configuration A1 - Components properties - Group of rows - 3. . . . .	91
A.3	FAILNOMORE - Configuration A1 - Row/Group resistances - 4. . . . .	91
A.4	FAILNOMORE - Configuration A1 - Lever arms and $F_{i,Rd}^+$ & $F_{i,Rd}^-$ resistance values - 5. & 6.	92
A.5	FAILNOMORE - Configuration A1 - Characteristic M-N resistance points - 7. . . . .	94
A.6	FAILNOMORE - Configuration A2 - Components properties - Group of rows - 3. . . . .	95
A.7	FAILNOMORE - Configuration A2 - Components properties - Group of rows - 3. . . . .	95
A.8	FAILNOMORE - Configuration A2 - Row/Group resistances - 4. . . . .	96
A.9	FAILNOMORE - Configuration A2 - Lever arms and $F_{i,Rd}^+$ & $F_{i,Rd}^-$ resistance values - 5. & 6.	96
A.10	FAILNOMORE - Configuration A2 - Characteristic M-N resistance points - 7. . . . .	96
A.11	FAILNOMORE - Configuration B1 - Components properties - Individual rows - 3. . . . .	97
A.12	FAILNOMORE - Configuration B1 - Components properties - Group of rows - 3. . . . .	98
A.13	FAILNOMORE - Configuration B1 - Row/Group resistances - 4. . . . .	98
A.14	FAILNOMORE - Configuration B1 - Lever arms and $F_{i,Rd}^+$ & $F_{i,Rd}^-$ resistance values - 5. & 6. .	98
A.15	FAILNOMORE - Configuration B1 - Characteristic M-N resistance points - 7. . . . .	98
A.16	FAILNOMORE - Configuration B3 - Components properties - Individual rows - 3. . . . .	100

A.17	FAILNOMORE - Configuration B3 - Components properties - Group of rows - 3.	100
A.18	FAILNOMORE - Configuration B3 - Row/Group resistances - 4.	100
A.19	FAILNOMORE - Configuration B3 - Lever arms and $F_{i,Rd}^+$ & $F_{i,Rd}^-$ resistance values - 5. & 6.	101
A.20	FAILNOMORE - Configuration B3 - Characteristic M-N resistance points - 7.	101
A.21	FAILNOMORE - Configuration C2 - Components properties - Individual rows - 3.	102
A.22	FAILNOMORE - Configuration C2 - Components properties - Group of rows - 3.	103
A.23	FAILNOMORE - Configuration C2 - Row/Group resistances - 4.	104
A.24	FAILNOMORE - Configuration C2 - Lever arms and $F_{i,Rd}^+$ & $F_{i,Rd}^-$ resistance values - 5. & 6.	104
A.25	FAILNOMORE - Configuration C2 - Characteristic M-N resistance points - 7.	104
A.26	FAILNOMORE - Configuration C3 - Components properties - Individual rows - 3.	105
A.27	FAILNOMORE - Configuration C3 - Components properties - Group of rows - 3.	106
A.28	FAILNOMORE - Configuration C3 - Row/Group resistances - 4.	107
A.29	FAILNOMORE - Configuration C3 - Lever arms and $F_{i,Rd}^+$ & $F_{i,Rd}^-$ resistance values - 5. & 6.	107
A.30	FAILNOMORE - Configuration C3 - Characteristic M-N resistance points - 7.	107
B.1	Coimbra - Flush end-plate configuration - Components properties - Individual rows - 3.	109
B.2	Coimbra - Flush end-plate configuration - Components properties - Group of rows - 3.	109
B.3	Coimbra - Flush end-plate configuration - Row/Group resistances - 4.	109
B.4	Coimbra - Flush end-plate config. - Lever arms and $F_{i,Rd}^+$ & $F_{i,Rd}^-$ resistance values - 5. & 6.	109
B.5	Coimbra - Flush end-plate configuration - Theoretical - Characteristic M-N resistance points - 7.	109
B.6	Coimbra - Flush end-plate configuration - Minimum - Characteristic M-N resistance points - 7.	110
B.7	Coimbra - Flush end-plate configuration - Mean - Characteristic M-N resistance points - 7.	110
B.8	Coimbra - Flush end-plate configuration - Maximum - Characteristic M-N resistance points - 7.	110
B.9	Coimbra - Extended end-plate configuration - Components properties - Individual rows - 3.	111
B.10	Coimbra - Extended end-plate configuration - Components properties - Group of rows - 3.	112
B.11	Coimbra - Extended end-plate configuration - Row/Group resistances - 4.	112
B.12	Coimbra - Extended end-plate config. - Lever arms and $F_{i,Rd}^+$ & $F_{i,Rd}^-$ resistance values - 5. & 6.	112
B.13	Coimbra - Extended end-plate config. - Theoretical - Characteristic M-N resistance points - 7.	112
B.14	Coimbra - Extended end-plate config. - Minimum - Characteristic M-N resistance points - 7.	112
B.15	Coimbra - Extended end-plate config. - Mean - Characteristic M-N resistance points - 7.	113
B.16	Coimbra - Extended end-plate config. - Maximum - Characteristic M-N resistance points - 7.	113

# Chapter 1

## Introduction

For many years now, the characterisation of structural steel joints has been the subject of extensive research and efforts, among others in [3, 18, 25], aimed at better understanding their behaviour and improving their design. Although joints are typically subjected only to shear ( $V$ ) and/or bending ( $M$ ) forces in most common configurations, they can also face the presence of axial ( $N$ ) forces in connected members. This situation can arise, for example, in moment-resisting column bases, in joints with inclined beams in industrial frames, or increasingly in cases where structural robustness must be assessed under various exceptional event scenarios, particularly through the application of the alternative load path method. Illustrations of these different configurations are shown in Figures 1.1a, 1.1b, & 1.1c, respectively.

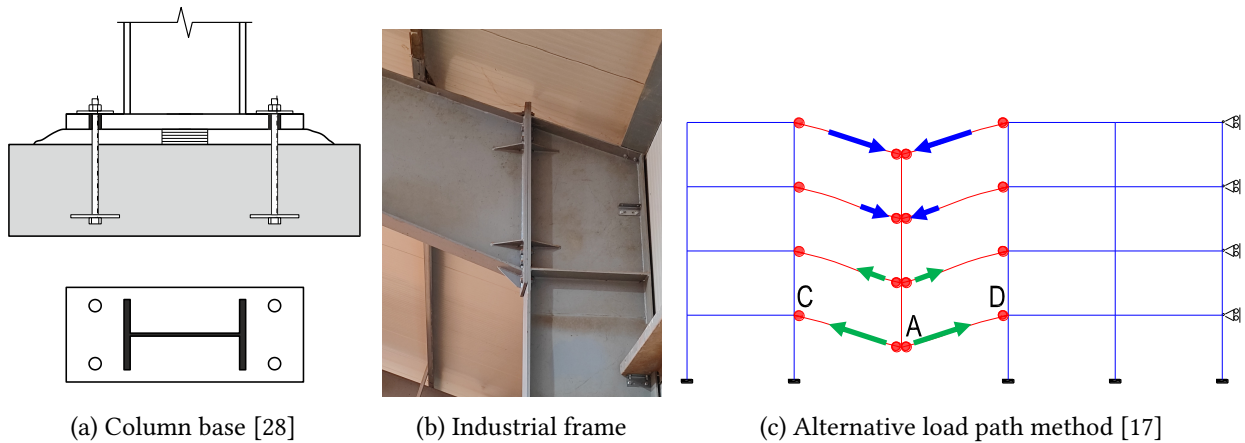


Figure 1.1: Examples of structural steel joints under M-N

Thanks to the component method, developed notably by J.-P. Jaspart & K. Weynand and implemented in EN 1993-1-8:2005 [7], it is theoretically possible to characterise any structural steel joint, provided that all its active components have been fully identified, characterised, and assembled. However, the assembly procedure currently recommended by the standard is not suitable for joints under M-N. To design this type of joint, only a simplified M-N interaction criterion is proposed, as shown in Figure 1.2. It should also be noted that the standard provides neither a methodology for determining joint resistance under pure axial loading ( $N_{Rd,tension}$  &  $N_{Rd,compression}$ ), nor a scientific justification for the threshold value ( $5\% N_{Rd,beam}$ ) below which the presence of an axial force can be completely ignored.

To address this gap, F. Cerfontaine developed a universal analytical method in his Ph.D. thesis [3], which allows the derivation of a comprehensive resistance interaction curve for both ductile and non-ductile joints under M-N. He also identified several safety concerns associated with the current interaction criterion defined in the standard.

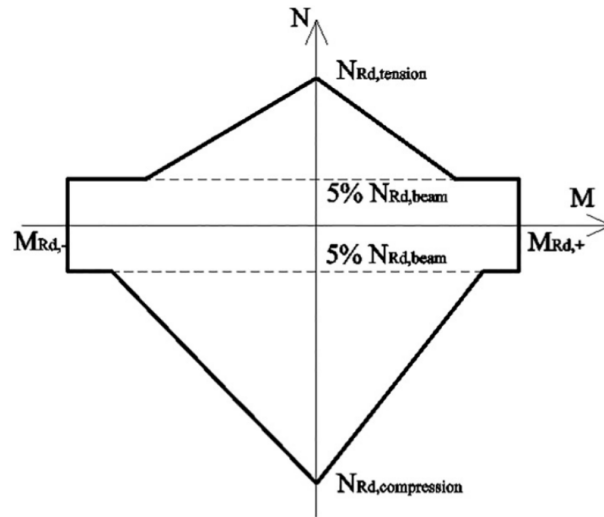


Figure 1.2: EN 1993-1-8:2005 - Current M-N interaction criterion proposed [19]

This Master thesis therefore aligns with the extensive research efforts previously conducted at the University of Liège by F. Cerfontaine [3] and J.-F. Demonceau [18], the latter having extended the range of applications of the Cerfontaine model to steel-concrete composite joints.

First, a state-of-the-art review is conducted to provide a concise overview of the key information related to the topic. Subsequently, advanced analytical and numerical models are employed to characterise various joint configurations subjected to bending and axial forces. The results obtained from the Cerfontaine model will be analysed and compared with those generated by the COP software [20] and with the experimental tests carried out at the University of Coimbra [13, 14, 15]. In addition, a parametric analysis of several mechanical and geometrical joint properties will also be performed.

Drawing on the acquired knowledge, a critical and objective assessment will be carried out on the M-N interaction criteria proposed in the current and the upcoming versions of the European standard (EN 1993-1-8:2005 [7] & EN 1993-1-8:2024 [11]). Then, on the basis of the identified shortcomings, several new M-N interaction criteria will be suggested. The calculation procedures associated with these design recommendations will also be presented in detail, particularly with regard to their potential inclusion in a future version of Eurocode 3.

# Chapter 2

## State-of-the-art

In this second chapter, a brief overview of the most relevant knowledge on the topic of this Master thesis is proposed. The component method, which is the current reference for characterising and designing structural steel joints, will first be introduced. Next, a brief summary of the research carried out by F. Cerfontaine on joints subjected to bending and axial forces, as part of his Ph.D. thesis, will be presented. Finally, a brief description of the finite element numerical model developed at the University of Liège is provided.

### 2.1 Standard model

Historically, joints in steel structures were typically assumed to be pinned or rigid to perform structural analyses. However, numerous studies have since shown that the actual behaviour of these joints is significantly more complex than these simplified assumptions. These studies have also shown that considering this complexity can not only help optimise the design of the joints themselves but also improve the conception of the entire structure, ultimately leading to indirect economic and ecological benefits.

It is, among other things, for all these reasons that a general approach to design structural steel joints, commonly known as the component method, has been introduced since several versions of Eurocode 3. The core principle of this method is to consider each joint as a unique assembly of various elements, referred to as components, each characterised by specific mechanical properties and behaviours. This conceptual view of the joint can be likened, by analogy, to Lego constructions, where each brick is unique, but their combinations enable the creation of an infinite variety of configurations.

Therefore, the first step of the component method involves identifying the various active components of the joint that will be analysed. For this purpose, Table 6.1 of EN 1993-1-8:2005 [7] can be used as a reference to identify the active components of structural steel joints. Components specific to steel-concrete composite joints also exist and are available in EN 1994-1-1:2005 [5] and in the Ph.D. thesis of J.-F. Demonceau [18]. In Figure 2.1, the active components of a typical beam-to-column joint are identified and located under a pure hogging bending moment. The names, the abbreviations and the zone to which these components belong are, as for them, listed in Table 2.1.

In a second step, each identified component must be fully characterised in terms of its mechanical behaviour. In fact, the resistance, stiffness, and ductility capacity of each component must be determined in order to model them as equivalent translational or rigid springs in the final step of the method. To achieve this, the numerous formulas and tables provided in the standards must be used. Many information and application examples can also be found in the book "Design of joints in steel and composite structures" written by J.-P. Jaspart and K. Weynand [28].

Table 2.1: Names and abbreviations of the relevant components

Component name	Abbreviation	Zone
Column web panel in shear	CWS	Shear
Column web in transverse compression	CWC	Compression
Beam flange and web in compression	BFC	
Bolts in tension	BT	Tension
Column flange in transverse bending	CFB	
Column web in transverse tension	CWT	
End-plate in bending	EPB	
Beam web in tension	BWT	

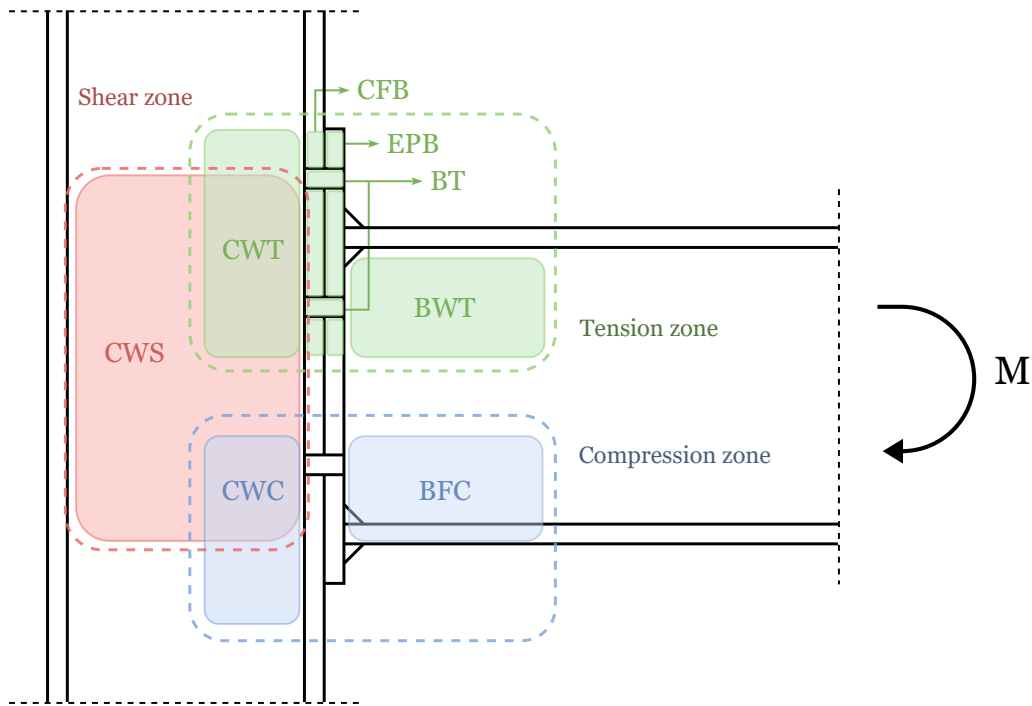


Figure 2.1: Active components of a typical joint under pure hogging bending moment [30]

Once all the mechanical properties of the components have been determined, the third and final step of the method, known as the assembly procedure, can be performed. During this procedure, the components of the joint configuration under study are modelled as translational and rigid springs, and assembled to form a mechanical model that accurately represents the actual behaviour of the joint. As mentioned above, the properties used to define the behaviour laws of these springs are directly derived from the characterisation step. An example of such a mechanical model is shown in Figure 2.2 for a typical beam-to-column joint with an extended end-plate.

This model allows a complete characterisation of the joint behaviour, provided that it is predominantly subject to bending. By applying the assembly procedure described in [7] or [28], as done in the COP software [20], it becomes possible to derive the pure bending resistance of the joint  $M_{j,Rd}$ , its initial rotational stiffness  $S_{j,ini}$ , and in some cases its rotation capacity  $\phi$ . With regard to these values and the criteria provided in the standards, the joint can finally be classified in terms of resistance (full-strength, partial-strength, or pinned), stiffness (rigid, semi-rigid, or pinned), or ductility (ductile, semi-ductile, or brittle). These properties can also be used directly to model the joint as a rotational spring within the framework of structural analyses [27].



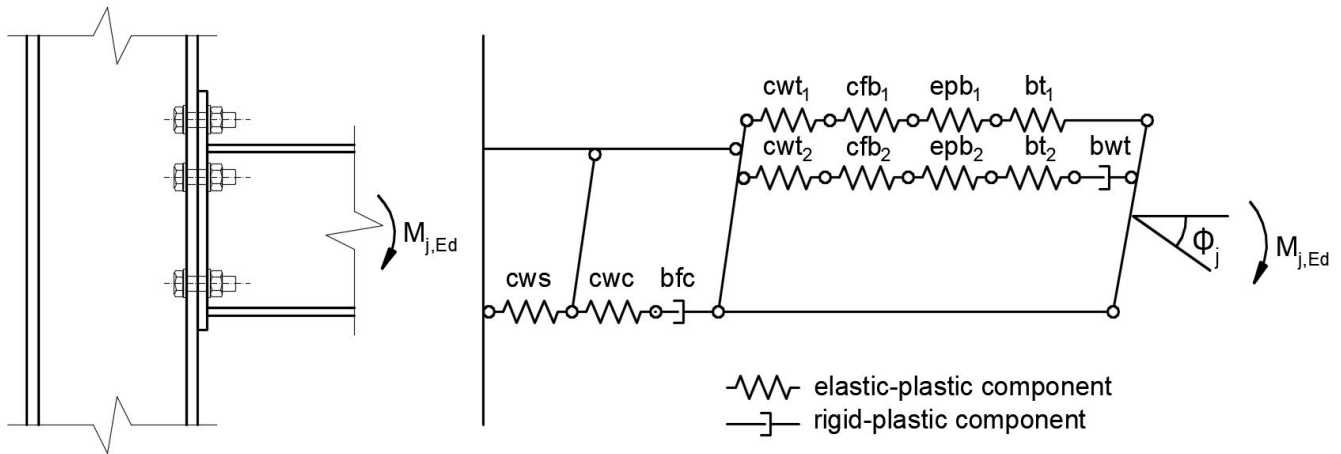


Figure 2.2: Mechanical model of a typical extended end-plate beam-to-column joint [21]

## 2.2 Analytical model

In his Ph.D. thesis [3], F. Cerfontaine starts with the observation that the current assembly procedure recommended by the European standard does not allow the characterisation of joints under M-N.

From this observation, he initially focused on developing a numerical calculation procedure capable of characterising this category of joints. To achieve this, he notably returned to the first two steps of the component method and the fundamental principles behind the assembly procedure. Based on the results provided by this new model, he revealed significant differences with the M-N interaction criteria proposed in the standards and highlighted the lack of safety associated with them.

However, because of the complexity involved in using this numerical model, he subsequently developed an analytical calculation procedure. By applying the static theorem and its assumptions, he was able to propose a first complete analytical characterisation procedure for deriving a resistance interaction curve, accounting for group effects and stress interaction phenomena in the column. Thanks to additional developments aimed at evaluating the deformation state of ductile joints at failure, he was also able to extend this model to joints exhibiting non-ductile behaviours.

As part of his thesis, he finally carried out a comparison between the results of his analytical models and those from experimental campaigns conducted at the University of Prague and the University of Coimbra. These studies led him to conclude that the model developed can accurately predict the resistance capacity of joints under M-N. However, the model did not show good accuracy in predicting the stiffness of the joint.

## 2.3 Numerical model

In recent years, a new mechanical joint model has been developed at the University of Liège, drawing on the latest research on structural steel joints. This new mechanical model was developed to propose an alternative to the current analytical assembly procedure outlined in EN 1993-1-8:2005 [7] (see Figure 2.2), while improving it by integrating the latest developments in the field [12, 29]. Indeed, substantial improvements have been introduced, particularly regarding the shear behaviour of the column web panel, and also to directly account for group effects in the model.



Once all joint components are fully characterised using the analytical formulas provided in the standard, this new mechanical model enables the prediction of structural joint behaviour under M–N interaction, for any applied loading cycle. The Figure 2.3 illustrates this one for a typical single-sided joint with an extended end-plate, subjected to combined bending and axial forces.

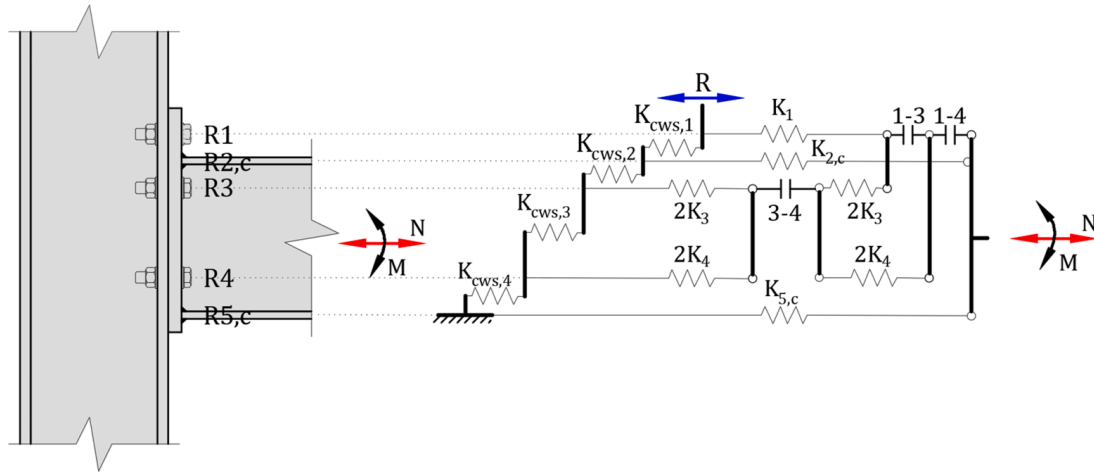


Figure 2.3: New mechanical model of a typical single-sided joint with an extended end-plate [22]

Subsequently, in collaboration with the Greisch design office, this mechanical model was implemented in the FINELG finite element software [23] through the development of a new structural joint element, named ASSEMBLA. This new element will be used in the framework of this thesis to perform several local numerical simulations of joints under M–N. If needed, further information on the mechanical model and its integration in FINELG can be found in the Article [22].

# Chapter 3

## Advanced models

### 3.1 Objectives

The central theme and primary objective of this third chapter is to provide a comprehensive review of the most advanced models for characterising and designing structural steel joints subjected to bending and axial forces. To this end, analytical and numerical methods will be directly applied to various beam-to-column joint configurations derived from the literature or experimental investigations. Furthermore, the results of these application cases will be thoroughly analysed, and comparisons between the different approaches will be made.

First, a detailed analytical study will be conducted on six theoretical joint configurations inspired by the FAILNOMORE project [16], applying the component method and the Cerfontaine model, both briefly introduced in the state-of-the-art chapter. The results will subsequently be compared with those obtained from the commercial software COP, to validate its applicability for future analyses within this thesis.

In a second step, the resistance predictions of the M-N interaction curves, derived using the Cerfontaine model, will be evaluated by comparing them with the results of an experimental campaign conducted at the University of Coimbra. For this purpose, multiple calculations have been carried out, notably taking into account the actual mechanical and geometrical properties of the tested flush and extended end-plate joint configurations.

Subsequently, a parametric analysis of various geometrical and mechanical properties of the joints is performed for three different configurations, including one featuring an inclined connected beam. The purpose of this study is to emphasise the influence of the variations of these properties on the M-N resistance interaction curves and to provide a rationale for the resulting changes. This will also be a valuable opportunity to highlight the emergence of non-ductile joint behaviour.

Finally, local numerical studies will be carried out on three FAILNOMORE joint configurations, which have already been analytically analysed, using the new structural joint element recently implemented in the FINELG finite element software [23]. The results of these models will be compared to the analytical ones, and the benefits of employing such numerical analyses will be clearly highlighted.

Regarding the overall organisation of the chapter, it will follow a standard structure, beginning with a methodology description, followed by a database presentation, and concluding with a results and discussion section.

## 3.2 Methodology

This section presents the various methodologies, tools, and calculation procedures employed to characterise all the joints examined in this thesis. To illustrate and summarise the sequence and nature of the successive steps required to carry out the analytical approach, the methodology tree shown in Figure 3.1 was developed. Since this thesis focusses primarily on ductile joints, only the calculation steps necessary for designing this type of joint are included in this chart and explained in detail in the following pages. As Figure 3.1 is a key component of this work, it will be frequently referenced throughout the remainder of this document, particularly through the coloured numbers assigned to each step.

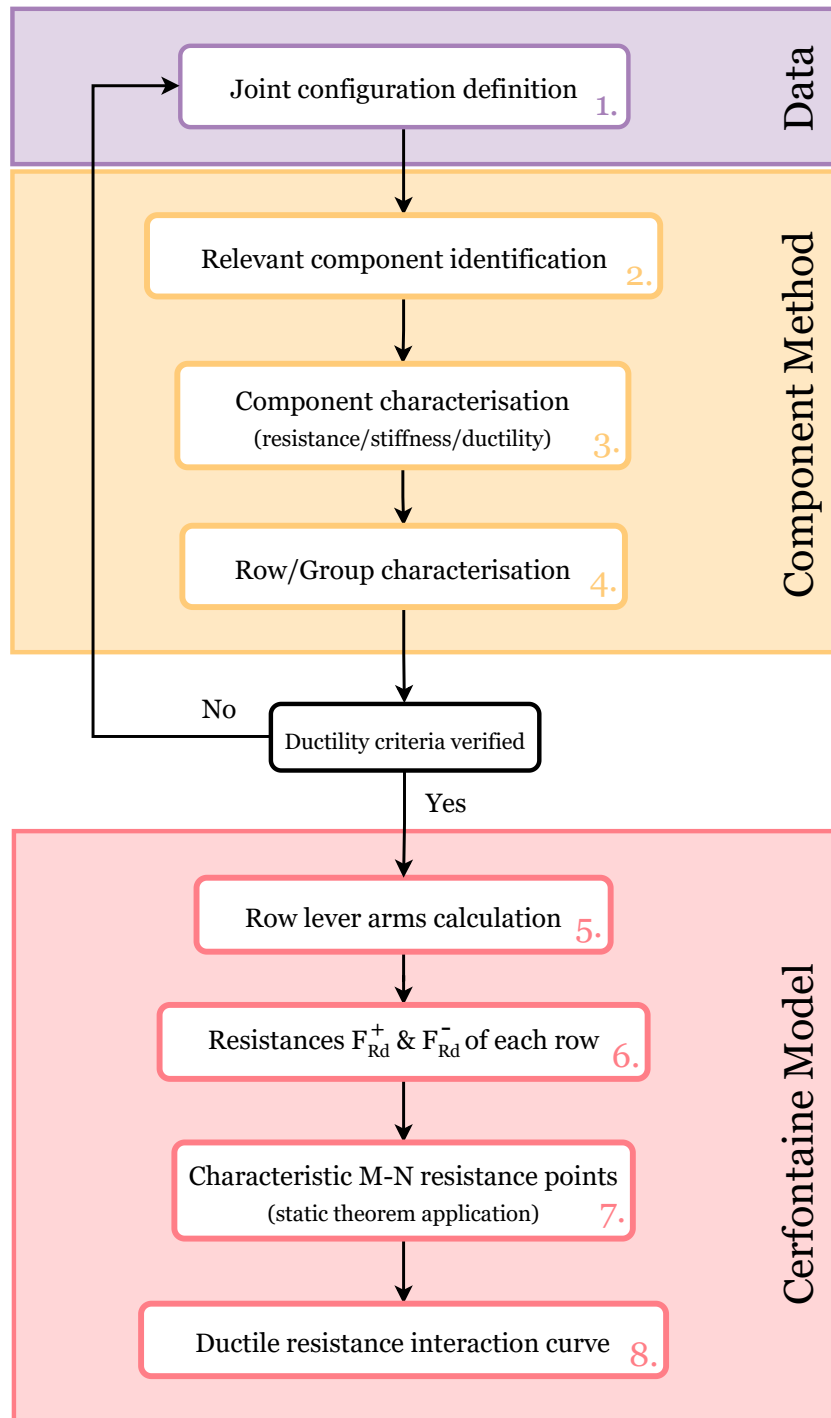


Figure 3.1: Methodology steps to analytically design ductile joints under M-N

### 3.2.1 Component method

In this first subsection, the component method, which was briefly introduced in Chapter 2, will be discussed in greater detail. In fact, after defining the joint configuration to be studied, it is one of the two key steps in the design of joints under M-N, as shown by the methodology tree in Figure 3.1.

Although the component method will be presented here as generally as possible, only the sections relevant to the joint configurations discussed in this thesis will be described. All equations and information provided in this subsection are primarily sourced from EN 1993-1-8:2005 [7] or from the book "Design of joints in steel and composite structures" [28]. However, for some specific formulas, their origin is directly referenced in the paragraphs preceding the latter.

#### Relevant component identification - 2.

The component method, which technically allows the design of any joint within a steel or composite structure, first requires the precise identification of all the different components that together form the studied joint configuration. It is therefore crucial here to understand the path followed by the tension and compression forces developing within the joint. For that, Table 6.1 of EN 1993-1-8:2005 [7], which compiles all the components currently known for steel structures, can be used.

For all joint configurations treated within the framework of this Master thesis, only the components listed in Table 2.1 and illustrated in Figure 2.1 will be useful. For the sake of simplicity, only their abbreviations will be used to refer to them throughout the remainder of this document.

These eight components can also be divided into two distinct categories: one grouping all the components related to the compression rows of the joint (CWS/CWC/BFC) and the other for the components of the tension rows (BT/CFB/CWT/EPB/BWT). This categorisation will later be helpful in determining the critical component that leads to the failure of each row of the joint.

#### Component characterisation - 3.

Having identified all relevant components, it is now necessary to determine, for each of these, the following three properties : their resistance  $F_{Rd}$ , their stiffness  $k$ , and their ductility. In fact, each constitutive component of the joint can individually be characterised by an elastic perfectly plastic behaviour law  $F - \Delta$ , as illustrated in Figure 3.2, based on the values of these mechanical properties. However, an exception must be made for the BT component, which needs to be characterised using a simple elastic law due to its brittle failure mode.

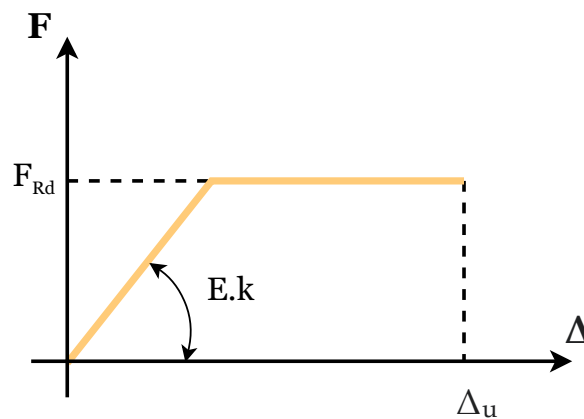


Figure 3.2: Component characterisation - Elastic perfectly plastic behaviour law  $F - \Delta$

The resistance values and stiffness coefficients can be easily derived by applying the various specific equations and formulas presented in the following pages, for each of the components listed in Table 2.1. However, for ductility, it is not yet possible to compute a precise value of the deformation capacity, such as  $\Delta_u$ . Therefore, the different components must be simply classified as ductile or non-ductile on the basis of the validation of certain criteria.

### Column web panel in shear - CWS

#### Resistance

The slenderness of the column web panel must first be checked using the following criterion :

$$\frac{d_c}{t_{wc}} \leq 69\epsilon \quad \text{and} \quad \epsilon = \sqrt{\frac{235}{f_{y,wc}}} \quad (3.1)$$

The design resistance of an unstiffened column web panel can then be computed and directly "turned" into a "beam-force" resistance using the transformation parameter  $\beta$ .

$$V_{wp,Rd} = \frac{0.9f_{y,wc} A_{vc}}{\sqrt{3}\gamma_{M0}} \quad (3.2)$$

$$F_{wp,Rd} = \frac{V_{wp,Rd}}{\beta} \quad (3.3)$$

with the following parameters :

- $\beta$  The transformation parameter [-]
- $\gamma_{M0}$  The partial safety factor for resistance of cross-sections whatever the class is [-]
- $\epsilon$  A coefficient depending on  $f_y$  [-]
- $A_{vc}$  The shear area of the column [mm<sup>2</sup>]
- $d_c$  The clear depth of the column web [mm]
- $f_{y,wc}$  The design yield strength of the column web [MPa]
- $F_{wp,Rd}$  The "beam-force" resistance of the column web panel [N]
- $t_{wc}$  The thickness of the column web [mm]
- $V_{wp,Rd}$  The design plastic shear resistance of the column web panel [N]

In this thesis, the transformation parameter  $\beta$ , which depends on the ratio between the web panel shear force and the compressive and tensile connection forces, will be kept constant throughout the entire component characterisation procedure. A safe approximate value of this parameter can be determined using Table 5.4 of EN 1993-1-8:2005 [7], based notably on the type of joint configuration encountered (single-sided or double-sided).

#### Ductility

The CWS component is recognised for its high deformation capacity, which allows plastic redistribution between the rows of the joint. Therefore, it is considered as a ductile component.

### Column web in transverse compression - CWC

#### Resistance

For a bolted end-plate connection, the effective compression width can be expressed as :

$$b_{eff,c,wc} = t_{fb} + 2\sqrt{2}a_p + 5(t_{fc} + s) + s_p \quad (3.4)$$

for a rolled I or H section column :  $s = r_c$

with :

- $a_p$  The throat thickness of the welds between the beam flanges and the end-plate [mm]
- $r_c$  The root radius of the column [mm]
- $s_p$  The total dispersion length at 45° through the end-plate (at least  $t_{ep}$  and up to  $2t_{ep}$ ) [mm]
- $t_{ep}$  The thickness of the end-plate [mm]
- $t_{fb}$  The thickness of the beam flange [mm]
- $t_{fc}$  The thickness of the column flange [mm]

The design resistance of the column web in transverse compression can then be computed as :

$$F_{c,wc,Rd} = \frac{\omega k_{wc} b_{eff,c,wc} t_{wc} f_{y,wc}}{\gamma_{M0}} \quad (3.5)$$

The reduction factor  $k_{wc}$ , which accounts for the possible stress interaction with the maximum longitudinal stress  $\sigma_{com,Ed}$  in the column, must be calculated based on the formulas provided in Section 6.2.6.2(2) of EN 1993-1-8:2005 [7]. The shear stress interaction coefficient  $\omega$  can be obtained from Table 6.3 of EN 1993-1-8:2005 [7], given the value of the transformation parameter  $\beta$ .

However, this resistance value must be limited to the result computed using the following equation to account for any instability failure mode of the web under transverse compression, such as crushing, crippling, etc.

$$F_{c,wc,Rd} \leq \frac{\omega k_{wc} \rho b_{eff,c,wc} t_{wc} f_{y,wc}}{\gamma_{M1}} \quad (3.6)$$

The slenderness of the plate  $\bar{\lambda}_p$  and the reduction factor for plate buckling  $\rho$  are defined by Equations (3.7) to (3.9).

$$\bar{\lambda}_p = 0.932 \sqrt{\frac{b_{eff,c,wc} d_c f_{y,wc}}{E t_{wc}^2}} \quad (3.7)$$

$$\text{if } \bar{\lambda}_p \leq 0.72 : \quad \rho = 1.0 \quad (3.8)$$

$$\text{if } \bar{\lambda}_p > 0.72 : \quad \rho = \frac{\bar{\lambda}_p - 0.2}{\bar{\lambda}_p^2} \quad (3.9)$$

where :

- $\gamma_{M1}$  The partial safety factor for resistance of members to instability assessed by member checks [-]
- $\bar{\lambda}_p$  The plate slenderness [-]
- $\rho$  The reduction factor for plate buckling [-]
- $E$  The Young modulus of the steel [MPa]

### **Stiffness**

The stiffness coefficient of an "unstiffened column web in transverse compression" is defined as :

$$k_2 = \frac{0.7b_{eff,c,wc} t_{wc}}{d_c} \quad (3.10)$$

### **Ductility**

Today, the deformation capacity of the CWC component is not yet fully mastered. No equation is currently provided in EN 1993-1-8:2005 [7] to estimate this property of the component. However, recent research conducted at the University of Liège has led to a better characterisation of this component and suggests new analytical expressions for this purpose. Among other findings, experimental tests have shown that the CWC component generally exhibits good deformation capacity, although this may be significantly compromised when failure is associated with an instability of the column web. Therefore, in this thesis, it was chosen to consider the CWC component as ductile. If necessary, more information on the subject can be found in "Characterization of unstiffened column webs in transverse compression in steel beam-to-column joints" [26].

## **Beam flange and web in compression - BFC**

### **Resistance**

The design compression resistance of the combined beam flange and web can be derived simply using the following equation :

$$F_{c,fb,Rd} = \frac{M_{c,Rd}}{h_b - t_{fb}} \quad (3.11)$$

with :

- $h_b$  The depth of the beam [mm]
- $M_{c,Rd}$  The design moment resistance of the beam cross-section, as defined in EN 1993-1-1:2005 [6]

### **Stiffness**

The stiffness coefficient of the BFC component has by definition to be set to :

$$k_7 = \infty \quad (3.12)$$

### **Ductility**

The ductility of the BFC component can be determined by knowing the beam cross-section class, which is already required to compute the  $M_{c,Rd}$  value. Therefore, a class 1 or 2 beam must be used to consider the component as ductile.

### **Bolts in tension - BT**

#### **Resistance**

The design tension resistance of one non-countersunk bolt can be computed as :

$$F_{t,Rd} = \frac{k_2 f_{ub} A_s}{\gamma_{M2}} \quad (3.13)$$

where  $k_2 = 0.9$  for non-countersunk bolts

#### **Stiffness**

The stiffness coefficient for a group of two bolts in tension must be derived as follows :

$$L_b = t_{fc} + t_{ep} + 2h_w + \frac{k_b + m_n}{2} \quad (3.14)$$

$$k_{10} = \frac{1.6A_s}{L_b} \quad (3.15)$$

with :

- $\gamma_{M2}$  The partial factor for resistance of cross-sections in tension to fracture [-]
- $A_s$  The tensile stress area of the bolt in the threaded part [mm<sup>2</sup>]
- $f_{ub}$  The ultimate tensile strength of the bolt [MPa]
- $h_w$  The thickness of a washer [mm]
- $k_2$  A coefficient depending on the bolt type [-]
- $k_b$  The height of the bolt head [mm]
- $L_b$  The bolt elongation length [mm]
- $m_n$  The height of the nut [mm]

### **Ductility**

The BT component is always considered brittle and therefore does not allow plastic redistribution between the rows of the joint.

### **Column flange in transverse bending - CFB**

Here, two different calculations can be performed. The first will lead to the determination of an individual row resistance, while the second provides the resistance of the group mechanism that is potentially developing in the column flange, between several tension rows of the joint.



For this purpose, an equivalent T-stub flange can be studied. The resistance and failure mode of the latter can in fact be linked to the behaviour of an unstiffened column flange in bending that presents similar geometrical properties. Three distinct failure modes can occur that lead to the failure of the component :

- Mode n°1 Complete yielding of the T-stub flange
- Mode n°2 Bolts failure with yielding of the T-stub flange
- Mode n°3 Bolts failure

### Individual row resistance

First, the main geometrical properties of the equivalent T-stub flange must be determined based on Figure 3.3 or as defined in Figure 3.5.

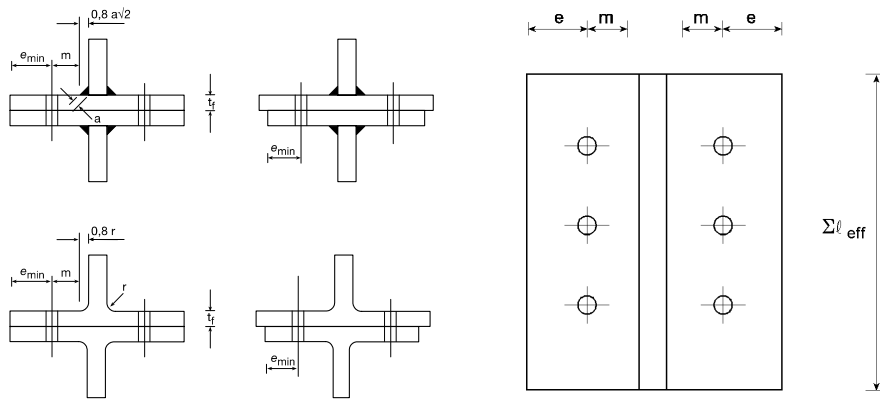


Figure 3.3: Dimensions of an equivalent T-stub flange [7]

Then, two different effective lengths ( $l_{eff,cp}$  &  $l_{eff,nc}$ ) of the equivalent T-stub flange must be calculated, each corresponding to one of the two patterns of plastic lines that can form around the bolts (circular and non-circular). Both effective lengths can be obtained based on the formulas presented in Figure 3.4, function of the longitudinal location of the bolt-row in the column flange. Since none of the joint configurations in this thesis were studied as placed at the extremity of the column profiles, all their tension rows can, individually, be considered as inner bolt rows.

Once these two values are calculated, the effective lengths  $l_{eff,1}$  and  $l_{eff,2}$  associated with a failure mode n°1 and a failure mode n°2 can be obtained, as indicated in Figure 3.4. These values can then be used in the following equations to derive the design plastic moment resistance of the equivalent T-stub flange, for each of these two failure modes.

$$M_{pl,1,Rd} = \frac{0.25 \sum l_{eff,1} t_{fc}^2 f_{y,fc}}{\gamma_{M0}} \quad (3.16)$$

$$M_{pl,2,Rd} = \frac{0.25 \sum l_{eff,2} t_{fc}^2 f_{y,fc}}{\gamma_{M0}} \quad (3.17)$$

where :

- $f_{y,fc}$  The design yield strength of the column flange [MPa]
- $M_{pl,i,Rd}$  The design plastic moment resistance of an equivalent T-stub flanges for mode  $i$  [Nmm]

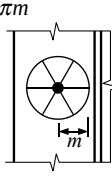
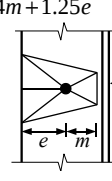
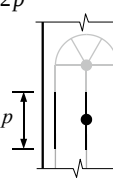
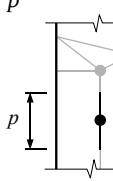
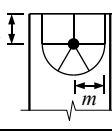
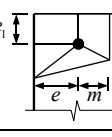
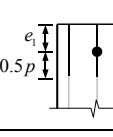
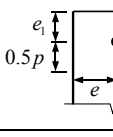
Bolt-row location	Bolt-row considered individually		Bolt-row considered as part of a group of bolt-rows	
	Circular patterns $\ell_{eff,cp}$	Non-circular patterns $\ell_{eff,nc}$	Circular patterns $\ell_{eff,cp}$	Non-circular patterns $\ell_{eff,nc}$
Inner bolt-row				
End bolt-row	The smaller of: $2\pi m$ $\pi m + 2e_1$ 	The smaller of: $4m + 1.25e$ $2m + 0.625e + e_1$ 	The smaller of: $\pi m + p$ $2e_1 + p$ 	The smaller of: $2m + 0.625e + 0.5p$ $e_1 + 0.5p$ 
Mode 1	$\ell_{eff,1} = \min(\ell_{eff,cp}; \ell_{eff,nc})$		$\Sigma \ell_{eff,1} = \min(\Sigma \ell_{eff,cp}; \Sigma \ell_{eff,nc})$	
Mode 2	$\ell_{eff,2} = \ell_{eff,nc}$		$\Sigma \ell_{eff,2} = \Sigma \ell_{eff,nc}$	

Figure 3.4: Effective lengths for an unstiffened column flange in a bolted connection [28]

Three design tension resistances of the equivalent T-stub flange, one for each of the failure modes previously stated, must now be calculated using the formulas provided in Figure 3.5. The prying forces are always assumed to develop here. In this thesis, for failure mode n°1, the calculation method n°2 (alternative method) without backing plates is used.

Finally, the design resistance of the equivalent T-stub flange, and thus that of the CFB component, can be determined by keeping the smallest  $F_{T,i,Rd}$  value, a value that is necessarily associated with the failure mode that will occur first.

$$F_{T,Rd} = \min(F_{T,1,Rd}; F_{T,2,Rd}; F_{T,3,Rd}) \quad (3.18)$$

with :

- $F_{T,i,Rd}$  The design tension resistance of a T-stub flange for mode  $i$  [N]

### Group mechanism resistance

A similar calculation procedure to the one that has just been presented can be applied to determine the design resistance of a group mechanism that appears between several tension rows. The geometrical properties of the equivalent T-stub flange to be used are identical to those already derived, with the exception of its length.

The main difference here lies essentially in the calculation of the effective lengths. In fact, the different bolt-rows must now be considered as part of a group of bolt-rows in Figure 3.4, and their locations must be defined in terms of their relative position within the group mechanism. The two extremity bolt-rows of the group will thus be considered as end bolt-rows, while the others will be assimilated to inner bolt-rows.

	Prying forces may develop, i.e. $L_b \leq L_b^*$		No prying forces
<b>Mode 1</b>	Method 1	Method 2 (alternative method)	$F_{T,1-2,Rd} = \frac{2M_{pl,1,Rd}}{m}$
without backing plates	$F_{T,1,Rd} = \frac{4M_{pl,1,Rd}}{m}$	$F_{T,1,Rd} = \frac{(8n - 2e_w)M_{pl,1,Rd}}{2mn - e_w(m + n)}$	
with backing plates	$F_{T,1,Rd} = \frac{4M_{pl,1,Rd} + 2M_{bp,Rd}}{m}$	$F_{T,1,Rd} = \frac{(8n - 2e_w)M_{pl,1,Rd} + 4nM_{bp,Rd}}{2mn - e_w(m + n)}$	
<b>Mode 2</b>	$F_{T,2,Rd} = \frac{2M_{pl,2,Rd} + n\Sigma F_{t,Rd}}{m + n}$		
<b>Mode 3</b>	$F_{T,3,Rd} = \Sigma F_{t,Rd}$		

Mode 1: Complete yielding of the flange  
Mode 2: Bolt failure with yielding of the flange  
Mode 3: Bolt failure

$L_b$  is - the bolt elongation length, taken equal to the grip length (total thickness of material and washers), plus half the sum of the height of the bolt head and the height of the nut or  
- the anchor bolt elongation length, taken equal to the sum of 8 times the nominal bolt diameter, the grout layer, the plate thickness, the washer and half the height of the nut

$L_b^* = \frac{8,8m^3 A_s}{\Sigma \ell_{eff,1} t_f^3}$

$F_{T,Rd}$  is the design tension resistance of a T-stub flange  
 $Q$  is the prying force

$M_{pl,1,Rd} = 0,25\Sigma \ell_{eff,1} t_f^2 f_y / \gamma_{M0}$

$M_{pl,2,Rd} = 0,25\Sigma \ell_{eff,2} t_f^2 f_y / \gamma_{M0}$

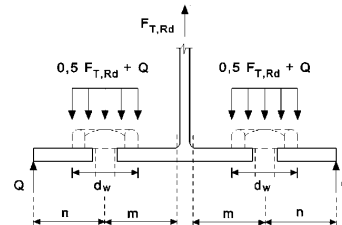
$M_{bp,Rd} = 0,25\Sigma \ell_{eff,1} t_{bp}^2 f_{y,bp} / \gamma_{M0}$

$n = e_{min}$  but  $n \leq 1,25m$

$F_{t,Rd}$  is the design tension resistance of a bolt, see Table 3.4;  
 $\Sigma F_{t,Rd}$  is the total value of  $F_{t,Rd}$  for all the bolts in the T-stub;  
 $\Sigma \ell_{eff,1}$  is the value of  $\Sigma \ell_{eff}$  for mode 1;  
 $\Sigma \ell_{eff,2}$  is the value of  $\Sigma \ell_{eff}$  for mode 2;  
 $e_{min}$ ,  $m$  and  $t_f$  are as indicated in Figure 6.2.  
 $f_{y,bp}$  is the yield strength of the backing plates;  
 $t_{bp}$  is the thickness of the backing plates;  
 $e_w = d_w / 4$ ;  
 $d_w$  is the diameter of the washer, or the width across points of the bolt head or nut, as relevant.

**NOTE 1:** In bolted beam-to-column joints or beam splices it may be assumed that prying forces will develop.

**NOTE 2:** In method 2, the force applied to the T-stub flange by a bolt is assumed to be uniformly distributed under the washer, the bolt head or the nut, as appropriate, see figure, instead of concentrated at the centre-line of the bolt. This assumption leads to a higher value for mode 1, but leaves the values for  $F_{T,1-2,Rd}$  and modes 2 and 3 unchanged.

Figure 3.5: Design resistance  $F_{T,Rd}$  of a T-stub flange [7]

### Stiffness

The stiffness coefficient of the CFB component can be computed by taking  $\ell_{eff}$  as the smallest of the effective lengths (individually or as part of a bolt group) that have already been determined during the resistance calculation procedures.

$$k_4 = \frac{0,9\ell_{eff} t_{fc}^3}{m^3} \quad (3.19)$$

### **Ductility**

The ductility of the CFB component can be determined as a function of the failure mode associated with the  $F_{T,i,Rd}$  value retained in Equation (3.18). If either mode n°1 or mode n°2 is critical, which, as a reminder, corresponds to a full or partial yielding of the T-stub flange, and if Equation (3.20) is satisfied, then the CFB component can be considered as ductile. Instead, if the critical mode is mode n°3, it should be considered as brittle.

$$\min (F_{T,1,Rd} ; F_{T,2,Rd}) \leq 1.9F_{t,Rd} \quad (3.20)$$

Note that only the ductility of the individual bolt-rows needs to be assessed, as a group mechanism cannot be brittle if all the rows composing it individually exhibit ductile behaviours. It should also be mentioned that, in general, an additional criterion must be satisfied in order to carry out a global plastic analysis of the structure (see Section 6.4.2 of EN 1993-1-8:2005 [7]). However, since this type of analysis is not performed in this thesis, it is not necessary to verify it.

### **Column web in transverse tension - CWT**

Similarly to the CFB component, the resistance of the CWT component can be derived for an individual tension row, as well as for a group mechanism forming between several of them.

### **Resistance**

The design resistance of the CWT component can be calculated based on the following equation:

$$F_{t,wc,Rd} = \frac{\omega b_{eff,t,wc} t_{wc} f_{y,wc}}{\gamma_{M0}} \quad (3.21)$$

In this equation, the effective width  $b_{eff,t,wc}$  should be considered equal to the effective length  $l_{eff,i}$  corresponding to the critical failure mode obtained, for the same row or group, for the CFB component ( $l_{eff,1}$  for mode n°1 and  $l_{eff,2}$  for mode n°2 or mode n°3). The shear stress interaction coefficient  $\omega$  can again be obtained from Table 6.3 of EN 1993-1-8:2005 [7], given the value of the transformation parameter  $\beta$ .

### **Stiffness**

The effective width  $b_{eff,t,wc}$  used to compute the stiffness coefficient of the CWT component is actually identical to the effective length  $l_{eff}$  already employed in Equation (3.19).

$$k_3 = \frac{0.7 b_{eff,t,wc} t_{wc}}{d_c} \quad (3.22)$$

### **Ductility**

The CWT component can be considered ductile, provided that normalised steel is used for the column.

### End-plate in bending - EPB

As for the CFB component, the resistance and failure mode of the EPB component can be deduced from the study of an equivalent T-stub flange having similar geometrical properties. The general principle of the calculation procedure being identical to the one already presented for the CFB component, only the specificities for the EPB component will be specified hereafter.

#### Individual row resistance

The different tensions rows on the end-plate can be subdivided into three distinct categories regarding their location towards the two tension flanges of the beam welded to it, these last ones acting indeed as stiffener for the end-plate:

- The bolt-row outside tension flanges of beam (only in case of extended end-plate)
- The first bolt-row inside tension flanges of beam (bolt-row adjacent to a stiffener in Figure 3.7)
- Other inner or end bolt-rows

The geometric dimensions required throughout the resistance calculation procedure can easily be determined on the basis of Figure 3.3, Figure 3.5, and both schemes of Figure 3.6, depending on the category of the row considered.

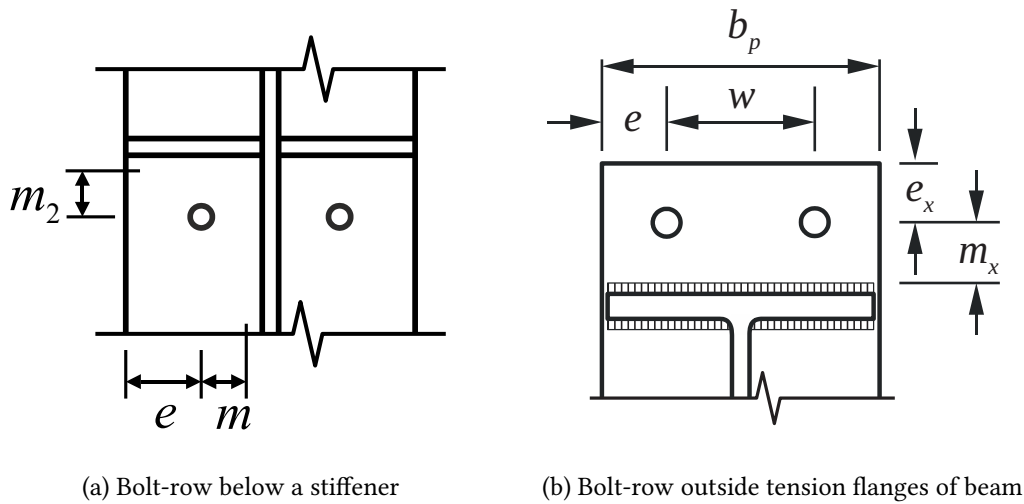


Figure 3.6: Schemes of the geometric dimensions for bolt-rows close to a stiffener [28]

Due to the presence of stiffeners, which alter the shape of the plastic hinge lines that can form around the bolt rows, the new equations presented in Figure 3.7 and Figure 3.8 must, respectively, be used for the categories of the first bolt-row inside the beam tension flanges and of the bolt-row outside the beam tension flanges. For the remaining category, the equations presented in Figure 3.4 must be applied.

The following equations, used to determine the value of the parameter  $\alpha$  in Figure 3.7, are sourced from EN 1993-1-8:2024 [11] and serve as an analytical alternative to the graphical determination method currently proposed in the standard.

$$\alpha = 4 + 1.67 \frac{e}{m} \left( \frac{m}{m_2} \right)^{0.67} \quad (3.23)$$

$$\text{but } \alpha \geq 4 + 1.25 \frac{e}{m} \quad \text{and} \quad \alpha \leq 8 \quad (3.24)$$

The end of the calculations is then the same as for the CFB component, the thickness of the column flange  $t_{fc}$  being simply replaced by the thickness of the end-plate  $t_{ep}$  in Equations (3.16) & (3.17).

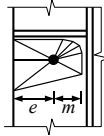
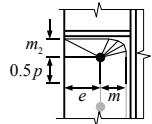
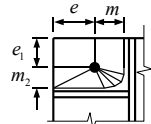
Bolt-row location	Bolt-row considered individually		Bolt-row considered as part of a group of bolt rows	
	Circular patterns $\ell_{eff,cp}$	Non-circular patterns $\ell_{eff,nc}$	Circular patterns $\ell_{eff,cp}$	Non-circular patterns $\ell_{eff,nc}$
Bolt-row adjacent to a stiffener	$2\pi m$	$\alpha m$ 	$\pi m + p$	$0.5p + \alpha m - (2m + 0.625e)$ 
End bolt-row adjacent to a stiffener	The smaller of: $2\pi m$ $\pi m + 2e_1$	The smaller of: $e_1 + \alpha m - (2m + 0.625e)$ 	not relevant	not relevant
Values for $\alpha$ should be obtained from Figure 6.5 For inner bolt-rows and end bolt-row not adjacent to a stiffener, see Table 6.2				

Figure 3.7: Effective lengths for a stiffened column flange in a bolted connection [28]

Bolt-row location *)	Bolt-row considered individually		Bolt-row considered as part of a group of bolt-rows	
	Circular patterns $\ell_{eff,cp}$	Non-circular patterns $\ell_{eff,nc}$	Circular patterns $\ell_{eff,cp}$	Non-circular patterns $\ell_{eff,nc}$
Bolt-row outside tension flange of beam	Smallest of: $2\pi m_x$ $\pi m_x + w$ $\pi m_x + 2e$	Smallest of: $4m_x + 1.25e_x$ $2m_x + 0.625e_x + e$ $0.5b_p$ $2m_v + 0.625e_v + 0.5w$	not relevant	not relevant
Mode 1	$\ell_{eff,1} = \min\left(\ell_{eff,cp}; \ell_{eff,nc}\right)$		$\Sigma \ell_{eff,1} = \min\left(\Sigma \ell_{eff,cp}; \Sigma \ell_{eff,nc}\right)$	
Mode 2	$\ell_{eff,2} = \ell_{eff,nc}$		$\Sigma \ell_{eff,2} = \Sigma \ell_{eff,nc}$	
*) For the first bolt-row below tension flange of beam, see <i>Bolt-row adjacent to a stiffener</i> in Table 6.3.				
*) For other inner bolt-rows or other end bolt-rows, see Table 6.2				

Figure 3.8: Effective lengths for an extended end-plate [28]

### Group mechanism resistance

For the resistances of the group mechanisms, the same steps as those presented for an individual row resistance must be followed once again, but this time with the bolt-rows considered as part of a group of bolt-rows in Figures 3.4, 3.7, & 3.8. It must also be specified that the presence of stiffeners, such as the tension flanges of the welded beam, prevents any appearance of group mechanisms connecting bolt-rows located on each side from these stiffeners.

**Stiffness**

The stiffness coefficient of the EPB component can be computed by taking  $l_{eff}$  as the smallest of the effective lengths (individually or as part of a bolt group) that have already been determined during the resistance calculation procedure.

$$k_5 = \frac{0.9 l_{eff} t_{ep}^3}{m^3} \quad (3.25)$$

**Ductility**

The ductility of the EPB component can be determined in the same manner as the CFB component, with the failure mode to consider nevertheless being the one obtained at the end of the EPB resistance calculation procedure.

**Beam web in tension - BWT**

The resistance of the BWT component can be derived for an individual tension row and for a group mechanism that forms between several of them. However, this component does not need to be characterised for the bolt-row outside the beam tension flanges, as the latter is not located in front of the beam web.

**Resistance**

The design resistance of the BWT component can be calculated on the basis of the following equation:

$$F_{t,wb,Rd} = \frac{b_{eff,t,wb} t_{wb} f_{y,wb}}{\gamma_{M0}} \quad (3.26)$$

with :

- $f_{y,wb}$  The design yield strength of the beam web [MPa]

In this equation, the effective width  $b_{eff,t,wb}$  should be considered equal to the effective length  $l_{eff,i}$  corresponding to the critical failure mode obtained, for the same row or group, for the EPB component ( $l_{eff,1}$  for mode n°1 and  $l_{eff,2}$  for mode n°2 or mode n°3).

**Stiffness**

The stiffness coefficient of the BWT component has by definition to be set to :

$$k_8 = \infty \quad (3.27)$$

**Ductility**

The BWT component can be considered ductile, provided that normalised steel is used for the beam.

### Row/Group characterisation - 4.

Once all components of Table 2.1 have been fully characterised for all individual rows and group mechanisms of the joint studied, their properties must be "assembled" together to derive the resistance  $F_{ii,Rd}$ , stiffness, and ductility of each row, as well as the resistance  $F_{ki,Rd}$  of the groups. To achieve this, a connection can be made here with the division of components into two different categories (compression and tension) in Table 2.1 and the mechanical model in Figure 2.2.

#### **Resistance**

From here, the resistance of the tension and compression components will be defined as positive and negative, respectively, according to Belgian sign conventions on internal forces and to ensure consistency with the subsequent calculations.

Since the translational/rigid springs used to model the various components of the individual tension and compression rows are arranged in series, the overall resistance of these rows is necessarily governed by the resistance of the weakest component, also referred to as the critical component. An identical logic can be followed to determine the resistance of the group mechanisms.

Since the brittle failure of bolts in tension is already taken into account through the mode n°3 in the CFB and EPB components, the resistance of the BT component should not be considered when determining the resistance of a row or group.

#### **Stiffness**

For each individual row, an equivalent stiffness  $k_{eq}$  is typically calculated based on the stiffness coefficients of the components associated with that row. However, since this property is not required for analytically determining the plastic resistance of ductile joints under M-N, the derivation of this equivalent stiffness will not be further elaborated. In this thesis, the stiffness coefficients of the components are exclusively used to characterise the behaviour of the springs from the new mechanical model implemented in the FINELG software, as described in Section 3.2.7.

#### **Ductility**

The ductility of an individual row can be easily determined by knowing the ductility of the critical component of that row. As previously mentioned, a group is necessarily ductile if all the bolt-rows that compose this latter are themselves ductile.



### 3.2.2 Cerfontaine model

The purpose of this second subsection consists in providing comprehensive tools to apply the calculation procedure to derive a complete M-N resistance interaction curve, procedure developed in detail by F. Cerfontaine in his PhD thesis [3]. However, as part of this work, only the steps presented in Figure 3.1, required to compute the full ductile resistance interaction curve of a joint, will be detailed. To apply this calculation procedure, it is essential to ensure that all critical joint components are ductile (see Section 3.2.1) and that all welds can be considered as full-strength.

For the sake of uniformity and universality, a general row notation will be adopted and followed throughout the calculation procedure. The total number of rows in the joint will be denoted as  $n$ . Numbers from 1 to  $n$  will be assigned to each of these rows, moving through the joint from top to bottom, as shown in Figure 3.9. The top and bottom compression rows of the joint will also respectively be designated as "up" and "inf" rows.

#### Row lever arms calculation - 5.

Initially, the lever arms of the joint rows  $h_i$  need to be determined. To achieve this, a reference axis must be defined, around which the resistance bending moment of the joint will be calculated afterwards. In this thesis, the beam axis has been selected as reference.

The rows located above this axis will be defined with positive lever arms, while the rows located below the axis will have negative lever arms, as illustrated on Figure 3.9. The locations of the compression and tension rows are respectively defined as the mid-thickness of the beam flanges and the centre of the bolt holes.

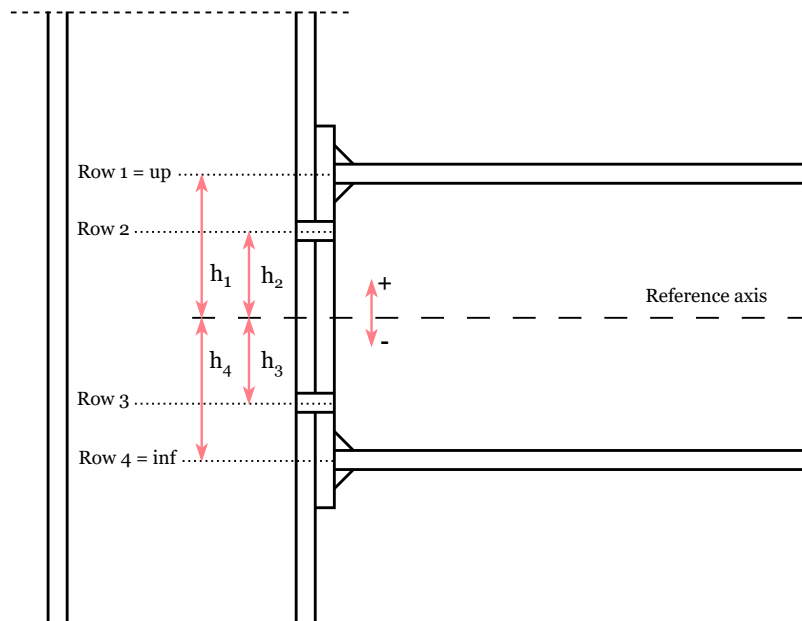


Figure 3.9: Illustration of the lever arms of a typical beam-to-column joint

#### Resistances $F_{Rd}^+$ & $F_{Rd}^-$ of each row - 6.

Before starting the computation of these resistance values, it is necessary to specify the sign convention used for the bending moments in this thesis. Indeed, the hogging and sagging bending moments, which respectively induce compression in the bottom and top flange of the beam under pure bending, will be defined here as positive and negative, respectively.

Knowing the individual resistance of each row  $F_{ii,Rd}$  and their respective lever arms  $h_i$ , it would be possible to compute the plastic resistance of the joint under hogging and sagging bending moments. However, it must not be forgotten that group mechanisms may potentially form between multiple tension rows, preventing some rows from reaching their full resistance and therefore leading to premature yielding of the joint.

To account for this phenomenon, but also to optimise the resistance of the joint under hogging and sagging bending moments, it is necessary to maximise the resistance of the tension rows located the furthest from the respective compression centre, while ensuring that the group mechanism resistances are never exceeded. The so-defined row resistances accounting for group effects are named  $F_{i,Rd}^+$  &  $F_{i,Rd}^-$ , with the + or - sign placed in superscript indicating the sign of the bending moment to which they are associated. They can both be computed using the two next equations.

$$\text{For } (i = 1, \dots, n) \left\{ F_{i,Rd}^+ = \min \left[ \text{For } (k = 1, \dots, i) \left\{ F_{ki,Rd} - \sum_{j=k}^{i-1} \max \left[ F_{j,Rd}^+ ; 0 \right] \right\} \right] \right\} \quad (3.28)$$

$$\text{For } (i = n, \dots, 1) \left\{ F_{i,Rd}^- = \min \left[ \text{For } (k = n, \dots, i) \left\{ F_{ik,Rd} - \sum_{j=i+1}^k \max \left[ F_{j,Rd}^- ; 0 \right] \right\} \right] \right\} \quad (3.29)$$

where :

- $F_{i,Rd}^+$                       The design resistance of row  $i$  under hogging bending moment [N]
- $F_{i,Rd}^-$                       The design resistance of row  $i$  under sagging bending moment [N]
- $F_{ki,Rd} = F_{ik,Rd}$         The design resistance of the group occurring from row  $k$  to row  $i$  [N]
- $F_{ii,Rd}$                       The design resistance of row  $i$  [N]

Note that, if some  $ki$  groups appearing in Equations (3.28) and (3.29) cannot occur in reality, their resistances must be considered infinite in these equations.

### Characteristic M-N resistance points - 7.

Knowing the  $F_{i,Rd}^+$  &  $F_{i,Rd}^-$  values of each row, it is now possible to compute some characteristic M-N resistance points of the joint. For this purpose, the static theorem will be applied. As a reminder, the static theorem allows assuming any effort distribution within the joint, provided that the following two conditions are met :

- The internal and external forces must be in equilibrium ;
- The behaviour of the components must be respected in terms of resistance and ductility capacity.

When applying the static theorem to joints, it is also necessary to ensure, in addition to its two conditions, that the displacement compatibility between components is respected.

Therefore, for any ductile joint configuration,  $2n+2$  full plastic distributions of internal forces can be defined ( $n+1$  using  $F_{Rd}^+$  and  $n+1$  using  $F_{Rd}^-$  resistance values), assuming that all the rows present an infinite ductility. Even if this assumption is not correct regarding the real behaviour of the components, these distributions can still be considered as valid, as the lack of ductility is balanced by the post-yielding strain hardening, which is completely neglected here.

Then, for each of these  $2n+2$  distributions, the M-N resistance of the joint can be calculated by formulating the horizontal and rotational equilibrium equations between internal and external forces. This also allows meeting the first condition of the static theorem.

To determine all the characteristic M-N resistance points, the simple mathematical procedures expressed hereunder can be followed. The main principle involves starting from the distribution of the joint under pure compression, where all compressions rows are considered active, and then to progressively deactivate or activate the rows until reaching a distribution where only tension rows are active. This deactivation or activation of the rows must be carried out from top to bottom or vice versa, depending on whether hogging or sagging bending moments are considered. The  $2n + 2$  distributions which need to be obtain for the typical beam-to-column joint from Figure 3.9 are schematized in Figures 3.10 & 3.11.

**For  $F_{Rd}^+$  resistance values**

$$init. \rightarrow active = F_{Rd}^+ < 0 : M_{1,Rd}^+ = \sum F_{Rd}^+ h \text{ active} ; N_{1,Rd}^+ = \sum F_{Rd}^+ \text{ active} \quad (3.30)$$

$$For (i = 1, \dots, n) \left\{ active[i] = F_{Rd}^+[i] > 0 : M_{i+1,Rd}^+ = \sum F_{Rd}^+ h \text{ active} ; N_{i+1,Rd}^+ = \sum F_{Rd}^+ \text{ active} \right\} \quad (3.31)$$

**For  $F_{Rd}^-$  resistance values**

$$init. \rightarrow active = F_{Rd}^- < 0 : M_{1,Rd}^- = \sum F_{Rd}^- h \text{ active} ; N_{1,Rd}^- = \sum F_{Rd}^- \text{ active} \quad (3.32)$$

$$For (i = n, \dots, 1) \left\{ active[i] = F_{Rd}^-[i] > 0 : M_{n-i+2,Rd}^- = \sum F_{Rd}^- h \text{ active} ; N_{n-i+2,Rd}^- = \sum F_{Rd}^- \text{ active} \right\} \quad (3.33)$$

with :

- *active* A vector containing boolean data [-]
- $F_{Rd}^+$  A vector containing all the  $F_{i,Rd}^+$  resistance values [kN]
- $F_{Rd}^-$  A vector containing all the  $F_{i,Rd}^-$  resistance values [kN]
- $h$  A vector containing all the  $h_i$  lever arm values [m]
- $(M_{i,Rd}^+ ; N_{i,Rd}^+)$  The M-N coordinates of point  $i$  using  $F_{Rd}^+$  resistance values [kNm ; kN]
- $(M_{i,Rd}^- ; N_{i,Rd}^-)$  The M-N coordinates of point  $i$  using  $F_{Rd}^-$  resistance values [kNm ; kN]

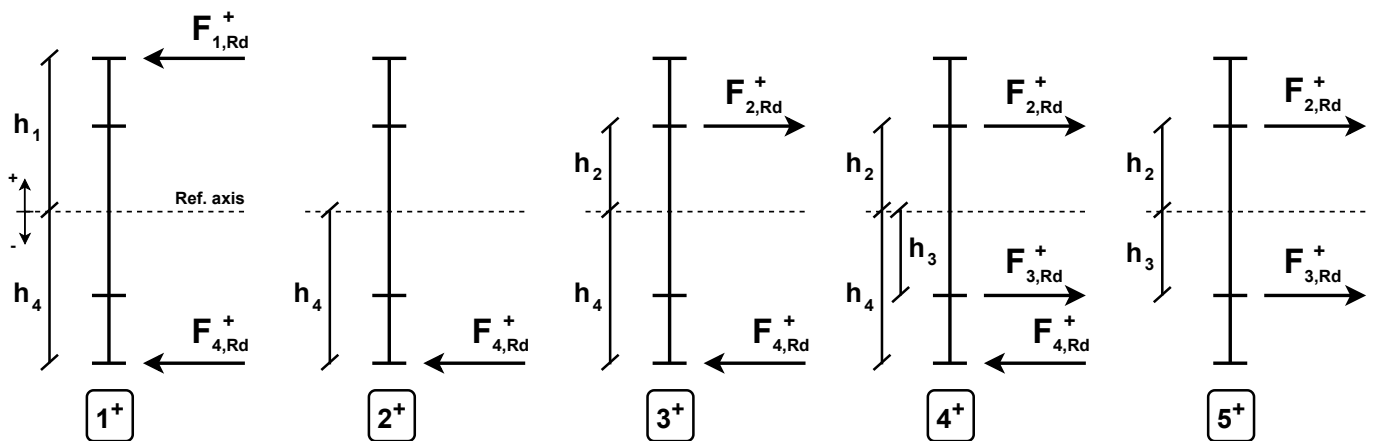


Figure 3.10: Hogging bending moment -  $n + 1$  distributions of internal forces of the joint from Figure 3.9

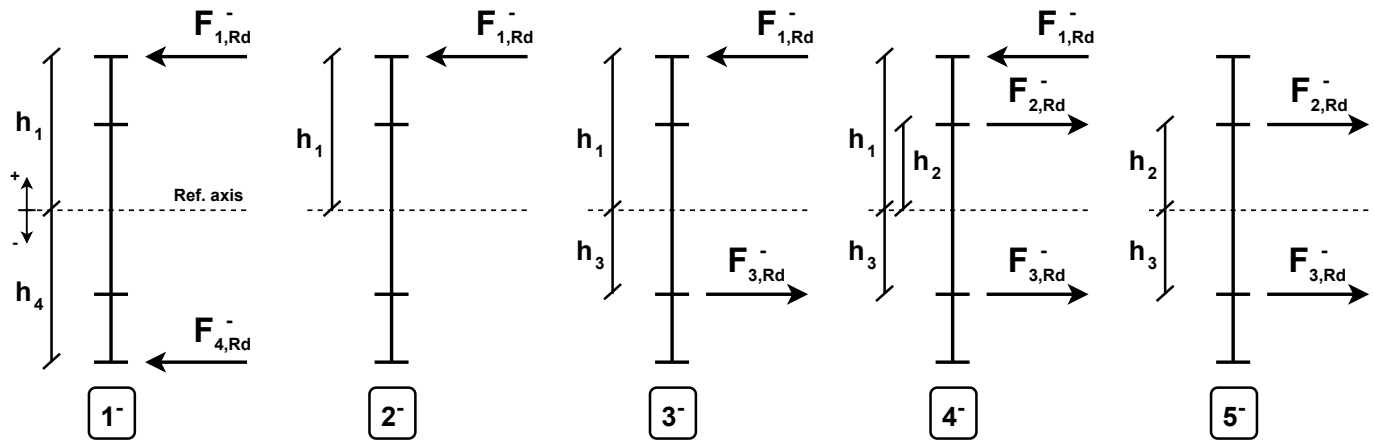


Figure 3.11: Sagging bending moment -  $n + 1$  distributions of internal forces of the joint from Figure 3.9

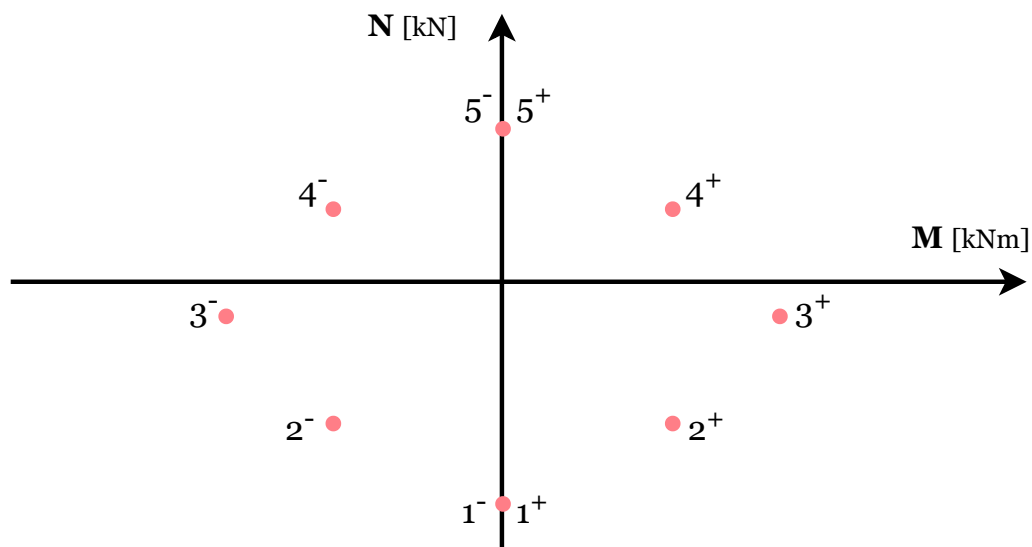


Figure 3.12: Characteristic M-N resistance points of the joint from Figure 3.9

Once all the calculations are complete, the  $2n+2$  characteristic M-N resistance points can be graphically represented on a figure with M-N axes, as shown in Figure 3.12 for the typical beam-to-column joint configuration from Figure 3.9.

Some comments on the graphical results from Figure 3.12 can already be addressed here. Indeed, if the studied joint configuration is perfectly symmetrical around the two beam reference axes (y-y and z-z), the characteristic M-N resistance points of this joint must also be symmetrical around the vertical axis of the graph.

However, it should be noted that the  $1^{+/-}$  and  $(n+1)^{+/-}$  characteristic M-N resistance points are not always confused and/or located on the vertical axis of the figure. They are indeed confused and located on the vertical axis only when the joint is symmetrical and the  $F_{Rd}^+$  &  $F_{Rd}^-$  vectors are identical.

#### Ductile resistance interaction curve - 8.

Finally, to derive the full ductile resistance interaction curve of the joint, all the characteristic M-N resistance points can be linearly connected two by two, as illustrated on Figure 3.13.

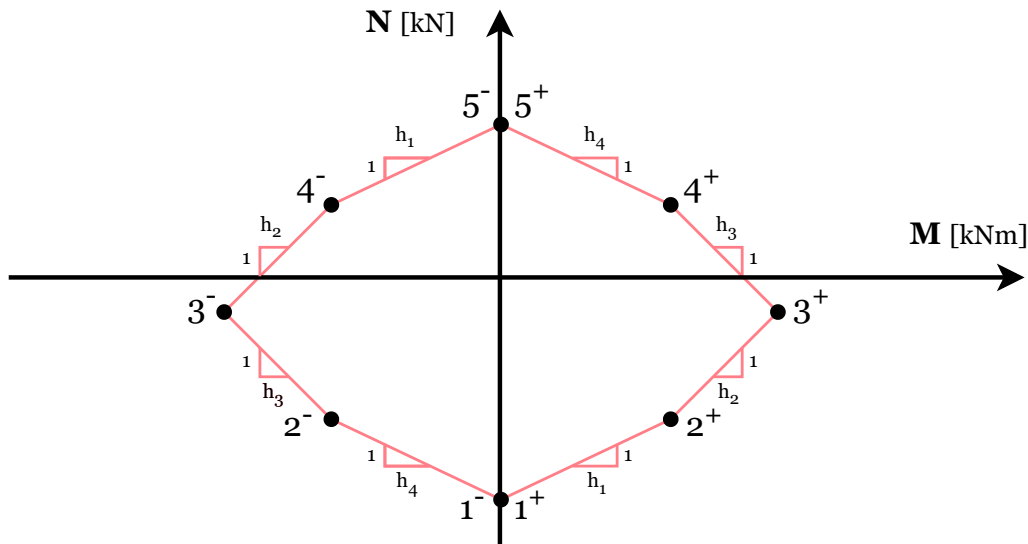


Figure 3.13: Ductile resistance interaction curve of the joint from Figure 3.9

The slope  $\Delta M / \Delta N$  of these straight lines between two characteristic points correspond to the lever arm value  $h_i$  of the row whose resistance varies from zero to  $F_{i,Rd}^{+/-}$  between these two points. For instance, between the points  $2^+$  and  $3^+$  in Figure 3.13, the resistance of the row n°2 will increase from zero to  $F_{2,Rd}^+$  with a slope  $\Delta M / \Delta N$  equal to  $h_2$ . Therefore, the two opposite straight segments on the interaction curve, along which a row  $i$  is activated or deactivated, are necessarily parallel. In Figure 3.13, these are the segments  $2^+ - 3^+$  and  $3^- - 4^-$  for the row n°2.

A change in the sign of the slope can also be observed at the level of the points  $3^{+/-}$ . This variation can be simply explained by the fact that the rows located on either side of the beam reference axis present opposing lever arm signs.

Based on the graphical representation of the ductile resistance interaction curve of the joint, it is possible to determine whether any pair of forces  $M_{Ed}$  &  $N_{Ed}$  applied to the joint will lead or not to its failure. Indeed, if the point of coordinates  $(M_{Ed} ; N_{Ed})$  is located within or on the interaction curve, then the joint can withstand these loads, regardless of the loading cycle followed by the joint up to this point.

### 3.2.3 Python implementation

To facilitate the application of the entire methodology presented in Figure 3.1 and detailed in the previous pages of this thesis, Python codes have been fully developed for the various joint configurations presented in Sections 3.3.1 & 3.3.2. Indeed, introducing in entry the geometrical and mechanical requested data of the joint configuration to study, these codes allow to compute the entire ductile resistance interaction curve of this joint. They are available for download and consultation on [GitLab](#).

### 3.2.4 COP software

COP [20] is a software that allows civil engineers to define and design steel joints quickly and easily, based on the rules prescribed in EN 1993-1-8:2005 [7]. It has initially jointly been developed by the University of Aachen and the University of Liège by J.-P. Jaspart and K. Weynand. Nowadays, COP is still under continuous development by the design office Feldmann + Weynand in close collaboration with the University of Liège.

Although the current commercial version of the software does not yet incorporate the complete model established by F. Cerfontaine, a beta version of COP that includes the derivation of ductile or non-ductile resistance interaction curves is currently under development. The access and the usage of this beta version were made possible by K. Weynand in the context of this Master thesis.

Therefore, most of the joint configurations in this thesis have been studied in two different ways: once using the Python codes, and once using the COP beta version. The objective was to compare the results obtained from both methods, as they are expected to provide the same resistance interaction curves.

### 3.2.5 Parametric analysis

This subsection outlines the methodology used to perform the parametric analysis. The main objective of this parametric analysis is to highlight how variations in certain geometrical or mechanical properties of the joint affect its M-N resistance interaction curve. In total, three different beam-to-column joint configurations will be studied and subjected to modifications: two "standard" configurations (A1 & C2) inspired by the FAILNOMORE project [16], and one configuration with an inclined beam, sourced from the Ph.D. thesis of F. Cerfontaine [3]. All relevant information and initial properties of these three joint configurations are presented in Section 3.3 of this thesis.

Naturally, this parametric analysis will not cover all geometrical and mechanical properties of the joint. Accordingly, seven of them have been selected. These properties were chosen with the aim of individually affecting specific components of the joints, in order to clearly assess the influence of each on the interaction curve.

The seven properties retained are the following:

- The column steel grade
- The beam steel grade
- The end-plate steel grade
- The bolts steel grade
- The thickness of the end-plate
- The thickness of the column flange
- The transformation parameter  $\beta$

The entire parametric analysis was carried out using the beta version of the COP software [20], chosen for its user-friendliness and its ability to generate both ductile and non-ductile resistance interaction curves. Prior to its use, a validation will be performed in Section 3.4.1 to ensure that the results are consistent with those of the analytical procedure. Since only ductile joints are analytically addressed in this thesis, it will nevertheless be necessary to assume the validity of the non-ductile resistance interaction curves generated by COP.

### 3.2.6 FINELG software

FINELG [23] is a non-linear calculation software based on finite element method. Initially developed at the University of Liège within the ArGENCo department, it is now also being further developed in collaboration with the R&D department of the Greisch design office. Among other applications, it can be used to study the actual behaviour of both 2D and 3D steel structures, taking into account, for instance, the elasto-plastic

constitutive laws of steel or the presence of semi-rigid joints. Once all calculations have been performed, the results can then be easily plotted and visualised using the DESFIN software, which was developed in parallel with the finite element software.

As part of this thesis, the FINELG software is used to carry out several local numerical studies of beam-to-column joints subjected to bending and axial forces. The methodology followed to perform these analyses is described in detail in Section 3.2.7.

### 3.2.7 Finite element modelling

To evaluate whether the new mechanical model shown in Figure 2.3 can reproduce the analytical results obtained using the Cerfontaine model, local numerical studies were conducted on three of the six FAILNOMORE joint configurations (A1, B1 & C2) presented in Section 3.3, using the FINELG FE software and its ASSEMBLA structural joint element.

To achieve this, each FAILNOMORE joint was modelled using two distinct element types : the structural joint element ASSEMBLA (type 240) for the joint itself, and classical 3D beam elements (type 85) for the connected steel profiles. To define an ASSEMBLA element, it is notably necessary to specify the coordinates of the four points that correspond to the extremities of the joint. These coordinates can be easily calculated, since the four points are consistently located at the mid-thickness of the flanges of the connected sections. The column and the beam, for their part, can be simply defined by creating a 3D beam element between their end points, which can then be subdivided into several sub-elements. The three local numerical models that have been created are illustrated in Figures 3.14a to 3.14c.

Due to the use of 3D beam elements (type 85), support conditions must be defined at the three extremities of the models for all seven degrees of freedom (7 DOF). For the column, rotation around the y-axis at both ends and vertical displacement at the top were left unconstrained. At the right end of the beam, only the out-of-plane displacement was restrained to ensure that bending occurs exclusively in the XZ plane.

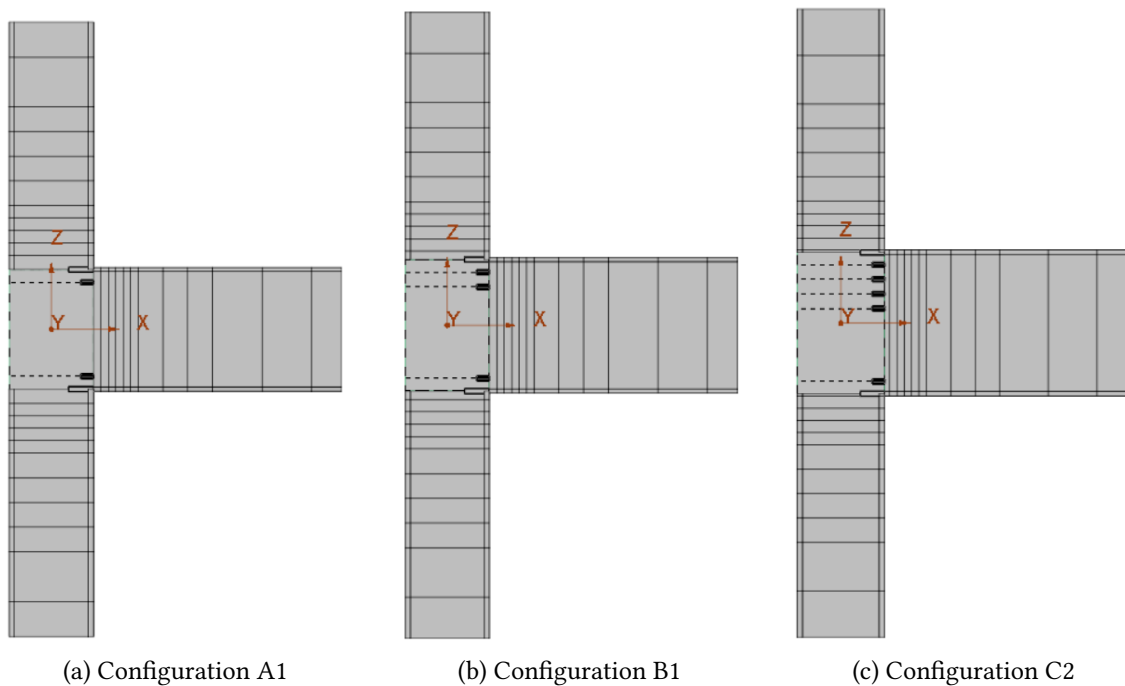


Figure 3.14: Local numerical studies - FAILNOMORE joints configurations numerical models

Once the global geometry of the joint has been defined, a complementary file (.mci) must still be completed. This file summarises all the mechanical properties of the components and group mechanisms, along with additional geometrical details, such as the total number of rows or even their vertical positioning.

As illustrated in Figure 2.3, the tension/compression components/rows and the column web subpanels are simulated using non-linear extensional spring elements, whereas the group mechanisms are modelled by fuse elements. The four distinct behaviour laws assigned to these elements are illustrated in Figures 3.15a to 3.15d. It can be observed that the assigned law depends not only on the type of element but also on the joint zone to which it belongs (compression, tension, or shear). The values used to define these laws are directly obtained from the characterisation of the components and group mechanisms (see Section 3.2.1), carried out as part of the component method procedure.

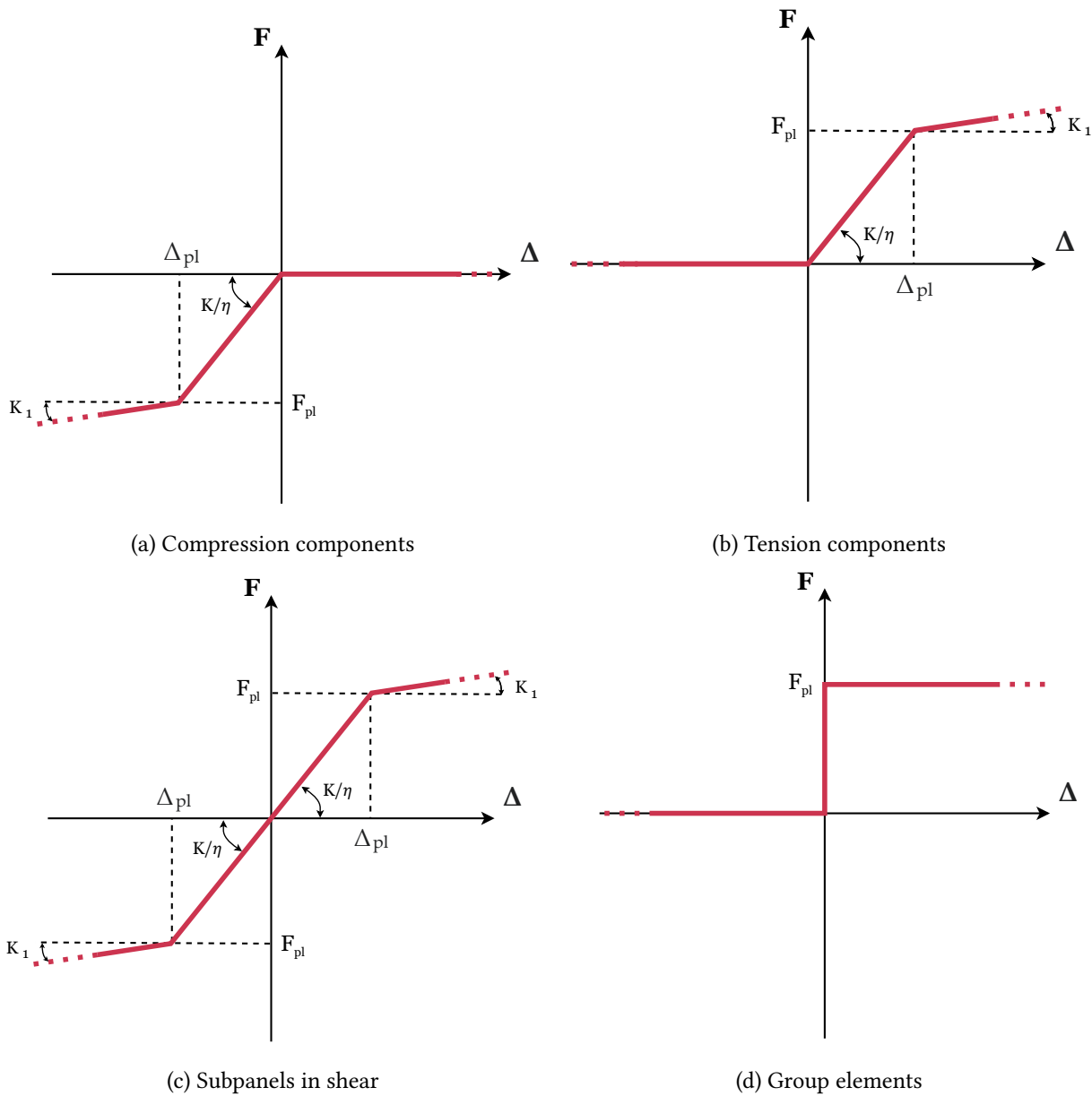


Figure 3.15: Local numerical studies - Behaviour laws associated to the different elements



Accordingly, the stiffness  $K$  of a component can be simply calculated by multiplying its stiffness coefficient  $k$  by its Young modulus  $E$ . However, in the case of bilinear behaviour laws, this value must subsequently be divided by the stiffness modification factor  $\eta$ , whose value depends on the type of joint considered. For bolted end-plate beam-to-column joints, this value is set to two (see Table 2.7 in the book "Design of joints in steel and composite structures" [28]). Although post-yielding strain hardening is entirely neglected, a post-yielding stiffness  $K_1$  is nevertheless introduced solely to ensure numerical convergence of the models. As recommended in EN 1993-1-14 [10], this value has been set to 1/10,000 of the stiffness  $K$ . Finally, the plastic resistance  $F_{pl}$  can be taken equal to the design resistance  $F_{Rd}$  of the corresponding component or group mechanism.

Before proceeding with the actual calculation, the loading cycle to be applied to the joint still needs to be defined. To compare the numerical results with the ones from the Cerfontaine model,  $2n + 2$  distinct loading cycles were generated, each corresponding to a characteristic M-N resistance point of the studied joint configuration. Each loading cycle begins with the gradual application of an axial force, the magnitude of which depends on the N-coordinate of the targeted characteristic point. Then, once the joint is fully axially charged, a bending moment is applied incrementally to the joint by imposing a vertical force at the free end of the connected beam. The magnitude of this point load is randomly assigned. Finally, the loading cycle is stopped either when the joint reaches its full plastic distribution or when numerical convergence is no longer achieved. The final applied bending moment is then taken as the joint maximum bending resistance under the imposed axial force.

By providing the loading applied at each calculation step and the behaviour laws of all elements in the joint mechanical model, FINELG can thus iteratively compute the incremental displacements of the various elements and, consequently, the corresponding distribution of internal forces. The resulting distorted joint configuration then serves as the initial state for the next calculation step, and so on. In FINELG, these calculations are primarily carried out using stiffness matrices. To achieve this, linear constraints have also been incorporated into the model to ensure displacement compatibility between springs arranged in series or parallel, and to enforce the Euler-Bernoulli hypothesis (plane section assumption). Finally, the ductility of all components and group mechanisms is assumed to be infinite. However, this assumption is not problematic, as all three locally studied FAILNOMORE joint configurations can be considered as ductile (see Section 3.4.1).

### 3.3 Database

In this section, the geometrical and mechanical data of the nine beam-to-column joint configurations studied during this Master's thesis are compiled. These have been organized into three subsections based on the joint configuration "category" to which they belong (FAILNOMORE, Coimbra & Cerfontaine). These properties are either directly presented in various tables with their sources or only their origins are specified.

#### 3.3.1 FAILNOMORE joint configurations

Six different joint configurations, inspired by those illustrated at Figure 87 of the FAILNOMORE project [16], have been analysed. Even though the joints treated in this thesis are almost identical to those from the project, some geometrical modifications have been made to these, notably on the height of the end-plate or even on the throat thickness of the welds.

These six configurations can be subdivided into three subcategories based on the number of bolt rows and the beam profile employed. Each of these subcategories is associated to a capital letter (A, B & C). The number (1, 2 & 3) placed after the latter corresponds to the column profile used in this joint configuration. A summary of the names and the connected profiles of these different joints is provided in Table 3.1 below.

Table 3.1: FAILNOMORE - Names and connected profiles of the different joint configurations [16]

Joint name	Beam steel profile	Column steel profile
A1	IPE 500	HEB 340
A2	IPE 500	HEB 360
B1	IPE 550	HEB 340
B3	IPE 550	HEM 300
C2	IPE 600	HEB 360
C3	IPE 600	HEM 300

The relevant geometrical properties of the beam and column steel profiles are regrouped in Table 3.2. The dimensions of the end-plates of the different joints configurations are, as for them, indicated on the technical drawings from Figures 3.16 to 3.21. The steel grade used for the beams, columns, and end-plates is S355 for these six joints.

Table 3.2: FAILNOMORE - Steel sections relevant geometrical properties [2]

Steel section	h [mm]	b [mm]	d [mm]	$t_w$ [mm]	$t_f$ [mm]	r [mm]	A [mm <sup>2</sup> ]	$A_{v,z}$ [mm <sup>2</sup> ]	$W_{pl,y}$ [mm <sup>3</sup> ]
IPE 500	500	200	426	10.2	16	21	11,552	5,987	2,194,000
IPE 550	550	210	467.6	11.1	17.2	24	13,442	7,234	2,787,000
IPE 600	600	220	514	12	19	24	15,600	8,378	3,512,000
HEB 340	340	300	243	12	21.5	27	17,090	5,608	2,408,000
HEB 360	360	300	261	12.5	22.5	27	18,063	6,059	2,682,000
HEM 300	340	310	208	21	39	27	30,308	9,052	4,077,000

The throat thickness of the welds between the beams (flanges and web) and the end-plates has been set to 9 mm to ensure that they are considered full-strength double fillet welds. This value was calculated based on the criterion proposed in Table 1. of the FAILNOMORE project [16].

The bolts used in the six configurations are of type M24 10.9. Their main mechanical and geometrical properties are listed in Table 3.3 below. Additional required properties of the bolts, nuts and washers have for their part respectively being extracted from EN ISO 4014 [8], EN ISO 4032 [9] and EN ISO 7089 [4].

Table 3.3: FAILNOMORE - Bolts geometrical & mechanical properties [1]

Bolt type	d [mm]	d <sub>0</sub> [mm]	s [mm]	A <sub>s</sub> [mm <sup>2</sup> ]	A <sub>g</sub> [mm <sup>2</sup> ]	f <sub>yb</sub> [MPa]	f <sub>ub</sub> [MPa]
M24 10.9	24	26	36	353	452	900	1,000

### Technical drawings

Finally, one technical drawing has been realised for each of the six FAILNOMORE joint configurations. These drawings regroup some of the previously mentioned informations, but also the last missing geometric properties. All the dimensions indicated on these are in millimetres. The row numeration introduced in 3.2.2 and used within the Cerfontaine model procedure is also indicated on these technical drawings.

#### Configuration A1

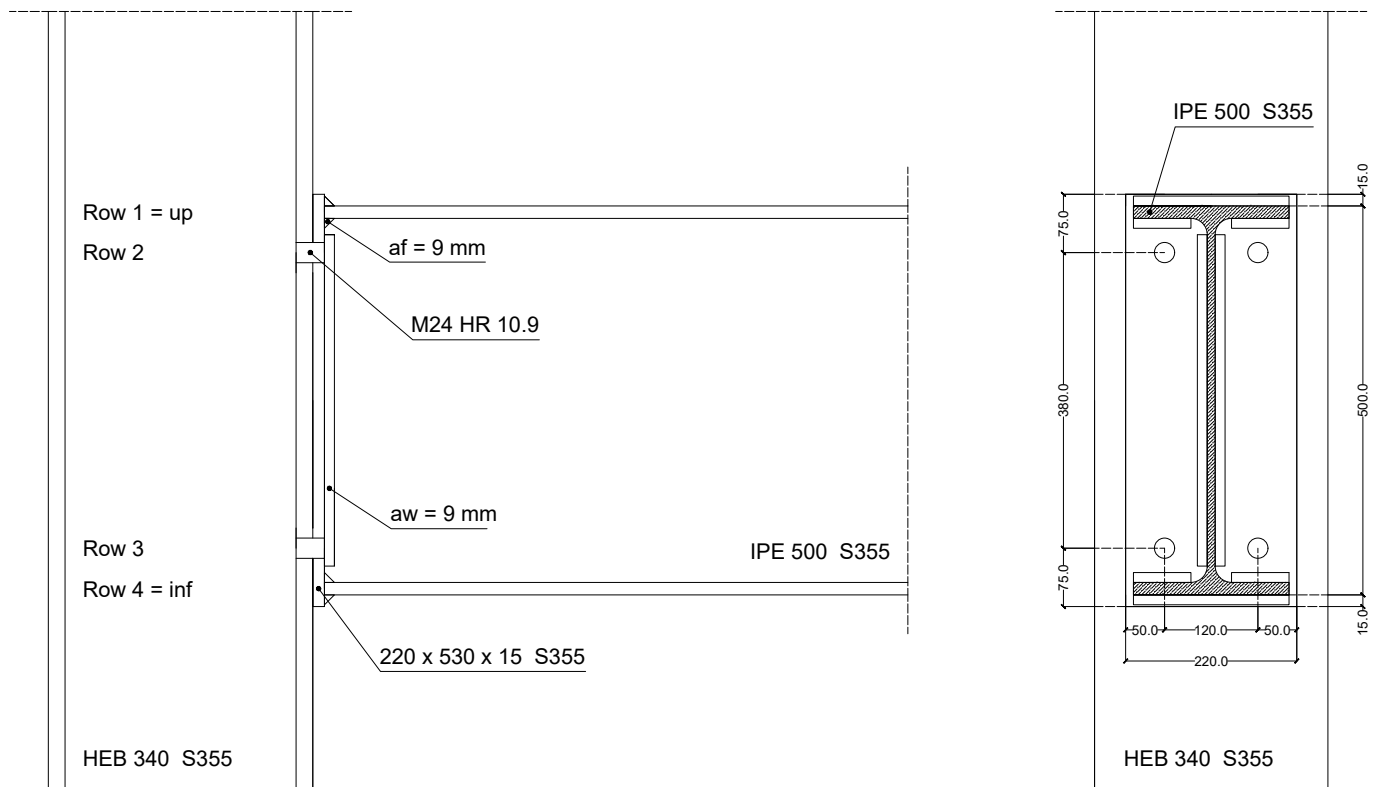


Figure 3.16: FAILNOMORE - Joint configuration A1 - Technical drawing

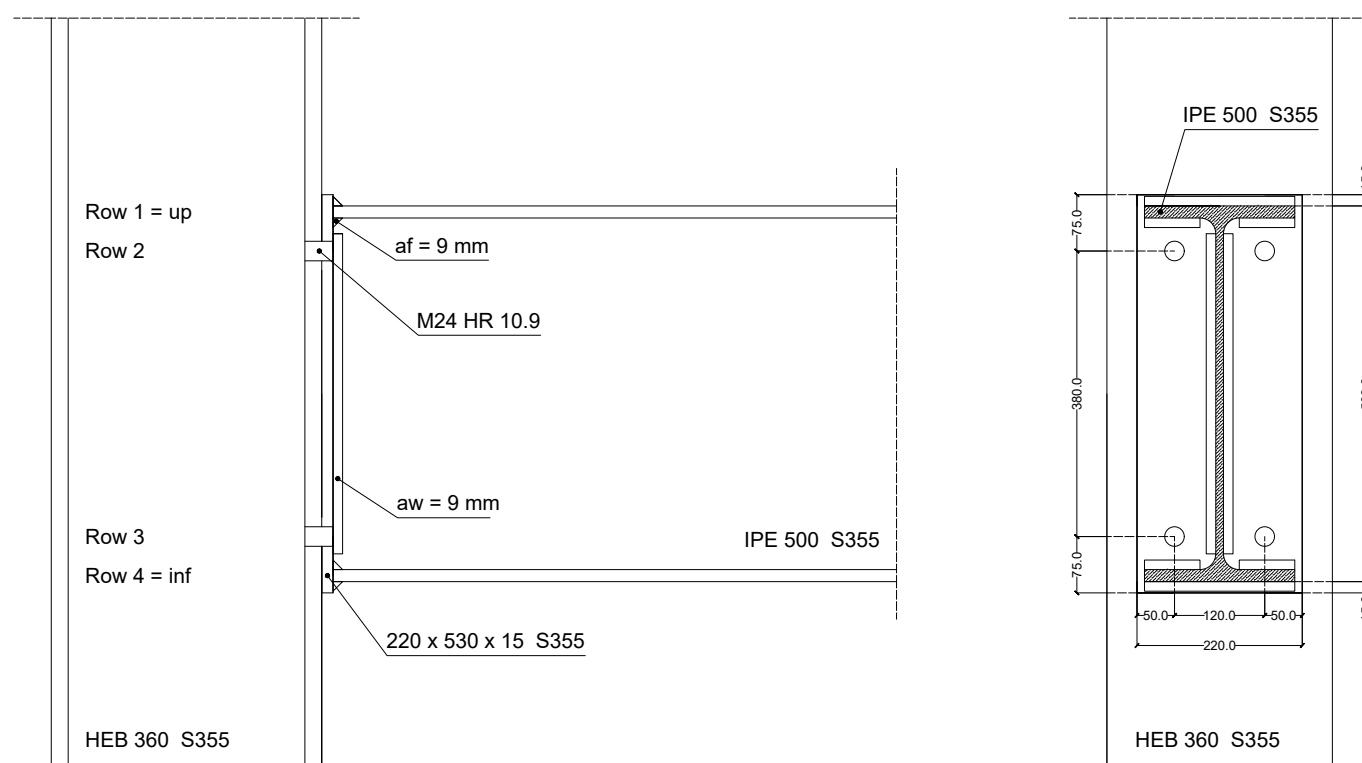
**Configuration A2**

Figure 3.17: FAILNOMORE - Joint configuration A2 - Technical drawing

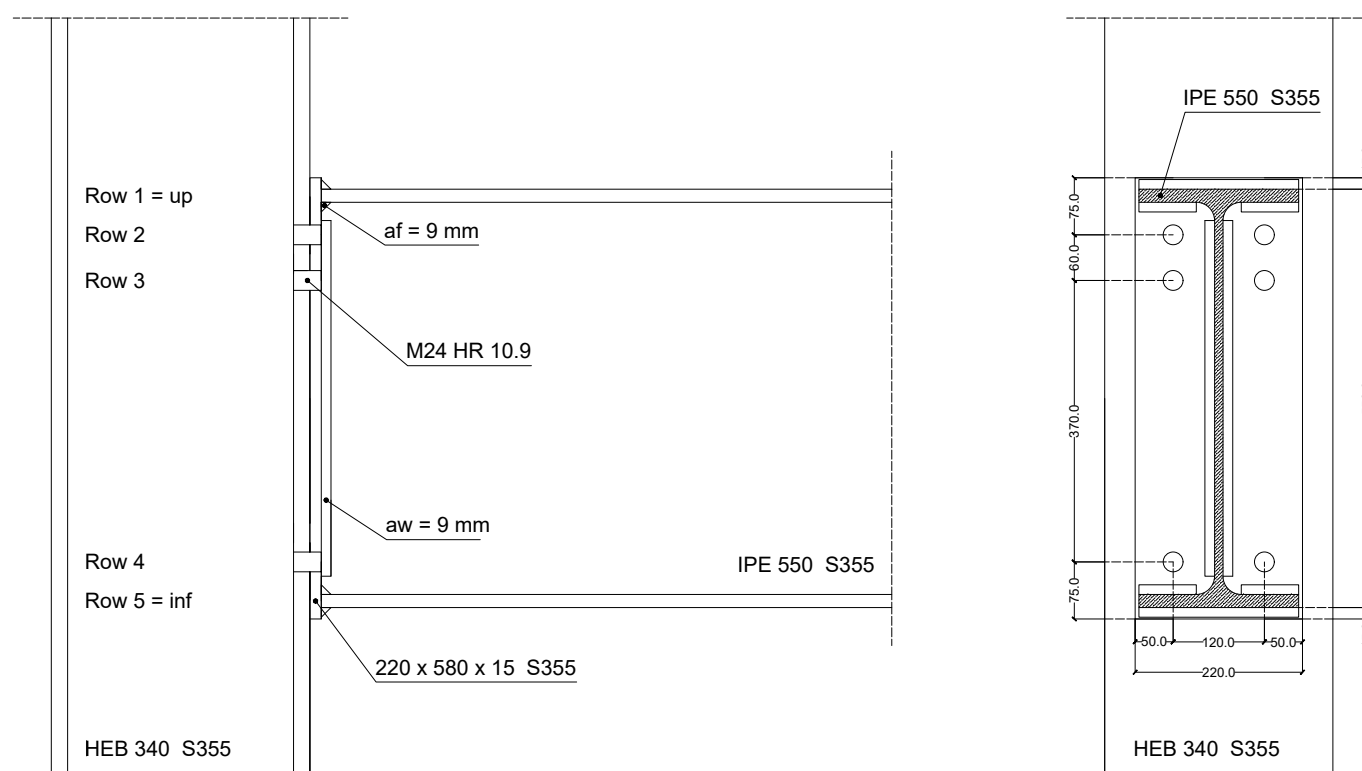
**Configuration B1**

Figure 3.18: FAILNOMORE - Joint configuration B1 - Technical drawing

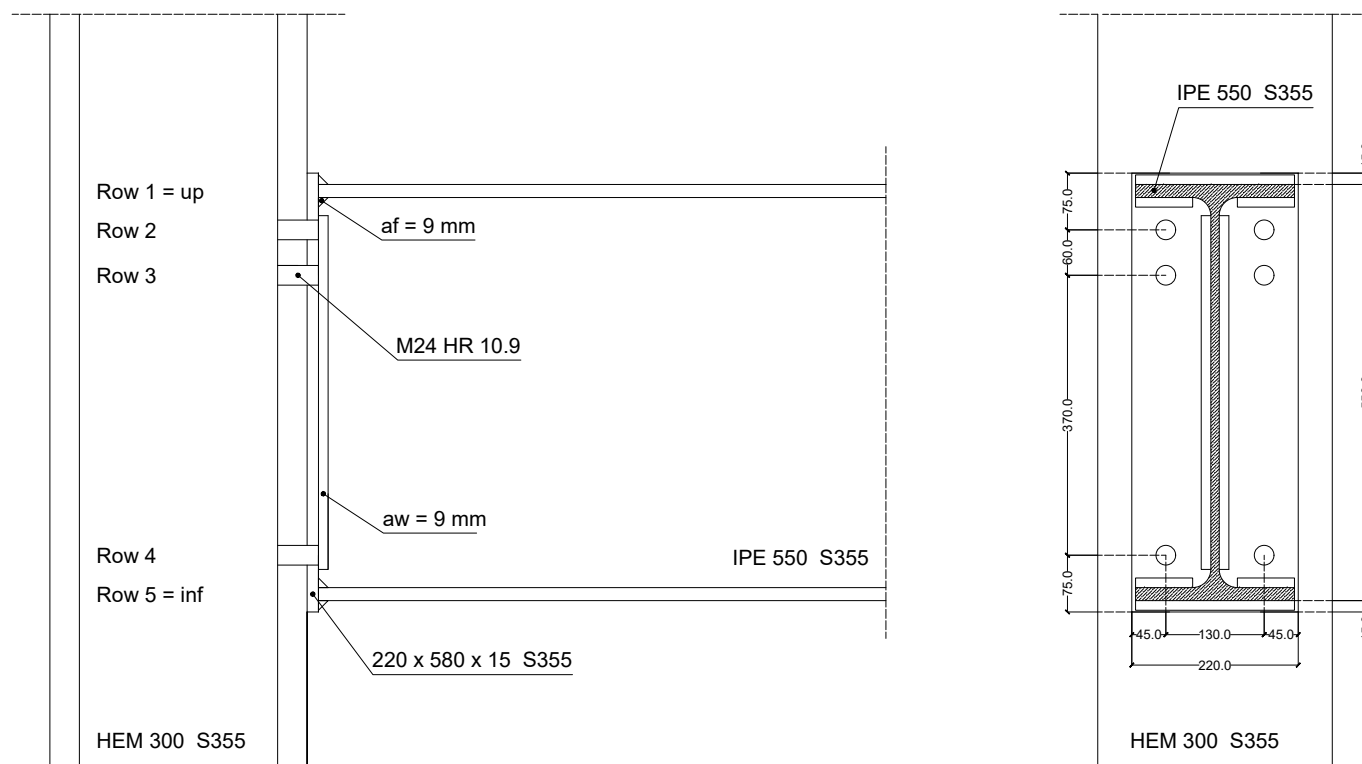
**Configuration B3**

Figure 3.19: FAILNOMORE - Joint configuration B3 - Technical drawing

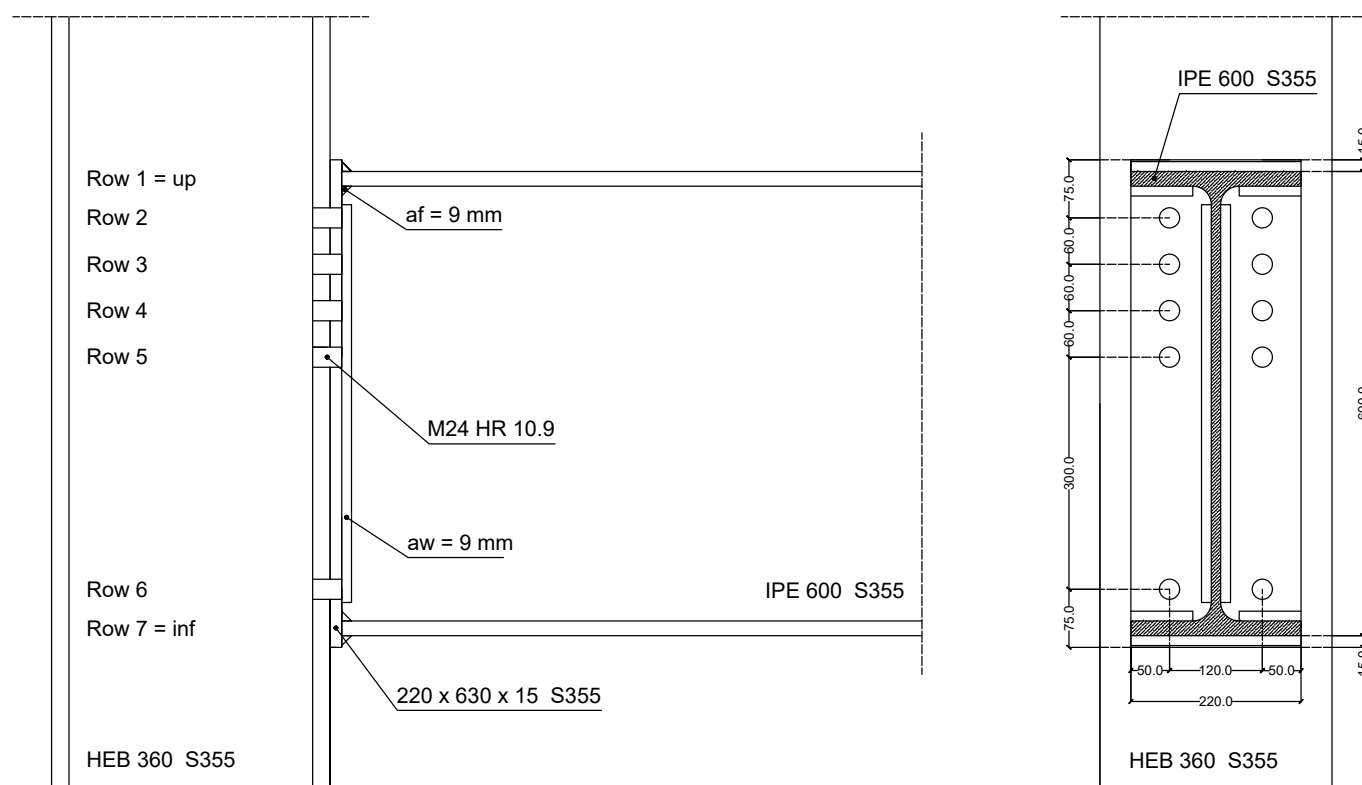
**Configuration C2**

Figure 3.20: FAILNOMORE - Joint configuration C2 - Technical drawing

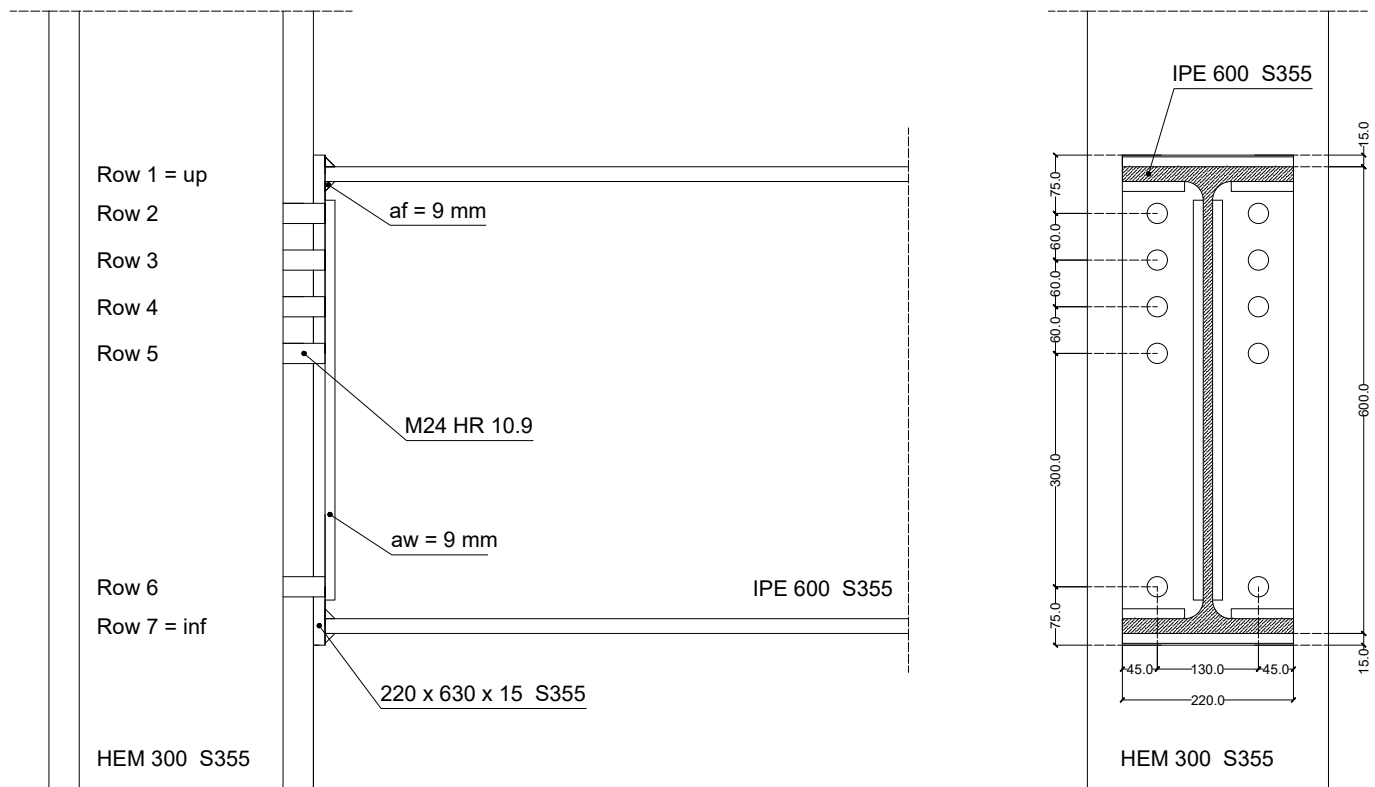
**Configuration C3**

Figure 3.21: FAILNOMORE - Joint configuration C3 - Technical drawing

**3.3.2 Coimbra joint configurations**

This second subsection presents all the necessary data to derive the ductile resistance interaction curves for the two joint configurations that were experimentally tested at the University of Coimbra. It also introduces the laboratory measurements used in the calculations, along with the test results that will be analysed afterwards.

The experimental campaign and the employed experimental setup will, as for them, not be described in the framework of this thesis. However, multiple informations about these latter can be found in the PhD thesis of L.R.O. de Lima [15] or in the Articles [13] & [14]. Nonetheless, it is important to emphasize that several inconsistencies have been identified among these three documents, and therefore, the reliability of the experimental data presented here cannot be fully guaranteed.

The properties of the bolts and steel profiles listed in Tables 3.4 & 3.5 are purely theoretical. The real geometrical dimensions of the different tested joints configurations are provided in Appendix B.3. The theoretical steel grade used for the beam, column, and end-plate is S275 for both joint configurations.

Table 3.4: Coimbra - Steel sections theoretical geometrical properties [2]

Steel section	h [mm]	b [mm]	d [mm]	$t_w$ [mm]	$t_f$ [mm]	r [mm]	A [mm <sup>2</sup> ]	$A_{v,z}$ [mm <sup>2</sup> ]	$W_{pl,y}$ [mm <sup>3</sup> ]
IPE 240	240	120	190.4	6.2	9.8	15	3,912	1,914	366,600
HEB 240	240	240	164	10	17	21	10,600	3,322	1,053,000

The bolts used in the two configurations are of type M20 10.9. Their theoretical geometrical and mechanical properties are listed in Table 3.5. Additional required properties of the bolts, nuts and washers have for their part respectively being extracted from EN ISO 4014 [8], EN ISO 4032 [9] and EN ISO 7089 [4].

Table 3.5: Coimbra - Bolts theoretical geometrical & mechanical properties [1]

Bolt type	d [mm]	d <sub>0</sub> [mm]	s [mm]	A <sub>s</sub> [mm <sup>2</sup> ]	A <sub>g</sub> [mm <sup>2</sup> ]	f <sub>yb</sub> [MPa]	f <sub>ub</sub> [MPa]
M20 10.9	20	22	30	245	314	900	1,000

The throat thickness of the welds connecting the beam flanges and web to the end plates is 8 mm. This value complies with the criterion specified in Table 1. of the FAILNOMORE project [16], and therefore the welds can be classified as full-strength double fillet welds.

### Technical drawings

As with the FAILNOMORE joints, technical drawings have been produced for both joint configurations tested at Coimbra. These drawings summarize most of the informations previously provided, along with additional geometrical dimensions. They also show the row numbering used in the calculation procedure of the Cerfontaine model. All indicated dimensions are theoretical and given in millimetres.

#### Flush end-plate configuration

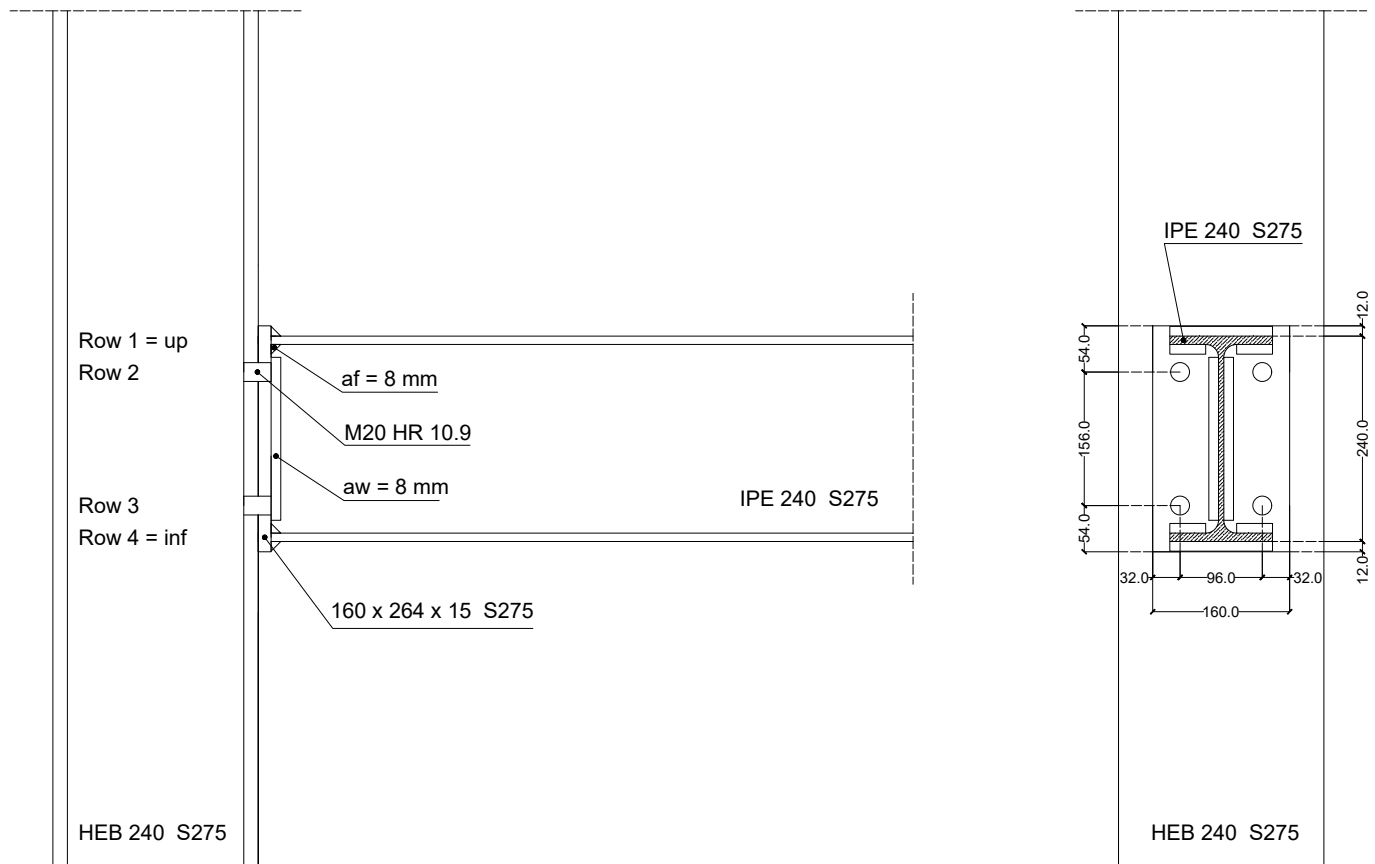


Figure 3.22: Coimbra - Flush end-plate joint configuration - Technical drawing

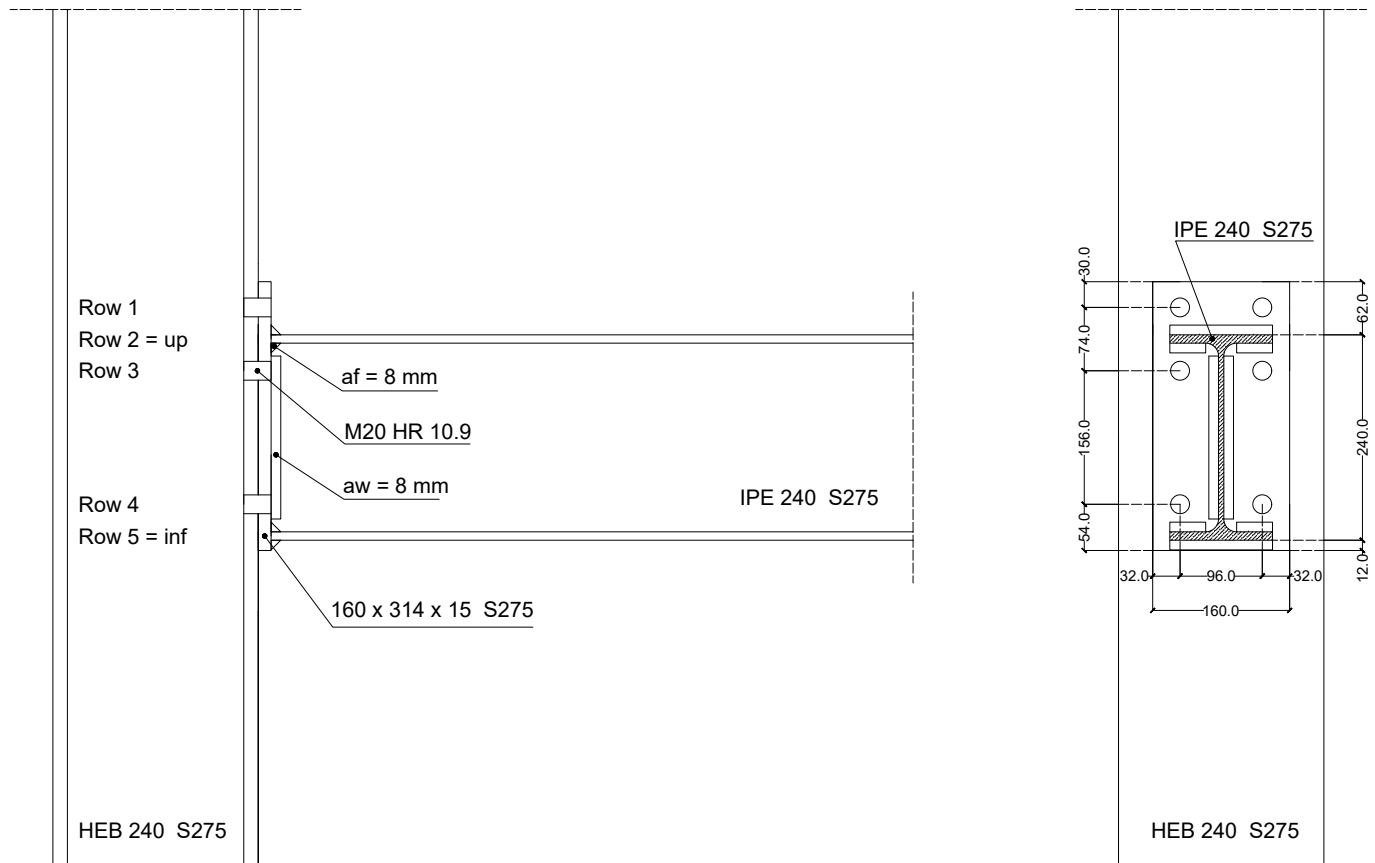
**Extended end-plate configuration**

Figure 3.23: Coimbra - Extended end-plate joint configuration - Technical drawing

**Experimental results**

In Table 3.6, the mean mechanical properties and the associated standard deviations are presented for all the steel elements that compose the joints. These values were obtained from multiple tensile tests conducted in the laboratory. It can already be observed that the mean yield strengths of the elements, with the exception of the bolts, are significantly higher than the theoretical value of 275 MPa. The high standard deviation values also indicate a significant variability of this property among the different coupons, and consequently among the various joints that were tested during the experimental campaign.

Table 3.6: Coimbra - Mean steel mechanical properties and standard deviations [13] &amp; [15]

	Mean values [MPa]			Standard deviation [MPa]		
	$f_y$	$f_u$	E	$f_y$	$f_u$	E
Beam web	363.4	454.3	203,713	17.64	7.49	7,214
Beam flange	340.14	448.23	215,222	18.08	7.38	3,017
Column web	372.02	477.29	206,936	28.56	19.59	8,206
Column flange	342.95	448.79	220,792	5.68	27.39	9,516
End-plate	369.44	503.45	200,248	10.62	8.05	1,694.36
Bolts	939.67	1,018.67	/	/	/	/

The minimum and maximum mechanical properties measured for all components of the joints are also provided in Table 3.7. These values simply correspond to the lowest and highest results obtained from tensile tests conducted on coupons taken from identical steel elements.



Table 3.7: Coimbra - Minimum and maximum steel mechanical properties measured in laboratory [15]

	Minimum [MPa]			Maximum [MPa]		
	$f_y$	$f_u$	E	$f_y$	$f_u$	E
Beam web	332.32	438.76	190,443	380.25	461.98	211,839
Beam flange	312.13	435.2	212,497	365.83	458.9	221,813
Column web	340.16	454.39	199,055	399.38	495.28	218,456
Column flange	337.94	410.06	210,434	350.09	472.93	232,937
End-plate	356.71	497.08	198,936	380.91	514.44	202,161
Bolts	914	980	/	974	1,067	/

The experimental values of axial force and bending moment recorded at the failure of the flush end-plate and extended end-plate joint configurations are presented in Tables 3.8 & 3.9, respectively. During each experimental test, a predefined axial force was first fully applied to the joint, followed by a gradual increase in the bending moment until joint failure occurred. All joints were tested exclusively under hogging bending moments.

Table 3.8: Coimbra - Flush end-plate configuration - Experimental results [13]

Experimental tests	$N$ [kN]	$M$ [kNm]
FE1 (pure bending)	0.0	68.4
FE3 (-4% $N_{pl}$ )	-52.7	76.7
FE4 (-8% $N_{pl}$ )	-105.6	73.5
FE5 (-20% $N_{pl}$ )	-265.0	78.5
FE6 (-27% $N_{pl}$ )	-345.0	72.4
FE7 (-20% $N_{pl}$ )	-265.0	80.0
FE8 (+10% $N_{pl}$ )	130.6	62.8
FE9 (+20% $N_{pl}$ )	264.9	52.3

Table 3.9: Coimbra - Extended end-plate configuration - Experimental results [15]

Experimental tests	$N$ [kN]	$M$ [kNm]
EE1 (pure bending)	0.0	118.7
EE2 (-10% $N_{pl}$ )	-135.94	125.4
EE5 (-15% $N_{pl}$ )	-193.3	118.1
EE3 (-20% $N_{pl}$ )	-259.2	113.2
EE4 (-27% $N_{pl}$ )	-363.5	111.9
EE6 (+10% $N_{pl}$ )	127.2	111.5
EE7 (+20% $N_{pl}$ )	257.9	101.0

### 3.3.3 Cerfontaine thesis example

This last joint configuration comes directly from the Ph.D. thesis of F. Cerfontaine [3] where it has already been treated in detail. Within the scope of this thesis, it will only be used for the parametric analysis and has therefore not been examined analytically. However, all the information that needs to be implemented in the beta version of COP is presented here.

The geometrical properties of the steel profiles are listed in Tables 3.10, while the geometrical and mechanical properties of the bolts are presented in Table 3.11. The beam, the column, and the end plate are all made of S355 steel. A technical drawing of the joint is finally available in Figure 3.24.

Table 3.10: Cerfontaine example - Steel sections geometrical properties [2]

Steel section	h [mm]	b [mm]	d [mm]	$t_w$ [mm]	$t_f$ [mm]	r [mm]	A [mm <sup>2</sup> ]	$A_{v,z}$ [mm <sup>2</sup> ]	$W_{pl,y}$ [mm <sup>3</sup> ]
IPE 600	600	220	514	12	19	24	15,600	8,378	3,512,000
HEB 400	400	300	298	13.5	24	27	19,780	6,997	3,231,000

Table 3.11: Cerfontaine example - Bolts geometrical & mechanical properties [1]

Bolt type	d [mm]	$d_0$ [mm]	s [mm]	$A_s$ [mm <sup>2</sup> ]	$A_g$ [mm <sup>2</sup> ]	$f_{yb}$ [MPa]	$f_{ub}$ [MPa]
M24 8.8	24	26	36	353	452	640	800

Regarding the welds, it should be noted that the throat thickness of the welds between the beam web and the end-plate  $a_w$  does not satisfy the criterion to qualify as full-strength double fillet welds, as recommended in Table 1 of the FAILNOMORE project [16]. However, this is the case for the other welds in the joint.

### Technical drawing

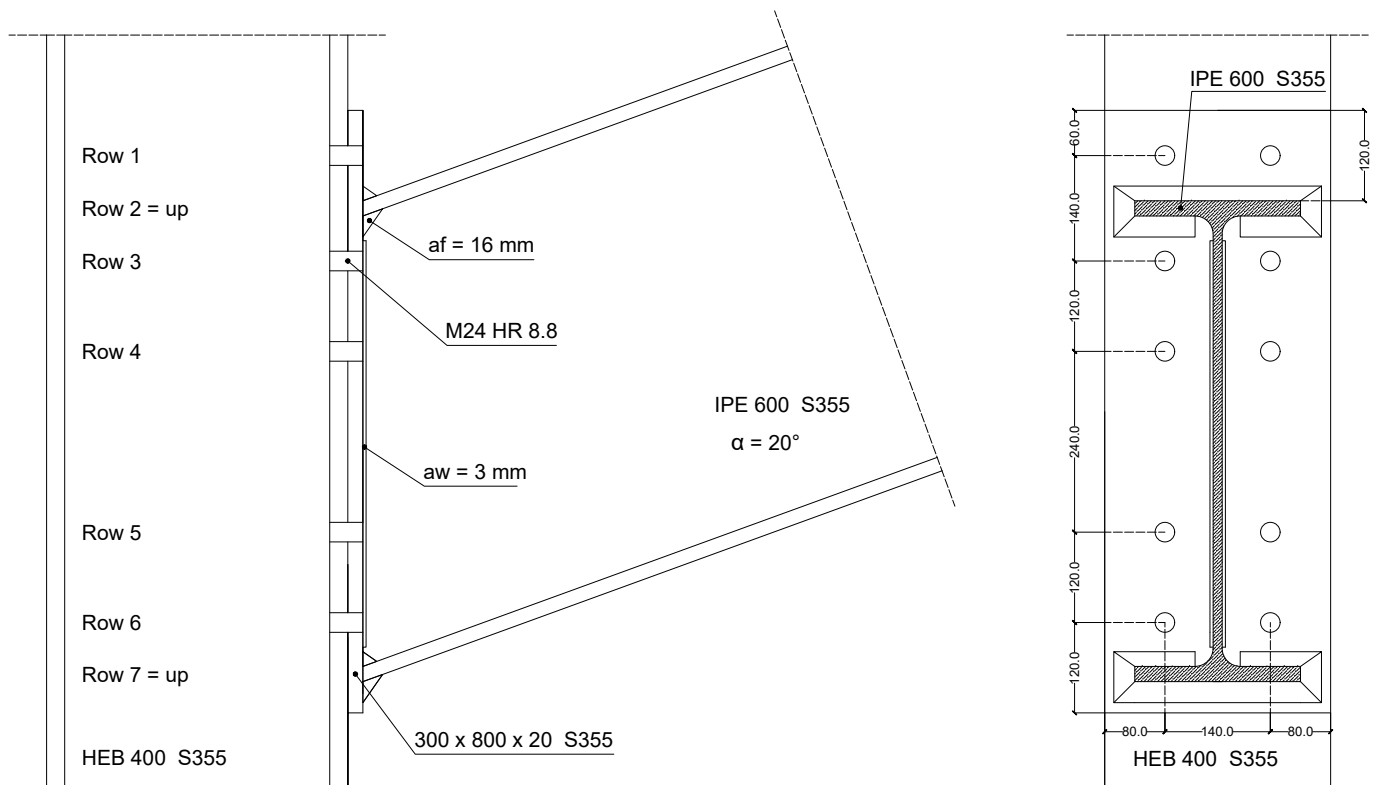


Figure 3.24: Cerfontaine thesis example - Technical drawing

## 3.4 Results and discussions

### 3.4.1 FAILNOMORE joint configurations

As a reminder, the main focus of this subsection is to compare the ductile resistance interaction curves obtained analytically and via the beta version of COP for the FAILNOMORE joint configurations, in order to validate COP as a tool for conducting the parametric analysis. Note that the six FAILNOMORE joints comply with the two ductility criteria required to use the Cerfontaine model (see Section 3.2.2).

For a matter of relevance and space, only the results obtained for the A1, B1 and C2 FAILNOMORE joint configurations will be presented in this subsection. In fact, it does not seem very interesting to discuss all six configurations, since the only change between two joints of a subcategory being the column steel profile employed. However, the results for the six joint configurations are provided in Appendix A of this thesis. For each of them, tables summarizing the results computed at different steps of the calculation procedure introduced in sections 3.2.1 & 3.2.2 are provided. To serve as an example, the complete and detailed derivation of the interaction curve for joint configuration A1 is described in section A.1.

The ductile resistance interaction curves of the six FAILNOMORE joint configurations are, as for them, illustrated at Figures 3.25 to 3.27. They are presented two by two in function of the joint subcategory to which they belong (A, B & C).

#### Configuration A1 - Analytical results

##### *Component method*

The row numbers written in the first column of the tables correspond to those of the Cerfontaine model convention which are indicated on the technical drawings in Figures 3.16 to 3.21. If many rows present exactly the same resistance and stiffness properties for all their components, a unique line in the tables will be used to present their properties.

In Tables 3.12 & 3.13, the bold component resistances allow to highlight the component which will lead to the failure of this row, or in other words, the critical component of the latter. It fits here again to underline that the BT component resistance does not need to be considered when identifying the critical component of the tension rows, this failure mode being already taken into account through the mode n°3 of the CFB and EPB components.

Note that in Table 3.12 and in the similar tables for the other joints, the resistance  $F_{Rd}$  of the BT component is expressed for only one bolt while its stiffness  $k$  is expressed for the two bolts of the row.

Table 3.12: FAILNOMORE - Configuration A1 - Components properties - Individual rows - 3.

Individual rows	Component abbreviation	$F_{Rd}$ [kN]	$k$ [mm]
Compression row n°1/4	CWS	-1,034.655	/
	CWC	<b>-919.843</b>	10.412
	BFC	-1,609.235	$\infty$
Tension row n°2/3	BT	254.16	9.001
	CFB	508.32	53.536
	CWT	887.99	7.037
	EPB	<b>386.24</b>	9.496
	BWT	1,012.28	$\infty$

The joint possessing only two tension bolts-rows, it is logical that only one group mechanism can form between these two latter. The resistances of the various components where this group can form are listed in Table 3.13.

Table 3.13: FAILNOMORE - Configuration A1 - Components properties - Group of rows - 3.

Group of rows	Component abbreviation	$F_{Rd}$ [kN]
Group mechanism 23	CFB	1,016.64
	CWT	1,457.58
	EPB	<b>830.94</b>
	BWT	2,526.55

Table 3.14: FAILNOMORE - Configuration A1 - Row/Group resistances - 4.

i	$F_{[i,i],Rd}$ [kN]	$F_{[i-1,i],Rd}$ [kN]	Critical Component
1 = sup	-919.84	$\infty$	CWC
2	386.24	$\infty$	EPB
3	386.24	830.94	EPB
4 = inf	-919.84	$\infty$	CWC

### *Cerfontaine model*

In Table 3.15, the resistances values  $F_{i,Rd}^+$  &  $F_{i,Rd}^-$  are identical for each of the rows. This observation can indeed be explained by the perfect symmetry of the joint around the two beam axes, but also by the fact that the plastic resistance of group mechanism 23 is greater than the sum of the individual plastic resistances of the rows composing it. There is therefore no group effect on the individual resistances of the rows.

Table 3.15: FAILNOMORE - Configuration A1 - Levers arms and  $F_{i,Rd}^+$  &  $F_{i,Rd}^-$  resistance values - 5. & 6.

i	$h_i$ [m]	$F_{i,Rd}^+$ [kN]	$F_{i,Rd}^-$ [kN]
1 = sup	0.242	-919.84	-919.84
2	0.19	386.24	386.24
3	-0.19	386.24	386.24
4 = inf	-0.242	-919.84	-919.84

In view of the results from Table 3.15, the characteristic M-N resistance points for this configuration must necessarily be symmetrically arranged around the vertical axis, which is indeed the case as shown with the results of Table 3.16.

Table 3.16: FAILNOMORE - Configuration A1 - Characteristic M-N resistance points - 7.

N°	$M_{Rd}^+$ [kNm]	$N_{Rd}^+$ [kN]	$M_{Rd}^-$ [kNm]	$N_{Rd}^-$ [kN]
1	0.0	-1,839.68	0.0	-1,839.68
2	222.6	-919.84	-222.6	-919.84
3	295.98	-533.6	-295.98	-533.6
4	222.6	-147.36	-222.6	-147.36
5	0.0	772.48	0.0	772.48

### Configuration A1 - COP results

The characteristic M-N resistance points obtained with the beta version of COP are presented in Table 3.17. These results are, as expected, almost perfectly identical to those derived analytically and presented in Table 3.16. The small variations observed are probably due to the difference in decimal precision used in the python codes and in COP.

Table 3.17: FAILNOMORE - Configuration A1 - COP - Characteristic M-N resistance points

N°	$M_{Rd}^+$ [kNm]	$N_{Rd}^+$ [kN]	$M_{Rd}^-$ [kNm]	$N_{Rd}^-$ [kN]
1	0.0	-1,839.66	0.0	-1,839.66
2	222.6	-919.83	-222.6	-919.83
3	295.99	-533.57	-295.99	-533.57
4	222.6	-147.32	-222.6	-147.32
5	0.0	772.51	0.0	772.51

However, to objectively compare the ductile resistance interaction curves that can be drawn from these two sets of points, the Hausdorff distance between the two curves has been computed. Indeed, in this context, the Hausdorff distance corresponds to the maximum measurable distance between any point on one curve and the nearest point on the other curve. This value is calculated in the python codes using the shapely library.

To disregard the unit difference between the two graph axes, the two curves have been normalised to a dimensionless form. To achieve this, the coordinates of the characteristic M-N resistance points from both interaction curves were normalised by dividing them by the maximum absolute value of their respective axes. For this configuration, the dimensionless Hausdorff distance is equal to  $4.9 \times 10^{-5}$ , which is clearly negligible when compared to a value of one, and thus confirms the strong similarity between the results obtained from both approaches.

**Configuration B1 - Analytical results**

Identical tables to the ones already presented for the joint configuration A1 are provided for this configuration and the next one.

Table 3.18: FAILNOMORE - Configuration B1 - Components properties - Individual rows - 3.

Individual rows	Component abbreviation	$F_{Rd}$ [kN]	$k$ [mm]
Compression row n°1/5	CWS	-1,034.655	/
	CWC	<b>-920.936</b>	10.45
	BFC	-1,856.954	$\infty$
Tension row n°2	BT	254.16	9.001
	CFB	508.32	39.72
	CWT	888.05	5.221
	EPB	<b>388.041</b>	6.645
	BWT	1,101.487	$\infty$
Tension row n°3	BT	254.16	9.001
	CFB	508.32	39.72
	CWT	888.05	5.221
	EPB	<b>371.112</b>	5.245
	BWT	944.028	$\infty$
Tension row n°4	BT	254.16	9.001
	CFB	508.32	53.54
	CWT	888.05	7.037
	EPB	<b>388.041</b>	9.739
	BWT	1,101.487	$\infty$

Table 3.19: FAILNOMORE - Configuration B1 - Components properties - Group of rows - 3.

Group of rows	Component abbreviation	$F_{Rd}$ [kN]
Group mechanism 23	CFB	904.815
	CWT	1,036.026
	EPB	<b>683.076</b>
	BWT	1,337.917
Group mechanism 34	CFB	1,016.64
	CWT	1,451.022
	EPB	<b>814.41</b>
	BWT	2,559.472
Group mechanism 24	CFB	1,524.96
	CWT	1,490.931
	EPB	<b>1,126.375</b>
	BWT	2,953.362

Table 3.20: FAILNOMORE - Configuration B1 - Row/Group resistances - 4.

i	$F_{[i,i],Rd}$ [kN]	$F_{[i-1,i],Rd}$ [kN]	$F_{[i-2,i],Rd}$ [kN]	Critical Component
1 = sup	-920.93	$\infty$	$\infty$	CWC
2	388.04	$\infty$	$\infty$	EPB
3	371.11	683.07	$\infty$	EPB
4	388.04	814.41	1,126.37	EPB
5 = inf	-920.93	$\infty$	$\infty$	CWC

Contrary to the results presented for the configuration A1, the  $F_{i,Rd}^+$  &  $F_{i,Rd}^-$  resistance values from Table 3.21 are no longer identical for each row. This change is logically attributed to the new proximity between rows n°2 & n°3. It indeed results in lower group resistances and prevents some tension rows to reach their individual plastic resistances.

Table 3.21: FAILNOMORE - Configuration B1 - Lever arms and  $F_{i,Rd}^+$  &  $F_{i,Rd}^-$  resistance values - 5. & 6.

i	$h_i$ [m]	$F_{i,Rd}^+$ [kN]	$F_{i,Rd}^-$ [kN]
1 = sup	0.266	-920.93	-920.93
2	0.215	388.04	311.96
3	0.155	295.03	371.11
4	-0.215	388.04	388.04
5 = inf	-0.266	-920.93	-920.93

Table 3.22: FAILNOMORE - Configuration B1 - Characteristic M-N resistance points - 7.

N°	$M_{Rd}^+$ [kNm]	$N_{Rd}^+$ [kN]	$M_{Rd}^-$ [kNm]	$N_{Rd}^-$ [kN]
1	0.0	-1,841.87	0.0	-1,841.87
2	245.33	-920.93	-245.33	-920.93
3	328.76	-532.89	-328.76	-532.89
4	374.49	-237.86	-271.24	-161.78
5	291.06	150.18	-204.17	150.18
6	45.73	1,071.11	41.16	1,071.11

The ductile resistance interaction curve of the joint B1 is also no longer symmetrical with respect to the vertical axis, due to the geometrical asymmetry of the configuration, as indicated by the characteristic M-N resistance points from Table 3.22

### Configuration B1 - COP results

Table 3.23: FAILNOMORE - Configuration B1 - COP - Characteristic M-N resistance points

N°	$M_{Rd}^+$ [kNm]	$N_{Rd}^+$ [kN]	$M_{Rd}^-$ [kNm]	$N_{Rd}^-$ [kN]
1	0.0	-1,841.85	0.0	-1,841.85
2	245.33	-920.92	-245.33	-920.92
3	328.77	-532.87	-328.77	-532.87
4	374.50	-237.84	-271.24	-161.76
5	291.06	150.22	-204.17	150.22
6	45.73	1,071.14	41.17	1,071.14

Once again, the results extracted from COP and presented in Table 3.23 are concordant with the analytical results obtained with python codes. The differences are still due to the decimal precision employed to realise the calculations. The dimensionless Hausdorff distance is this time equal to  $2.04 \times 10^{-5}$ .

### Configuration C2 - Analytical results

Table 3.24: FAILNOMORE - Configuration C2 - Components properties - Individual rows - 3.

Individual rows	Component abbreviation	$F_{Rd}$ [kN]	$k$ [mm]
Compression row n°1/7	CWS	-1,117.85	/
	CWC	<b>-981.628</b>	10.37
	BFC	-2,145.886	$\infty$
Tension row n°2	BT	254.16	8.86
	CFB	508.32	46.44
	CWT	930.675	5.047
	EPB	<b>390.517</b>	6.932
	BWT	1,196.956	$\infty$
Tension row n°3/4	BT	254.16	8.86
	CFB	508.32	18.51
	CWT	930.675	2.011
	EPB	<b>372.125</b>	2.166
	BWT	1,012.903	$\infty$
Tension row n°5	BT	254.16	8.86
	CFB	508.32	46.44
	CWT	930.675	5.047
	EPB	<b>372.125</b>	5.376
	BWT	1,012.903	$\infty$
Tension row n°6	BT	254.16	8.86
	CFB	508.32	62.32
	CWT	930.675	6.772
	EPB	<b>390.517</b>	9.94
	BWT	1,196.956	$\infty$



Table 3.25: FAILNOMORE - Configuration C2 - Components properties - Group of rows - 3.

Group of rows	Component abbreviation	$F_{Rd}$ [kN]
Group mechanism 23	CFB	938.833
	CWT	1,090.414
	EPB	<b>686.968</b>
	BWT	1,452.556
Group mechanism 34	CFB	938.833
	CWT	1,090.414
	EPB	<b>668.575</b>
	BWT	1,268.503
Group mechanism 24	CFB	1,295.767
	CWT	1,221.368
	EPB	<b>903.536</b>
	BWT	1,708.156
Group mechanism 45	CFB	938.833
	CWT	1,090.414
	EPB	<b>668.575</b>
	BWT	1,268.503
Group mechanism 35	CFB	1,295.767
	CWT	1,221.368
	EPB	<b>806.18</b>
	BWT	1,524.103
Group mechanism 25	CFB	1,652.7
	CWT	1,327.704
	EPB	<b>1,038.736</b>
	BWT	1,963.756
Group mechanism 56	CFB	1,016.64
	CWT	1,483.573
	EPB	<b>789.134</b>
	BWT	2,474.956
Group mechanism 46	CFB	1,524.96
	CWT	1,540.389
	EPB	<b>1,085.584</b>
	BWT	2,730.556
Group mechanism 36	CFB	1,950.834
	CWT	1,586.924
	EPB	<b>1,382.034</b>
	BWT	2,986.156
Group mechanism 26	CFB	2,307.767
	CWT	<b>1,625.303</b>
	EPB	1,696.876
	BWT	3,425.809

Table 3.26: FAILNOMORE - Configuration C2 - Row/Group resistances - 4.

i	$F_{[i,i],Rd}$ [kN]	$F_{[i-1,i],Rd}$ [kN]	$F_{[i-2,i],Rd}$ [kN]	$F_{[i-3,i],Rd}$ [kN]	$F_{[i-4,i],Rd}$ [kN]	Crit. Comp.
1 = sup	-981.62	$\infty$	$\infty$	$\infty$	$\infty$	CWC
2	390.51	$\infty$	$\infty$	$\infty$	$\infty$	EPB
3	372.12	686.96	$\infty$	$\infty$	$\infty$	EPB
4	372.12	668.57	903.53	$\infty$	$\infty$	EPB
5	372.12	668.57	806.18	1,038.73	$\infty$	EPB
6	390.51	789.13	1,085.58	1,382.03	1,625.3	EPB & CWT
7 = inf	-981.62	$\infty$	$\infty$	$\infty$	$\infty$	CWC

Table 3.27: FAILNOMORE - Configuration C2 - Lever arms and  $F_{i,Rd}^+$  &  $F_{i,Rd}^-$  resistance values - 5. & 6.

i	$h_i$ [m]	$F_{i,Rd}^+$ [kN]	$F_{i,Rd}^-$ [kN]
1 = sup	0.29	-981.62	-981.62
2	0.24	390.51	232.55
3	0.18	296.45	137.6
4	0.12	216.56	296.45
5	0.06	135.2	372.12
6	-0.24	390.51	390.51
7 = inf	-0.29	-981.62	-981.62

Table 3.28: FAILNOMORE - Configuration C2 - Characteristic M-N resistance points - 7.

N°	$M_{Rd}^+$ [kNm]	$N_{Rd}^+$ [kN]	$M_{Rd}^-$ [kNm]	$N_{Rd}^-$ [kN]
1	0.0	-1,963.25	0.0	-1,963.25
2	285.16	-981.62	-285.16	-981.62
3	378.88	-591.11	-378.88	-591.11
4	432.24	-294.66	-356.56	-218.98
5	458.23	-78.09	-320.98	77.46
6	466.34	57.1	-296.21	215.07
7	372.62	447.62	-240.4	447.62
8	87.46	1,429.25	44.76	1,429.25

### Configuration C2 - COP results

Table 3.29: FAILNOMORE - Configuration C2 - COP - Characteristic M-N resistance points

N°	$M_{Rd}^+$ [kNm]	$N_{Rd}^+$ [kN]	$M_{Rd}^-$ [kNm]	$N_{Rd}^-$ [kN]
1	0.0	-1,963.20	0.0	-1,963.20
2	285.16	-981.60	-285.16	-981.60
3	378.87	-591.13	-378.87	-591.13
4	432.23	-294.68	-356.54	-219
5	458.20	-78.28	-320.97	77.45
6	466.31	56.92	-296.20	215.05
7	372.60	447.39	-240.44	447.39
8	87.44	1,429	44.72	1,429

The computed dimensionless Hausdorff distance is  $1.37 \times 10^{-4}$ , which is slightly higher than before but still remains really acceptable.

Given the similarity of the analytical and COP results for the different joints, it can finally be concluded that both calculation methods can accurately derive the full ductile resistance interaction curve of joints. This validation of the beta version of COP therefore now allows its serene usage within the framework of the parametric study described in Section 3.2.5.

### Ductile resistance interaction curves

The six ductile resistance interaction curves of the FAILNOMORE joint configurations are represented on Figures 3.25 to 3.27. For a matter of continuity and consistency, a unique colour has been attributed to each joint configuration. Indeed, these several colours will be employed as a common thread in the rest of this thesis to designate the joints to which they are associated.

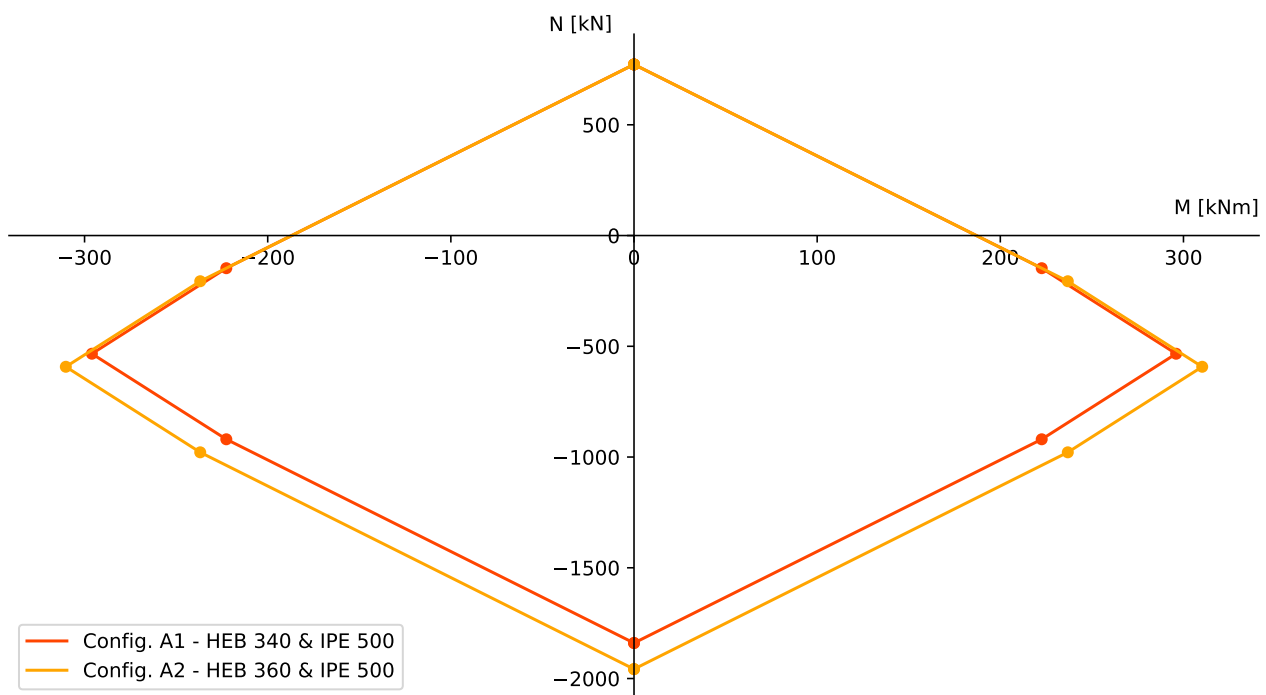


Figure 3.25: FAILNOMORE - Joint configurations A1 & A2 - Ductile resistance interaction curves - 8.

As previously mentioned, the ductile resistance interaction curves for configurations A1 & A2 had necessarily to be symmetrical with respect to the vertical axis, due to their symmetries around the beam axes. The points of maximum compression and tension resistance also had to be logically located on the vertical axis, since the  $F_{Rd}^+$  &  $F_{Rd}^-$  vectors are perfectly identical.

Moreover, the Figure 3.25 allows to highlight a slight enlargement of the interaction curve in the compression area of the graph when a HEB 360 column profile is used instead of a HEB 340. The HEB 360 section presenting higher web and flange thicknesses, the resistances of the CWS & CWC components are both increased, thereby impacting the distributions of internal forces where compression rows are active. This is indeed the case here, since only the characteristic M-N resistance points  $1^{+/-}$  to  $4^{+/-}$  have seen their coordinates affected by this modification.

Similar comments can be made for the ductile resistance interactions curves from Figures 3.26 & 3.27. However, the use of an HEM 300 profile having also required an increase of the horizontal spacing between the bolts of same rows, it is perfectly logical here to observe, in addition, a small reduction of the curve in the tension region of the graph. Indeed, this increase in horizontal spacing brings the bolts closer to the edges of the end-plate and the column flange, impacting the plastic line patterns of these components and consequently reducing their individual and group mechanism resistances.

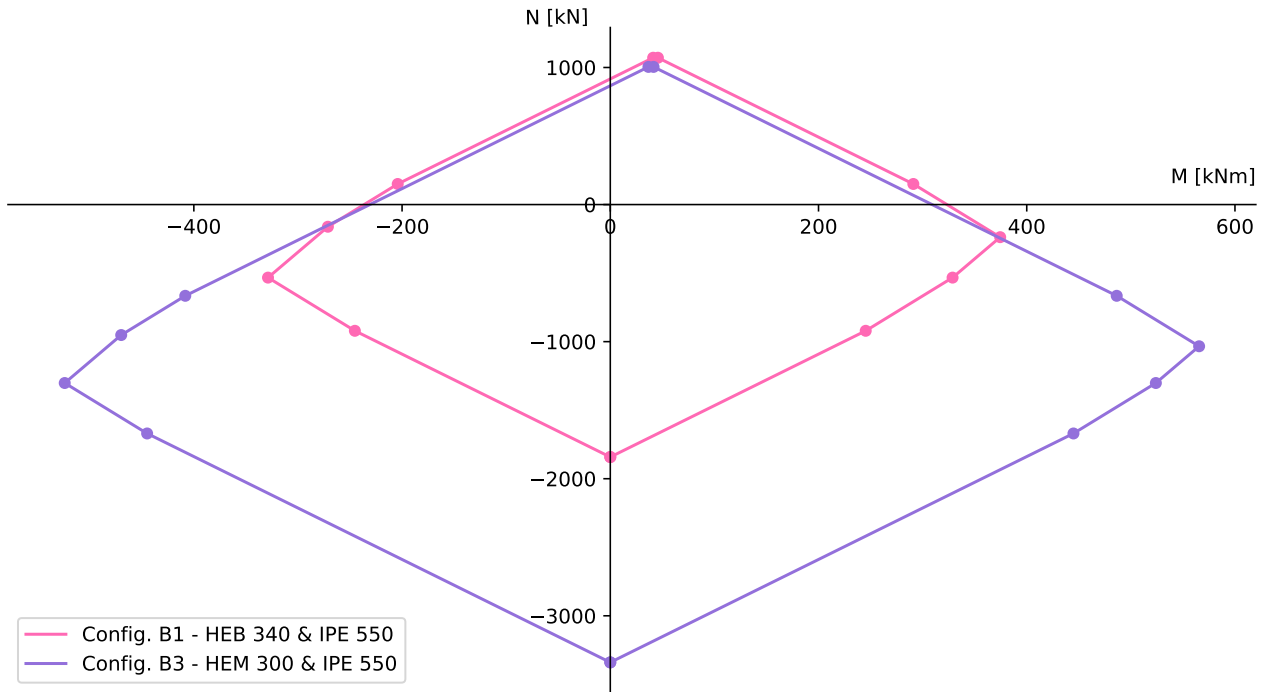


Figure 3.26: FAILNOMORE - Joint configurations B1 & B3 - Ductile resistance interaction curves - 8.

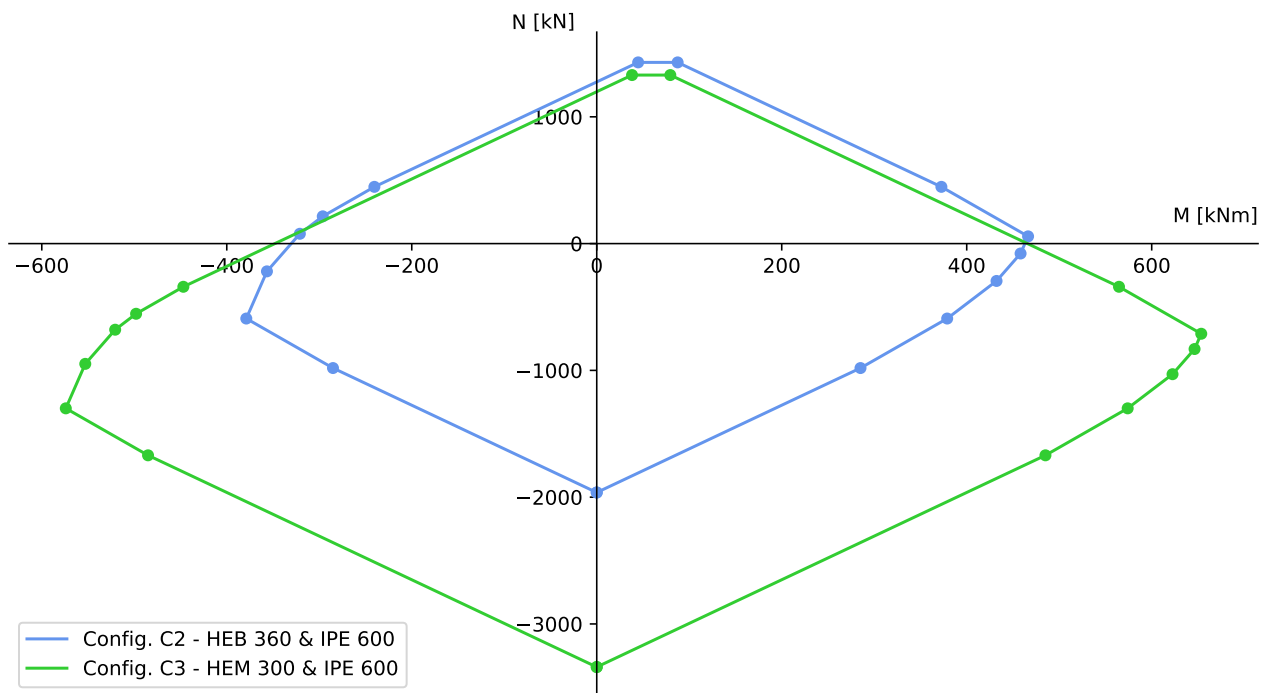


Figure 3.27: FAILNOMORE - Joint configurations C2 & C3 - Ductile resistance interaction curves - 8.

### 3.4.2 Coimbra joint configurations

This subsection compares the experimental results presented in Section 3.3.2 with several analytically derived ductile resistance interaction curves, to assess whether these curves can accurately predict the joint plastic resistance. Both joint configurations tested at Coimbra comply with the two ductility criteria that must be verified to apply the Cerfontaine model (see Section 3.2.2).

Taking into account the steel mechanical properties measured in the laboratory and listed in Tables 3.6 & 3.7, four distinct ductile resistance interaction curves were derived for the two joint configurations. One of the curves will be obtained using the theoretical mechanical properties of the various steel elements, while the other three will be based on the minimum, mean, and maximum mechanical properties determined from tensile tests on coupons. The theoretical geometrical properties have as for them been used for all of the curves.

Only the results computed using the theoretical mechanical properties of steel will be presented for all stages of the methodology tree shown in Figure 3.1. Similar results can indeed be obtained for the other three sets of mechanical properties by simply employing them into the equations of the calculation procedure. However, when considering the actual ultimate strength value of the bolts, the safety factor  $\gamma_{M2}$  is set to 1.0. All characteristic M–N resistance points of the four ductile resistance interaction curves are listed hereafter for both joint configurations.

#### Flush end-plate configuration

##### *Theoretical mechanical properties*

Table 3.30: Coimbra - Flush end-plate configuration - Components properties - Individual rows - 3.

Individual rows	Component abbreviation	$F_{Rd}$ [kN]	$k$ [mm]
Compression row n°1/4	CWS	-474.837	/
	CWC	-507.089	10.16
	BFC	<b>-437.945</b>	$\infty$
Tension row n°2/3	BT	176.4	7.649
	CFB	326.984	40.47
	CWT	445.374	7.026
	EPB	<b>264.442</b>	13.24
	BWT	366.629	$\infty$

Table 3.31: Coimbra - Flush end-plate configuration - Components properties - Group of rows - 3.

Group of rows	Component abbreviation	$F_{Rd}$ [kN]
Group mechanism 23	CFB	627.476
	CWT	616.478
	EPB	<b>516.392</b>
	BWT	686.548

Table 3.32: Coimbra - Flush end-plate configuration - Row/Group resistances - 4.

i	$F_{[i,i],Rd}$ [kN]	$F_{[i-1,i],Rd}$ [kN]	Critical Component
1 = sup	-437.94	$\infty$	BFC
2	264.44	$\infty$	EPB
3	264.44	516.39	EPB
4 = inf	-437.94	$\infty$	BFC

Table 3.33: Coimbra - Flush end-plate config. - Lever arms and  $F_{i,Rd}^+$  &  $F_{i,Rd}^-$  resistance values - 5. & 6.

i	$h_i$ [m]	$F_{i,Rd}^+$ [kN]	$F_{i,Rd}^-$ [kN]
1 = sup	0.115	-437.94	-437.94
2	0.078	264.44	251.95
3	-0.078	251.95	264.44
4 = inf	-0.115	-437.94	-437.94

Table 3.34: Coimbra - Flush end-plate configuration - Theoretical - Characteristic M-N resistance points - 7.

N°	$M_{Rd}^+$ [kNm]	$N_{Rd}^+$ [kN]	$M_{Rd}^-$ [kNm]	$N_{Rd}^-$ [kN]
1	0.0	-875.89	0.0	-875.89
2	50.4	-437.94	-50.4	-437.94
3	71.03	-173.5	-71.03	-173.5
4	51.38	78.44	-51.38	78.44
5	0.97	516.39	-0.97	516.39

**Minimum mechanical properties**

Table 3.35: Coimbra - Flush end-plate configuration - Minimum - Characteristic M-N resistance points - 7.

N°	$M_{Rd}^+$ [kNm]	$N_{Rd}^+$ [kN]	$M_{Rd}^-$ [kNm]	$N_{Rd}^-$ [kN]
1	0.0	-994.15	0.0	-994.15
2	57.21	-497.08	-57.21	-497.08
3	83.03	-166.06	-83.03	-166.06
4	58.48	148.75	-58.48	148.75
5	1.26	645.82	-1.26	645.82

**Mean mechanical properties**

Table 3.36: Coimbra - Flush end-plate configuration - Mean - Characteristic M-N resistance points - 7.

N°	$M_{Rd}^+$ [kNm]	$N_{Rd}^+$ [kN]	$M_{Rd}^-$ [kNm]	$N_{Rd}^-$ [kN]
1	0.0	-1,083.36	0.0	-1,083.36
2	62.35	-541.68	-62.35	-541.68
3	89.15	-198.09	-89.15	-198.09
4	63.66	128.73	-63.66	128.73
5	1.31	670.41	-1.31	670.41

**Maximum mechanical properties**

Table 3.37: Coimbra - Flush end-plate configuration - Maximum - Characteristic M-N resistance points - 7.

N°	$M_{Rd}^+$ [kNm]	$N_{Rd}^+$ [kN]	$M_{Rd}^-$ [kNm]	$N_{Rd}^-$ [kN]
1	0.0	-1,165.19	0.0	-1,165.19
2	67.06	-582.59	-67.06	-582.59
3	94.96	-224.86	-94.96	-224.86
4	68.41	115.58	-68.41	115.58
5	1.35	698.17	-1.35	698.17

**Extended end-plate configuration*****Theoretical steel mechanical properties***

Table 3.38: Coimbra - Extended end-plate configuration - Components properties - Individual rows - 3.

Individual rows	Component abbreviation	$F_{Rd}$ [kN]	$k$ [mm]
Tension row n°1	BT	176.4	7.095
	CFB	326.984	33.04
	CWT	445.374	5.737
	EPB	<b>243.932</b>	20.11
Compression row n°2	CWS	-474.837	/
	CWC	-524.723	10.77
	BFC	<b>-437.945</b>	$\infty$
Tension row n°3/4	BT	176.4	7.095
	CFB	326.984	28.27
	CWT	445.374	4.909
	EPB	<b>264.442</b>	13.24
	BWT	366.629	$\infty$
Compression row n°5	CWS	-474.837	/
	CWC	-507.089	10.16
	BFC	<b>-437.945</b>	$\infty$

Table 3.39: Coimbra - Extended end-plate configuration - Components properties - Group of rows - 3.

Group of rows	Component abbreviation	$F_{Rd}$ [kN]
Group mechanism 13	CFB	571.488
	CWT	<b>543.378</b>
Group mechanism 34	CFB	627.476
	CWT	616.478
	EPB	<b>516.392</b>
	BWT	686.548
Group mechanism 14	CFB	871.98
	CWT	<b>660.889</b>

Table 3.40: Coimbra - Extended end-plate configuration - Row/Group resistances - 4.

i	$F_{[i,i],Rd}$ [kN]	$F_{[i-1,i],Rd}$ [kN]	$F_{[i-2,i],Rd}$ [kN]	$F_{[i-3,i],Rd}$ [kN]	Critical Component(s)
1	243.93	$\infty$	$\infty$	$\infty$	EPB
2 = sup	-437.94	$\infty$	$\infty$	$\infty$	BFC
3	264.44	$\infty$	543.38	$\infty$	EPB & CWT
4	264.44	516.39	$\infty$	660.89	EPB & CWT
5 = inf	-437.94	$\infty$	$\infty$	$\infty$	BFC

Table 3.41: Coimbra - Extended end-plate config. - Lever arms and  $F_{i,Rd}^+$  &  $F_{i,Rd}^-$  resistance values - 5. & 6.

i	$h_i$ [m]	$F_{i,Rd}^+$ [kN]	$F_{i,Rd}^-$ [kN]
1	0.152	243.93	144.49
2 = sup	0.115	-437.94	-437.94
3	0.078	264.44	251.95
4	-0.078	152.51	264.44
5 = inf	-0.115	-437.94	-437.94

Table 3.42: Coimbra - Extended end-plate config. - Theoretical - Characteristic M-N resistance points - 7.

N°	$M_{Rd}^+$ [kNm]	$N_{Rd}^+$ [kN]	$M_{Rd}^-$ [kNm]	$N_{Rd}^-$ [kN]
1	0.0	-875.89	0.0	-875.89
2	37.07	-631.96	-50.4	-437.94
3	87.48	-194.01	-71.03	-173.5
4	108.11	70.43	-51.38	78.44
5	96.21	222.94	-0.97	516.39
6	45.8	660.89	20.99	660.89

**Minimum mechanical properties**

Table 3.43: Coimbra - Extended end-plate config. - Minimum - Characteristic M-N resistance points - 7.

N°	$M_{Rd}^+$ [kNm]	$N_{Rd}^+$ [kN]	$M_{Rd}^-$ [kNm]	$N_{Rd}^-$ [kN]
1	0.0	-994.15	0.0	-994.15
2	45.94	-691.88	-57.21	-497.07
3	103.16	-194.8	-83.03	-166.06
4	128.98	136.21	-58.48	148.75
5	114.61	320.41	-1.26	645.82
6	57.39	817.48	24.83	817.48

**Mean mechanical properties**

Table 3.44: Coimbra - Extended end-plate config. - Mean - Characteristic M-N resistance points - 7.

N°	$M_{Rd}^+$ [kNm]	$N_{Rd}^+$ [kN]	$M_{Rd}^-$ [kNm]	$N_{Rd}^-$ [kN]
1	0.0	-1,083.36	0.0	-1,083.36
2	47.72	-769.4	-62.35	-541.68
3	110.07	-227.71	-89.15	-198.09
4	136.87	115.88	-63.66	128.73
5	118.42	352.37	-1.31	670.41
6	56.08	894.05	32.68	894.05



### Maximum mechanical properties

Table 3.45: Coimbra - Extended end-plate config. - Maximum - Characteristic M-N resistance points - 7.

N°	$M_{Rd}^+$ [kNm]	$N_{Rd}^+$ [kN]	$M_{Rd}^-$ [kNm]	$N_{Rd}^-$ [kN]
1	0.0	-1,165.19	0.0	-1,165.19
2	49.83	-837.38	-67.06	-582.59
3	116.88	-254.79	-94.96	-224.86
4	144.79	102.95	-68.4	115.58
5	123.39	377.21	-1.35	698.17
6	56.34	959.8	38.42	959.8

### Ductile resistance interaction curves with experimental results

In Figures 3.28 & 3.29, the four ductile resistance interactions curves derived for the two joint configurations are plotted, as well as the multiple points whose coordinates have experimentally been obtained. The M-N coordinates of these points are presented in Tables 3.8 & 3.9 for the flush end-plate and the extended end-plate configurations, respectively.

To potentially conclude that the Cerfontaine model can accurately predict the plastic resistance of the joints, all experimental points should ideally lie between the minimum and maximum ductile resistance interaction curves. This is indeed because these two curves were respectively derived based on the most pessimistic and most optimistic combination of actual steel mechanical properties. However, as shown in Figures 3.28 & 3.29, this is not actually the case for either of the joint configurations.

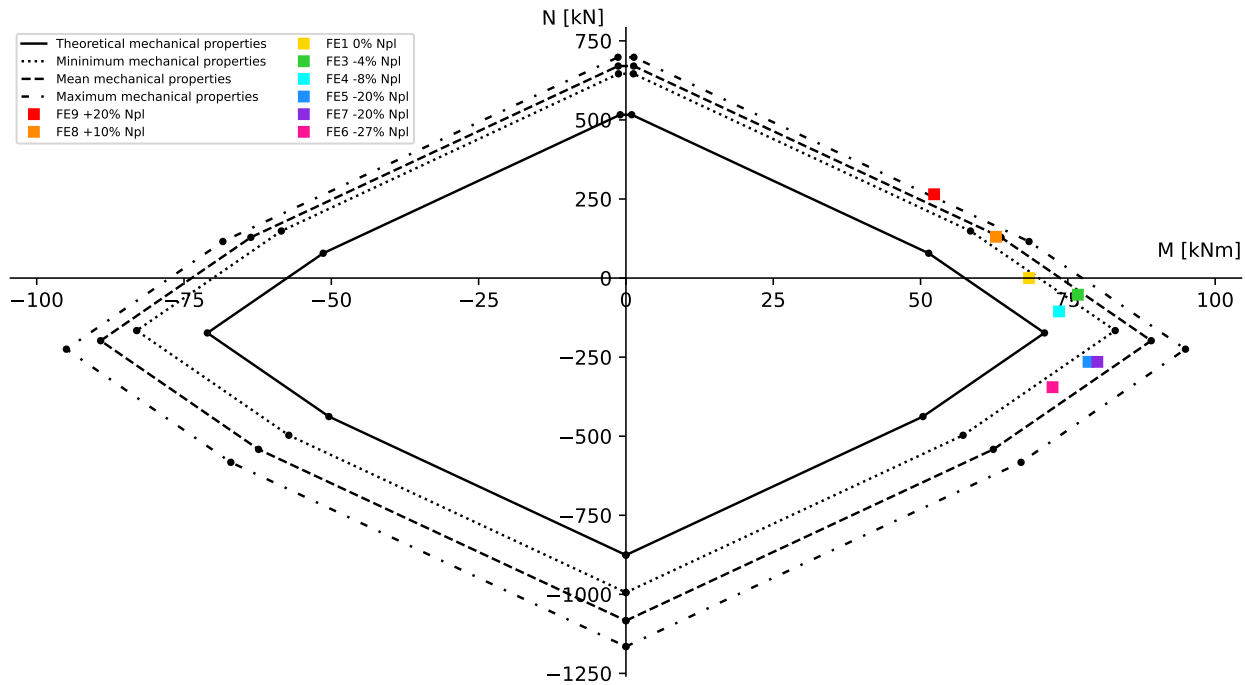


Figure 3.28: Coimbra - Flush end-plate configuration - Ductile curves and experimental results

Concerning the flush end-plate joint configuration, it can be first observed that most of the experimental points are indeed located between the two curves. However, it should also be noted that the results of the FE1 and FE4 tests fall within the minimum ductile resistance interaction curve, indicating a premature

yielding of the joint compared to the prediction provided by this lower-bound curve. For these two cases, the Cerfontaine model thus overestimates the actual resistance and must therefore be considered unsafe. Finally, based on the position of the FE9 point, it can be concluded in this case that the model is slightly conservative, which is absolutely not an issue.

Similar observations can be made for the extended end-plate joint configuration. However, for this second configuration, the lack of safety of the Cerfontaine model is more pronounced than for the previous one, as the EE6 and EE7 experimental points lie even further away from the minimum ductile resistance interaction curve.

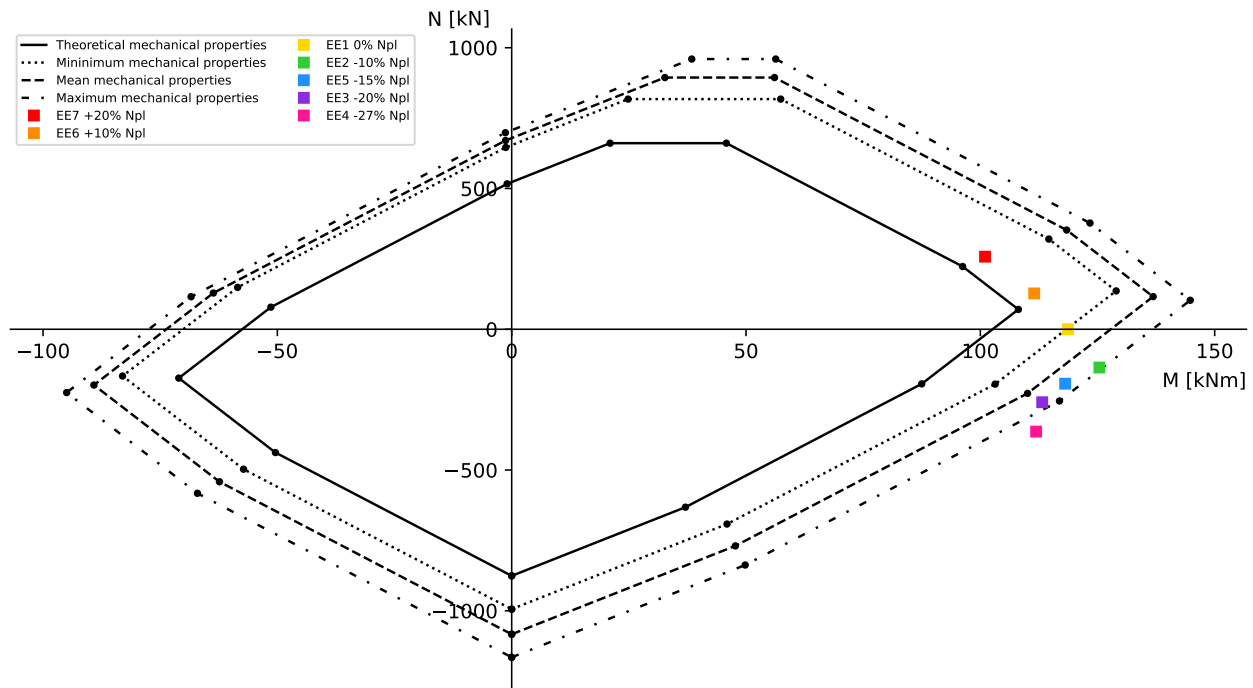


Figure 3.29: Coimbra - Extended end-plate configuration - Ductile curves and experimental results

In light of these results, some additional calculations were carried out to assess whether using the joint geometrical properties measured in the laboratory could potentially lead to different conclusions. Indeed, a review of the actual values listed in Appendix B.3 clearly shows that the discrepancy between the expected and actual dimensions is sometimes significant. However, these variations tend to average out, with the differences being either positive or negative depending on the specific test considered.

Nevertheless, the end-plate always exhibits a greater thickness than the one defined in the theoretical configurations (15 mm). Across all combined tests, the measured thickness values range from 15.16 mm to 15.77 mm. Since the EPB component is critical for the tension rows in both tested joint configurations, the four ductile resistance interaction curves for the flush and extended end-plate joints were once again derived using two distinct mean thickness values. These new curves are illustrated in Figures 3.30 & 3.31.

As expected, increasing the thickness of the end-plate expands the area enclosed by the four M-N resistance interaction curves in all directions of the graph. Therefore, when comparing the relative positions of the experimental points in Figures 3.28 & 3.29 with those in Figures 3.30 & 3.31, it can be observed that, in the latter graphs, the problematic points lie slightly further from the lower-bound curve. Therefore, taking into account the actual geometrical properties of the joint does not explain the observed discrepancies and even leads to the conclusion of a greater lack of safety of the Cerfontaine model.

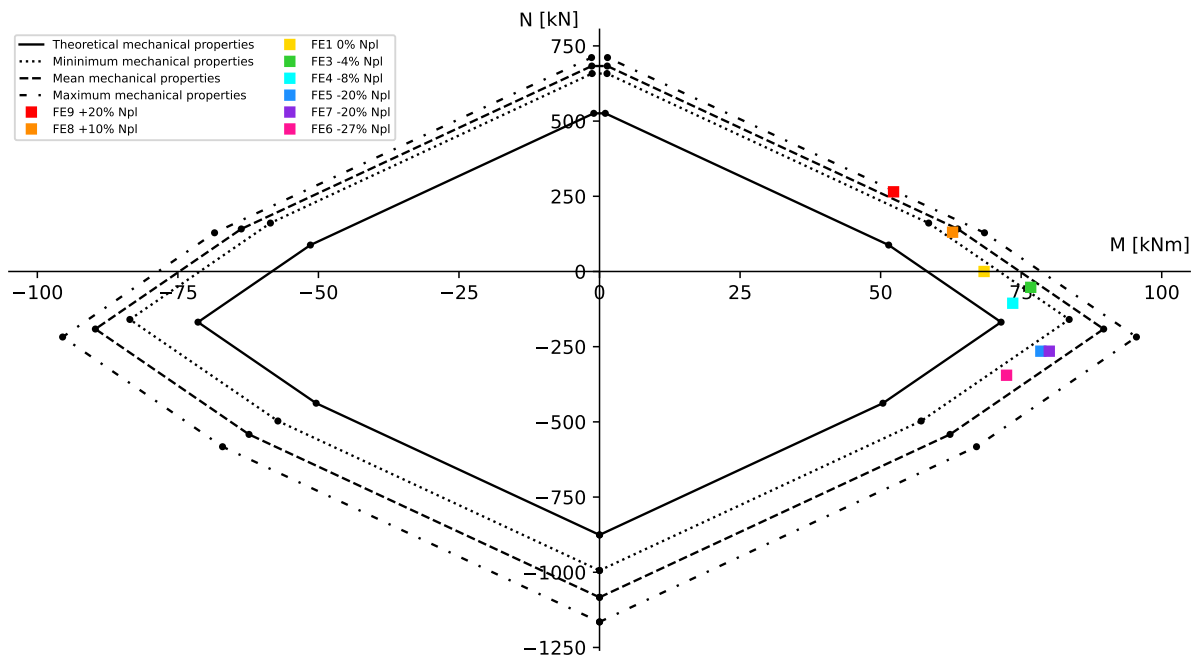


Figure 3.30: Coimbra - Flush end-plate configuration - Mean end-plate thickness ( $t_{ep} = 15.38$  mm)

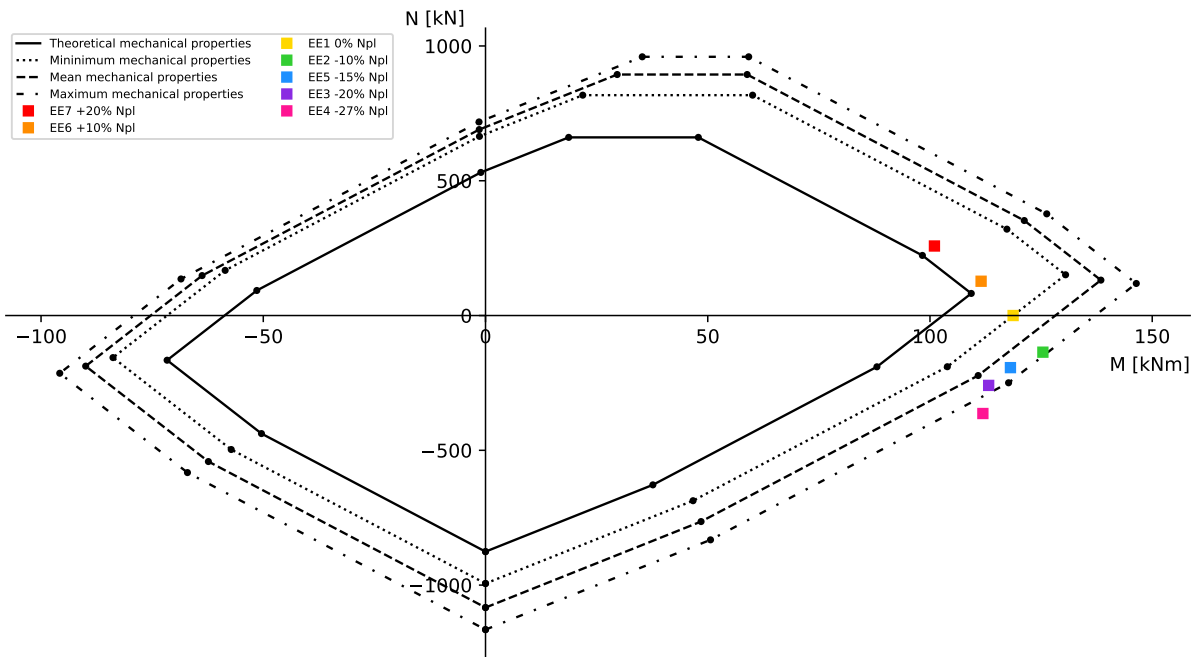


Figure 3.31: Coimbra - Extended end-plate configuration - Mean end-plate thickness ( $t_{ep} = 15.58$  mm)

In parallel with this thesis, another Master thesis investigating joints subjected to M-N interaction is currently underway at the University of Coimbra. This second thesis also builds on the same experimental results, but will instead compare them with numerical finite element simulations performed using the ABAQUS software. According to their initial feedback, the results they obtained appear to be consistent with those presented in this thesis. It may therefore be interesting to see, once their work is completed, whether their final conclusions align with the results established in the present study.

Although the analysis of these experimental results tends to conclude that the Cerfontaine model is unsafe, it remains important to put these findings into perspective. Indeed, several questions are still being raised about the quality and reliability of these experimental results. Moreover, the Cerfontaine model has already demonstrated good accuracy when compared with the results of other experimental campaigns, particularly those involving tests on steel and composite joints, carried out respectively in Prague and Coimbra. More information about these tests and their comparison can be found in [3, 19, 24].

### 3.4.3 Parametric analysis

In this subsection, the results of the parametric analysis, whose methodology was detailed in Section 3.2.5, are presented and discussed. Since variations in the different joint properties generally lead to similar observations across the three studied configurations, only the most relevant results for each property will be presented here. The remaining figures are available in Appendix C. As a reminder, all results were generated using the beta version of the COP software.

#### *Column steel grade*

It can be immediately observed in Figure 3.32 that the resistance interaction curves plotted differ from those previously presented in this thesis. Indeed, these curves are no longer composed of  $2n + 2$  characteristic M-N resistance points, the slopes between these points do not always correspond to the lever arms of the rows, and the curves exhibit inflection points. All these new characteristics of the curves are, in fact, typical of non-ductile resistance interaction curves.

In the case of non-ductile joints, such as the example from the Cerfontaine thesis, the calculation procedure described in Section 3.2.2 cannot be applied to derive the M-N resistance interaction curves. Indeed, the infinite ductility assumption is no longer satisfied, which prevents the definition of the  $2n + 2$  full plastic distributions of internal forces. Therefore, to determine the force distributions under which the failure of the joint will occur, it is necessary to follow an iterative process that accounts for the stiffness of the different rows and the ductility limit of the non-ductile ones. Moreover, the loading cycle followed by the joint now plays a major role, as the limited ductility of certain rows prevents any further plastic redistribution among them.

Since the main objective of this Master thesis is not focused on the M-N characterisation of non-ductile joints, the specific aspects related to them will not be discussed further here. However, much more information on this topic can be found in the Ph.D. thesis of F. Cerfontaine [3]. Nevertheless, the apparition of non-ductile behaviours will still be underlined and justified throughout this parametric analysis.

For all the curves shown in Figure 3.32, the non-ductility can be simply explained by the fact that both the CFB and EPB components of at least one tension row are consistently associated with the failure mode n°3.

Beyond highlighting the non-ductility of the joint, additional insights can be drawn from Figure 3.29. It can indeed be observed that, on the compression side of the graph, the area enclosed by the non-ductile resistance interaction curves decreases or increases depending on whether the steel grade of the column profile decreases or increases, respectively. This evolution can logically be attributed to the variation in the resistance of the CWS and CWC components, which, as demonstrated by Equations (3.2) & (3.5), depends on the design yield strength of the column web. It can also be deduced that the BFC component is never the critical component of the compression rows.

Then, it can be noted that the maximum tensile resistance of the joint decreases, compared to the initial curve, as the steel grade of the column is reduced. This observation is also associated with an increase in the horizontal distance between the two points of maximum tensile resistance. Indeed, as the steel grade of the column decreases, group mechanisms forming in the column web become increasingly critical, thereby preventing certain rows from reaching their maximum tensile resistance. These group mechanisms also result in a greater disparity in force distribution under hogging and sagging bending moments, which manifests itself as wider horizontal flat regions.

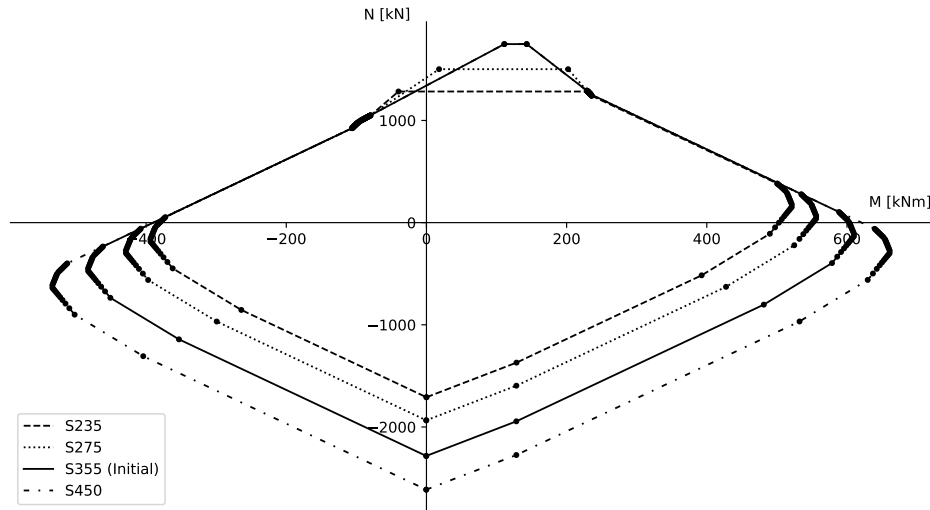


Figure 3.32: Parametric analysis - Cerfontaine example - Variation of the column steel grade

Finally, it can be underlined that using a column made of S455 steel does not enhance the maximum tension resistance compared to using S355 steel. In fact, this increase couldn't affect the resistance of the tension rows in any case, since the CWT and CFB components were already non-critical for most of them in the initial configuration.

### Beam steel grade

Based on Figure 3.33, it can be stated that changing the steel grade of the beam profile has no impact whatsoever on the ductile resistance interaction curve of configuration C2. Therefore, it can also be concluded that the BFC and BWT components are consistently non-critical for the compression and tension rows, respectively. These observations are identical for the two other joint configurations, as shown in Appendix C.

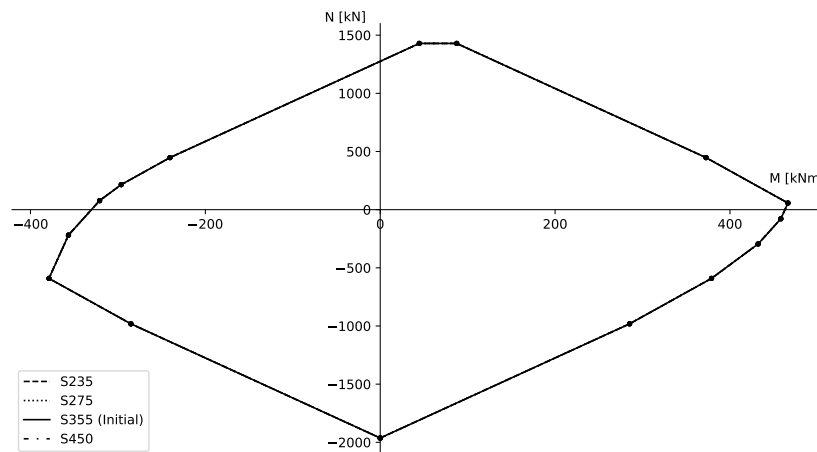


Figure 3.33: Parametric analysis - Configuration C2 - Variation of the beam steel grade

### End-plate steel grade

In Figure 3.34, it can be observed that, on the compression side of the graph, variations in the end-plate steel grade do not significantly affect the M-N resistance interaction curves. This observation is, in fact, logical, as this property does not appear in the equations governing the components of the compression rows. In contrast, on the opposite side of the graph, the maximum tension resistance of the joint shows slight variations around the initial curve. It is also worth noting that when S235 steel is used for the end-plate, the shape of the M-N resistance interaction changes. In fact, due to the reduced steel grade, the EPB component in all tension rows exhibits only ductile failure modes and has become their critical component, thus making the joint ductile.

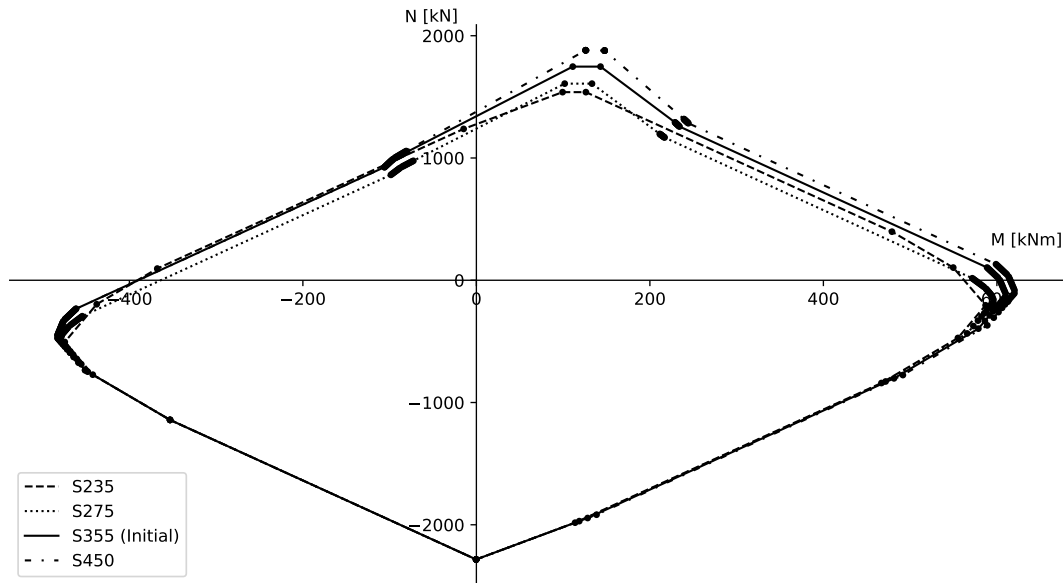


Figure 3.34: Parametric analysis - Cerfontaine example - Variation of the end-plate steel grade

### Bolts steel grade

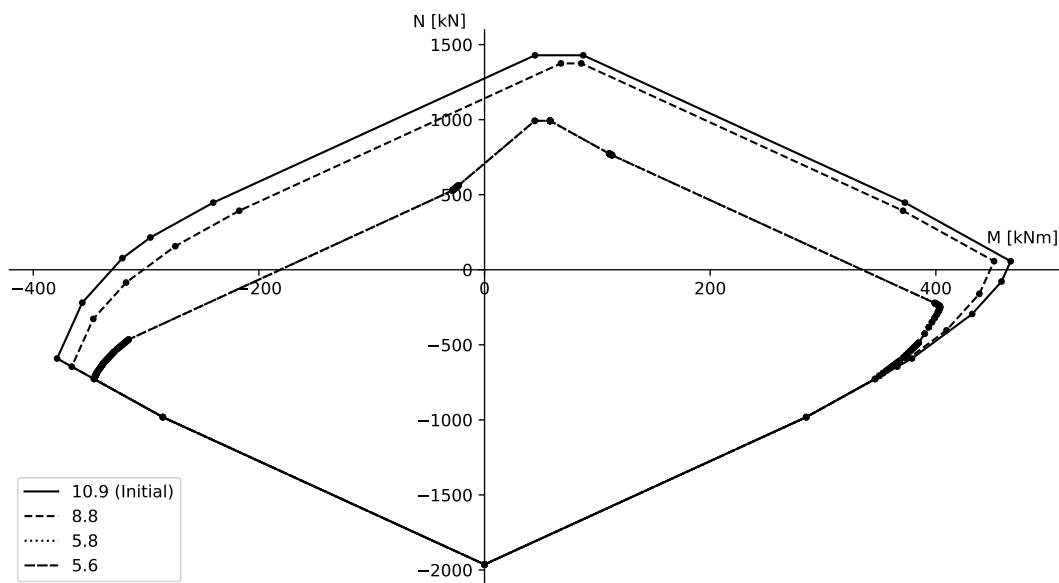


Figure 3.35: Parametric analysis - Configuration C2 - Variation of the bolts steel grade

The Figure 3.35 clearly illustrates the importance of the bolts steel grade on the behaviour of the joint and its M-N resistance interaction curve. Indeed, when high-strength bolts of grade 10.9 or 8.8 are used, the CFB and EPB components of all the tension rows exhibit failure modes n°1 or n°2, allowing the joint to be classified as ductile. Logically, the two corresponding ductile resistance interaction curves differ only in the region where the tension rows are active.

However, if lower-grade bolts are used, their design tensile resistance decreases significantly, shifting the failure modes of the CFB and EPB components to mode n°3 and resulting in a non-ductile joint. As expected, the two non-ductile resistance interaction curves shown in Figure 3.35 overlap, since the ultimate tensile strengths of grade 5.8 and 5.6 bolts are identical and equal to 500 MPa.

### ***End-plate thickness increase***

In Figure 3.36, the end-plate thickness is gradually increased from 15 mm to 30 mm. In the segments of the M-N resistance interaction curves where the tension rows are active, this increase globally leads to a higher joint resistance. However, when the end-plate becomes too thick, the resistance of the EPB component associated with failure modes n°1 and n°2 generally exceeds the tensile resistance of the bolts, causing the loss of its ductile behaviour. This explains the shift to a non-ductile resistance interaction curve as the end-plate thickness reaches 25 mm.

The increase of the end-plate thickness finally generates a very slight improvement of the compression resistance of the joint. In fact, the CWC component, which is critical for the compression rows in this case, experiences a resistance increase as the end-plate becomes thicker. This is because this joint property is taken into account in the calculation of the effective compression width, as shown in Equation (3.4).

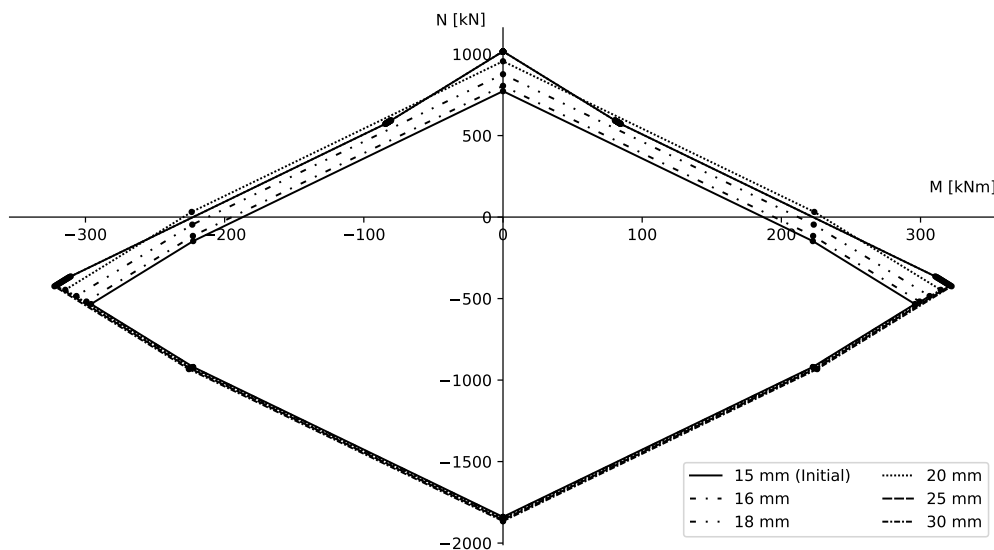


Figure 3.36: Parametric analysis - Configuration A1 - Increase of the end-plate thickness

### ***End-plate thickness decrease***

Quite logically, the opposite observations to those made for Figure 3.36 can now be seen in Figure 3.37, when the thickness of the end-plate is reduced. In this case, the M-N resistance interaction curve transitions from non-ductile to ductile when the end-plate thickness is equal to or less than 16 mm. The compression part of the curves slightly decreases. Finally, the overall tension resistance of the joint decreases, as the design plastic moment resistance of the equivalent T-stub flanges reduces with decreasing end-plate thickness, as shown in Equations (3.16) and (3.17).

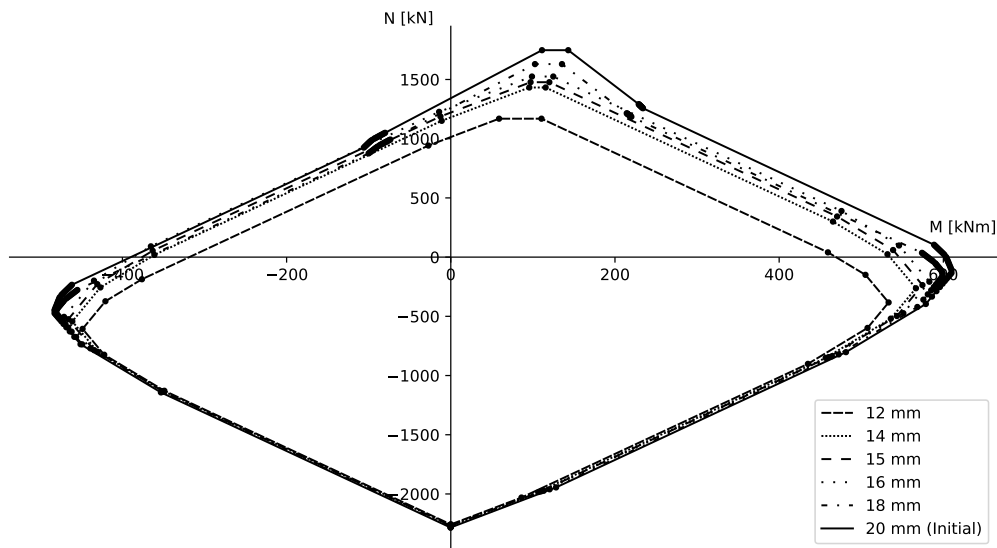


Figure 3.37: Parametric analysis - Cerfontaine example - Decrease of the end-plate thickness

### *Column flange thickness decrease*

In order to reduce the column web thickness without altering the other properties of the column profile, fictitious column sections were created in COP. As shown in Figure 3.38, the maximum tensile resistance of the joint remains unaffected by the reduction until the column flange thickness drops to 12 mm. This sudden change in the ductile resistance interaction curve corresponds to the transition from the EPB to the CFB component as the critical element of the tension rows. All characteristic M-N resistance points involving an active compression row are also affected by the reduction in column flange thickness. Indeed, this latter contributes greatly to the value of the effective compression width of the CWC component.

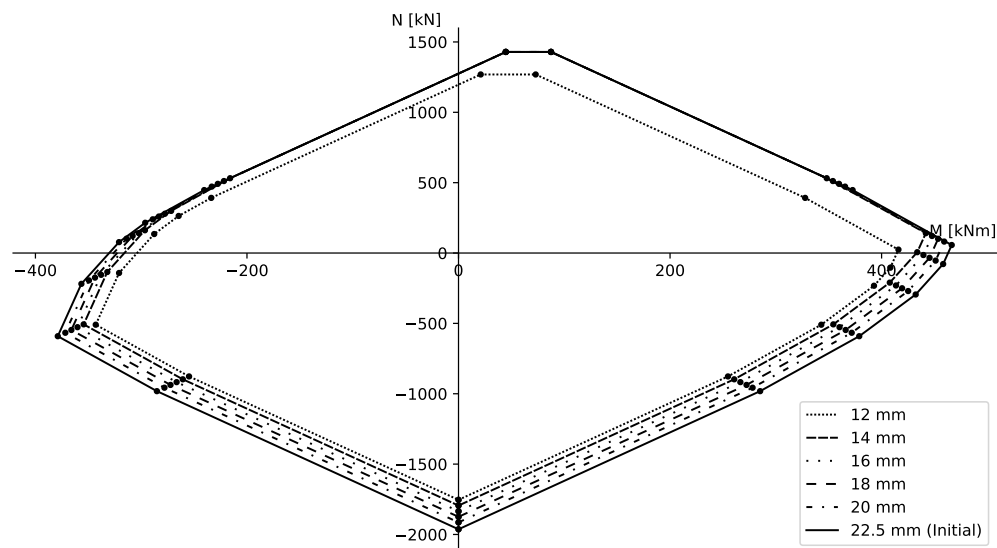


Figure 3.38: Parametric analysis - Configuration C2 - Decrease of the column flange thickness

### *Transformation parameter $\beta$*

In Figure 3.39, distinct constant values of the transformation parameter  $\beta$  were used to generate each of the illustrated ductile resistance interaction curves. As a reminder, this parameter reflects the ratio between the web panel shear force and the compressive and tensile connection forces.



It can initially be observed that the maximum tension resistance of the joint is unaffected by the value of  $\beta$ . This is simply explained by the fact that the resistance of the EPB component, which is here the critical one, is independent of the transformation parameter value. However, in the case of compression rows, the CWC component is directly influenced by the value of  $\beta$  through the shear stress interaction coefficient  $\omega$ . As the value of  $\beta$  increases, the resistance of the CWC component is thus increasingly reduced.

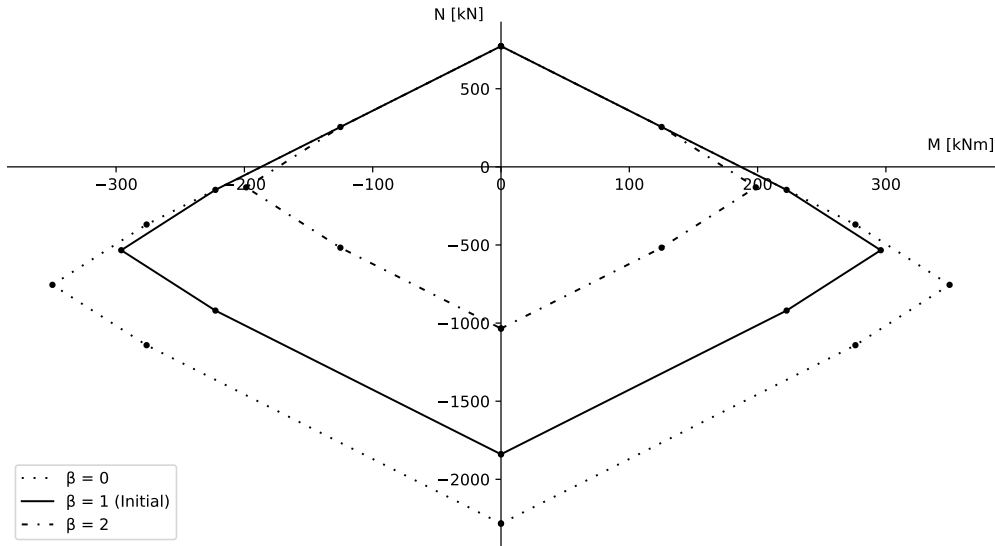


Figure 3.39: Parametric analysis - Configuration A1 - Variation of the transformation parameter  $\beta$

Even if Figure 3.36 clearly illustrates the evolution of the M-N resistance interaction curve with respect to constant values of the transformation parameter  $\beta$ , it is appropriate to point out a minor inconsistency in this approach. Indeed, although perfectly conservative, using a single approximate value of  $\beta$  for the entire curve does not actually align with most of the distributions of internal forces that can be defined. For instance, it is incorrect to use a  $\beta$  value of 1 or 2 when the joint is under pure compression, since the column web panel is not subjected to any shear in this loading condition. It would therefore be ideal to perform an iterative calculation of the transformation parameter for each of the  $2n + 2$  distributions of internal forces that may be encountered along the ductile resistance interaction curve. Further details on this iterative process can be found in the Ph.D. thesis of F. Cerfontaine [3].

### 3.4.4 Local finite element analysis

This subsection presents and discusses the results obtained from the numerical models of three FAILNOMORE joint configurations (A1, B1 & C2). As this thesis does not examine the effects of dividing the column web panel into subpanels, the analysis has been limited to local studies of FAILNOMORE joints in which the CWS component is non-critical. The data used to geometrically model these joints and to define the behaviour laws of each component of the mechanical model are not repeated here, as they are already detailed in Sections 3.3.1 & 3.4.1.

For each joint configuration, the numerical coordinates of the characteristic M-N resistance curve are provided in Tables 3.46 to 3.48. In addition to these points, the joint rotations  $\phi^{+/-}$  computed by FINELG at the end of the various loading cycles are also provided. To objectively compare these results with the analytical ones obtained using the calculation procedure shown in Figure 3.1, dimensionless Hausdorff distances have been computed once again. The methodology used to derive them is exactly the same as the one described in Section 3.4.1 for comparing the analytical and COP ductile resistance interaction curves.

### Configuration A1

The characteristic M-N resistance points of the joint configuration A1 are listed in Table 3.46. Several observations can be drawn from the comparison between these results and those presented in Table 3.16.

First, the axial force values in both tables are exactly the same. However, this result is not surprising, since the analytical value is used as a reference to define the axial force that must be fully applied to the joint at the beginning of each loading cycle.

Then, when the bending moment values are examined, it can be observed that the numerical results are generally very close to the analytical ones, although they occasionally remain slightly higher. It can also be noted that this difference tends to increase as the joint rotation becomes more significant. These slight increases can be directly attributed to the post-yielding stiffness  $K_1$  used, for reasons of numerical convergence, in the bilinear behaviour laws of the compression and tension components, as illustrated in Figures 3.15a & 3.15b. Indeed, to achieve certain plastic distributions of internal forces, as the ones corresponding to the points  $4^{+/-}$ , the compression and tension rows at the extremities of the joint must continue to deform significantly after reaching their plastic limit, in order to allow the remaining rows to yield, without any increase in their resistance. However, due to the post-yielding stiffness, these rows see their resistance very slightly increased during their deformation, which in turn leads to a higher bending moment capacity of the joint.

With regard to the joint rotation values, it can be observed that for certain characteristic M-N resistance points, the rotation is exactly zero, indicating that the joint undergoes pure horizontal translation. Logically, this only occurs when the bending resistance of the joint under the corresponding axial load is also zero. To achieve some plastic distributions of internal forces, the joint may, on the other hand, sometimes need to undergo higher levels of rotation. Although these rotation values are calculable, they remain purely indicative, since the actual rotational capacity of the joint cannot currently be evaluated according to the standard. Nevertheless, it can be stated that these results are of a reasonable order of magnitude compared to the values typically observed during experimental campaigns (see Articles [13] & [14]).

Table 3.46: Local numerical studies - Configuration A1 - Characteristic M-N resistance points

N°	$M_{Rd}^+$ [kNm]	$N_{Rd}^+$ [kN]	$\phi^+$ [mrad]	$M_{Rd}^-$ [kNm]	$N_{Rd}^-$ [kN]	$\phi^-$ [mrad]
1	0.0	-1,839.68	0.0	0.0	-1,839.68	0.0
2	222.61	-919.84	5.08	-222.61	-919.84	-5.08
3	295.99	-533.6	9.74	-295.99	-533.6	-9.74
4	223.63	-147.36	72.59	-223.63	-147.36	-72.59
5	0.0	772.48	0.0	0.0	772.48	0.0

Finally, the dimensionless Hausdorff distance between the two ductile resistance interaction curves, derived from the analytical and numerical sets of characteristic M-N resistance points, has been determined. For the FAILNOMORE configuration A1, this distance is equal to 0.00227. This very low value therefore objectively confirms the strong agreement between both sets of results.

### Configuration B1

Similar remarks to those already made regarding the results of configuration A1 can also be made about the results of joint configurations B1 & C2. For this second FAILNOMORE joint, the dimensionless Hausdorff

distance is equal to 0.00243, once again clearly highlighting the similarity between the analytical and numerical sets of characteristic M-N resistance points.

Table 3.47: Local numerical studies - Configuration B1 - Characteristic M-N resistance points

N°	$M_{Rd}^+$ [kNm]	$N_{Rd}^+$ [kN]	$\phi^+$ [mrad]	$M_{Rd}^-$ [kNm]	$N_{Rd}^-$ [kN]	$\phi^-$ [mrad]
1	0.0	-1,841.87	0.0	0.0	-1,841.87	0.0
2	245.36	-920.93	5.17	-245.34	-920.93	-4.33
3	329.38	-532.89	36.76	-328.77	-532.89	-8.44
4	374.5	-237.86	9.9	-271.33	-161.78	-36.65
5	291.09	150.18	87.18	-205.5	150.18	-70.39
6	45.73	1,071.11	-26.83	41.16	1,071.11	-37.66

### Configuration C2

For configuration C2, the calculated dimensionless Hausdorff distance is 0.00231. In light of these three results, it can be concluded that the local numerical studies conducted using the FINELG software also enable, just as the Cerfontaine model, the precise derivation of the characteristic M-N resistance points of ductile joints.

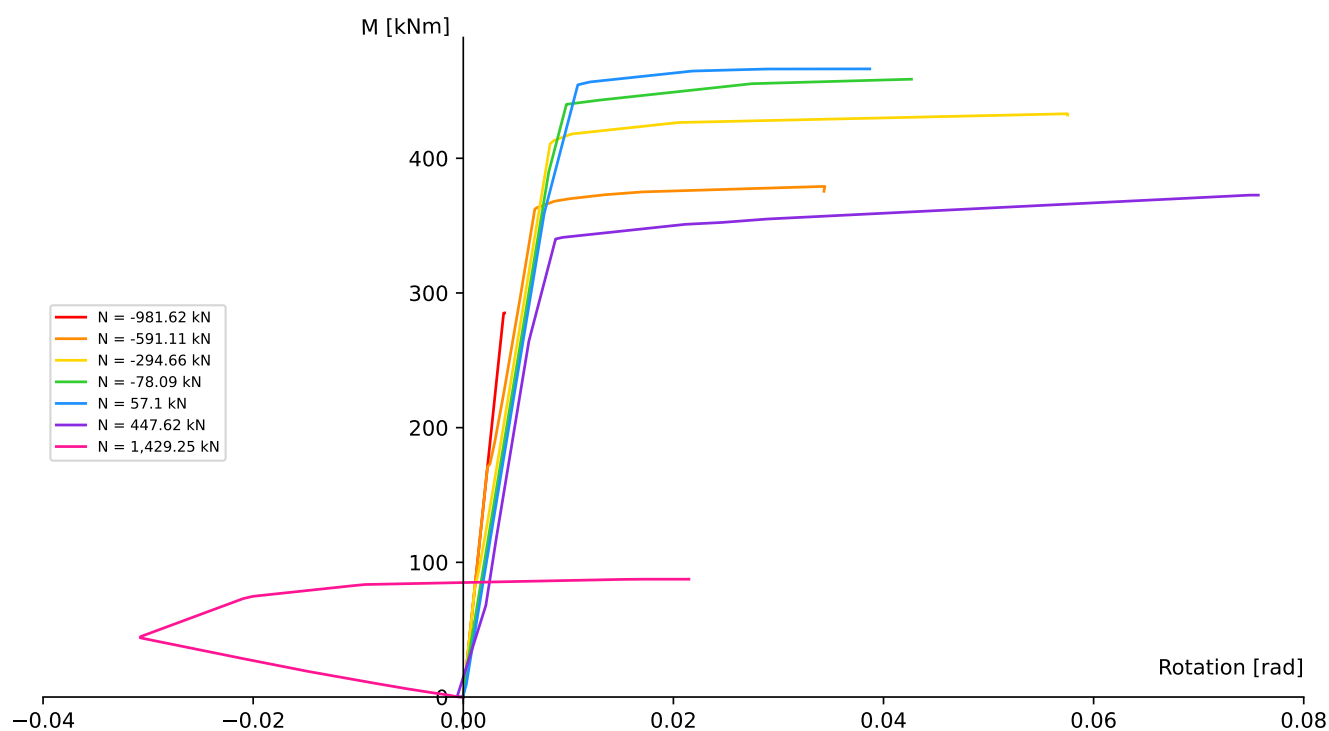
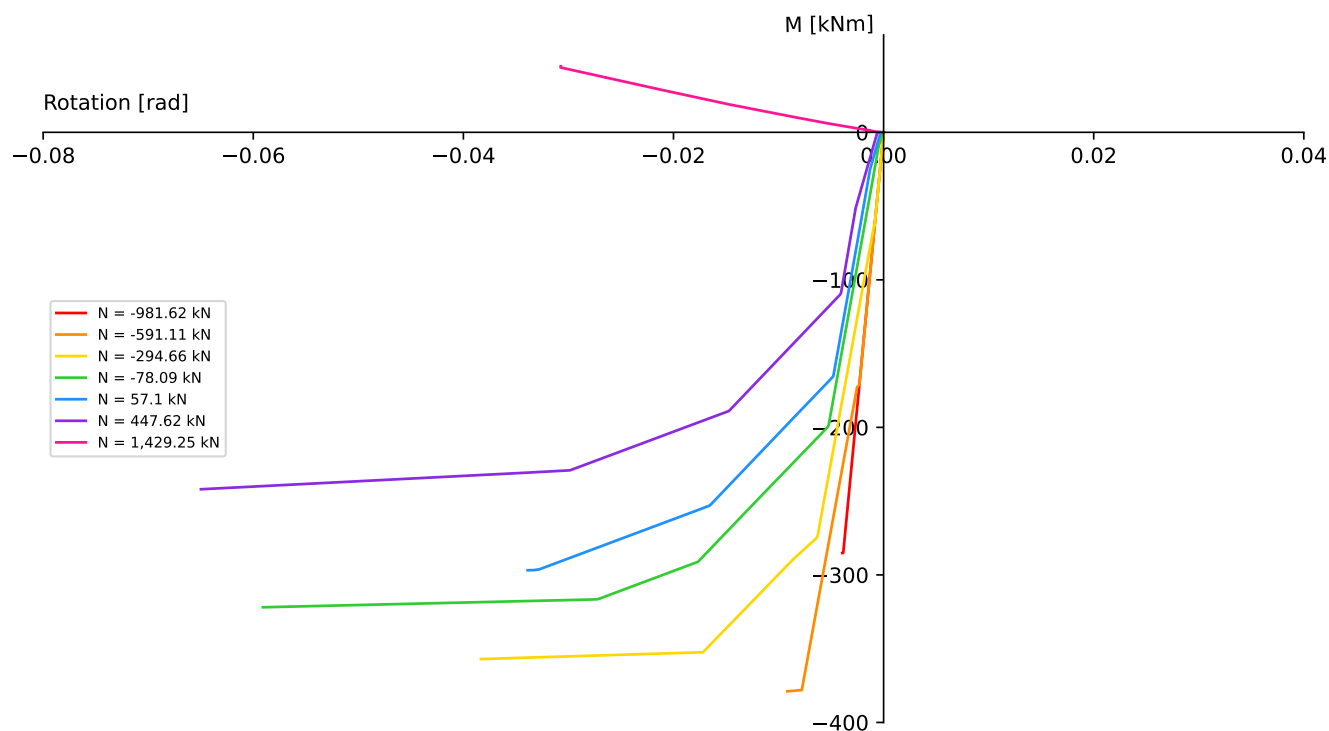
Table 3.48: Local numerical studies - Configuration C2 - Characteristic M-N resistance points

N°	$M_{Rd}^+$ [kNm]	$N_{Rd}^+$ [kN]	$\phi^+$ [mrad]	$M_{Rd}^-$ [kNm]	$N_{Rd}^-$ [kN]	$\phi^-$ [mrad]
1	0.0	-1,963.25	0.0	0.0	-1,963.25	0.0
2	285.16	-981.62	3.93	-285.16	-981.62	-3.93
3	379.13	-591.11	34.41	-378.91	-591.11	-9.17
4	433.06	-294.66	57.54	-357.04	-218.98	-38.33
5	458.72	-78.09	42.66	-321.94	77.46	-59.08
6	466.37	57.1	38.69	-296.83	215.07	-33.88
7	372.65	447.62	75.67	-241.94	447.62	-64.98
8	87.48	1,429.25	17.28	44.8	1,429.25	-30.73

Additionally, for this configuration only, the  $M - \phi$  curves computed by FINELG for the various characteristic M-N resistance points are presented in Figures 3.40 & 3.41. These two graphs aim to illustrate both the variation in joint rotational stiffness throughout a single loading cycle and the effect of axial force magnitude on this mechanical property.

First, it can be clearly observed that the rotational stiffness of the joint remains relatively high as long as at least one compression row is active (N° 2 to 7). Moreover, this stiffness tends to increase slightly as the compressive force applied to the joint increases. On the other hand, when only tension rows are active, as it is the case for point N°8 in both graphs, the value of the stiffness drops significantly. Finally, it should be noted that stiffness reductions along a single curve may result from the progressive yielding of individual rows, their deactivation, or the formation of group mechanisms. Stiffness gains, as for them, are attributed to the activation of rows.

In light of these results, it can thus be concluded that the presence of an axial force in the connected beam influences the rotational stiffness of the joint. Consequently, the ability to account for these variations using ASSEMBLA elements during numerical structural analyses, particularly in robustness studies, represents a significant advancement over traditional joint modelling with rotational springs of constant properties.

Figure 3.40: Local numerical studies - Configuration C2 -  $M - \phi$  curves - Hogging bending momentFigure 3.41: Local numerical studies - Configuration C2 -  $M - \phi$  curves - Sagging bending moment

# Chapter 4

## M-N design recommendations

### 4.1 Objectives

In this chapter, a critical analysis of the current M-N interaction criteria recommended in the European standards (EN 1993-1-8:2005 [7] & EN 1993-1-8:2024 [11]) will be carried out. Building on the identified weaknesses, three new M-N interaction criteria will be proposed to address these issues, and the general equations used to derive them will be thoroughly presented, particularly with a view to their potential integration into a future version of the standard. Furthermore, these criteria will be applied to the six FAILNOMORE joint configurations to demonstrate their practical benefits and highlight their applicability. They will also be applied to a counter-example to clearly demonstrate the boundaries of their applicability.

### 4.2 Interaction criteria according to standards

The M–N interaction criteria included in both versions of the standard follow the same methodological approach, but differ in the values they employ. Indeed, the core assumption consists in considering that the joint can sustain its resistances under pure bending, and thus not being subjected to M-N interaction, until reaching defined axial force values. Beyond these thresholds, a horizontal line must then be followed to reconnect with the linear interaction criteria which can be drawn between the pure bending resistances of the joint and the pure axial resistances of this one. A representation of these two M-N interaction criteria is shown in Figure 4.1 for the joint configuration A1.

The main difference between the current version of the standard (EN 1993-1-8:2005 [7]) and the next version to be published (EN 1993-1-8:2024 [11]) therefore lies in the definition of the threshold values. In EN 1993-1-8:2005, these values are set at 5% of the design plastic resistance of the beam cross-section, symmetrically on both sides of the horizontal axis, where, on the other hand, in EN 1993-1-8:2024, they are fixed to 5% of the axial design plastic resistances of the joint, assuming no applied moment. Consequently, this second criterion will logically exhibit shorter "non-interaction" ranges, as the beam is significantly stronger in axial direction than the joint.

At this stage, some remarks can already be made regarding these M–N interaction criteria. In fact, although both approaches require the calculation of the pure axial resistances of the joint in order to plot the criteria, none of the standards currently provides a procedure to do so. However, the computation of these resistances is not direct, even when the Cerfontaine model is applied. This is only true when the joint is symmetrical and there is no group effect on the resistances of individual rows, or in other words, when the  $F_{Rd}^+$  &  $F_{Rd}^-$  vectors are identical. In this thesis, only the joint configurations A1 & A2 are in this situation, which underlines well the non-generality of these conditions.

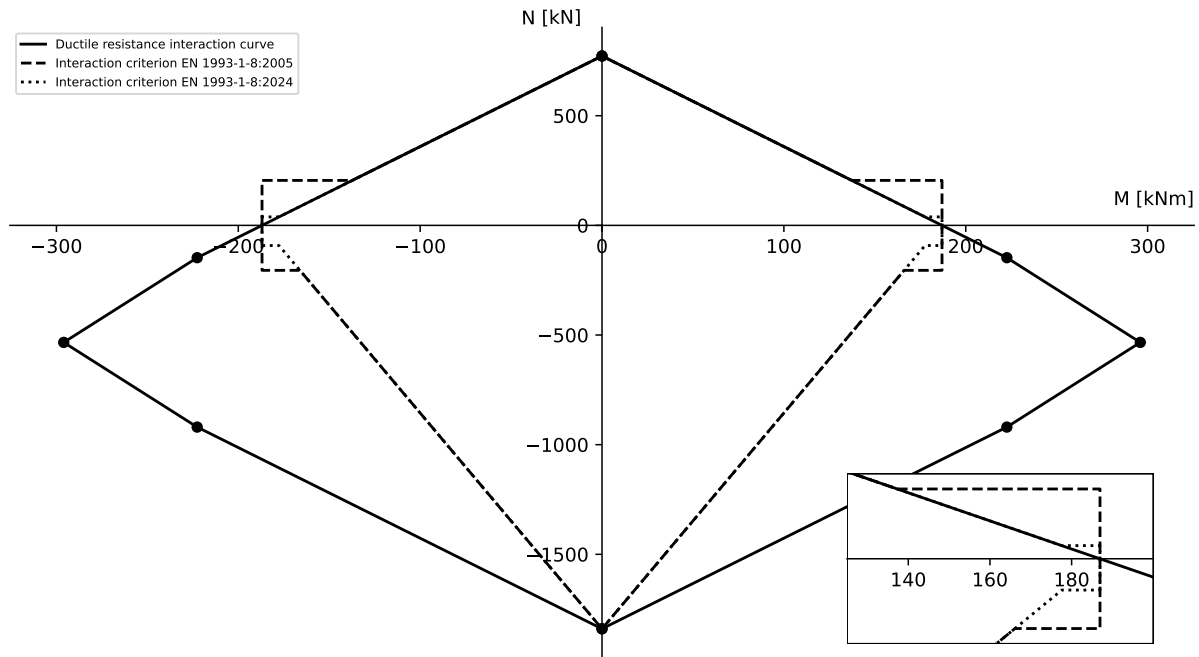


Figure 4.1: FAILNOMORE - Joint configuration A1 - M-N interaction criteria according to standards

Therefore, this Master thesis adopts modified threshold values for the criterion of EN 1993-1-8:2024, setting them at 5% of the maximum tension or compression forces the joint can sustain, as these results can be easily obtained using the Cerfontaine model. The pure axial resistances of the joint, as for them, were geometrically determined from the intersection of the ductile resistance interaction curves with the vertical axes of the graphs.

For the criterion from EN 1993-1-8:2005, the design plastic resistance of the beam cross-section, used to determine the threshold values, can be easily calculated using Equation (3.34). However, it should be emphasised that in reality there is no solid scientific basis to support the use of this value. It seems indeed inappropriate, in any case, to define the M-N "non-interaction" range of the joint based on the axial plastic resistance of the connected beam.

$$N_{b,pl,Rd} = \frac{A_b f_{yb}}{\gamma_{M0}} \quad (4.1)$$

with :

- $A_b$  The cross-section area of the beam [mm<sup>2</sup>]
- $f_{yb}$  The design yield strength of the beam [MPa]
- $N_{b,pl,Rd}$  The axial design plastic resistance of the beam [N]

The threshold values of both criteria are presented in Table 4.1 for the joint configuration A1.

Table 4.1: FAILNOMORE - Joint configuration A1 - Threshold values

Resistance value	$N$ [kN]	5% $N$ [kN]
$ N_{b,pl,Rd} $	4,100.96	205.04
$N_{t,j,pl,Rd}$	772.48	38.62
$N_{c,j,pl,Rd}$	-1,839.68	-91.98

where :

- $N_{t,j,pl,Rd} = N_{n+1,Rd}^{+/-}$  The tension design plastic resistance of the joint [N]
- $N_{c,j,pl,Rd} = N_{1,Rd}^{+/-}$  The compression design plastic resistance of the joint [N]

Nevertheless, the most important observation regarding these two M-N interaction criteria remains the insecure regions, which are clearly visible in Figure 4.1. It can indeed be noted that, in certain regions of the graph, the standard criteria predict higher joint resistances than those indicated by the ductile resistance interaction curve. However, the size of these insecure areas depends on the criterion considered, since these regions consistently appear within the "non-interaction" ranges defined by the standards.

Although, in most FAILNOMORE joint configurations, such as the one shown in Figure 4.1, the insecure regions appear only on one side of the horizontal axis, they can also be observed on both sides depending on the shape of the ductile resistance interaction curve, as illustrated in Figure 4.8 for configuration C2.

Finally, it should also be emphasised that, in certain other regions of the graphs, the standard criteria can sometimes be overly conservative when compared to the ductile resistance interaction curves. Even if this is a strong advantage in terms of safety, these large unexploited areas prevent the full exploitation of the joint resistance capacity. Revising these criteria could therefore lead to more effective optimisation of the joint during the design phase, from both structural and economic perspectives.

### 4.3 Proposed new interaction criteria

As part of this thesis, three new M-N interaction criteria have been developed with a view to a potential future inclusion in the European standard. The establishment of these new criteria was dictated by two main guidelines. First, offer a simplified alternative to the derivation of the complete ductile resistance interaction curve of the joint. The idea was indeed to shorten the calculation procedure of the Cerfontaine model so that, even when the joint configuration to design becomes highly complex, the computations could still be carried out quickly, and potentially even by hand. Second, address the various issues identified in the current M-N interaction criteria proposed in the standards.

However, although these new interaction criteria offer valuable alternatives to the Cerfontaine model presented in Section 3.2.2, they will never fully replace the calculation of the complete ductile resistance interaction curve, which remains the most accurate method for designing ductile joints subjected to M-N loading. Their usage is of course also limited to joints that meet the two ductility criteria enounced in Section 3.2.2, which are required for deriving ductile resistance interaction curves.

For the sake of consistency, the three new interaction criteria will be introduced progressively, starting with the one requiring the fewest calculations and ending with the most complex. For each of them, the general equations used to determine the coordinates of their defining points will be presented. Once again, the joint configuration A1 will be used as an example. Similar results for the other five FAILNOMORE joint configurations are indeed also presented on the following pages.

#### 4.3.1 Six-point criterion

First, to derive this new M-N interaction criterion, as well as the next two, it will always be necessary to dispose of the lever arms and the  $F_{i,Rd}^{+}$  &  $F_{i,Rd}^{-}$  values for each row of the joint. This corresponds to

calculation steps 2. through 6. in the methodology tree shown in Figure 3.1.

Once all the required data have been obtained, the six characteristic points of the new criterion, noted  $A^{+/-}$ ,  $B^{+/-}$  &  $C^{+/-}$  in this thesis, can be determined. These six points correspond to the six "extremity" points of the full ductile resistance interaction curve of the joint. The formulas required to compute their coordinates are presented in Equations (3.35) to (3.40).

The six characteristic points must then be connected in pairs with straight lines to form the outline of the M-N interaction criterion, as illustrated in Figure 4.2 for joint configuration A1. For the configurations A1 & A2, this criterion however comes down to four points, as the points  $A^{+/-}$  and the points  $C^{+/-}$  are confused on the graph, due to the same reasons as previously discussed.

#### Points $A^{+/-}$

$$A^+ \rightarrow active = F_{Rd}^+ < 0 : M_{A^+} = \sum F_{Rd}^+ h \text{ active} ; N_{A^+} = \sum F_{Rd}^+ \text{ active} \quad (4.2)$$

$$A^- \rightarrow active = F_{Rd}^- < 0 : M_{A^-} = \sum F_{Rd}^- h \text{ active} ; N_{A^-} = \sum F_{Rd}^- \text{ active} \quad (4.3)$$

#### Points $B^{+/-}$

$$B^+ \rightarrow active = F_{Rd}^+ h > 0 : M_{B^+} = \sum F_{Rd}^+ h \text{ active} ; N_{B^+} = \sum F_{Rd}^+ \text{ active} \quad (4.4)$$

$$B^- \rightarrow active = F_{Rd}^- h < 0 : M_{B^-} = \sum F_{Rd}^- h \text{ active} ; N_{B^-} = \sum F_{Rd}^- \text{ active} \quad (4.5)$$

#### Points $C^{+/-}$

$$C^+ \rightarrow active = F_{Rd}^+ > 0 : M_{C^+} = \sum F_{Rd}^+ h \text{ active} ; N_{C^+} = \sum F_{Rd}^+ \text{ active} \quad (4.6)$$

$$C^- \rightarrow active = F_{Rd}^- > 0 : M_{C^-} = \sum F_{Rd}^- h \text{ active} ; N_{C^-} = \sum F_{Rd}^- \text{ active} \quad (4.7)$$

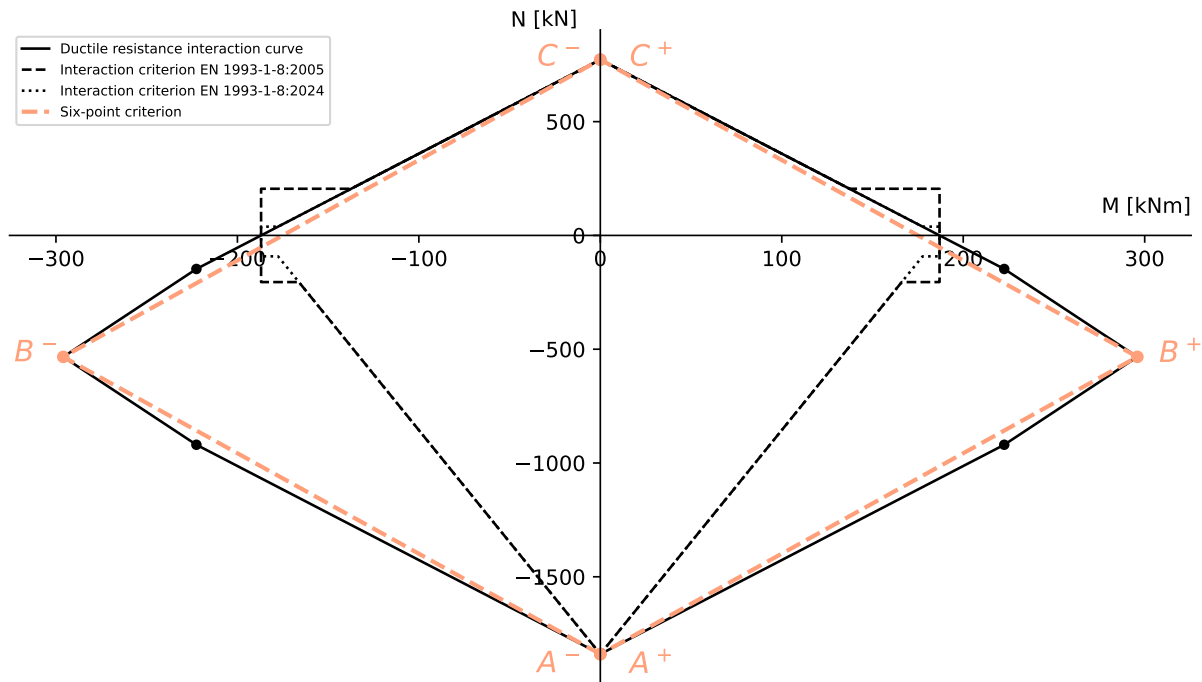


Figure 4.2: FAILNOMORE - Joint configuration A1 - Six-point criterion



The simplicity of deriving this criterion is likely its greatest advantage, as it requires only six easily computable points to be plotted. As visible on Figure 4.2, this new M-N interaction criterion is completely inscribed in the ductile resistance interaction curve, thereby ensuring the safe design of the joint. It also enables the capture of a significantly larger portion of the area compared to the two existing criteria, improving the use of the full resistance capacity of the joint. However, this criterion does not include "non-interaction" ranges, which could potentially be a drawback for some engineers.

### 4.3.2 Eight-point criterion without "non-interaction" thresholds

To enhance the portion of the ductile resistance interaction curve captured by the criterion, while recreating a connection with the current standard criteria, this second new M-N interaction criterion proposes adding the two pure bending resistances of the joint to the six characteristic points already defined for the previous criterion. These two additional points will be denoted as  $D^{+/-}$  in the framework of this thesis. Their coordinates can be simply derived based on the assembly procedure described in Section 6.2.7.2 of EN 1993-1-8:2005 [7].

The application of this second criterion to the joint configuration A1 is available in Figure 4.3 just hereunder. On this same figure, it can be observed that the addition of these two points indeed slightly increase the area covered by the criterion. However, this increase can sometimes be much more significant, as illustrated in Figures 4.6, 4.8 & 4.9 for configurations B1, C2 & C3, respectively.

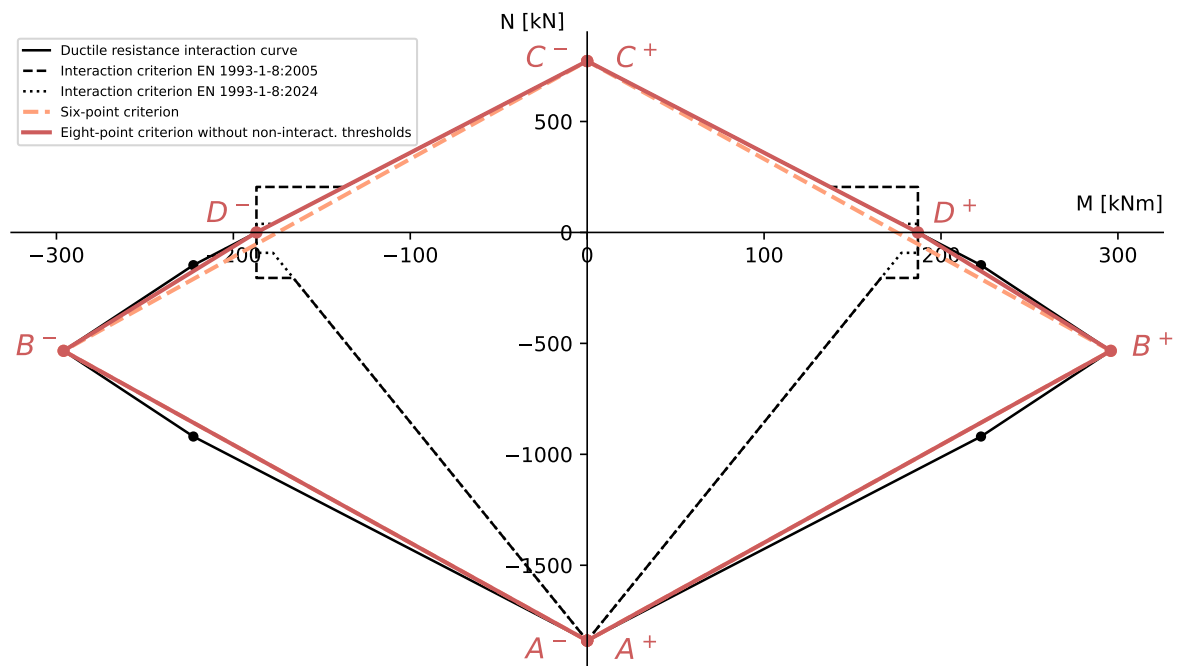


Figure 4.3: FAILNOMORE - Joint configuration A1 - Eight-point criterion without non-interact. thresholds

To objectively assess the difference between this new criterion and the standard ones, the horizontal distances between the extremity points of the "non-interaction" ranges of the latter and the corresponding points of the new interaction criterion with identical axial resistance values are calculated. For most FAILNOMORE joint configurations, these distances also directly correspond to the gap over which the standard criteria are either unsafe or conservative. These results are presented in Table 4.2 for the configuration A1, and on the following pages for the other FAILNOMORE joints.

In all these tables, the coordinates ( $M_{D+/-}$  ;  $N$ ) correspond to the extremity points of the "non-interaction" ranges, while the ( $M_{\cap}$  ;  $N$ ) coordinates, as for them, are the ones of the points located on this second proposed criterion. The  $\%M_{D+/-}$  values are calculated by dividing the horizontal distance value  $\Delta M$  with the associated  $M_{D+/-}$  pure bending resistance.

Based on these  $\%M_{D+/-}$  values, it can thus be confirmed that both standard criteria are, to varying degrees, either unsafe or conservative in certain regions of the graph, depending on the joint configuration and the criterion considered. This insecure range generally hovers around 20% for the EN 1993-1-8:2005 interaction criterion, which is significant and clearly highlights the need to revise this criterion. On the other hand, despite the fact that the EN 1993-1-8:2024 criterion exhibits smaller insecure ranges (up to 10%), it still does not ensure safety across all joint configurations.

Table 4.2: FAILNOMORE - Joint configuration A1 - Horizontal gap - "Non-interaction" thresholds

Standard	N [kN]	Hogging bending moment [kNm]				Sagging bending moment [kNm]			
		$M_{D+}$	$M_{\cap}$	$\Delta M$	$\%M_{D+}$ [-]	$M_{D-}$	$M_{\cap}$	$\Delta M$	$\%M_{D-}$ [-]
EN 1993-1-8:2005	205.04	186.95	137.32	-49.63	<b>-26.55</b>	-186.95	-137.32	49.63	<b>-26.55</b>
	-205.04	186.95	228.84	41.89	22.41	-186.95	-228.84	-41.89	22.41
EN 1993-1-8:2024	38.62	186.95	177.6	-9.35	<b>-5.0</b>	-186.95	-177.6	9.35	<b>-5.0</b>
	-91.98	186.95	205.74	18.79	10.05	-186.95	-205.74	-18.79	10.05

A similar analysis has also been carried out to quantify the gap between the pure bending resistances of the joint  $M_{D+/-}$  and its maximum bending resistances  $M_{B+/-}$  as predicted by the ductile resistance interaction curve. The results are provided in Table 4.3 for configuration A1.

Table 4.3: FAILNOMORE - Joint configuration A1 - Horizontal gap - Maximum bending moment

Hogging bending moment [kNm]				Sagging bending moment [kNm]			
$M_{D+}$	$M_{B+}$	$ \Delta M $	$ \%M_{D+} $ [-]	$M_{D-}$	$M_{B-}$	$ \Delta M $	$ \%M_{D-} $ [-]
186.95	295.98	109.03	58.32	-186.95	-295.98	109.03	58.32

### 4.3.3 Eight-point criterion with "non-interaction" thresholds

The purpose of this last M-N interaction criterion is to meet the request from some engineers to incorporate "non-interaction" ranges, as it is currently the case with the criteria defined in the standards. This thesis therefore proposes to incorporate these "non-interaction" ranges into the eight-point criterion by simply extending a vertical line from the pure bending resistances of the joint, until it intersects the criterion curve again. As a result, they will no longer appear on both sides of the horizontal axis, but only on the sides corresponding to the locations of the  $B^{+/-}$  points. Their size is also no longer constant, as it strongly depends on the shape of the eight-point criterion, as visible in Figures 4.4 to 4.9.

The coordinates of the intersection points, whose N-values may serve as new thresholds, can be directly determined from the coordinates of the other characteristic points, using the Thales theorem. They are noted  $E^{+/-}$  in Figure 4.4. The general formulas to use are presented in Equations (3.41) & (3.42).

Note that if the points  $B^{+/-}$  came to be located on the horizontal axis of the graph, it would then be impossible to create a "non-interaction" range without compromising the safety of the design.

**Points  $E^{+/-}$**

$$E^+ \rightarrow \begin{cases} \text{if } (N_{B^+} > 0) : M_{E^+} = M_{D^+} ; N_{E^+} = N_{C^+} - \frac{(N_{C^+} - N_{B^+})(M_{D^+} - M_{C^+})}{(M_{B^+} - M_{C^+})} \\ \text{if } (N_{B^+} < 0) : M_{E^+} = M_{D^+} ; N_{E^+} = N_{A^+} - \frac{(N_{A^+} - N_{B^+})(M_{D^+} - M_{A^+})}{(M_{B^+} - M_{A^+})} \end{cases} \quad (4.8)$$

$$E^- \rightarrow \begin{cases} \text{if } (N_{B^-} > 0) : M_{E^-} = M_{D^-} ; N_{E^-} = N_{C^-} - \frac{(N_{C^-} - N_{B^-})(M_{D^-} - M_{C^-})}{(M_{B^-} - M_{C^-})} \\ \text{if } (N_{B^-} < 0) : M_{E^-} = M_{D^-} ; N_{E^-} = N_{A^-} - \frac{(N_{A^-} - N_{B^-})(M_{D^-} - M_{A^-})}{(M_{B^-} - M_{A^-})} \end{cases} \quad (4.9)$$

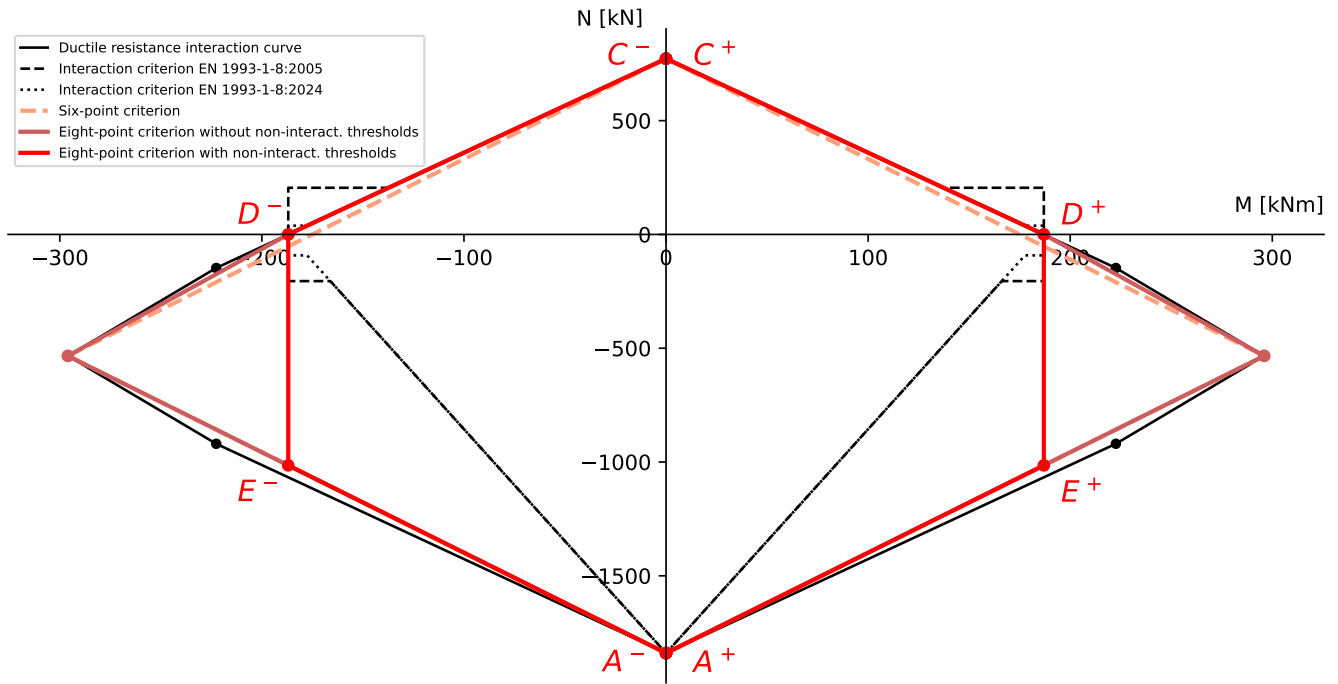


Figure 4.4: FAILNOMORE - Joint configuration A1 - Eight-point criterion with non-interact. thresholds

Although these "non-interaction" ranges exclude the use of the triangular areas defined by the points  $(D^+B^+E^+)$  &  $(D^-B^-E^-)$ , this does not appear to be an issue, as these regions in the M-N interaction criteria and the ductile resistance interaction curve are always difficult to exploit. It is indeed primordial to ensure that, in these regions, both the axial force  $N_{Ed}$  and the bending moment  $M_{Ed}$  applied to the joint are generated by the same load. Otherwise, if  $N_{Ed}$  decreases or increases rapidly while  $M_{Ed}$  remains constant, the resulting point may fall outside the interaction criterion or the ductile resistance interaction curve, which would indicate joint failure.

## 4.4 Application examples

### Configuration A2

Table 4.4: FAILNOMORE - Joint configuration A2 - Threshold values

Resistance value	$N$ [kN]	$5\% N$ [kN]
$ N_{b,pl,Rd} $	4,100.96	205.04
$N_{t,j,pl,Rd}$	772.42	38.62
$N_{c,j,pl,Rd}$	-1,957.41	-97.87

Table 4.5: FAILNOMORE - Joint configuration A2 - Horizontal gap - "Non-interaction" thresholds

Standard	$N$ [kN]	Hogging bending moment [kNm]				Sagging bending moment [kNm]			
		$M_{D+}$	$M_{\cap}$	$\Delta M$	$\% M_{D+}$ [-]	$M_{D-}$	$M_{\cap}$	$\Delta M$	$\% M_{D-}$ [-]
EN 1993-1-8:2005	205.04	186.95	137.32	-49.63	<b>-26.55</b>	-186.95	-137.32	49.63	<b>-26.55</b>
	-205.04	186.95	229.61	42.66	22.82	-186.95	-229.61	-42.66	22.82
EN 1993-1-8:2024	38.62	186.95	177.6	-9.35	<b>-5.0</b>	-186.95	-177.6	9.35	<b>-5.0</b>
	-97.87	186.95	207.31	20.36	10.89	-186.95	-207.31	-20.36	10.89

Table 4.6: FAILNOMORE - Joint configuration A2 - Horizontal gap - Maximum bending moment

Hogging bending moment [kNm]				Sagging bending moment [kNm]			
$M_{D+}$	$M_{B+}$	$ \Delta M $	$ \% M_{D+} $ [-]	$M_{D-}$	$M_{B-}$	$ \Delta M $	$ \% M_{D-} $ [-]
186.95	310.22	123.28	65.94	-186.95	-310.22	123.28	65.94

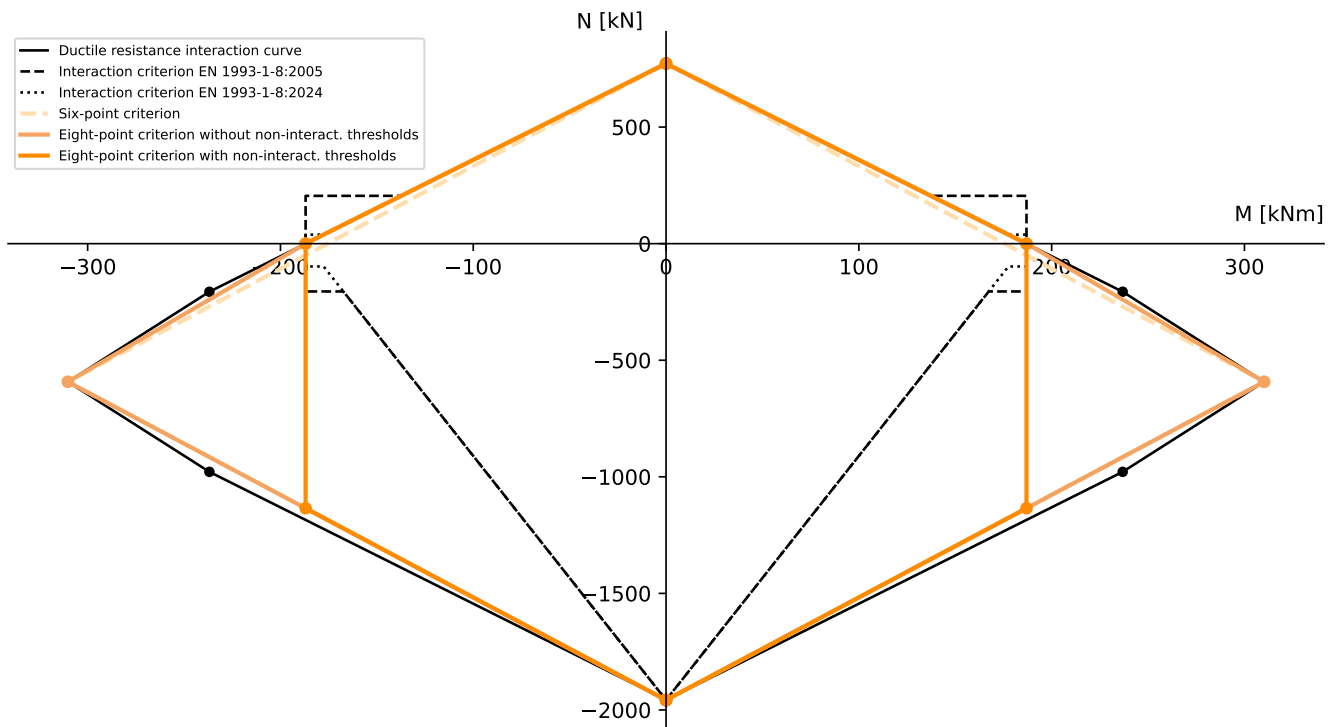


Figure 4.5: FAILNOMORE - Joint configuration A2 - New M-N interaction criteria

**Configuration B1**

Table 4.7: FAILNOMORE - Joint configuration B1 - Threshold values

Resistance value	$N$ [kN]	$5\% N$ [kN]
$ N_{b,pl,Rd} $	4,771.91	238.59
$N_{t,j,pl,Rd}$	1,071.11	53.55
$N_{c,j,pl,Rd}$	-1,841.87	-92.03

Table 4.8: FAILNOMORE - Joint configuration B1 - Horizontal gap - "Non-interaction" thresholds

Standard	N [kN]	Hogging bending moment [kNm]				Sagging bending moment [kNm]			
		$M_{D+}$	$M_{\cap}$	$\Delta M$	$\%M_{D+}$ [-]	$M_{D-}$	$M_{\cap}$	$\Delta M$	$\%M_{D-}$ [-]
EN 1993-1-8:2005	238.59	323.36	261.52	-61.84	<b>-19.13</b>	-236.47	-174.62	61.84	<b>-26.15</b>
	-238.59	323.36	374.32	50.96	15.76	-236.47	-277.79	-41.32	17.48
EN 1993-1-8:2024	53.55	323.36	309.48	-13.88	<b>-4.29</b>	-236.47	-222.59	13.88	<b>-5.87</b>
	-92.03	323.36	343.16	19.8	6.12	-236.47	-252.42	-15.95	6.75

Table 4.9: FAILNOMORE - Joint configuration B1 - Horizontal gap - Maximum bending moment

Hogging bending moment [kNm]				Sagging bending moment [kNm]			
$M_{D+}$	$M_{B+}$	$ \Delta M $	$ \%M_{D+} $ [-]	$M_{D-}$	$M_{B-}$	$ \Delta M $	$ \%M_{D-} $ [-]
323.36	374.49	51.14	15.81	-236.47	-271.24	92.3	39.03

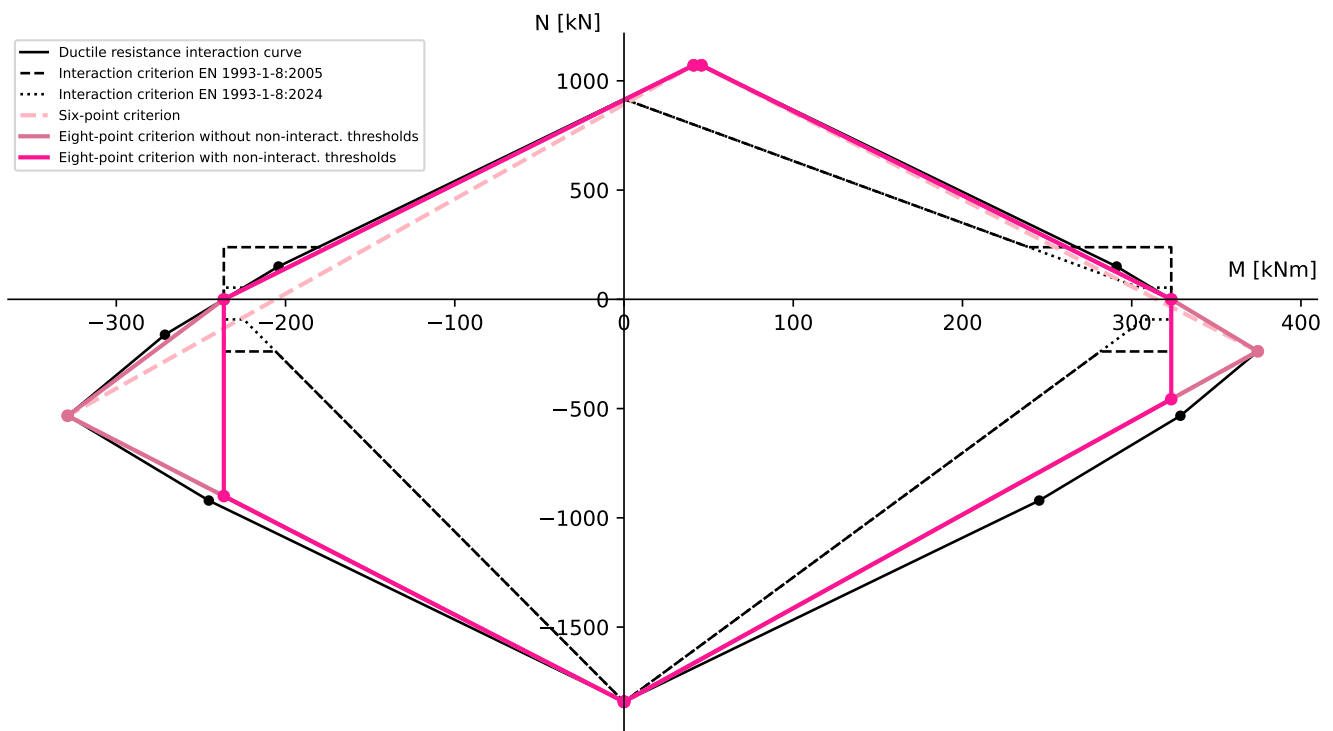


Figure 4.6: FAILNOMORE - Joint configuration B1 - New M-N interaction criteria

**Configuration B3**

Table 4.10: FAILNOMORE - Joint configuration B3 - Threshold values

Resistance value	$N$ [kN]	$5\% N$ [kN]
$ N_{b,pl,Rd} $	4,771.91	238.59
$N_{t,j,pl,Rd}$	1,004.3	50.21
$N_{c,j,pl,Rd}$	-3,339.89	-166.99

Table 4.11: FAILNOMORE - Joint configuration B3 - Horizontal gap - "Non-interaction" thresholds

Standard	N [kN]	Hogging bending moment [kNm]				Sagging bending moment [kNm]			
		$M_{D+}$	$M_{\cap}$	$\Delta M$	$\%M_{D+}$ [-]	$M_{D-}$	$M_{\cap}$	$\Delta M$	$\%M_{D-}$ [-]
EN 1993-1-8:2005	238.59	308.94	245.42	-63.52	<b>-20.56</b>	-230.75	-167.23	63.52	<b>-27.53</b>
	-238.59	308.94	368.17	59.23	19.17	-230.75	-284.5	-53.75	23.29
EN 1993-1-8:2024	50.21	308.94	295.57	-13.37	<b>-4.33</b>	-230.75	-217.38	13.37	<b>-5.79</b>
	-166.99	308.94	350.39	41.46	13.42	-230.75	-268.37	-37.62	16.3

Table 4.12: FAILNOMORE - Joint configuration B3 - Horizontal gap - Maximum bending moment

Hogging bending moment [kNm]				Sagging bending moment [kNm]			
$M_{D+}$	$M_{B+}$	$ \Delta M $	$ \%M_{D+} $ [-]	$M_{D-}$	$M_{B-}$	$ \Delta M $	$ \%M_{D-} $ [-]
308.94	565.57	256.63	83.07	-230.75	-524.01	293.27	127.09

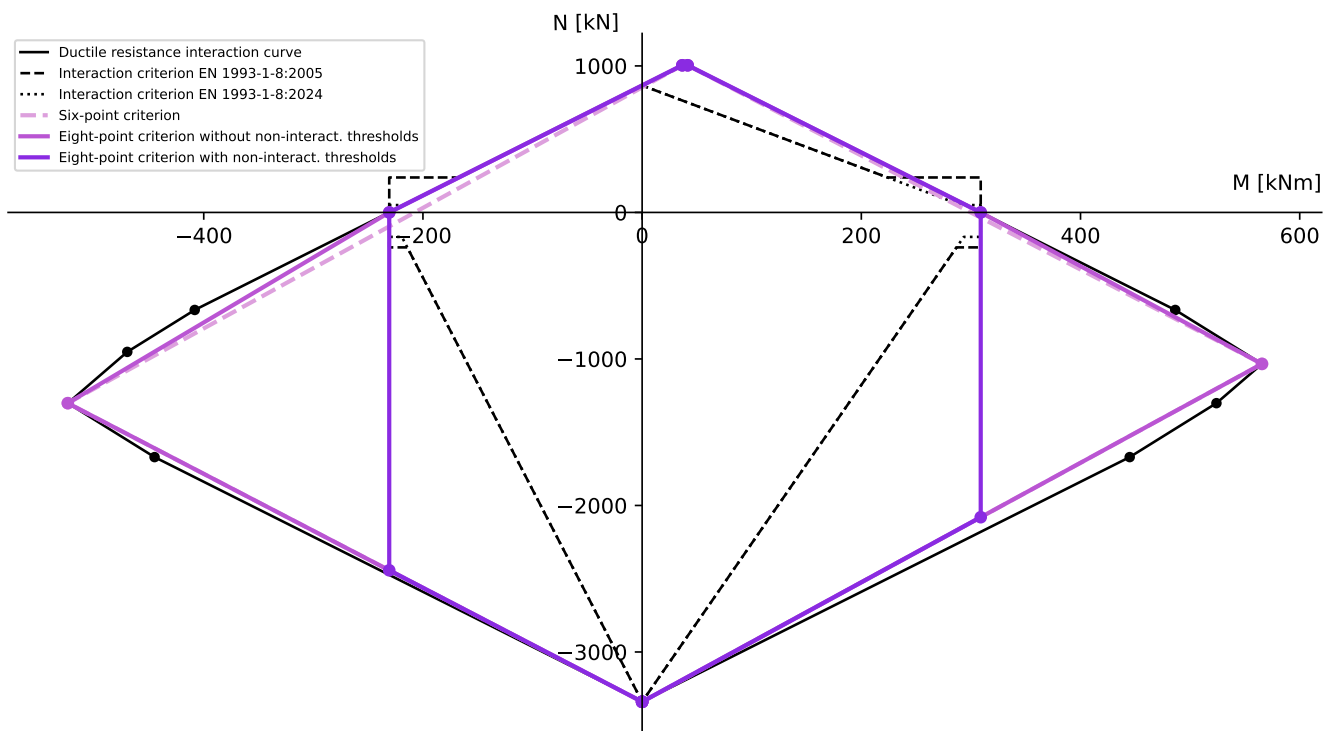


Figure 4.7: FAILNOMORE - Joint configuration B3 - New M-N interaction criteria

## Configuration C2

Table 4.13: FAILNOMORE - Joint configuration C2 - Threshold values

Resistance value	$N$ [kN]	$5\% N$ [kN]
$ N_{b,pl,Rd} $	5,538	276.9
$N_{t,j,pl,Rd}$	1,429.25	71.46
$N_{c,j,pl,Rd}$	-1,963.25	-98.16

Table 4.14: FAILNOMORE - Joint configuration C2 - Horizontal gap - "Non-interaction" thresholds

Standard	N [kN]	Hogging bending moment [kNm]				Sagging bending moment [kNm]			
		$M_{D+}$	$M_{\cap}$	$\Delta M$	$\%M_{D+}$ [-]	$M_{D-}$	$M_{\cap}$	$\Delta M$	$\%M_{D-}$ [-]
EN 1993-1-8:2005	276.9	462.89	405.66	-57.23	<b>-12.36</b>	-330.26	-257.6	72.65	<b>-22.0</b>
	-276.9	462.89	397.6	-65.29	<b>-14.1</b>	-330.26	-353.04	-22.78	6.9
EN 1993-1-8:2024	71.46	462.89	462.38	-0.51	<b>-0.11</b>	-330.26	-311.51	18.75	<b>-5.68</b>
	-98.16	462.89	439.75	-23.15	<b>-5.0</b>	-330.26	-338.34	-8.08	2.45

Table 4.15: FAILNOMORE - Joint configuration C2 - Horizontal gap - Maximum bending moment

Hogging bending moment [kNm]				Sagging bending moment [kNm]			
$M_{D+}$	$M_{B+}$	$ \Delta M $	$ \%M_{D+} $ [-]	$M_{D-}$	$M_{B-}$	$ \Delta M $	$ \%M_{D-} $ [-]
462.89	466.34	3.46	0.75	-330.26	-378.88	48.63	14.72

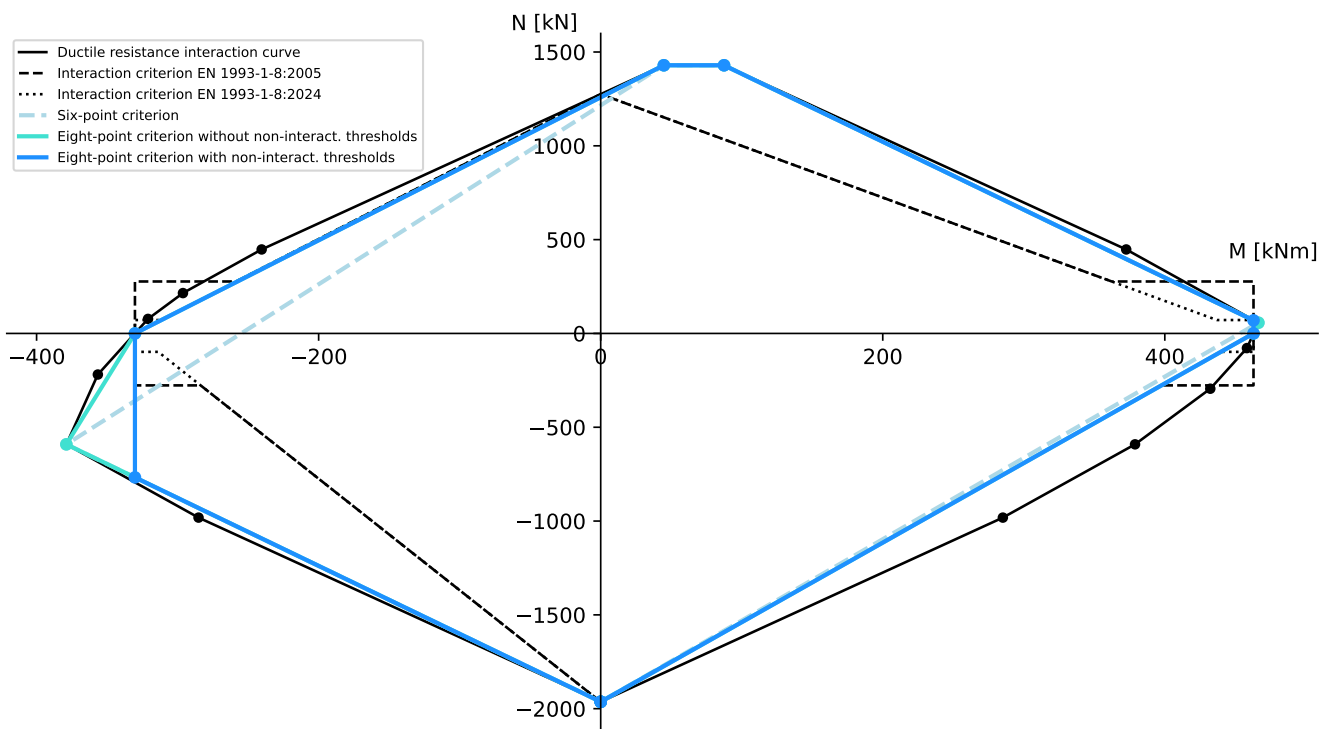


Figure 4.8: FAILNOMORE - Joint configuration C2 - New M-N interaction criteria

## Configuration C3

Table 4.16: FAILNOMORE - Joint configuration C3 - Threshold values

Resistance value	$N$ [kN]	$5\% N$ [kN]
$ N_{b,pl,Rd} $	5,538	276.9
$N_{t,j,pl,Rd}$	1,329.3	66.46
$N_{c,j,pl,Rd}$	-3,339.89	-166.99

Table 4.17: FAILNOMORE - Joint configuration C3 - Horizontal gap - "Non-interaction" thresholds

Standard	N [kN]	Hogging bending moment [kNm]				Sagging bending moment [kNm]			
		$M_{D+}$	$M_{\cap}$	$\Delta M$	$\%M_{D+}$ [-]	$M_{D-}$	$M_{\cap}$	$\Delta M$	$\%M_{D-}$ [-]
EN 1993-1-8:2005	276.9	465.14	384.82	-80.32	<b>-17.27</b>	-347.78	-267.38	80.4	<b>-23.12</b>
	-276.9	465.14	538.51	73.37	15.77	-347.78	-395.99	-48.21	13.86
EN 1993-1-8:2024	66.46	465.14	445.86	-19.28	<b>-4.15</b>	-347.78	-328.48	19.3	<b>-5.55</b>
	-166.99	465.14	509.39	44.25	9.51	-347.78	-376.86	-29.08	8.36

Table 4.18: FAILNOMORE - Joint configuration C3 - Horizontal gap - Maximum bending moment

Hogging bending moment [kNm]				Sagging bending moment [kNm]			
$M_{D+}$	$M_{B+}$	$ \Delta M $	$ \%M_{D+} $ [-]	$M_{D-}$	$M_{B-}$	$ \Delta M $	$ \%M_{D-} $ [-]
465.14	653.57	188.43	40.51	-347.78	-574.03	226.25	65.05

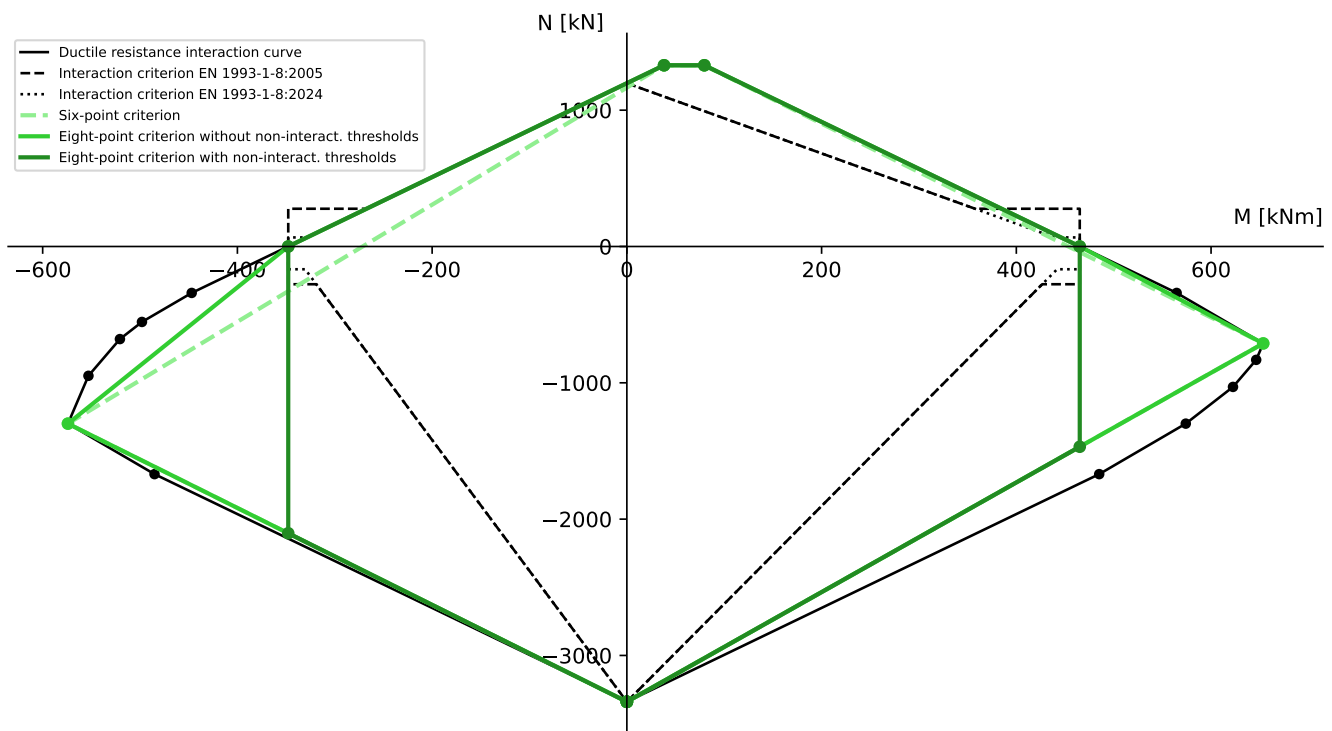


Figure 4.9: FAILNOMORE - Joint configuration C3 - New M-N interaction criteria



### Cerfontaine thesis example

For this final application example, the new M-N interaction criteria were applied to the example from the Cerfontaine thesis, which involves a non-ductile joint configuration (see Sections 3.3.3 & 3.4.3). The primary purpose of this counter-example is to demonstrate that the interaction criteria introduced in this chapter are only applicable to ductile joint configurations. Indeed, as illustrated in Figure 4.10, it is immediately clear that none of the criteria consistently falls within the non-ductile resistance interaction curve, particularly near the inflection points. Therefore, the safety and reliability of these three interaction criteria cannot be guaranteed and it should be concluded that their use should be avoided for this category of joints.

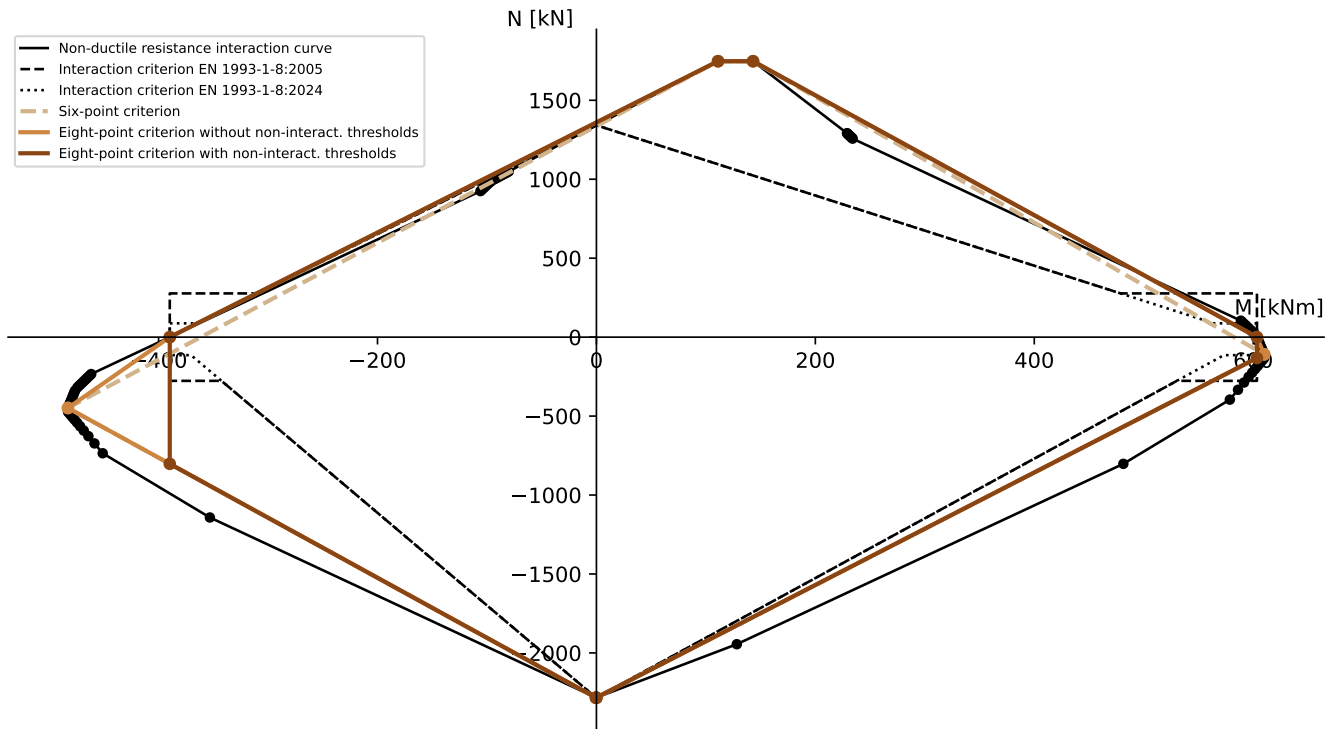


Figure 4.10: Cerfontaine example - New M-N interaction criteria

# Chapter 5

## Conclusions

The common thread and primary objective of this thesis was to develop and suggest new design recommendations that could potentially replace the M-N interaction criteria defined in both the current and upcoming versions of the European standard (EN 1993-1-8:2005 & EN 1993-1-8:2024).

Initially, a section of this thesis has been entirely dedicated to thoroughly explaining the practical implementation of the analytical and numerical models employed. This synthesis work enabled a comprehensive understanding of the different approaches, while highlighting the specific features and assumptions associated with each of them.

Building on these developments, a comprehensive set of Python-based computational routines has been developed to efficiently analytically characterise the various ductile joint configurations discussed in this document. The results produced by these routines were compared with those of the commercial COP software (beta version) and showed excellent agreement, thereby validating the use of the latter.

In a second phase, the test results of an experimental campaign carried out at the University of Coimbra were used to try to validate the Cerfontaine model. Unfortunately, significant discrepancies were observed between some analytical resistance predictions and experimental measurements, even when using the actual mechanical and geometrical properties of the joint. Since several questions related to these tests remain unanswered, it would be worthwhile to conduct further studies to address them. It would also be wise to wait for the conclusions of the Master thesis currently underway at the University of Coimbra before drawing any definitive conclusions about the reliability and the safety of the model.

Subsequently, a parametric analysis of various geometrical and mechanical properties of the joints was performed using the COP software exclusively. This study has notably shown that variations in several parameters, such as the bolt steel grade or the end-plate thickness, can significantly alter the behaviour of the joint, potentially causing a sudden shift from ductile to non-ductile response, and vice versa. The differences between the M-N resistance interaction curves and their derivation procedures for both types of joints have also been underlined. Thus, the results of this parametric analysis have clearly demonstrated the critical importance of both the selection and, even more so, the execution control of these properties. In fact, a slight variation of just a few millimetres or a higher actual steel grade can significantly affect the behaviour and/or the resistance of the joint.

Afterwards, three local numerical joint models were developed in the FINELG finite element software using a newly designed structural joint element, referred to as ASSEMBLA. By using the analytical results from the first two steps of the component method and applying forces iteratively to the model, it was demonstrated that these numerical models were able to converge to the characteristic M-N resistance

points obtained analytically. Unlike the current assembly procedure defined in the standard, these models also make it possible to account for variations in the rotational stiffness of the joint throughout the entire loading cycle, and to highlight the influence of axial force magnitude on this property.

In light of these observations, and as a further step, it could be of particular interest to explore the use of the ASSEMBLA element within the framework of a robustness analysis of a global structure subjected to a column loss scenario, and to compare the results with those obtained from an identical model in which the joints would simply be represented as rotational springs. It should be noted that such a study was initiated during this thesis, but unfortunately could not be completed due to the discovery of a software bug, which had not yet been identified by the developers and is currently being addressed. This is why the results related to the latter study have not been included in this manuscript.

Finally, rich of these learnings, a critical and objective review of the M-N interaction criterion of both versions of the European standard was carried out. This analysis led to three key findings: the lack of guidance in the standard for practical implementation, the complete absence of scientific justification for their use, and last but not least, the systematic apparition of insecure regions when they are overlaid with the ductile resistance interaction curves derived analytically.

To address the identified issues, three distinct M-N interaction criteria have been developed as part of this thesis, with a view to a potential inclusion in a future revision of the European standard. For each of these design recommendations, a comprehensive derivation procedure has been provided, along with several illustrative application examples. However, their use remains subject to the validation of the two ductility criteria outlined in this thesis, as demonstrated by a counter-example. Nevertheless, given the deserved evolution of the robustness requirements that structures must meet, it is highly likely that ductile joints will become the standard, thereby making these recommendations always applicable. It should also be emphasised that these criteria are simplified approaches and, as such, will never fully substitute the derivation of the complete interaction curve.

In conclusion, although this Master thesis represents a modest contribution to the vast research field of structural steel joint characterisation, with a particular focus on M-N interaction, it nonetheless marks a significant personal advancement beyond the basic knowledge I possessed prior to undertaking this work.

# Bibliography

- [1] Eurocode Applied. En1993 : Design of steel structures. <https://eurocodeapplied.com/design/en1993>. Accessed : February 2025.
- [2] ArcelorMittal. Sections and Merchant Bars - Sales Programme (Version 2024-2). [https://sections.arcelormittal.com/repository2/Sections/Sections\\_MB\\_ArcelorMittal\\_FR\\_EN\\_DE\\_V2024-2.pdf](https://sections.arcelormittal.com/repository2/Sections/Sections_MB_ArcelorMittal_FR_EN_DE_V2024-2.pdf). Accessed : May 2025.
- [3] Frédéric Cerfontaine. *Etude de l'interaction entre momen de flexion et effort normal dans les assemblages boulonnés*. PhD thesis, ULiège - Université de Liège, November 2003.
- [4] European committee for standardization. EN ISO 7089. : Plain washers - Normal series - Product grade A, June 2000.
- [5] European committee for standardization. EN 1994-1-1. Eurocode 4 : Design of composite steel and concrete structures - Part 1-1: General rules and rules for buildings, December 2004.
- [6] European committee for standardization. EN 1993-1-1. Eurocode 3 : Design of steel structures - Part 1-1 : General rules and rules for buildings, May 2005.
- [7] European committee for standardization. EN 1993-1-8. Eurocode 3 : Design of steel structures - Part 1-8 : Design of joints, May 2005.
- [8] European committee for standardization. EN ISO 4014. : Fasteners - Hexagon head bolts - Product grades A and B, July 2022.
- [9] European committee for standardization. EN ISO 4032. : Fasteners - Hexagon regular nuts (style 1), August 2023.
- [10] European committee for standardization. EN 1993-1-14. Eurocode 3 : Design of steel structures - Part 1-14 : Design assisted by finite element analysis, July 2024.
- [11] European committee for standardization. EN 1993-1-8. Eurocode 3 - Design of steel structures - Part 1-8 : Joints, March 2024.
- [12] Adrien Corman. *Characterization of the Full Non-Linear Behaviour up to Failure of the Sheared Panel Zone under Monotonic Loading Conditions*. PhD thesis, ULiège - Université de Liège [Faculté des Sciences Appliquées], Liège, Belgium, 09 December 2022.
- [13] L.R.O. de Lima, L. Simões da Silva, P.C.G. da S. Vellasco, and S.A.L. de Andrade. Behaviour of flush end-plate beam-to-column joints under bending and axial force. *Steel and Composite Structures*, 4(2):77–94, 2004.
- [14] L.R.O. de Lima, L. Simões da Silva, P.C.G. da S. Vellasco, and S.A.L. de Andrade. Experimental evaluation of extended endplate beam-to-column joints subjected to bending and axial force. *Engineering Structures*, 26(10):1333–1347, April 2004.
- [15] Luciano Rodrigues Ornelas de Lima. *Comportamento de Ligações com Placa de Extremidade em Estruturas de Aço Submetidas a Momento Fletor e Força Axial*. PhD thesis, PUC - Pontifical Catholic University of Rio de Janeiro, July 2003.

- [16] J.-F. Demonceau, Tudor Golea, J.-P. Jaspart, Ahmed Elghazouli, Zeyad Khalil, Aldina Santiago, Ana Francisca Santos, Luís Simões da Silva, Ulrike Kuhlmann, Georgios Skarmoutsos, Nadia Baldassino, Riccardo Zandonini, Martina Bernardi, Marco Zordan, Florea Dinu, Ioan Marginean, Jakab Dominiq, Dan Dubina, Freddy Wertz, Klaus Weynand, Renata Obiala, Miguel Candeias, Marion Charlier, and Omer Anwaar. *Design Recommendations against Progressive Collapse in Steel and Steel-Concrete Buildings [FAILNOMORE]*. ECCS – European Convention for Constructional Steelwork, December 2021.
- [17] Jean-François Demonceau. Natural and technological risks in civil engineering course : Alternative load path method chapter. ULiège - Université de Liège - Academic year 2024-2025.
- [18] Jean-François Demonceau. *Steel and composite building frames: sway response under conventional loading and developmet of membrane effects in beams further to an exceptional action*. PhD thesis, ULiège - Université de Liège, June 2008.
- [19] Jean-François Demonceau, Frédéric Cerfontaine, and Jean-Pierre Jaspart. Resistance of steel and composite connections under combined axial force and bending including group effects: Analytical procedures and comparison with laboratory tests. *Journal of Constructional Steel Research*, 160:320–331, 2019.
- [20] Feldmann + Weynand GmbH. COP - The connection program. <https://cop.fw-ing.de/index.php>. Accessed : May 2025.
- [21] Tudor Golea. Behaviour of Steel Joints Under Dynamic Actions. Master’s thesis, ULiège - Université de Liège, June 2020.
- [22] Tudor Golea, Adrien Corman, Julien Mathieu, Yves Duchêne, Jean-Pierre Jaspart, and Jean-François Demonceau. An innovative mechanical model for structural steel joints. *Engineering Structures*, 277:115459, 2023.
- [23] Greisch Design Office and University of Liège. FINELG : Non-linear finite element analysis program. [https://www.uee.uliege.be/cms/c\\_4017552/en/uee-finelg](https://www.uee.uliege.be/cms/c_4017552/en/uee-finelg). Accessed : May 2025.
- [24] Cécile Haremza, Aldina Santiago, Jean-François Demonceau, Jean-Pierre Jaspart, and Luís Simões da Silva. Composite joints under M-N at elevated temperatures. *Journal of Constructional Steel Research*, 124:173–186, 2016.
- [25] Jean-Pierre Jaspart. *Etude de la semi-rigidité des noeuds poutre-colonne et son influence sur la résistance et la stabilité des ossatures en acier*. PhD thesis, ULiège - Université de Liège, January 1991. Faculté des Sciences Appliquées, Département M. S. M.
- [26] Jean-Pierre Jaspart, Adrien Corman, and Jean-François Demonceau. Characterization of unstiffened column webs in transverse compression in steel beam-to-column joints. *Thin-Walled Structures*, 180:109848, 2022.
- [27] Jean-Pierre Jaspart and Vincent De Ville De Goyet. Etude expérimentale et numérique du comportement des structures composées de barres à assemblages semi-rigides. *Construction Métallique*, N°2, June 1988.
- [28] Jean-Pierre Jaspart and Klaus Weynand. *Design of joints in steel and composite structures*. ECCS – European Convention for Constructional Steelwork, 2016.
- [29] Julien Mathieu. Développement d’un modèle novateur de caractérisation du comportement précis d’assemblages de construction métallique et mixte acier-béton. Master’s thesis, ULiège - Université de Liège, June 2020.
- [30] Arnaud Neutelers. Improvement of the mechanical model for mode 1 t-stub plastic strength. Master’s thesis, ULiège - Université de Liège, June 2023.

# Appendix A

## FAILNOMORE joint configurations

### A.1 Configuration A1

In this section, all the calculation steps of the component method and the Cerfontaine model, described in Sections 3.2.1 & 3.2.2, are detailed for the FAILNOMORE joint configuration A1. All the geometrical and mechanical properties used in the equations of this appendix have already been presented in Section 3.3.1 of this thesis.

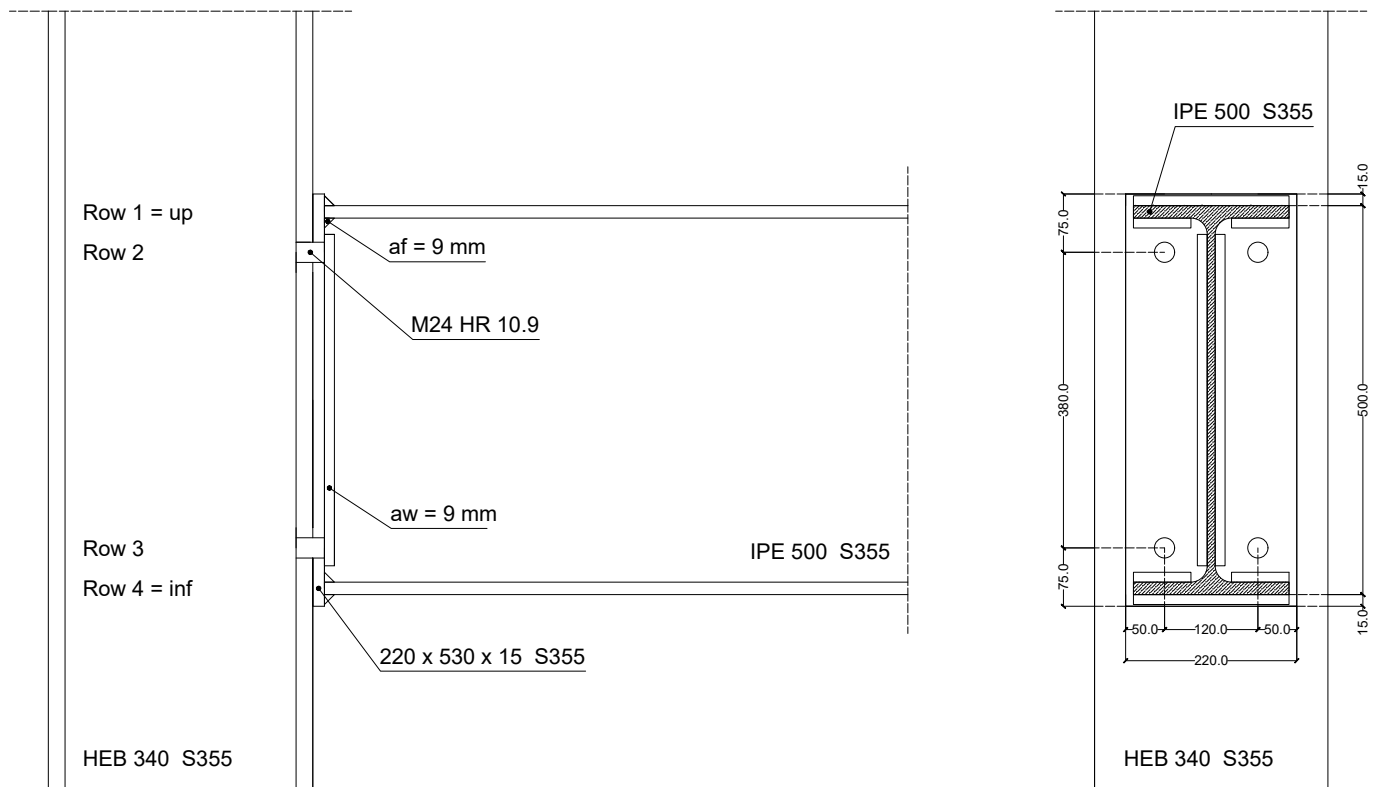


Figure A.1: FAILNOMORE - Joint configurations A1 - Technical drawing

#### A.1.1 Component characterisation - 3.

##### Column web panel in shear - CWS

##### *Resistance*

The joint configuration A1 being one-sided, the  $\beta$  transformation parameter can be taken equal to 1.

$$\epsilon = \sqrt{\frac{235}{f_{y,wc}}} = \sqrt{\frac{235}{355}} = 0.813 [-] \quad (A.1)$$

$$\frac{d_c}{t_{wc}} = \frac{243}{12} = 20.25 [-] \quad (A.2)$$

The following equations can be used provided that the criterion  $\frac{d_c}{t_{wc}} \leq 69\epsilon$  on the slenderness of the column web panel is respected, which is here the case for the HEB 340 steel profile.

$$V_{wp,Rd} = \frac{0.9 f_{y,wc} A_{vc}}{\sqrt{3} \gamma_{M0}} = \frac{0.9 \times 355 \times 5,609}{\sqrt{3} \times 1.0} = 1,034,655 [N] \quad (A.3)$$

$$F_{wp,Rd} = \frac{V_{wp,Rd}}{\beta} = \frac{1,034,655}{1.0} = 1,034,655 [N] \quad (A.4)$$

### Column web in transverse compression - CWC

#### Resistance

The HEB 340 steel profile being a rolled H section column, it comes that :

$$b_{eff,c,wc} = t_{fb} + 2\sqrt{2}a_p + 5(t_{fc} + s) + s_p = 16 + 2\sqrt{2} \times 9 + 5(21.5 + 27) + 2 \times 15 = 301.2 [mm] \quad (A.5)$$

Since no axial force or bending moment is applied to the column, the coefficient  $k_{wc}$  must be set to 1. With the transformation parameter  $\beta$  equal to 1, the shear stress interaction coefficient  $\omega$  can be obtained using the following expression :

$$\omega = \omega_1 = \frac{1}{\sqrt{1 + 1.3 \left( \frac{b_{eff,c,wc} t_{wc}}{A_{vc}} \right)^2}} = \frac{1}{\sqrt{1 + 1.3 \left( \frac{301.2 \times 12}{5,609} \right)^2}} = 0.805 [-] \quad (A.6)$$

The design resistance of the column web in transverse compression can then be computed as :

$$F_{c,wc,Rd} = \frac{\omega k_{wc} b_{eff,c,wc} t_{wc} f_{y,wc}}{\gamma_{M0}} = \frac{0.805 \times 1 \times 301.2 \times 12 \times 355}{1.0} = 1,034,085 [N] \quad (A.7)$$

To take into account a potential instability of the column web under transverse compression, the next equations must be used.

$$\bar{\lambda}_p = 0.932 \sqrt{\frac{b_{eff,c,wc} d_c f_{y,wc}}{E t_{wc}^2}} = 0.932 \sqrt{\frac{301.2 \times 243 \times 355}{210,000 \times 12^2}} = 0.864 [-] > 0.72 \quad (A.8)$$

$$\rho = \frac{\bar{\lambda}_p - 0.2}{\bar{\lambda}_p^2} = \frac{0.864 - 0.2}{0.864^2} = 0.889 [-] \quad (A.9)$$

$$F_{c,wc,Rd} \leq \frac{\omega k_{wc} \rho b_{eff,c,wc} t_{wc} f_{y,wc}}{\gamma_{M1}} = \frac{0.805 \times 1 \times 0.889 \times 301.2 \times 12 \times 355}{1.0} = 919,843 [N] \quad (A.10)$$

The resistance of the CWC component must thus be restricted to 919.843 kN.

#### Stiffness

$$k_2 = \frac{0.7 b_{eff,c,wc} t_{wc}}{d_c} = \frac{0.7 \times 301.2 \times 12}{243} = 10.412 [mm] \quad (A.11)$$

**Beam flange and web in compression - BFC****Resistance**

The IPE 500 beam made of S355 steel is classified as Class 1 under pure bending about the y-y axis (see ArcelorMittal sales programme [2]).

$$M_{c,Rd} = \frac{W_{pl,y} f_{yb}}{\gamma_{M0}} = \frac{2,194,000 \times 355}{1.0} = 778,870,000 \text{ [Nmm]} \quad (\text{A.12})$$

$$F_{c,fb,Rd} = \frac{M_{c,Rd}}{h_b - t_{fb}} = \frac{778,870,000}{500 - 16} = 1,609,235 \text{ [N]} \quad (\text{A.13})$$

where :

- $W_{pl,y}$  The beam plastic modulus around strong axis (y-y) [mm<sup>3</sup>]

**Stiffness**

$$k_7 = \infty \text{ [mm]} \quad (\text{A.14})$$

**Ductility**

With respect to the beam (IPE 500) cross-section class under pure bending (Class 1), the BFC component can be considered as ductile.

**Bolts in tension - BT****Resistance**

$$F_{t,Rd} = \frac{k_2 f_{ub} A_s}{\gamma_{M2}} = \frac{0.9 \times 1000 \times 353}{1.25} = 254,160 \text{ [N]} \quad (\text{A.15})$$

**Stiffness**

$$L_b = t_{fc} + t_{ep} + 2h_w + \frac{k_b + m_n}{2} = 21.5 + 15 + 2 \times 4 + \frac{15 + 21.5}{2} = 62.75 \text{ [mm]} \quad (\text{A.16})$$

$$k_{10} = \frac{1.6A_s}{L_b} = \frac{1.6 \times 353}{62.75} = 9.001 \text{ [mm]} \quad (\text{A.17})$$

**Column flange in transverse bending - CFB**

Given the perfect symmetry of the studied joint configuration about the beam axis, both tension rows must necessarily exhibit identical individual resistances for all tension components of the joint.

**Resistance - Tension row n°2/3**

The main geometrical properties of the equivalent T-stub flange can be computed as following :



$$e = \frac{b_c - b_{ep}}{2} + 50 = \frac{300 - 220}{2} + 50 = 90 \text{ [mm]} \quad (\text{A.18})$$

$$m = \frac{120}{2} - \frac{t_{wc}}{2} - 0.8r_c = \frac{120}{2} - \frac{12}{2} - 0.8 \times 27 = 32.4 \text{ [mm]} \quad (\text{A.19})$$

$$n = e_{min} = 50 \geq 1.25m = 40.5 \rightarrow n = 40.5 \text{ [mm]} \quad (\text{A.20})$$

$$e_w = \frac{d_w}{4} = \frac{44}{4} = 11 \text{ [mm]} \quad (\text{A.21})$$

with :

- $b_c$  The width of the column profile [mm]
- $b_{ep}$  The width of the end-plate [mm]
- $d_w$  The external diameter of the washer [mm]

The effective lengths can then be obtained based on Figure 3.4.

$$l_{eff,cp} = 2\pi m = 2\pi \times 32.4 = 203.575 \text{ [mm]} \quad (\text{A.22})$$

$$l_{eff,nc} = 4m + 1.25e = 4 \times 32.4 + 1.25 \times 90 = 242.1 \text{ [mm]} \quad (\text{A.23})$$

$$l_{eff,1} = \min(l_{eff,cp} ; l_{eff,nc}) = \min(203.575 ; 242.1) = 203.575 \text{ [mm]} \quad (\text{A.24})$$

$$l_{eff,2} = l_{eff,nc} = 242.1 \text{ [mm]} \quad (\text{A.25})$$

The  $F_{T,i,Rd}$  values can finally be obtained through :

$$M_{pl,1,Rd} = \frac{0.25 \sum l_{eff,1} t_{fc}^2 f_{y,fc}}{\gamma_{M0}} = \frac{0.25 \times 203.575 \times 21.5^2 \times 355}{1.0} = 8,351,609.12 \text{ [Nmm]} \quad (\text{A.26})$$

$$M_{pl,2,Rd} = \frac{0.25 \sum l_{eff,2} t_{fc}^2 f_{y,fc}}{\gamma_{M0}} = \frac{0.25 \times 242.1 \times 21.5^2 \times 355}{1.0} = 9,932,076.84 \text{ [Nmm]} \quad (\text{A.27})$$

$$F_{T,1,Rd} = \frac{(8n - 2e_w)M_{pl,1,Rd}}{2mn - e_w(m + n)} = \frac{(8 \times 40.5 - 2 \times 11) \times 8,351,609.12}{2 \times 32.4 \times 40.5 - 11 \times (32.4 + 40.5)} = 1,383,915 \text{ [N]} \quad (\text{A.28})$$

$$F_{T,2,Rd} = \frac{2M_{pl,2,Rd} + n \sum F_{t,Rd}}{m + n} = \frac{2 \times 9,932,076.84 + 40.5 \times 2 \times 254,160}{32.4 + 40.5} = 554,885 \text{ [N]} \quad (\text{A.29})$$

$$F_{T,3,Rd} = \sum F_{t,Rd} = 2 \times 254,160 = 508,320 \text{ [N]} \quad (\text{A.30})$$

In this case, the retained value is the one associated with failure mode n°3.

$$F_{T,Rd} = \min(F_{T,1,Rd} ; F_{T,2,Rd} ; F_{T,3,Rd}) = \min(1,383,915 ; 554,885 ; 508,320) = 508.320 \text{ [N]} \quad (\text{A.31})$$

### Resistance - Group mechanism 23

In this case, the values of  $\sum l_{eff,1}$  and  $\sum l_{eff,2}$  can be simply calculated as twice the effective length of a single row, considered as part of a group, due to the joint symmetry.

$$l_{eff,cp} = \pi m + p = \pi \times 32.4 + 380 = 481.787 \text{ [mm]} \quad (A.32)$$

$$l_{eff,nc} = 2m + 0.625e + 0.5p = 2 \times 32.4 + 0.625 \times 90 + 0.5 \times 380 = 311.05 \text{ [mm]} \quad (A.33)$$

$$\sum l_{eff,1} = \min(\sum l_{eff,cp} ; \sum l_{eff,nc}) = \min(2 \times 481.787 ; 2 \times 311.05) = 622.1 \text{ [mm]} \quad (A.34)$$

$$\sum l_{eff,2} = \sum l_{eff,nc} = 2 \times 311.05 = 622.1 \text{ [mm]} \quad (A.35)$$

with p the vertical spacing between the two tension rows in millimeters.

$$M_{pl,1,Rd} = \frac{0.25 \sum l_{eff,1} t_{fc}^2 f_{y,fc}}{\gamma_{M0}} = \frac{0.25 \times 622.1 \times 21.5^2 \times 355}{1.0} = 25,521,458.09 \text{ [Nmm]} \quad (A.36)$$

$$M_{pl,2,Rd} = \frac{0.25 \sum l_{eff,2} t_{fc}^2 f_{y,fc}}{\gamma_{M0}} = \frac{0.25 \times 622.1 \times 21.5^2 \times 355}{1.0} = 25,521,458.09 \text{ [Nmm]} \quad (A.37)$$

$$F_{T,1,Rd} = \frac{(8n - 2e_w)M_{pl,1,Rd}}{2mn - e_w(m + n)} = \frac{(8 \times 40.5 - 2 \times 11) \cdot 25,521,458.09}{2 \times 32.4 \times 40.5 - 11 \times (32.4 + 40.5)} = 422,907,014 \text{ [N]} \quad (A.38)$$

$$F_{T,2,Rd} = \frac{2M_{pl,2,Rd} + n \sum F_{t,Rd}}{m + n} = \frac{2 \times 25,521,458.09 + 40.5 \times 4 \times 254,160}{32.4 + 40.5} = 1,264,977 \text{ [N]} \quad (A.39)$$

$$F_{T,3,Rd} = \sum F_{t,Rd} = 4 \times 254,160 = 1,016,640 \text{ [N]} \quad (A.40)$$

The CFB design resistance for the group mechanism 23 is thus equal to :

$$F_{T,Rd} = \min(F_{T,1,Rd} ; F_{T,2,Rd} ; F_{T,3,Rd}) = \min(422,907,014 ; 1,264,977 ; 1,016,640) = 1,016,640 \text{ [N]} \quad (A.41)$$

### Stiffness

$$l_{eff} = \min(203.575 ; 242.1 ; 481.787 ; 311.05) = 203.575 \text{ [mm]} \quad (A.42)$$

$$k_4 = \frac{0.9 l_{eff} t_{fc}^3}{m^3} = \frac{0.9 \times 203.575 \times 21.5^3}{32.4^3} = 53.536 \text{ [mm]} \quad (A.43)$$

### Ductility

Since the CFB design resistance corresponds to failure mode n°3 for both individual tension rows, the CFB component must be assumed brittle for these latter.

### Column web in transverse tension - CWT

The transformation parameter  $\beta$  being still equal to 1, the shear stress interaction coefficient  $\omega$  can again be computed based on Equation (A.6).

### Resistance - Tension row n°2/3

$$b_{eff,t,wc} = l_{eff,2} = 242.1 \text{ [mm]} \quad (A.44)$$

$$\omega = \omega_1 = \frac{1}{\sqrt{1 + 1.3 \left( \frac{b_{eff,t,wc} t_{wc}}{A_{vc}} \right)^2}} = \frac{1}{\sqrt{1 + 1.3 \left( \frac{242.1 \times 12}{5,609} \right)^2}} = 0.861 \text{ [-]} \quad (A.45)$$

The design resistance of the CWT component can then be obtained by :

$$F_{t,wc,Rd} = \frac{\omega b_{eff,t,wc} t_{wc} f_{y,wc}}{\gamma_{M0}} = \frac{0.861 \times 242.1 \times 12 \times 355}{1.0} = 887,988 [N] \quad (A.46)$$

### **Resistance - Group mechanism 23**

The same steps can be followed for the group mechanism.

$$b_{eff,t,wc} = l_{eff,2} = 622.1 [mm] \quad (A.47)$$

$$\omega = \omega_1 = \frac{1}{\sqrt{1 + 1.3 \left( \frac{b_{eff,t,wc} t_{wc}}{A_{wc}} \right)^2}} = \frac{1}{\sqrt{1 + 1.3 \left( \frac{622.1 \times 12}{5609} \right)^2}} = 0.55 [-] \quad (A.48)$$

$$F_{t,wc,Rd} = \frac{\omega b_{eff,t,wc} t_{wc} f_{y,wc}}{\gamma_{M0}} = \frac{0.55 \times 622.1 \times 12 \times 355}{1.0} = 1,457,580 [N] \quad (A.49)$$

### **Stiffness**

$$b_{eff,t,wc} = \min(203.575 ; 242.1 ; 481.757 ; 311.05) = 203.575 [mm] \quad (A.50)$$

$$k_3 = \frac{0.7 b_{eff,t,wc} t_{wc}}{d_c} = \frac{0.7 \times 203.575 \times 12}{243} = 7.037 [mm] \quad (A.51)$$

### **Ductility**

The CWT component is ductile because a normalized steel grade is used for the column profile.

### **End-plate in bending - EPB**

#### **Resistance - Tension row n°2/3**

The new geometrical properties of the equivalent T-stub flange can be computed as following :

$$e = e_{min} = 50 [mm] \quad (A.52)$$

$$m = \frac{120}{2} - \frac{t_{wb}}{2} - 0.8\sqrt{2}a_p = \frac{120}{2} - \frac{10.2}{2} - 0.8\sqrt{2} \times 9 = 44.71 [mm] \quad (A.53)$$

$$m_2 = 60 - t_{fb} - 0.8\sqrt{2}a_p = 60 - 16 - 0.8\sqrt{2} \cdot 9 = 33.81 [mm] \quad (A.54)$$

$$n = e_{min} = 50 [mm] \quad (A.55)$$

where :

- $t_{wb}$  The thickness of the beam web [mm]

$$\alpha = 4 + 1.67 \frac{e}{m} \left( \frac{m}{m_2} \right)^{0.67} = 4 + 1.67 \times \frac{50}{44.71} \times \left( \frac{44.71}{33.81} \right)^{0.67} = 6.251 [-] \quad (A.56)$$

$$\text{but } \alpha \geq 4 + 1.25 \frac{e}{m} = 5.397 \quad \text{and} \quad \alpha \leq 8 \quad (A.57)$$

Since both tension rows are positioned close to the flanges of the beam profile, the latter can be considered as acting as horizontal stiffeners for the end-plate. The bolt rows can therefore be analyzed as adjacent to a stiffener in Figure 3.7.

$$l_{eff,cp} = 2\pi m = 2\pi \times 44.71 = 280.97 \text{ [mm]} \quad (\text{A.58})$$

$$l_{eff,nc} = \alpha m = 6.251 \times 44.71 = 279.56 \text{ [mm]} \quad (\text{A.59})$$

$$l_{eff,1} = \min(l_{eff,cp} ; l_{eff,nc}) = \min(280.97 ; 279.56) = 279.56 \text{ [mm]} \quad (\text{A.60})$$

$$l_{eff,2} = l_{eff,nc} = 279.56 \text{ [mm]} \quad (\text{A.61})$$

$$M_{pl,1,Rd} = \frac{0.25 \sum l_{eff,1} t_{ep}^2 f_{y,ep}}{\gamma_{M0}} = \frac{0.25 \times 279.56 \times 15^2 \times 355}{1.0} = 5,582,453.22 \text{ [Nmm]} \quad (\text{A.62})$$

$$M_{pl,2,Rd} = \frac{0.25 \sum l_{eff,2} t_{ep}^2 f_{y,ep}}{\gamma_{M0}} = \frac{0.25 \times 279.56 \times 15^2 \times 355}{1.0} = 5,582,453.22 \text{ [Nmm]} \quad (\text{A.63})$$

$$F_{T,1,Rd} = \frac{(8n - 2e_w)M_{pl,1,Rd}}{2mn - e_w(m + n)} = \frac{(8 \times 50 - 2 \times 11) \times 5,582,453.22}{2 \times 44.71 \times 50 - 11 \times (44.71 + 50)} = 615,354 \text{ [N]} \quad (\text{A.64})$$

$$F_{T,2,Rd} = \frac{2M_{pl,2,Rd} + n \sum F_{t,Rd}}{m + n} = \frac{2 \times 5,582,453.22 + 50 \times 2 \times 254,160}{44.71 + 50} = 386,241 \text{ [N]} \quad (\text{A.65})$$

$$F_{T,3,Rd} = \sum F_{t,Rd} = 2 \times 254,160 = 508,320 \text{ [N]} \quad (\text{A.66})$$

However, unlike the CFB component, the retained value here is associated with failure mode n°2.

$$F_{T,Rd} = \min(F_{T,1,Rd} ; F_{T,2,Rd} ; F_{T,3,Rd}) = \min(615,354 ; 386,241 ; 508,320) = 386,241 \text{ [N]} \quad (\text{A.67})$$

### Resistance - Group mechanism 23

The symmetry of the joint allows a new time for doubling the effective length computed for one bolt row, considered as part of a group, to calculate the total effective lengths of the failure modes.

$$l_{eff,cp} = \pi m + p = \pi \times 44.71 + 380 = 520.48 \text{ [mm]} \quad (\text{A.68})$$

$$l_{eff,nc} = 0.5p + \alpha m - (2m + 0.625e) = 348.87 \text{ [mm]} \quad (\text{A.69})$$

$$\sum l_{eff,1} = \min(\sum l_{eff,cp} ; \sum l_{eff,nc}) = \min(2 \times 520.48 ; 2 \times 348.87) = 697.75 \text{ [mm]} \quad (\text{A.70})$$

$$\sum l_{eff,2} = \sum l_{eff,nc} = 2 \times 348.87 = 697.75 \text{ [mm]} \quad (\text{A.71})$$

$$M_{pl,1,Rd} = \frac{0.25 \sum l_{eff,1} t_{ep}^2 f_{y,ep}}{\gamma_{M0}} = \frac{0.25 \times 697.75 \times 15^2 \times 355}{1.0} = 13,933,161.29 \text{ [Nmm]} \quad (\text{A.72})$$

$$M_{pl,2,Rd} = \frac{0.25 \sum l_{eff,2} t_{ep}^2 f_{y,ep}}{\gamma_{M0}} = \frac{0.25 \times 697.75 \times 15^2 \times 355}{1.0} = 13,933,161.29 \text{ [Nmm]} \quad (\text{A.73})$$

$$F_{T,1,Rd} = \frac{(8n - 2e_w)M_{pl,1,Rd}}{2mn - e_w(m + n)} = \frac{(8 \times 50 - 2 \times 11) \times 13,933,161.29}{2 \times 44.71 \times 50 - 11 \times (44.71 + 50)} = 1,535,853 \text{ [N]} \quad (A.74)$$

$$F_{T,2,Rd} = \frac{2M_{pl,2,Rd} + n \sum F_{t,Rd}}{m + n} = \frac{2 \times 13,933,161.29 + 50 \times 4 \times 254,160}{44.71 + 50} = 830,939 \text{ [N]} \quad (A.75)$$

$$F_{T,3,Rd} = \sum F_{t,Rd} = 4 \times 254,160 = 1,016,640 \text{ [N]} \quad (A.76)$$

The EPB design resistance for the group mechanism 23 is thus equal to :

$$F_{T,Rd} = \min(F_{T,1,Rd} ; F_{T,2,Rd} ; F_{T,3,Rd}) = \min(1,535,853 ; 830,939 ; 1,016,640) = 830,939 \text{ [N]} \quad (A.77)$$

### Stiffness

$$l_{eff} = \min(280.97 ; 279.56 ; 520.48 ; 348.87) = 279.56 \text{ [mm]} \quad (A.78)$$

$$k_5 = \frac{0.9l_{eff} t_{ep}^3}{m^3} = \frac{0.9 \times 279.56 \times 15^3}{44.71^3} = 9.496 \text{ [mm]} \quad (A.79)$$

### Ductility

Since the EPB design resistance corresponds to failure mode n°2 for both individual tension rows and Equation (A.80) is verified, the EPB component can be assumed as ductile.

$$F_{T,Rd} = 386,241 \leq 1.9F_{t,Rd} = 1.9 \times 254,160 = 482,904 \text{ [N]} \quad (A.80)$$

### Beam web in tension - BWT

#### Resistance - Tension row n°2/3

$$b_{eff,t,wb} = l_{eff,2} = 279.56 \text{ [mm]} \quad (A.81)$$

$$F_{t,wb,Rd} = \frac{b_{eff,t,wb} t_{wb} f_{y,wb}}{\gamma_{M0}} = \frac{279.56 \times 10.2 \times 355}{1.0} = 1,012,286 \text{ [N]} \quad (A.82)$$

#### Resistance - Group mechanism 23

$$b_{eff,t,wb} = l_{eff,2} = 697.75 \text{ [mm]} \quad (A.83)$$

$$F_{t,wb,Rd} = \frac{b_{eff,t,wb} t_{wb} f_{y,wb}}{\gamma_{M0}} = \frac{697.75 \times 10.2 \times 355}{1.0} = 2,526.552 \text{ [N]} \quad (A.84)$$

### Stiffness

$$k_8 = \infty \quad (A.85)$$

### Ductility

The BWT component is ductile because a normalized steel grade is used for the beam profile.

### Summary of component properties

Table A.1: FAILNOMORE - Configuration A1 - Components properties - Individual rows - 3.

Individual rows	Component abbreviation	$F_{Rd}$ [kN]	$k$ [mm]
Compression row n°1/4	CWS	-1,034.655	/
	CWC	-919.843	10.412
	BFC	-1,609.235	$\infty$
Tension row n°2/3	BT	254.16	9.001
	CFB	508.32	53.536
	CWT	887.99	7.037
	EPB	386.24	9.496
	BWT	1,012.28	$\infty$

Table A.2: FAILNOMORE - Configuration A1 - Components properties - Group of rows - 3.

Group of rows	Component abbreviation	$F_{Rd}$ [kN]
Group mechanism 23	CFB	1,016.64
	CWT	1,457.58
	EPB	830.94
	BWT	2,526.55

### A.1.2 Row/Group characterisation - 4.

#### Individual rows

The individual resistances of the joint rows can be computed as following :

$$F_{[1,1],Rd} = \max(-1,304.655 ; -919.843 ; -1,609.235) = -919.84 \text{ [kN]} \quad (\text{A.86})$$

$$F_{[2,2],Rd} = \min(508.32 ; 887.99 ; 386.24 ; 1,012.28) = 386.24 \text{ [kN]} \quad (\text{A.87})$$

$$F_{[3,3],Rd} = \min(508.32 ; 887.99 ; 386.24 ; 1,012.28) = 386.24 \text{ [kN]} \quad (\text{A.88})$$

$$F_{[4,4],Rd} = \max(-1,304.655 ; -919.843 ; -1,609.235) = -919.84 \text{ [kN]} \quad (\text{A.89})$$

#### Group mechanisms

The same principle is followed to obtain the resistance of the group mechanism 23.

$$F_{[2,3],Rd} = \min(1,016.64 ; 1,457.58 ; 830.94 ; 2,526.55) = 830.94 \text{ [kN]} \quad (\text{A.90})$$

Table A.3: FAILNOMORE - Configuration A1 - Row/Group resistances - 4.

i	$F_{[i,i],Rd}$ [kN]	$F_{[i-1,i],Rd}$ [kN]	Critical Component
1 = sup	-919.84	$\infty$	CWC
2	386.24	$\infty$	EPB
3	386.24	830.94	EPB
4 = inf	-919.84	$\infty$	CWC

### A.1.3 Row lever arms calculation - 5.

$$h_1 = \frac{h_b - t_{fb}}{2} = \frac{500 - 16}{2} = 242 \text{ [mm]} \quad (\text{A.91})$$

$$h_2 = \frac{p}{2} = \frac{380}{2} = 190 \text{ [mm]} \quad (\text{A.92})$$

$$h_3 = -h_2 = -190 \text{ [mm]} \quad (\text{A.93})$$

$$h_4 = -h_1 = -242 \text{ [mm]} \quad (\text{A.94})$$

### A.1.4 Resistances $F_{Rd}^+$ & $F_{Rd}^-$ of each row - 6.

$$F_{1,Rd}^+ = F_{[1,1],Rd} = -919.84 \text{ [kN]} \quad (\text{A.95})$$

$$F_{2,Rd}^+ = F_{[2,2],Rd} = 386.21 \text{ [kN]} \quad (\text{A.96})$$

$$F_{3,Rd}^+ = \min(F_{[2,3],Rd} - F_{2,Rd}^+; F_{[3,3],Rd}) = \min(444.66; 386.21) = 386.21 \text{ [kN]} \quad (\text{A.97})$$

$$F_{4,Rd}^+ = F_{[4,4],Rd} = -919.84 \text{ [kN]} \quad (\text{A.98})$$

$$F_{4,Rd}^- = F_{[4,4],Rd} = -919.84 \text{ [kN]} \quad (\text{A.99})$$

$$F_{3,Rd}^- = F_{[3,3],Rd} = 386.21 \text{ [kN]} \quad (\text{A.100})$$

$$F_{2,Rd}^- = \min(F_{[2,3],Rd} - F_{3,Rd}^-; F_{[2,2],Rd}) = \min(444.66; 386.21) = 386.21 \text{ [kN]} \quad (\text{A.101})$$

$$F_{1,Rd}^- = F_{[1,1],Rd} = -919.84 \text{ [kN]} \quad (\text{A.102})$$

Table A.4: FAILNOMORE - Configuration A1 - Lever arms and  $F_{i,Rd}^+$  &  $F_{i,Rd}^-$  resistance values - 5. & 6.

i	$h_i$ [m]	$F_{i,Rd}^+$ [kN]	$F_{i,Rd}^-$ [kN]
1 = sup	0.242	-919.84	-919.84
2	0.19	386.24	386.24
3	-0.19	386.24	386.24
4 = inf	-0.242	-919.84	-919.84

### A.1.5 Characteristic M-N resistance points - 7.

For  $F_{Rd}^+$  resistance values

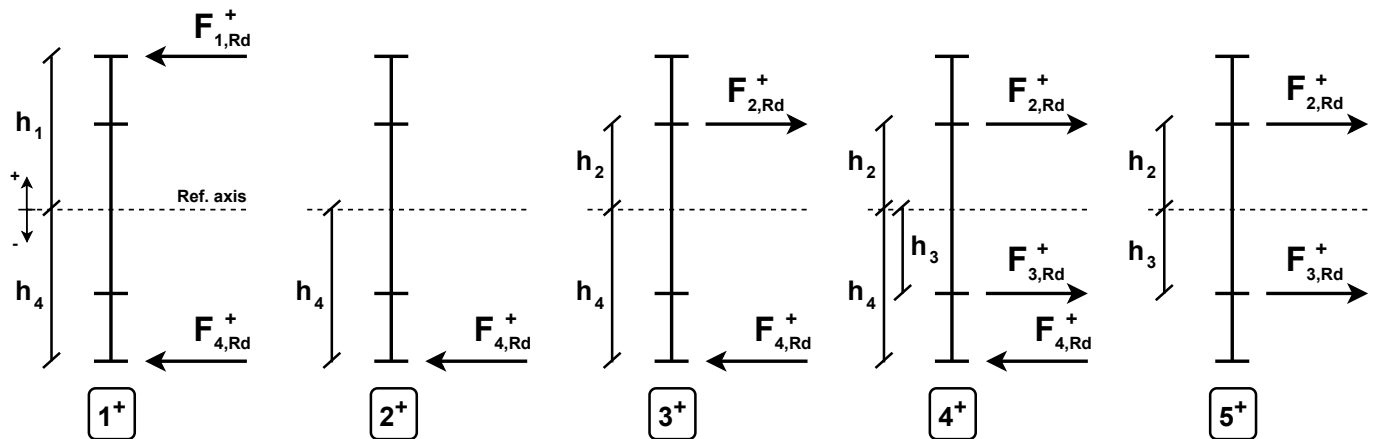


Figure A.2: FAILNOMORE - Configuration A1 - Hogging bending moment -  $n + 1$  distributions of int. forces

$$N_{1,Rd}^+ = F_{1,Rd}^+ + F_{4,Rd}^+ = -919.84 + (-919.84) = -1,839.68 \text{ [kN]} \quad (\text{A.103})$$

$$M_{1,Rd}^+ = F_{1,Rd}^+ h_1 + F_{4,Rd}^+ h_4 = -919.84 \times 0.242 + (-919.84 \times -0.242) = 0.0 \text{ [kNm]} \quad (\text{A.104})$$

$$N_{2,Rd}^+ = F_{4,Rd}^+ = -919.84 \text{ [kN]} \quad (\text{A.105})$$

$$M_{2,Rd}^+ = F_{4,Rd}^+ h_4 = -919.84 \times -0.242 = 222.6 \text{ [kNm]} \quad (\text{A.106})$$

$$N_{3,Rd}^+ = F_{2,Rd}^+ + F_{4,Rd}^+ = 386.24 + (-919.84) = -533.6 \text{ [kN]} \quad (\text{A.107})$$

$$M_{3,Rd}^+ = F_{2,Rd}^+ h_2 + F_{4,Rd}^+ h_4 = 386.24 \times 0.19 + (-919.84 \times -0.242) = 295.98 \text{ [kNm]} \quad (\text{A.108})$$

$$N_{4,Rd}^+ = F_{2,Rd}^+ + F_{3,Rd}^+ + F_{4,Rd}^+ = 386.24 + 386.24 + (-919.84) = -147.36 \text{ [kN]} \quad (\text{A.109})$$

$$M_{4,Rd}^+ = F_{2,Rd}^+ h_2 + F_{3,Rd}^+ h_3 + F_{4,Rd}^+ h_4 = 222.6 \text{ [kNm]} \quad (\text{A.110})$$

$$N_{5,Rd}^+ = F_{2,Rd}^+ + F_{3,Rd}^+ = 386.24 + 386.24 = 772.48 \text{ [kN]} \quad (\text{A.111})$$

$$M_{5,Rd}^+ = F_{2,Rd}^+ h_2 + F_{3,Rd}^+ h_3 = 0.0 \text{ [kNm]} \quad (\text{A.112})$$

For  $F_{Rd}^-$  resistance values

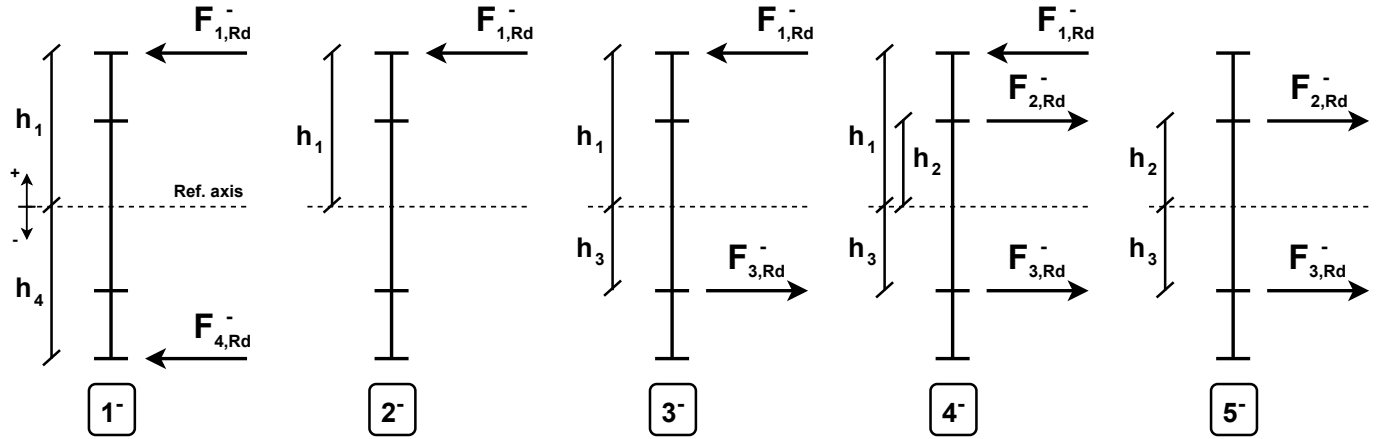


Figure A.3: FAILNOMORE - Configuration A1 - Sagging bending moment -  $n + 1$  distributions of int. forces

$$N_{1,Rd}^- = F_{1,Rd}^- + F_{4,Rd}^- = -919.84 + (-919.84) = -1,839.68 \text{ [kN]} \quad (\text{A.113})$$

$$M_{1,Rd}^- = F_{1,Rd}^- h_1 + F_{4,Rd}^- h_4 = -919.84 \times 0.242 + (-919.84 \times -0.242) = 0.0 \text{ [kNm]} \quad (\text{A.114})$$

$$N_{2,Rd}^- = F_{1,Rd}^- = -919.84 \text{ [kN]} \quad (\text{A.115})$$

$$M_{2,Rd}^- = F_{1,Rd}^- h_1 = -919.84 \times 0.242 = -222.6 \text{ [kNm]} \quad (\text{A.116})$$

$$N_{3,Rd}^- = F_{1,Rd}^- + F_{3,Rd}^- = -919.84 + 386.24 = -533.6 \text{ [kN]} \quad (\text{A.117})$$

$$M_{3,Rd}^- = F_{1,Rd}^- h_1 + F_{3,Rd}^- h_3 = -919.84 \times 0.242 + 386.24 \times -0.19 = -295.98 \text{ [kNm]} \quad (\text{A.118})$$

$$N_{4,Rd}^- = F_{1,Rd}^- + F_{2,Rd}^- + F_{3,Rd}^- = -919.84 + 386.24 + 386.24 = -147.36 \text{ [kN]} \quad (\text{A.119})$$

$$M_{4,Rd}^- = F_{1,Rd}^- h_1 + F_{2,Rd}^- h_2 + F_{3,Rd}^- h_3 = -222.6 \text{ [kNm]} \quad (\text{A.120})$$

$$N_{5,Rd}^- = F_{2,Rd}^- + F_{3,Rd}^- = 386.24 + 386.24 = 772.48 \text{ [kN]} \quad (\text{A.121})$$

$$M_{5,Rd}^- = F_{2,Rd}^- h_2 + F_{3,Rd}^- h_3 = 0.0 \text{ [kNm]} \quad (\text{A.122})$$



### Summary of characteristic M-N resistance points

Table A.5: FAILNOMORE - Configuration A1 - Characteristic M-N resistance points - 7.

N°	$M_{Rd}^+$ [kNm]	$N_{Rd}^+$ [kN]	$M_{Rd}^-$ [kNm]	$N_{Rd}^-$ [kN]
1	0.0	-1,839.68	0.0	-1,839.68
2	222.6	-919.84	-222.6	-919.84
3	295.98	-533.6	-295.98	-533.6
4	222.6	-147.36	-222.6	-147.36
5	0.0	772.48	0.0	772.48

### A.1.6 Ductile resistance interaction curve - 8.

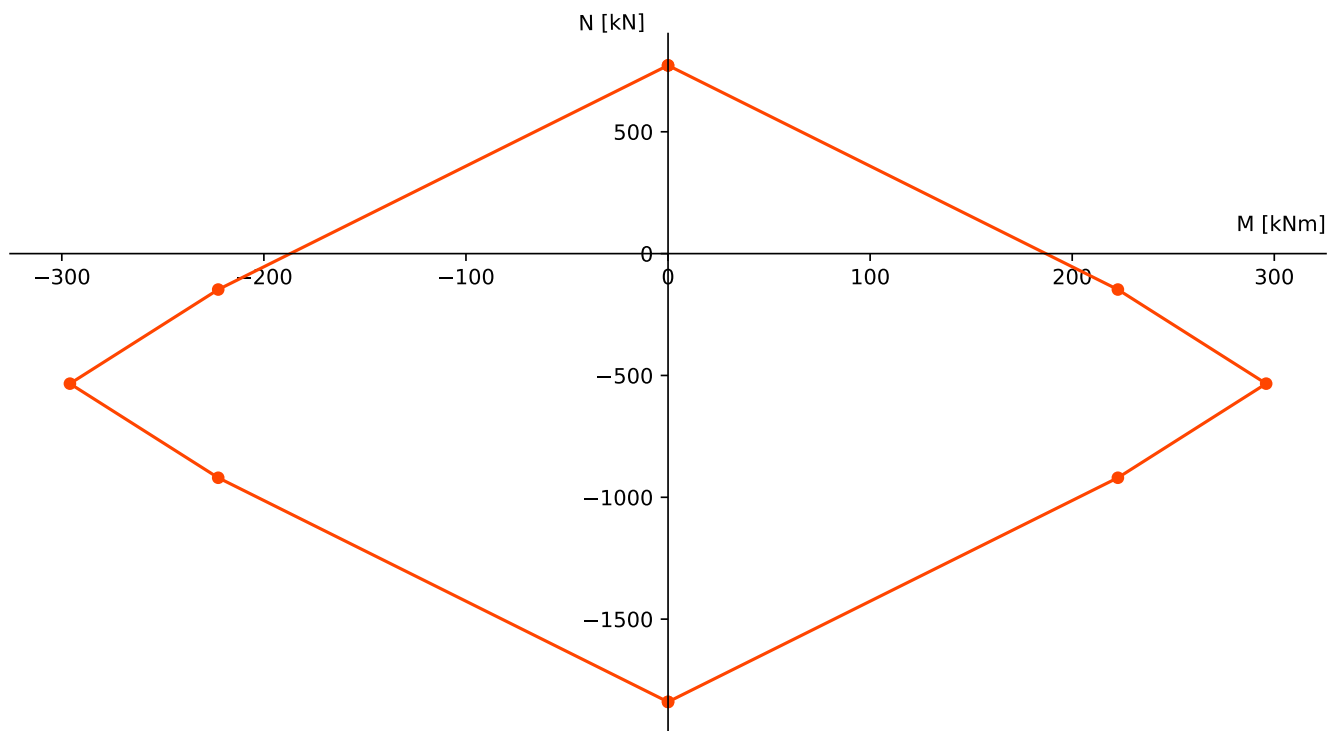


Figure A.4: FAILNOMORE - Joint configuration A1 - Ductile resistance interaction curve - 8.

## A.2 Configuration A2

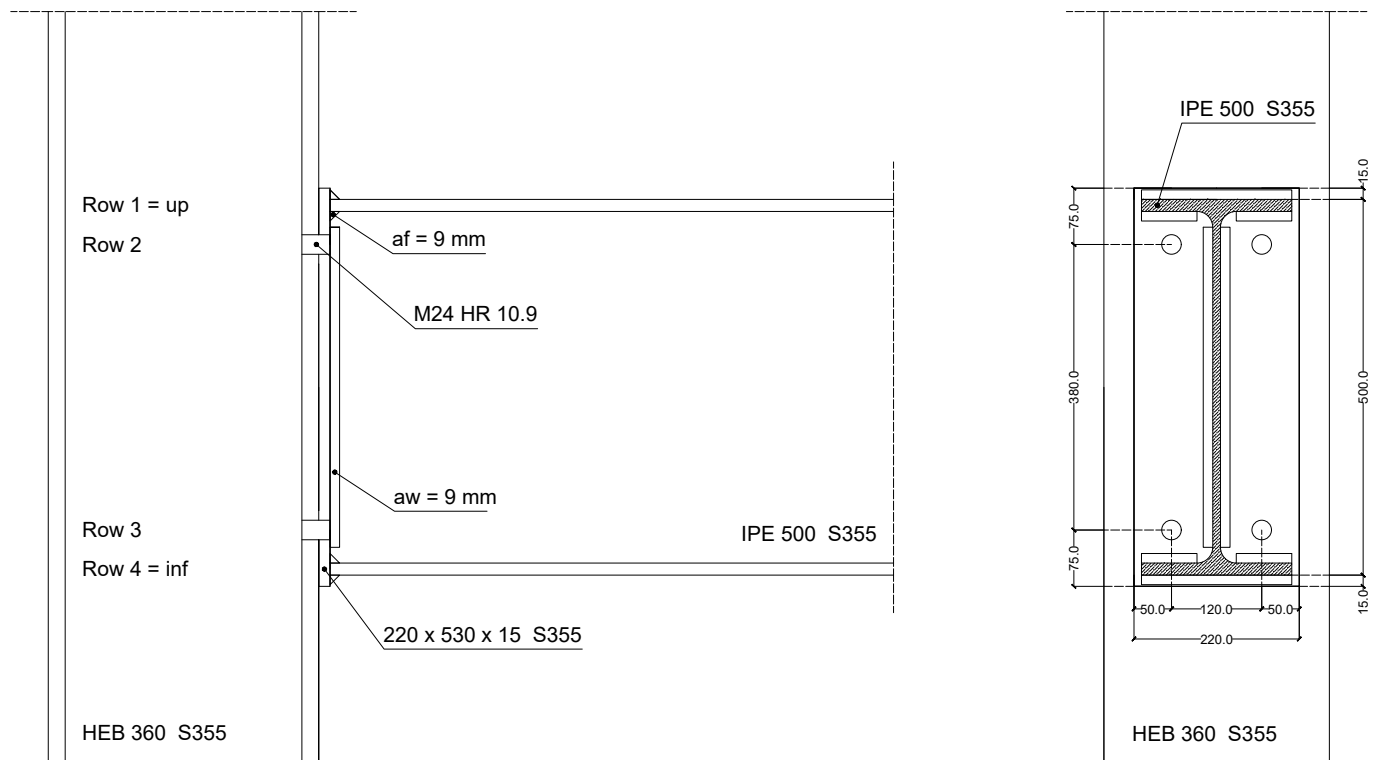


Figure A.5: FAILNOMORE - Joint configuration A2 - Technical drawing

Table A.6: FAILNOMORE - Configuration A2 - Components properties - Group of rows - 3.

Individual rows	Component abbreviation	$F_{Rd}$ [kN]	$k$ [mm]
Compression row n°1/4	CWS	-1,117.85	/
	CWC	<b>-978.706</b>	10.266
	BFC	-1,609.235	$\infty$
Tension row n°2/3	BT	254.16	9.0
	CFB	508.32	62.317
	CWT	930.675	6.772
	EPB	<b>386.21</b>	9.496
	BWT	1,012.28	$\infty$

Table A.7: FAILNOMORE - Configuration A2 - Components properties - Group of rows - 3.

Group of rows	Component abbreviation	$F_{Rd}$ [kN]
Group mechanism 23	CFB	1,016.64
	CWT	1,556.93
	EPB	<b>830.87</b>
	BWT	2,526.54

Table A.8: FAILNOMORE - Configuration A2 - Row/Group resistances - 4.

i	$F_{[i,i],Rd}$ [kN]	$F_{[i-1,i],Rd}$ [kN]	Critical Component
1 = sup	-978.7	$\infty$	CWC
2	386.21	$\infty$	EPB
3	386.21	830.87	EPB
4 = inf	-978.7	$\infty$	CWC

Table A.9: FAILNOMORE - Configuration A2 - Lever arms and  $F_{i,Rd}^+$  &  $F_{i,Rd}^-$  resistance values - 5. & 6.

i	$h_i$ [m]	$F_{i,Rd}^+$ [kN]	$F_{i,Rd}^-$ [kN]
1 = sup	0.242	-978.7	-978.7
2	0.19	386.21	386.21
3	-0.19	386.21	386.21
4 = inf	-0.242	-978.7	-978.7

Table A.10: FAILNOMORE - Configuration A2 - Characteristic M-N resistance points - 7.

N°	$M_{Rd}^+$ [kNm]	$N_{Rd}^+$ [kN]	$M_{Rd}^-$ [kNm]	$N_{Rd}^-$ [kN]
1	0.0	-1,957.41	0.0	-1,957.41
2	236.84	-978.7	-236.84	-978.7
3	310.22	-592.49	-310.22	-592.49
4	236.84	-206.28	-236.84	-206.28
5	0.0	772.42	0.0	772.42

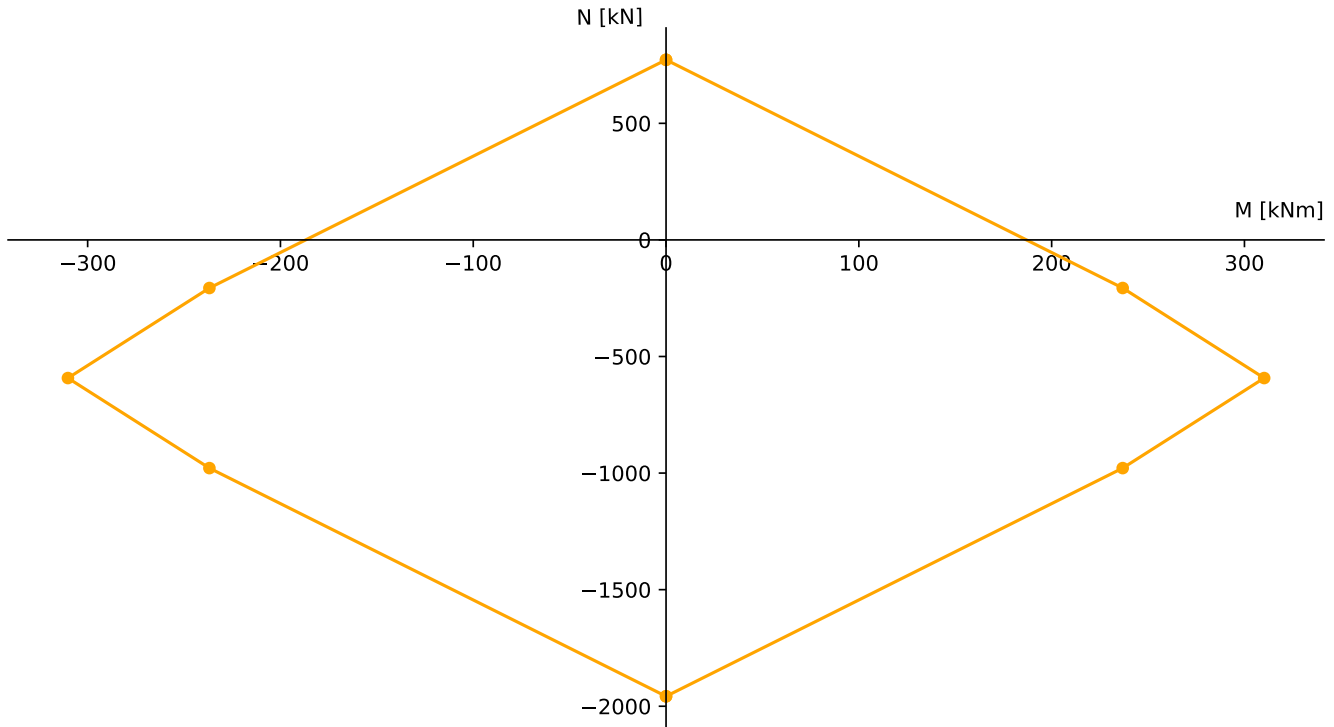


Figure A.6: FAILNOMORE - Joint configuration A2 - Ductile resistance interaction curve - 8.

## A.3 Configuration B1

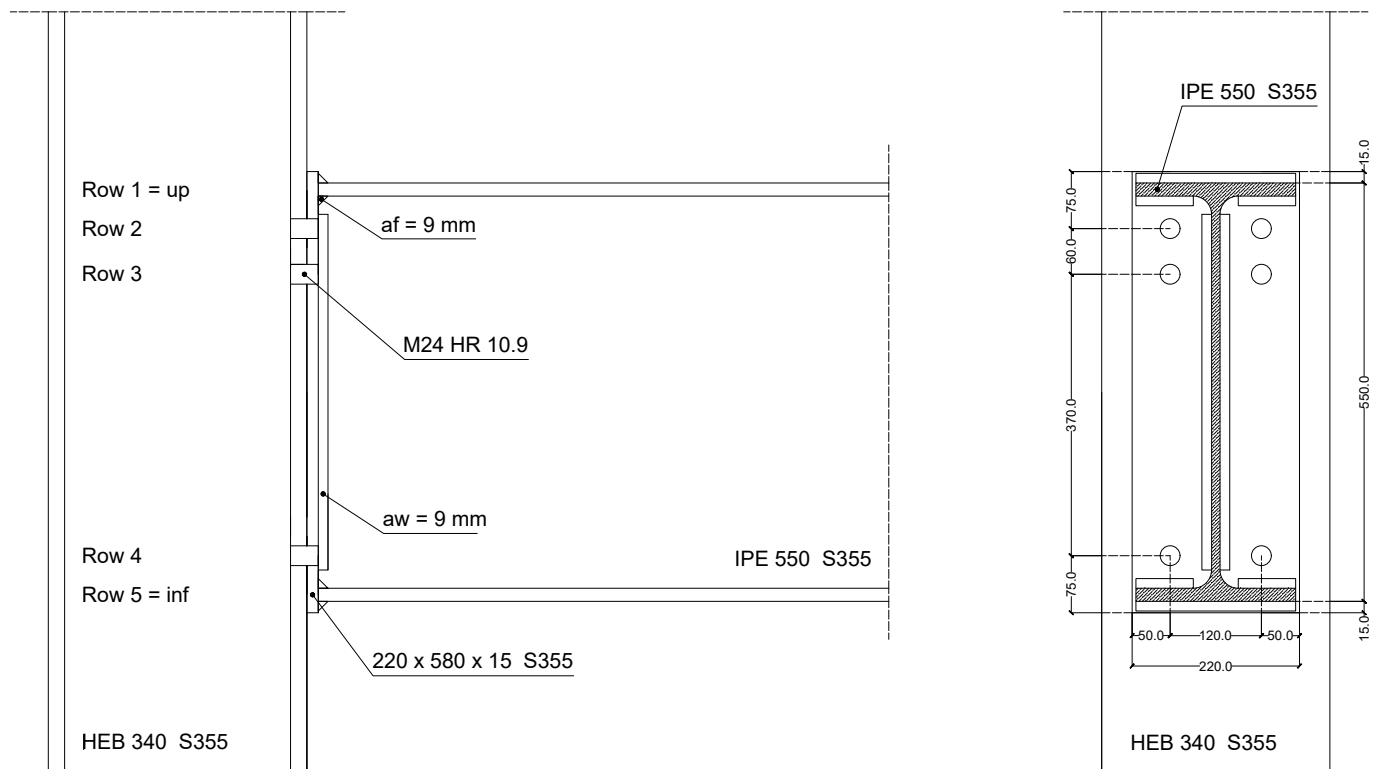


Figure A.7: FAILNOMORE - Joint configuration B1 - Technical drawing

Table A.11: FAILNOMORE - Configuration B1 - Components properties - Individual rows - 3.

Individual rows	Component abbreviation	$F_{Rd}$ [kN]	$k$ [mm]
Compression row n°1/5	CWS	-1,034.655	/
	CWC	<b>-920.936</b>	10.45
	BFC	-1,856.954	$\infty$
Tension row n°2	BT	254.16	9.001
	CFB	508.32	39.72
	CWT	888.05	5.221
	EPB	<b>388.041</b>	6.645
	BWT	1,101.487	$\infty$
Tension row n°3	BT	254.16	9.001
	CFB	508.32	39.72
	CWT	888.05	5.221
	EPB	<b>371.112</b>	5.245
	BWT	944.028	$\infty$
Tension row n°4	BT	254.16	9.001
	CFB	508.32	53.54
	CWT	888.05	7.037
	EPB	<b>388.041</b>	9.739
	BWT	1,101.487	$\infty$

Table A.12: FAILNOMORE - Configuration B1 - Components properties - Group of rows - 3.

Group of rows	Component abbreviation	$F_{Rd}$ [kN]
Group mechanism 23	CFB	904.815
	CWT	1,036.026
	EPB	<b>683.076</b>
	BWT	1,337.917
Group mechanism 34	CFB	1,016.64
	CWT	1,451.022
	EPB	<b>814.41</b>
	BWT	2,559.472
Group mechanism 24	CFB	1,524.96
	CWT	1,490.931
	EPB	<b>1,126.375</b>
	BWT	2,953.362

Table A.13: FAILNOMORE - Configuration B1 - Row/Group resistances - 4.

i	$F_{[i,i],Rd}$ [kN]	$F_{[i-1,i],Rd}$ [kN]	$F_{[i-2,i],Rd}$ [kN]	Critical Component
1 = sup	-920.93	$\infty$	$\infty$	CWC
2	388.04	$\infty$	$\infty$	EPB
3	371.11	683.07	$\infty$	EPB
4	388.04	814.41	1,126.37	EPB
5 = inf	-920.93	$\infty$	$\infty$	CWC

Table A.14: FAILNOMORE - Configuration B1 - Lever arms and  $F_{i,Rd}^+$  &  $F_{i,Rd}^-$  resistance values - 5. & 6.

i	$h_i$ [m]	$F_{i,Rd}^+$ [kN]	$F_{i,Rd}^-$ [kN]
1 = sup	0.266	-920.93	-920.93
2	0.215	388.04	311.96
3	0.155	295.03	371.11
4	-0.215	388.04	388.04
5 = inf	-0.266	-920.93	-920.93

Table A.15: FAILNOMORE - Configuration B1 - Characteristic M-N resistance points - 7.

N°	$M_{Rd}^+$ [kNm]	$N_{Rd}^+$ [kN]	$M_{Rd}^-$ [kNm]	$N_{Rd}^-$ [kN]
1	0.0	-1,841.87	0.0	-1,841.87
2	245.33	-920.93	-245.33	-920.93
3	328.76	-532.89	-328.76	-532.89
4	374.49	-237.86	-271.24	-161.78
5	291.06	150.18	-204.17	150.18
6	45.73	1,071.11	41.16	1,071.11

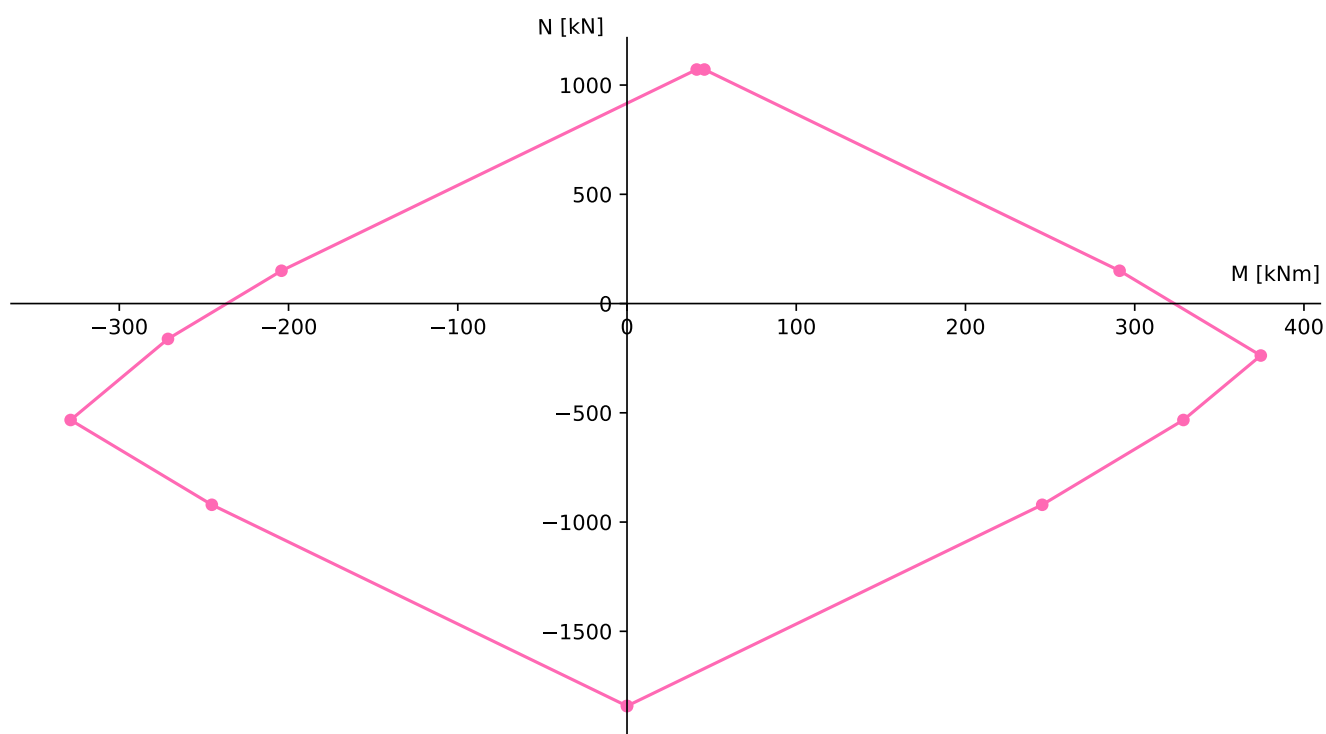


Figure A.8: FAILNOMORE - Joint configuration B1 - Ductile resistance interaction curve - 8.

## A.4 Configuration B3

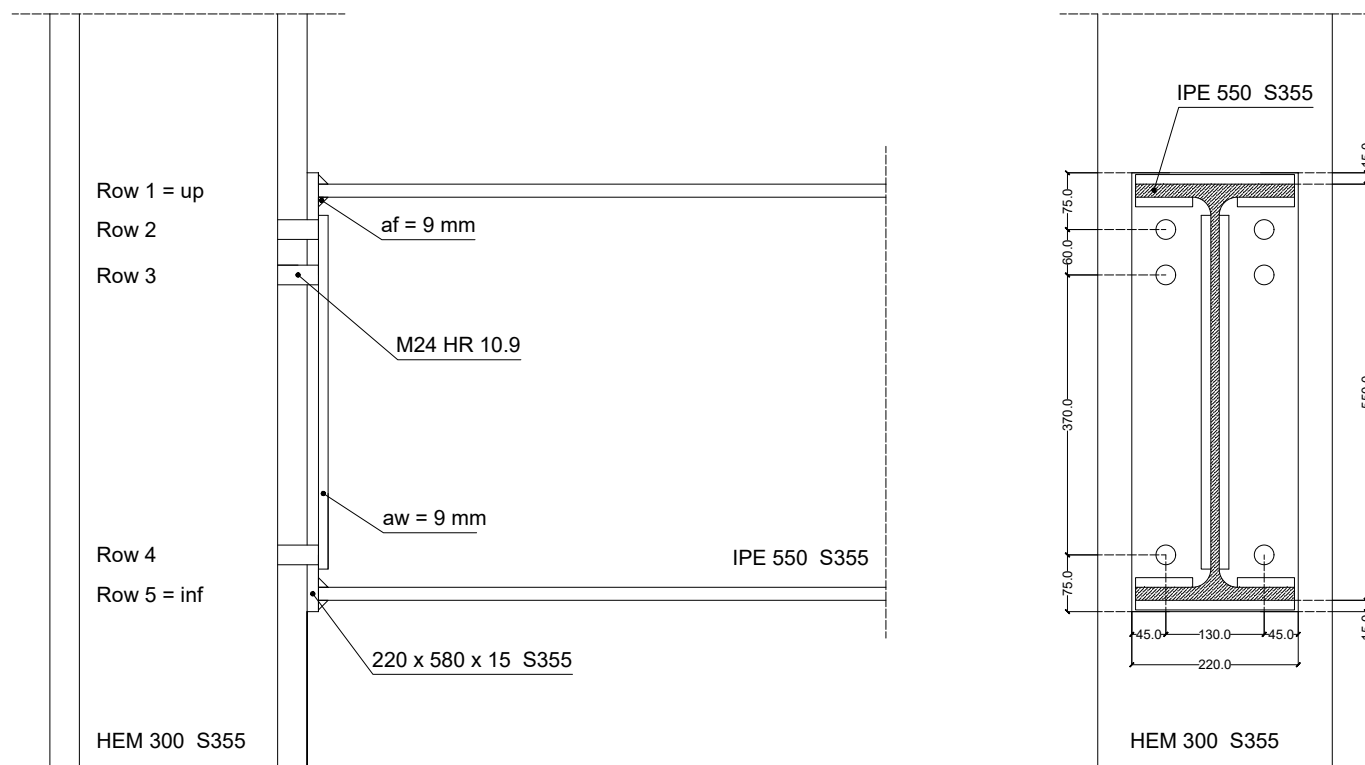


Figure A.9: FAILNOMORE - Joint configurations B3 - Technical drawing

Table A.16: FAILNOMORE - Configuration B3 - Components properties - Individual rows - 3.

Individual rows	Component abbreviation	$F_{Rd}$ [kN]	$k$ [mm]
Compression row n°1/5	CWS	<b>-1,669.95</b>	/
	CWC	-2,023.59	27.56
	BFC	-1,856.954	$\infty$
Tension row n°2	BT	254.16	7.038
	CFB	508.32	227.9
	CWT	1,528.834	10.75
	EPB	<b>368.116</b>	5.048
	BWT	1,166.933	$\infty$
Tension row n°3	BT	254.16	7.038
	CFB	508.32	227.9
	CWT	1,528.834	10.75
	EPB	<b>349.975</b>	3.979
	BWT	998.21	$\infty$
Tension row n°4	BT	254.16	7.038
	CFB	508.32	309.9
	CWT	1,528.834	14.61
	EPB	<b>368.116</b>	7.504
	BWT	1,166.933	$\infty$

Table A.17: FAILNOMORE - Configuration B3 - Components properties - Group of rows - 3.

Group of rows	Component abbreviation	$F_{Rd}$ [kN]
Group mechanism 23	CFB	1,016.64
	CWT	1,766.574
	EPB	<b>636.189</b>
	BWT	1,403.363
Group mechanism 34	CFB	1,016.64
	CWT	2,400.243
	EPB	<b>767.524</b>
	BWT	2,624.918
Group mechanism 24	CFB	1,524.96
	CWT	2,458.402
	EPB	<b>1,053.737</b>
	BWT	3,030.071

Table A.18: FAILNOMORE - Configuration B3 - Row/Group resistances - 4.

i	$F_{[i,i],Rd}$ [kN]	$F_{[i-1,i],Rd}$ [kN]	$F_{[i-2,i],Rd}$ [kN]	Critical Component
1 = sup	-1,669.94	$\infty$	$\infty$	CWS
2	368.11	$\infty$	$\infty$	EPB
3	349.97	636.19	$\infty$	EPB
4	368.11	767.52	1,053.73	EPB
5 = inf	-1,669.94	$\infty$	$\infty$	CWS

Table A.19: FAILNOMORE - Configuration B3 - Lever arms and  $F_{i,Rd}^+$  &  $F_{i,Rd}^-$  resistance values - 5. & 6.

i	$h_i$ [m]	$F_{i,Rd}^+$ [kN]	$F_{i,Rd}^-$ [kN]
1 = sup	0.266	-1,669.94	-1,669.94
2	0.215	368.11	286.21
3	0.155	268.07	349.97
4	-0.215	368.11	368.11
5 = inf	-0.266	-1,669.94	-1,669.94

Table A.20: FAILNOMORE - Configuration B3 - Characteristic M-N resistance points - 7.

N°	$M_{Rd}^+$ [kNm]	$N_{Rd}^+$ [kN]	$M_{Rd}^-$ [kNm]	$N_{Rd}^-$ [kN]
1	0.0	-3,339.89	0.0	-3,339.89
2	444.87	-1,669.94	-444.87	-1,669.94
3	524.01	-1,301.83	-524.01	-1,301.83
4	565.57	-1,033.75	-469.77	-951.85
5	486.42	-665.64	-408.23	-665.64
6	41.55	1,004.3	36.63	1,004.3

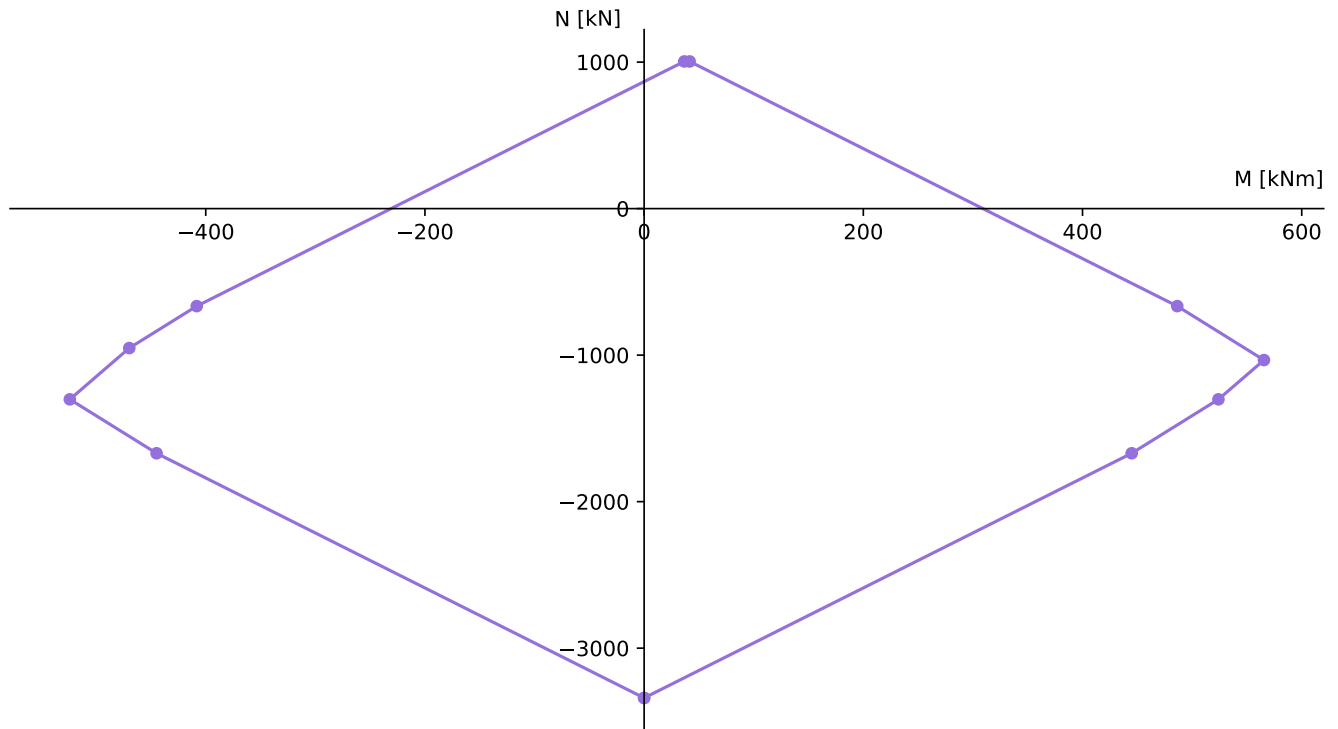


Figure A.10: FAILNOMORE - Joint configuration B3 - Ductile resistance interaction curve - 8.



## A.5 Configuration C2

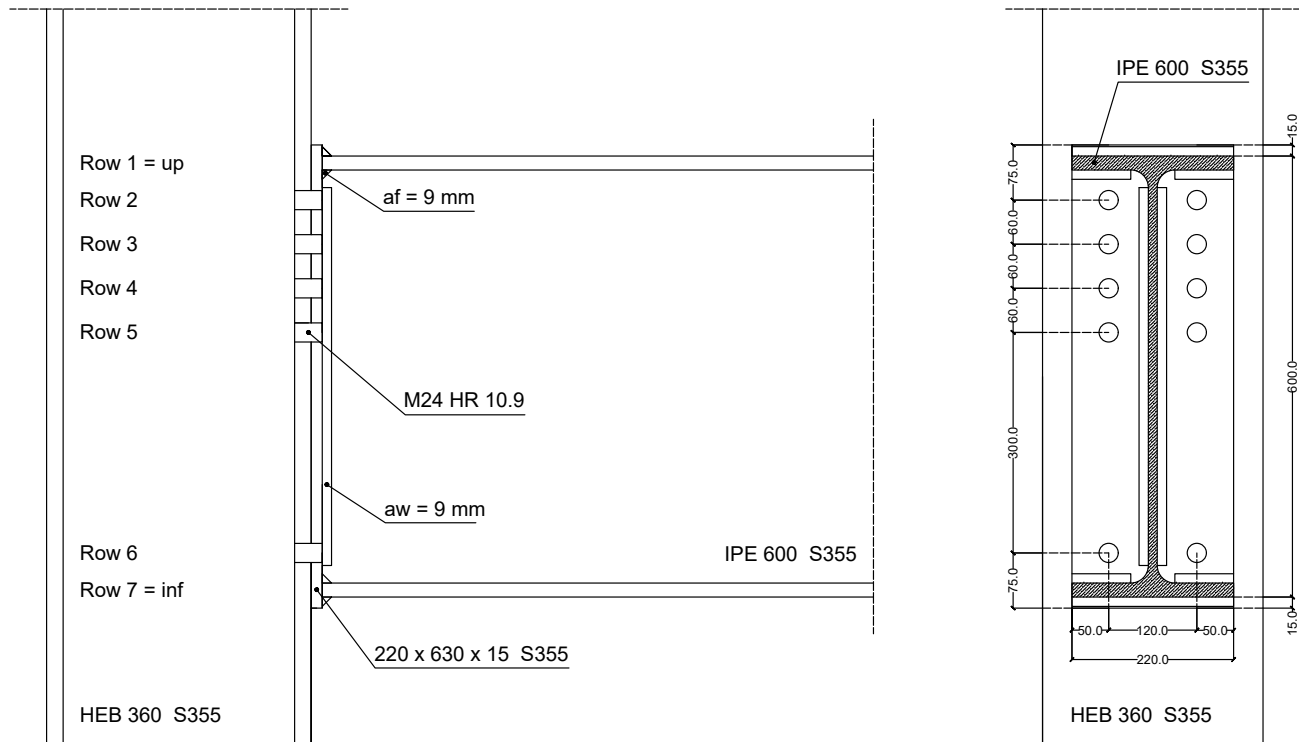


Figure A.11: FAILNOMORE - Joint configuration C2 - Technical drawing

Table A.21: FAILNOMORE - Configuration C2 - Components properties - Individual rows - 3.

Individual rows	Component abbreviation	$F_{Rd}$ [kN]	$k$ [mm]
Compression row n°1/7	CWS	-1,117.85	/
	CWC	<b>-981.628</b>	10.37
	BFC	-2,145.886	$\infty$
Tension row n°2	BT	254.16	8.86
	CFB	508.32	46.44
	CWT	930.675	5.047
	EPB	<b>390.517</b>	6.932
	BWT	1,196.956	$\infty$
Tension row n°3/4	BT	254.16	8.86
	CFB	508.32	18.51
	CWT	930.675	2.011
	EPB	<b>372.125</b>	2.166
	BWT	1,012.903	$\infty$
Tension row n°5	BT	254.16	8.86
	CFB	508.32	46.44
	CWT	930.675	5.047
	EPB	<b>372.125</b>	5.376
	BWT	1,012.903	$\infty$
Tension row n°6	BT	254.16	8.86
	CFB	508.32	62.32
	CWT	930.675	6.772
	EPB	<b>390.517</b>	9.94
	BWT	1,196.956	$\infty$

Table A.22: FAILNOMORE - Configuration C2 - Components properties - Group of rows - 3.

Group of rows	Component abbreviation	$F_{Rd}$ [kN]
Group mechanism 23	CFB	938.833
	CWT	1,090.414
	EPB	<b>686.968</b>
	BWT	1,452.556
Group mechanism 34	CFB	938.833
	CWT	1,090.414
	EPB	<b>668.575</b>
	BWT	1,268.503
Group mechanism 24	CFB	1,295.767
	CWT	1,221.368
	EPB	<b>903.536</b>
	BWT	1,708.156
Group mechanism 45	CFB	938.833
	CWT	1,090.414
	EPB	<b>668.575</b>
	BWT	1,268.503
Group mechanism 35	CFB	1,295.767
	CWT	1,221.368
	EPB	<b>806.18</b>
	BWT	1,524.103
Group mechanism 25	CFB	1,652.7
	CWT	1,327.704
	EPB	<b>1,038.736</b>
	BWT	1,963.756
Group mechanism 56	CFB	1,016.64
	CWT	1,483.573
	EPB	<b>789.134</b>
	BWT	2,474.956
Group mechanism 46	CFB	1,524.96
	CWT	1,540.389
	EPB	<b>1,085.584</b>
	BWT	2,730.556
Group mechanism 36	CFB	1,950.834
	CWT	1,586.924
	EPB	<b>1,382.034</b>
	BWT	2,986.156
Group mechanism 26	CFB	2,307.767
	CWT	<b>1,625.303</b>
	EPB	1,696.876
	BWT	3,425.809

Table A.23: FAILNOMORE - Configuration C2 - Row/Group resistances - 4.

i	$F_{[i,i],Rd}$ [kN]	$F_{[i-1,i],Rd}$ [kN]	$F_{[i-2,i],Rd}$ [kN]	$F_{[i-3,i],Rd}$ [kN]	$F_{[i-4,i],Rd}$ [kN]	Crit. Comp.
1 = sup	-981.62	$\infty$	$\infty$	$\infty$	$\infty$	CWC
2	390.51	$\infty$	$\infty$	$\infty$	$\infty$	EPB
3	372.12	686.96	$\infty$	$\infty$	$\infty$	EPB
4	372.12	668.57	903.53	$\infty$	$\infty$	EPB
5	372.12	668.57	806.18	1,038.73	$\infty$	EPB
6	390.51	789.13	1,085.58	1,382.03	1,625.3	EPB & CWT
7 = inf	-981.62	$\infty$	$\infty$	$\infty$	$\infty$	CWC

Table A.24: FAILNOMORE - Configuration C2 - Lever arms and  $F_{i,Rd}^+$  &  $F_{i,Rd}^-$  resistance values - 5. & 6.

i	$h_i$ [m]	$F_{i,Rd}^+$ [kN]	$F_{i,Rd}^-$ [kN]
1 = sup	0.29	-981.62	-981.62
2	0.24	390.51	232.55
3	0.18	296.45	137.6
4	0.12	216.56	296.45
5	0.06	135.2	372.12
6	-0.24	390.51	390.51
7 = inf	-0.29	-981.62	-981.62

Table A.25: FAILNOMORE - Configuration C2 - Characteristic M-N resistance points - 7.

N°	$M_{Rd}^+$ [kNm]	$N_{Rd}^+$ [kN]	$M_{Rd}^-$ [kNm]	$N_{Rd}^-$ [kN]
1	0.0	-1,963.25	0.0	-1,963.25
2	285.16	-981.62	-285.16	-981.62
3	378.88	-591.11	-378.88	-591.11
4	432.24	-294.66	-356.56	-218.98
5	458.23	-78.09	-320.98	77.46
6	466.34	57.1	-296.21	215.07
7	372.62	447.62	-240.4	447.62
8	87.46	1,429.25	44.76	1,429.25

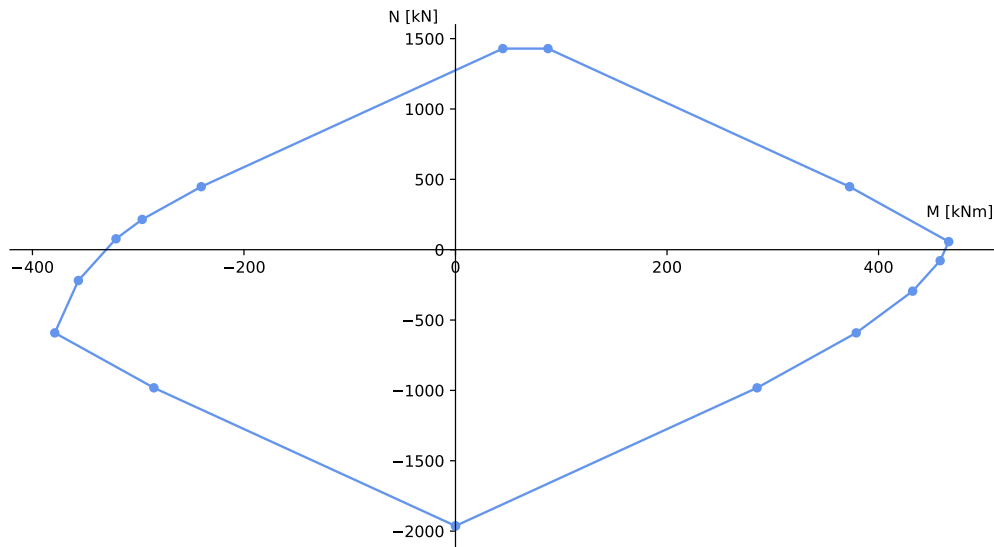


Figure A.12: FAILNOMORE - Joint configuration C2 - Ductile resistance interaction curve - 8.

## A.6 Configuration C3

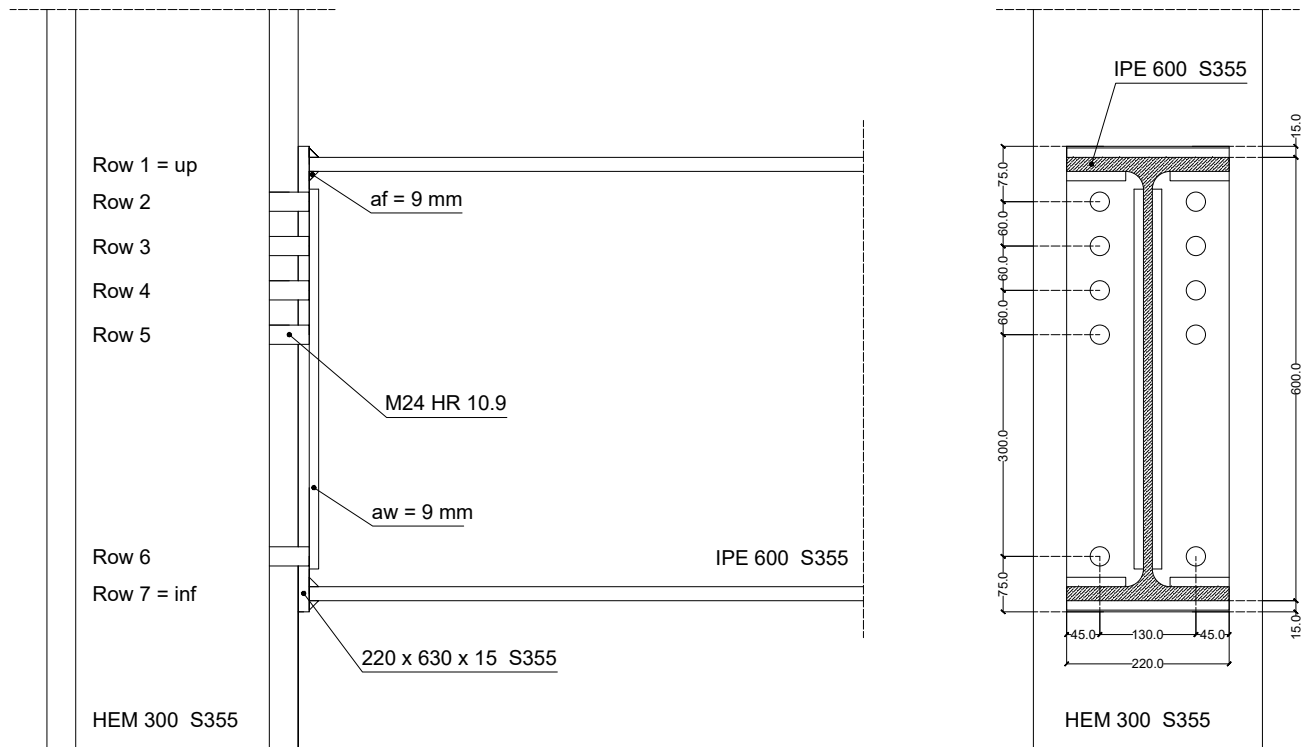


Figure A.13: FAILNOMORE - Joint configurations C3 - Technical drawing

Table A.26: FAILNOMORE - Configuration C3 - Components properties - Individual rows - 3.

Individual rows	Component abbreviation	$F_{Rd}$ [kN]	$k$ [mm]
Compression row n°1/7	CWS	<b>-1,669.947</b>	/
	CWC	-2,028.1	27.68
	BFC	-2,145.886	$\infty$
Tension row n°2	BT	254.16	7.038
	CFB	508.32	227.9
	CWT	1,528.834	10.75
	EPB	<b>370.481</b>	5.252
	BWT	1,267.554	$\infty$
Tension row n°3/4	BT	254.16	7.038
	CFB	508.32	89.95
	CWT	1,528.834	4.24
	EPB	<b>350.888</b>	1.567
	BWT	1,071.478	$\infty$
Tension row n°5	BT	254.16	7.038
	CFB	508.32	227.9
	CWT	1,528.834	10.75
	EPB	<b>350.888</b>	4.067
	BWT	1,071.478	$\infty$
Tension row n°6	BT	254.16	7.038
	CFB	508.32	309.9
	CWT	1,528.834	14.61
	EPB	<b>370.481</b>	7.752
	BWT	1,267.554	$\infty$

Table A.27: FAILNOMORE - Configuration C3 - Components properties - Group of rows - 3.

Group of rows	Component abbreviation	$F_{Rd}$ [kN]
Group mechanism 23	CFB	1,016.64
	CWT	1,766.574
	EPB	<b>639.84</b>
	BWT	1,523.154
Group mechanism 34	CFB	1,016.64
	CWT	1,766.574
	EPB	<b>620.247</b>
	BWT	1,327.078
Group mechanism 24	CFB	1,524.96
	CWT	1,955.191
	EPB	<b>838.356</b>
	BWT	1,778.754
Group mechanism 45	CFB	1,016.64
	CWT	1,766.574
	EPB	<b>620.247</b>
	BWT	1,327.078
Group mechanism 35	CFB	1,524.96
	CWT	1,955.191
	EPB	<b>745.942</b>
	BWT	1,582.678
Group mechanism 25	CFB	2,033.28
	CWT	2,103.968
	EPB	<b>958.824</b>
	BWT	2,034.354
Group mechanism 56	CFB	1,016.64
	CWT	2,314.702
	EPB	<b>742.007</b>
	BWT	2,545.554
Group mechanism 46	CFB	1,524.96
	CWT	2,389.306
	EPB	<b>1,011.366</b>
	BWT	2,801.154
Group mechanism 36	CFB	2,033.28
	CWT	2,449.524
	EPB	<b>1,280.725</b>
	BWT	3,056.754
Group mechanism 26	CFB	2,541.6
	CWT	2,498.588
	EPB	<b>1,569.678</b>
	BWT	3,508.431

Table A.28: FAILNOMORE - Configuration C3 - Row/Group resistances - 4.

i	$F_{[i,i],Rd}$ [kN]	$F_{[i-1,i],Rd}$ [kN]	$F_{[i-2,i],Rd}$ [kN]	$F_{[i-3,i],Rd}$ [kN]	$F_{[i-4,i],Rd}$ [kN]	Crit. Comp.
1 = sup	-1,669.94	$\infty$	$\infty$	$\infty$	$\infty$	CWS
2	370.48	$\infty$	$\infty$	$\infty$	$\infty$	EPB
3	350.88	639.84	$\infty$	$\infty$	$\infty$	EPB
4	350.88	620.24	838.35	$\infty$	$\infty$	EPB
5	350.88	620.24	745.94	958.82	$\infty$	EPB
6	370.48	742	1,011.36	1,280.72	1,569.67	EPB
7 = inf	-1,669.94	$\infty$	$\infty$	$\infty$	$\infty$	CWS

Table A.29: FAILNOMORE - Configuration C3 - Lever arms and  $F_{i,Rd}^+$  &  $F_{i,Rd}^-$  resistance values - 5. & 6.

i	$h_i$ [m]	$F_{i,Rd}^+$ [kN]	$F_{i,Rd}^-$ [kN]
1 = sup	0.29	-1,669.94	-1,669.94
2	0.24	370.48	212.88
3	0.18	269.36	125.69
4	0.12	198.51	269.36
5	0.06	120.46	350.88
6	-0.24	370.48	370.48
7 = inf	-0.29	-1,669.94	-1,669.94

Table A.30: FAILNOMORE - Configuration C3 - Characteristic M-N resistance points - 7.

N°	$M_{Rd}^+$ [kNm]	$N_{Rd}^+$ [kN]	$M_{Rd}^-$ [kNm]	$N_{Rd}^-$ [kN]
1	0.0	-3,339.89	0.0	-3,339.89
2	485.12	-1,669.94	-485.12	-1,669.94
3	574.03	-1,299.46	-574.03	-1,299.46
4	622.52	-1,030.1	-552.98	-948.57
5	646.34	-831.59	-520.65	-679.21
6	653.57	-711.12	-498.03	-553.52
7	564.65	-340.64	-446.94	-340.64
8	79.53	1,329.3	38.17	1,329.3

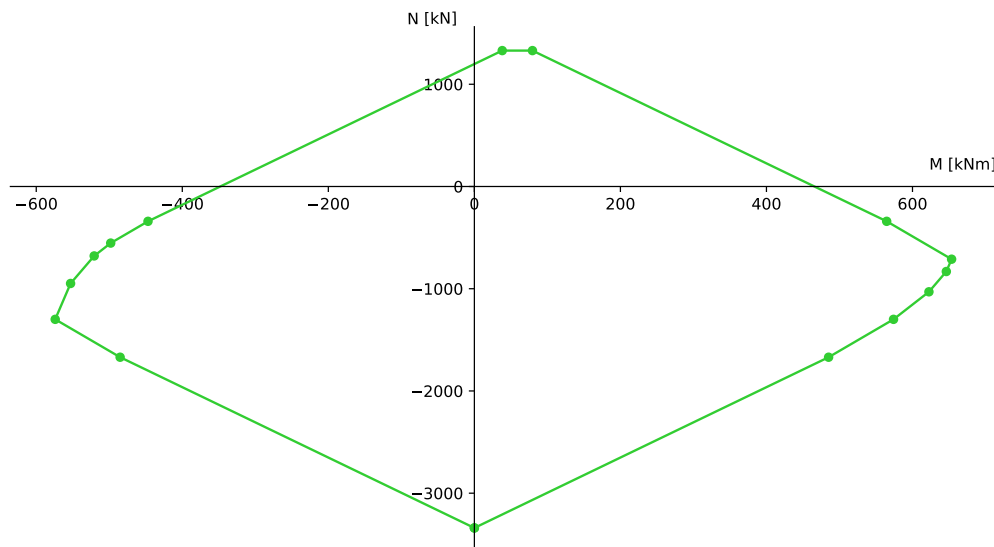


Figure A.14: FAILNOMORE - Joint configuration C3 - Ductile resistance interaction curve - 8.

# Appendix B

## Coimbra joint configurations

### B.1 Flush end-plate configuration

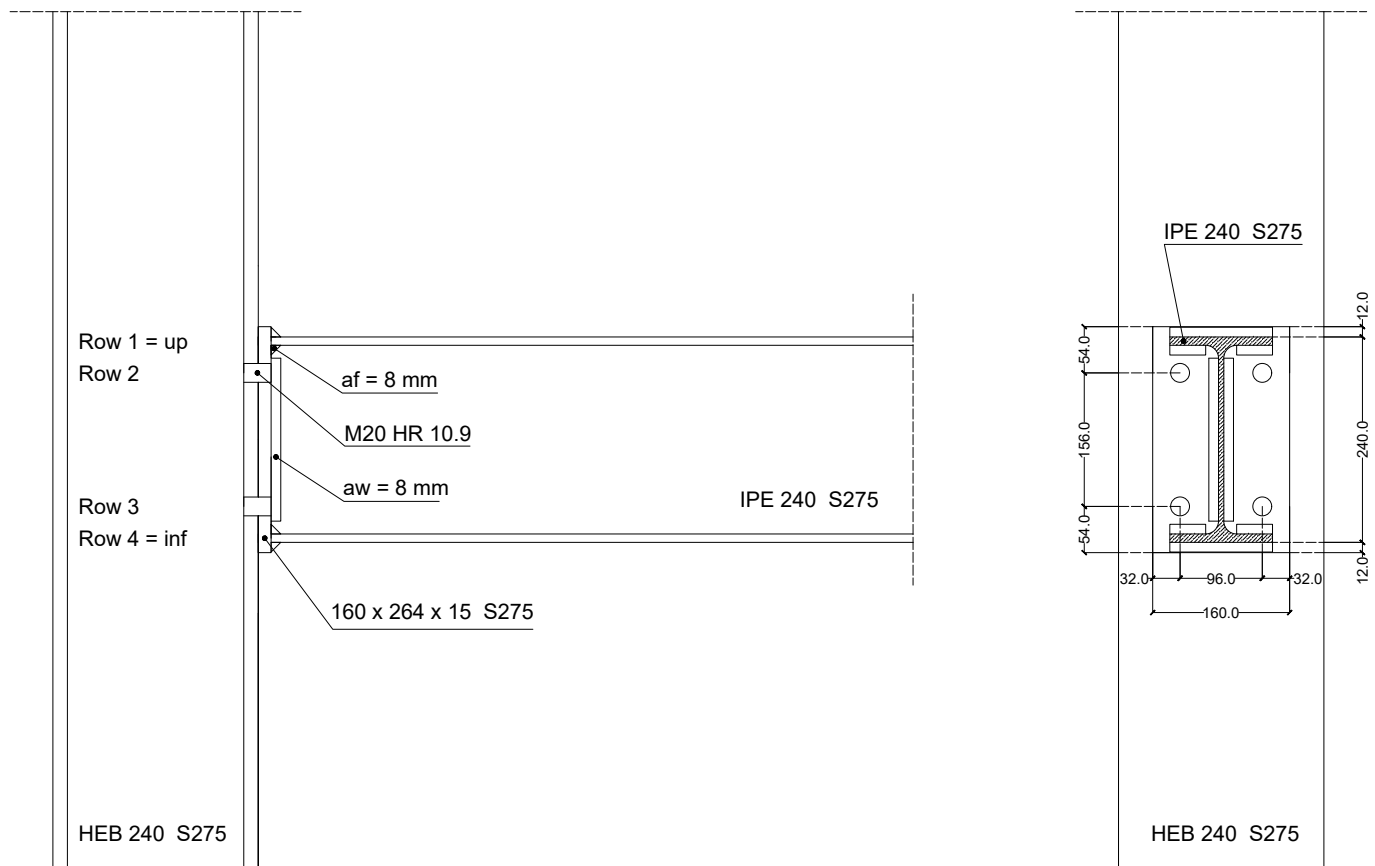


Figure B.1: Coimbra - Flush end-plate joint configuration - Technical drawing

***Theoretical mechanical properties***

Table B.1: Coimbra - Flush end-plate configuration - Components properties - Individual rows - 3.

Individual rows	Component abbreviation	$F_{Rd}$ [kN]	$k$ [mm]
Compression row n°1/4	CWS	-474.837	/
	CWC	-507.089	10.16
	BFC	<b>-437.945</b>	$\infty$
Tension row n°2/3	BT	176.4	7.649
	CFB	326.984	40.47
	CWT	445.374	7.026
	EPB	<b>264.442</b>	13.24
	BWT	366.629	$\infty$

Table B.2: Coimbra - Flush end-plate configuration - Components properties - Group of rows - 3.

Group of rows	Component abbreviation	$F_{Rd}$ [kN]
Group mechanism 23	CFB	627.476
	CWT	616.478
	EPB	<b>516.392</b>
	BWT	686.548

Table B.3: Coimbra - Flush end-plate configuration - Row/Group resistances - 4.

i	$F_{[i,i],Rd}$ [kN]	$F_{[i-1,i],Rd}$ [kN]	Critical Component
1 = sup	-437.94	$\infty$	BFC
2	264.44	$\infty$	EPB
3	264.44	516.39	EPB
4 = inf	-437.94	$\infty$	BFC

Table B.4: Coimbra - Flush end-plate config. - Lever arms and  $F_{i,Rd}^+$  &  $F_{i,Rd}^-$  resistance values - 5. & 6.

i	$h_i$ [m]	$F_{i,Rd}^+$ [kN]	$F_{i,Rd}^-$ [kN]
1 = sup	0.115	-437.94	-437.94
2	0.078	264.44	251.95
3	-0.078	251.95	264.44
4 = inf	-0.115	-437.94	-437.94

Table B.5: Coimbra - Flush end-plate configuration - Theoretical - Characteristic M-N resistance points - 7.

N°	$M_{Rd}^+$ [kNm]	$N_{Rd}^+$ [kN]	$M_{Rd}^-$ [kNm]	$N_{Rd}^-$ [kN]
1	0.0	-875.89	0.0	-875.89
2	50.4	-437.94	-50.4	-437.94
3	71.03	-173.5	-71.03	-173.5
4	51.38	78.44	-51.38	78.44
5	0.97	516.39	-0.97	516.39



**Minimum mechanical properties**

Table B.6: Coimbra - Flush end-plate configuration - Minimum - Characteristic M-N resistance points - 7.

N°	$M_{Rd}^+$ [kNm]	$N_{Rd}^+$ [kN]	$M_{Rd}^-$ [kNm]	$N_{Rd}^-$ [kN]
1	0.0	-994.15	0.0	-994.15
2	57.21	-497.08	-57.21	-497.08
3	83.03	-166.06	-83.03	-166.06
4	58.48	148.75	-58.48	148.75
5	1.26	645.82	-1.26	645.82

**Mean mechanical properties**

Table B.7: Coimbra - Flush end-plate configuration - Mean - Characteristic M-N resistance points - 7.

N°	$M_{Rd}^+$ [kNm]	$N_{Rd}^+$ [kN]	$M_{Rd}^-$ [kNm]	$N_{Rd}^-$ [kN]
1	0.0	-1,083.36	0.0	-1,083.36
2	62.35	-541.68	-62.35	-541.68
3	89.15	-198.09	-89.15	-198.09
4	63.66	128.73	-63.66	128.73
5	1.31	670.41	-1.31	670.41

**Maximum mechanical properties**

Table B.8: Coimbra - Flush end-plate configuration - Maximum - Characteristic M-N resistance points - 7.

N°	$M_{Rd}^+$ [kNm]	$N_{Rd}^+$ [kN]	$M_{Rd}^-$ [kNm]	$N_{Rd}^-$ [kN]
1	0.0	-1,165.19	0.0	-1,165.19
2	67.06	-582.59	-67.06	-582.59
3	94.96	-224.86	-94.96	-224.86
4	68.41	115.58	-68.41	115.58
5	1.35	698.17	-1.35	698.17

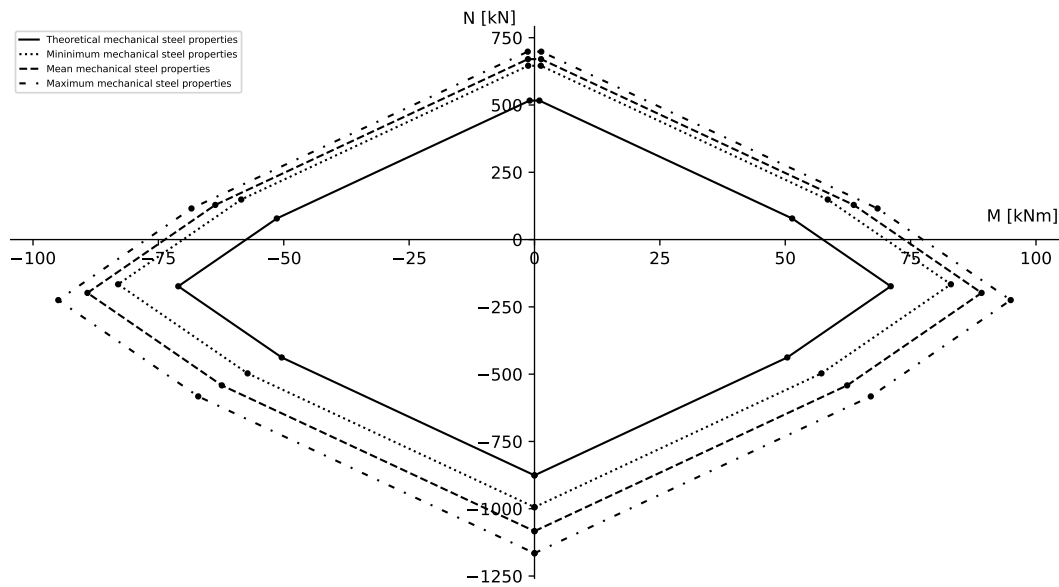


Figure B.2: Coimbra - Flush end-plate configuration - Four ductile resistance interaction curves - 8.

## B.2 Extended end-plate configuration

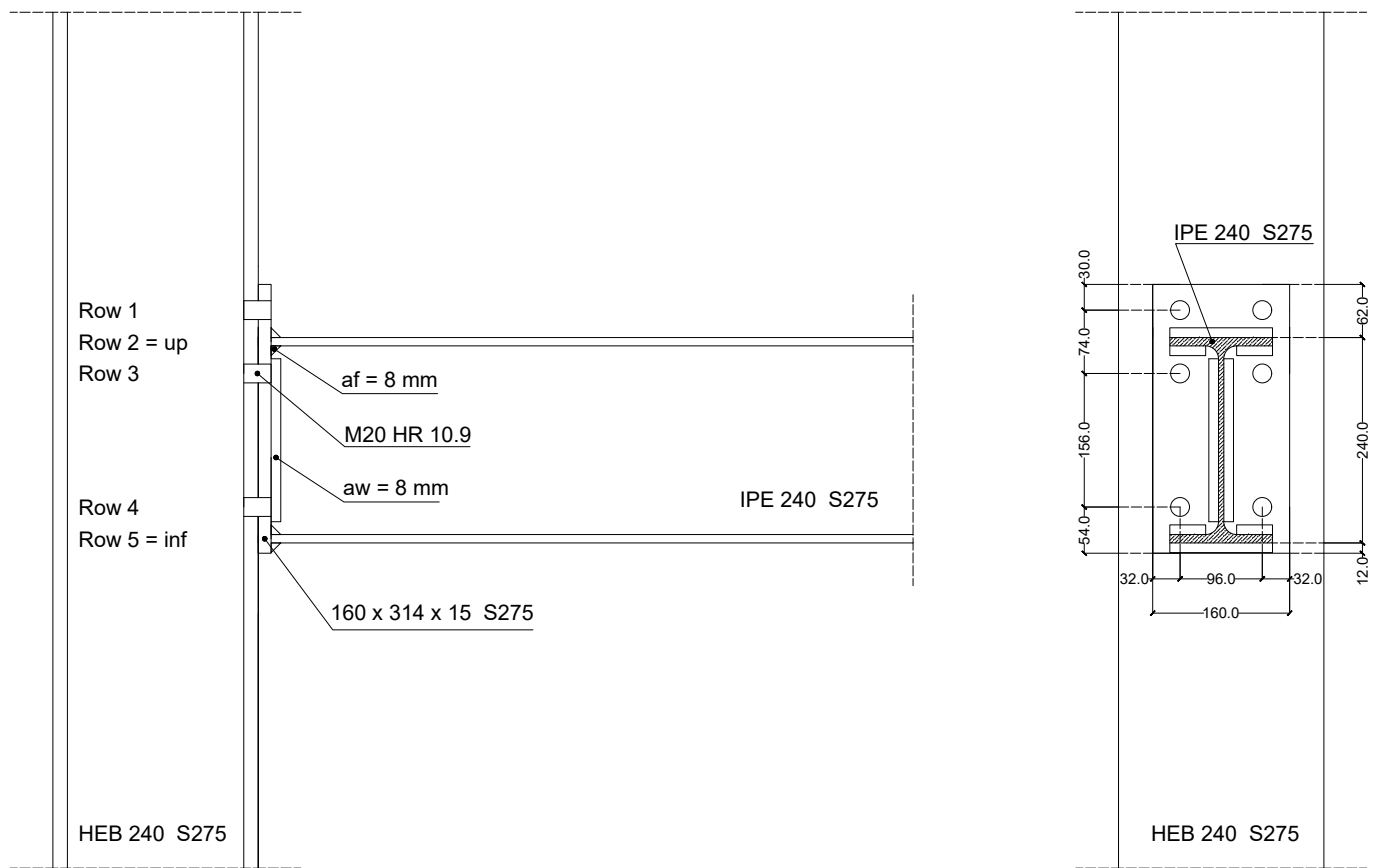


Figure B.3: Coimbra - Extended end-plate joint configuration - Technical drawing

### Theoretical mechanical properties

Table B.9: Coimbra - Extended end-plate configuration - Components properties - Individual rows - 3.

Individual rows	Component abbreviation	$F_{Rd}$ [kN]	$k$ [mm]
Tension row n°1	BT	176.4	7.095
	CFB	326.984	33.04
	CWT	445.374	5.737
	EPB	<b>243.932</b>	20.11
Compression row n°2	CWS	-474.837	/
	CWC	-524.723	10.77
	BFC	<b>-437.945</b>	$\infty$
Tension row n°3/4	BT	176.4	7.095
	CFB	326.984	28.27
	CWT	445.374	4.909
	EPB	<b>264.442</b>	13.24
	BWT	366.629	$\infty$
Compression row n°5	CWS	-474.837	/
	CWC	-507.089	10.16
	BFC	<b>-437.945</b>	$\infty$

Table B.10: Coimbra - Extended end-plate configuration - Components properties - Group of rows - 3.

Group of rows	Component abbreviation	$F_{Rd}$ [kN]
Group mechanism 13	CFB	571.488
	CWT	<b>543.378</b>
Group mechanism 34	CFB	627.476
	CWT	616.478
	EPB	<b>516.392</b>
	BWT	686.548
Group mechanism 14	CFB	871.98
	CWT	<b>660.889</b>

Table B.11: Coimbra - Extended end-plate configuration - Row/Group resistances - 4.

i	$F_{[i,i],Rd}$ [kN]	$F_{[i-1,i],Rd}$ [kN]	$F_{[i-2,i],Rd}$ [kN]	$F_{[i-3,i],Rd}$ [kN]	Critical Component(s)
1	243.93	$\infty$	$\infty$	$\infty$	EPB
2 = sup	-437.94	$\infty$	$\infty$	$\infty$	BFC
3	264.44	$\infty$	543.38	$\infty$	EPB & CWT
4	264.44	516.39	$\infty$	660.89	EPB & CWT
5 = inf	-437.94	$\infty$	$\infty$	$\infty$	BFC

Table B.12: Coimbra - Extended end-plate config. - Lever arms and  $F_{i,Rd}^+$  &  $F_{i,Rd}^-$  resistance values - 5. & 6.

i	$h_i$ [m]	$F_{i,Rd}^+$ [kN]	$F_{i,Rd}^-$ [kN]
1	0.152	243.93	144.49
2 = sup	0.115	-437.94	-437.94
3	0.078	264.44	251.95
4	-0.078	152.51	264.44
5 = inf	-0.115	-437.94	-437.94

Table B.13: Coimbra - Extended end-plate config. - Theoretical - Characteristic M-N resistance points - 7.

N°	$M_{Rd}^+$ [kNm]	$N_{Rd}^+$ [kN]	$M_{Rd}^-$ [kNm]	$N_{Rd}^-$ [kN]
1	0.0	-875.89	0.0	-875.89
2	37.07	-631.96	-50.4	-437.94
3	87.48	-194.01	-71.03	-173.5
4	108.11	70.43	-51.38	78.44
5	96.21	222.94	-0.97	516.39
6	45.8	660.89	20.99	660.89

**Minimum mechanical properties**

Table B.14: Coimbra - Extended end-plate config. - Minimum - Characteristic M-N resistance points - 7.

N°	$M_{Rd}^+$ [kNm]	$N_{Rd}^+$ [kN]	$M_{Rd}^-$ [kNm]	$N_{Rd}^-$ [kN]
1	0.0	-994.15	0.0	-994.15
2	45.94	-691.88	-57.21	-497.07
3	103.16	-194.8	-83.03	-166.06
4	128.98	136.21	-58.48	148.75
5	114.61	320.41	-1.26	645.82
6	57.39	817.48	24.83	817.48

**Mean mechanical properties**

Table B.15: Coimbra - Extended end-plate config. - Mean - Characteristic M-N resistance points - 7.

N°	$M_{Rd}^+$ [kNm]	$N_{Rd}^+$ [kN]	$M_{Rd}^-$ [kNm]	$N_{Rd}^-$ [kN]
1	0.0	-1,083.36	0.0	-1,083.36
2	47.72	-769.4	-62.35	-541.68
3	110.07	-227.71	-89.15	-198.09
4	136.87	115.88	-63.66	128.73
5	118.42	352.37	-1.31	670.41
6	56.08	894.05	32.68	894.05

**Maximum mechanical properties**

Table B.16: Coimbra - Extended end-plate config. - Maximum - Characteristic M-N resistance points - 7.

N°	$M_{Rd}^+$ [kNm]	$N_{Rd}^+$ [kN]	$M_{Rd}^-$ [kNm]	$N_{Rd}^-$ [kN]
1	0.0	-1,165.19	0.0	-1,165.19
2	49.83	-837.38	-67.06	-582.59
3	116.88	-254.79	-94.96	-224.86
4	144.79	102.95	-68.4	115.58
5	123.39	377.21	-1.35	698.17
6	56.34	959.8	38.42	959.8

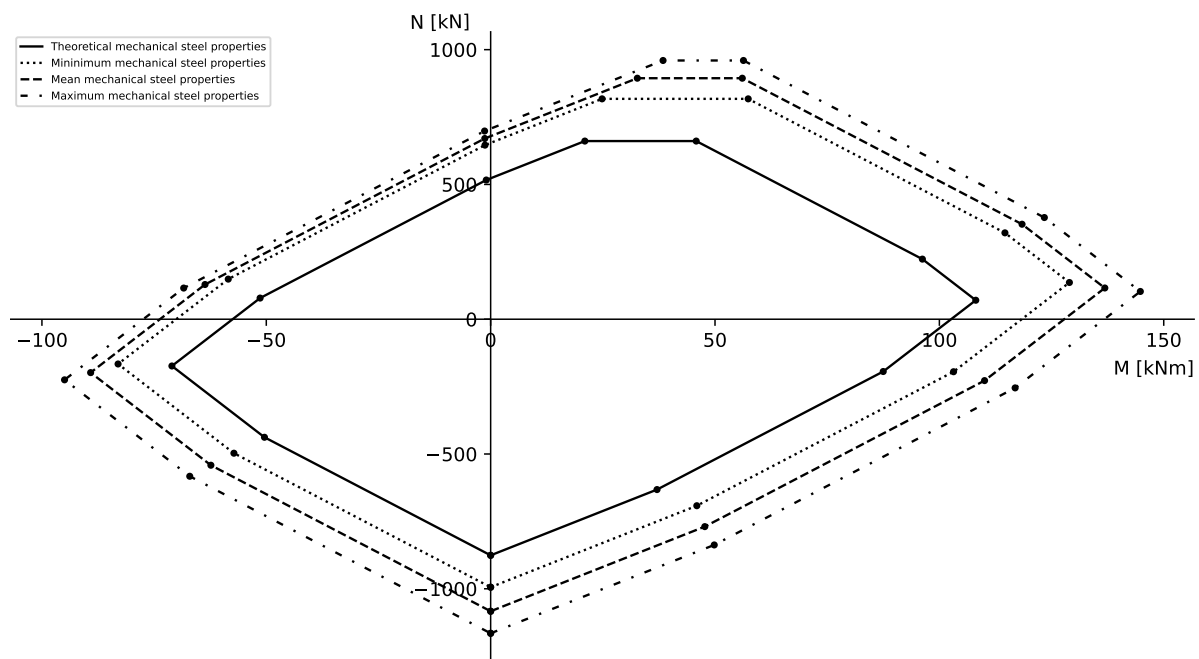


Figure B.4: Coimbra - Extended end-plate configuration - Four ductile resistance interaction curves - 8.

### B.3 Geometrical properties measured in laboratory

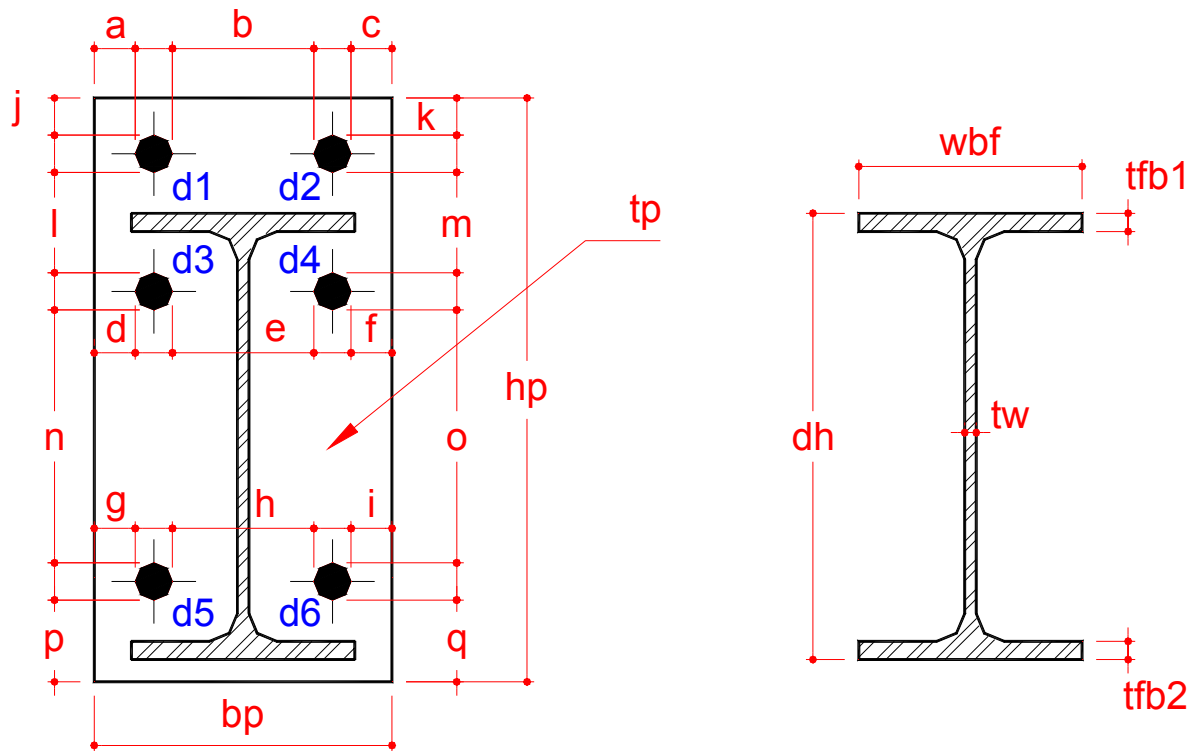


Figure B.5: Coimbra - End-plate and beam dimensions measured in laboratory [15]

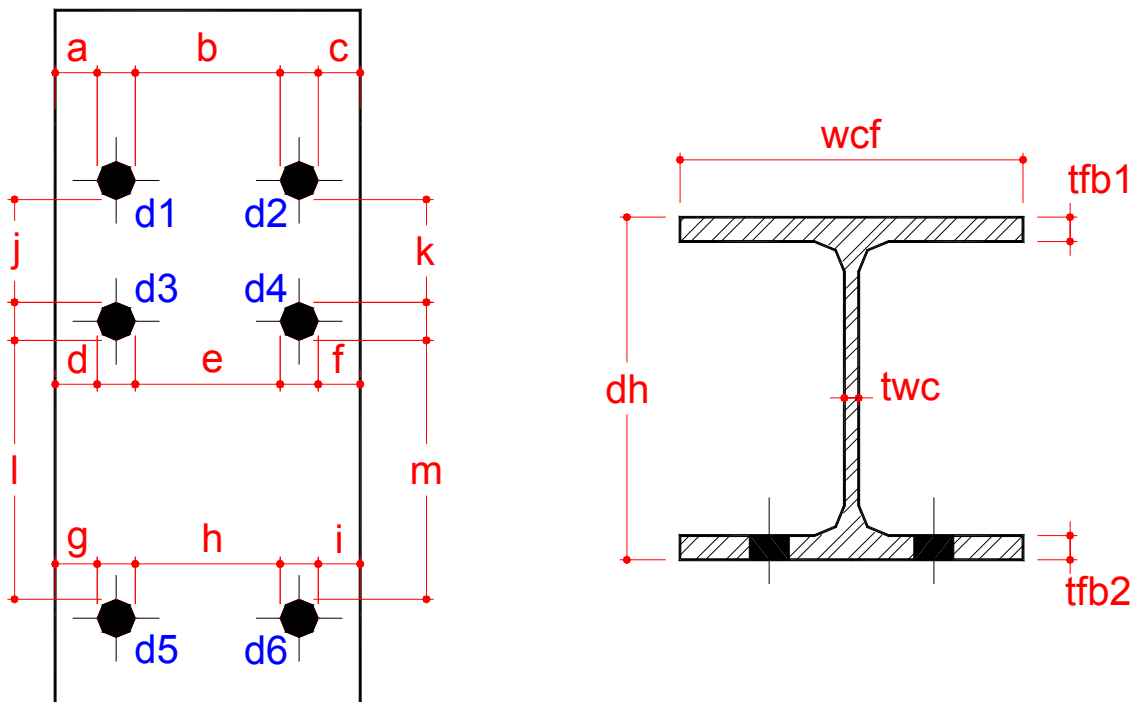


Figure B.6: Coimbra - Column dimensions measured in laboratory [15]

Ensaio	d	e	f	g	h	i	l
<b>nominal</b>	<b>21.00</b>	<b>74.00</b>	<b>21.00</b>	<b>21.00</b>	<b>74.00</b>	<b>21.00</b>	<b>43.00</b>
FE3	19.03	73.87	20.54	18.97	74.25	19.74	41.29
FE4	21.57	72.47	18.61	21.78	73.43	18.65	43.05
FE5	20.50	73.69	20.87	22.70	73.15	20.96	42.89
FE1	21.05	73.60	16.00	22.05	73.60	15.95	44.50
FE6	14.86	74.16	23.15	15.55	74.58	22.67	40.87
FE7	17.80	74.17	20.86	17.84	73.98	20.95	44.13
FE8	23.70	73.84	17.48	22.52	73.85	18.36	43.46
FE9	18.77	73.32	19.85	18.03	73.10	20.34	51.06
Ensaio	m	n	o	p	q	d1	d2
<b>nominal</b>	<b>43.00</b>	<b>134.00</b>	<b>134.00</b>	<b>43.00</b>	<b>43.00</b>	<b>22.00</b>	<b>22.00</b>
FE3	40.52	133.72	134.06	42.95	43.74	21.95	22.03
FE4	42.67	133.81	133.08	43.94	43.45	22.14	22.17
FE5	43.85	133.64	133.72	41.64	42.12	21.81	22.05
FE1	43.70	133.71	133.76	40.70	40.20	22.10	22.15
FE6	40.55	133.74	134.16	43.78	44.85	21.75	21.71
FE7	44.38	133.73	133.80	41.04	40.88	21.87	21.88
FE8	43.61	133.45	134.10	37.14	38.15	21.80	22.01
FE9	51.01	132.71	132.58	40.00	40.12	22.94	22.89
Ensaio	d3	d4	bp	hp	tp	tfb1	tfb2
<b>nominal</b>	<b>22.00</b>	<b>22.00</b>	<b>160.00</b>	<b>264.00</b>	<b>15.00</b>	<b>9.80</b>	<b>9.80</b>
FE3	22.03	22.11	158.01	263.86	15.52	10.18	9.56
FE4	21.65	21.87	157.14	264.22	15.18	9.46	9.75
FE5	21.94	22.25	156.58	262.46	15.24	9.33	9.84
FE1	22.15	22.15	154.90	261.96	15.35	8.91	9.42
FE6	21.72	21.83	155.63	263.46	15.52	9.50	9.49
FE7	21.91	21.94	157.52	263.73	15.55	9.36	9.69
FE8	21.86	21.84	159.49	258.27	15.16	9.65	8.93
FE9	23.06	23.01	158.40	262.57	15.55	10.14	9.31
Ensaio	tw	wbf	dh				
<b>nominal</b>	<b>6.20</b>	<b>120.00</b>	<b>240.00</b>				
FE3	6.90	121.54	241.06				
FE4	6.90	122.08	241.05				
FE5	6.90	120.87	241.23				
FE1	6.90	121.05	242.36				
FE6	6.70	121.56	242.10				
FE7	7.00	121.45	242.77				
FE8	6.90	121.83	242.53				
FE9	7.50	120.83	243.22				

Figure B.7: Coimbra - FE tests - Actual end-plate and beam geometrical properties [15]

Ensaio	d	e	f	g	h	i	l
<b>nominal</b>	<b>61.00</b>	<b>74.00</b>	<b>61.00</b>	<b>61.00</b>	<b>74.00</b>	<b>61.00</b>	<b>134.00</b>
<b>FE3</b>	61.74	73.47	62.00	61.05	73.95	61.86	134.15
<b>FE4</b>	61.55	73.68	61.84	62.04	73.54	62.15	133.96
<b>FE5</b>	61.05	73.66	62.03	60.93	72.61	62.44	134.09
<b>FE1</b>	60.15	73.30	59.95	59.70	72.95	59.80	133.83
<b>FE6</b>	61.06	73.74	60.34	61.20	73.76	60.45	133.69
<b>FE7</b>	61.57	73.72	61.77	61.18	74.07	61.50	133.43
<b>FE8</b>	60.89	73.76	61.81	60.60	73.88	62.56	133.74
<b>FE9</b>	62.05	73.42	61.20	61.59	74.26	61.14	134.44
Ensaio	m	d1	d2	d3	d4	tfb1	tfb2
<b>nominal</b>	<b>134.00</b>	<b>22.00</b>	<b>22.00</b>	<b>22.00</b>	<b>22.00</b>	<b>17.00</b>	<b>17.00</b>
<b>FE3</b>	133.83	21.95	22.12	21.52	22.20	16.57	16.48
<b>FE4</b>	133.74	22.66	22.58	22.54	22.52	16.41	16.33
<b>FE5</b>	134.15	22.03	22.15	21.91	21.84	16.57	16.86
<b>FE1</b>	133.69	22.60	22.40	22.60	22.15	15.44	15.10
<b>FE6</b>	133.43	22.14	21.95	22.06	21.87	15.52	15.35
<b>FE7</b>	133.17	22.06	22.12	22.24	21.96	16.38	16.49
<b>FE8</b>	133.75	21.81	21.52	21.78	21.95	16.56	16.58
<b>FE9</b>	134.61	22.16	22.20	22.03	22.06	15.88	15.94
Ensaio	tw	wcf	dh				
<b>nominal</b>	<b>10.00</b>	<b>240.00</b>	<b>240.00</b>				
<b>FE3</b>	10.46	241.37	240.95				
<b>FE4</b>	10.82	239.68	240.32				
<b>FE5</b>	10.12	240.30	240.52				
<b>FE1</b>	10.25	241.05	241.67				
<b>FE6</b>	10.33	240.71	240.39				
<b>FE7</b>	10.12	241.40	240.33				
<b>FE8</b>	10.06	240.61	240.10				
<b>FE9</b>	10.24	241.28	239.72				

Figure B.8: Coimbra - FE tests - Actual column geometrical properties [15]

Ensaio	a	b	c	d	e	f	g
nominal	21.00	74.00	21.00	21.00	74.00	21.00	21.00
EE1	18.53	72.55	20.32	18.27	72.53	20.44	17.76
EE5	21.24	72.27	18.15	21.35	72.38	18.34	21.11
EE3	19.47	73.71	19.52	19.93	73.09	19.27	20.37
EE4	22.59	73.34	17.12	22.26	73.32	16.24	22.58
EE2	18.79	74.55	19.68	19.46	73.48	19.49	19.78
EE7	20.37	73.63	17.21	20.52	73.61	17.89	20.00
EE6	18.27	73.21	20.81	18.01	74.28	20.33	17.22
Ensaio	h	i	j	k	l	m	n
nominal	74.00	21.00	21.00	21.00	52.00	52.00	134.00
EE1	72.43	20.76	22.67	22.54	50.02	50.40	132.08
EE5	73.35	19.25	22.12	22.51	50.37	50.43	132.27
EE3	72.70	19.15	22.12	22.33	51.22	51.53	132.80
EE4	73.58	16.35	22.61	21.93	51.14	51.04	133.23
EE2	73.54	19.12	22.08	21.77	51.37	51.18	132.78
EE7	73.58	18.56	21.18	22.64	51.02	51.30	133.20
EE6	73.51	20.39	21.99	22.78	51.07	51.12	132.55
Ensaio	o	p	q	d1	d2	d3	d4
nominal	134.00	43.00	43.00	22.00	22.00	22.00	22.00
EE1	132.10	40.08	40.08	23.48	23.46	23.57	23.64
EE5	132.36	40.54	40.36	23.59	23.57	23.59	23.74
EE3	132.33	39.74	40.41	22.76	22.62	22.70	22.69
EE4	132.76	40.23	40.29	22.66	22.58	22.54	22.52
EE2	132.73	40.11	40.05	22.06	22.65	22.44	22.57
EE7	133.15	40.76	40.21	22.78	22.85	22.84	22.81
EE6	133.33	39.85	39.29	22.80	22.21	22.69	21.96
Ensaio	d5	d6	bp	hp	tp	tfb1	tfb2
nominal	22.00	22.00	160.00	316.00	15.00	9.80	9.80
EE1	23.67	23.71	158.34	315.93	15.57	9.19	9.45
EE5	22.80	23.01	159.17	315.98	15.51	9.60	9.48
EE3	22.78	22.82	157.24	314.73	15.48	9.11	9.29
EE4	22.91	22.89	154.54	314.01	15.77	9.95	9.41
EE2	22.69	22.77	158.58	313.72	15.65	10.21	9.45
EE7	22.85	22.76	158.88	315.72	15.54	9.98	9.36
EE6	22.93	22.70	157.72	313.39	15.54	9.33	9.06
Ensaio	tw	wbf	dh				
nominal	6.20	120.00	240.00				
EE1	7.30	120.96	241.84				
EE5	7.60	120.55	242.06				
EE3	7.50	120.68	242.29				
EE4	7.90	121.26	242.49				
EE2	7.60	121.20	243.82				
EE7	7.20	120.84	242.41				
EE6	7.30	120.39	243.01				

Figure B.9: Coimbra - EE tests - Actual end-plate and beam geometrical properties [15]

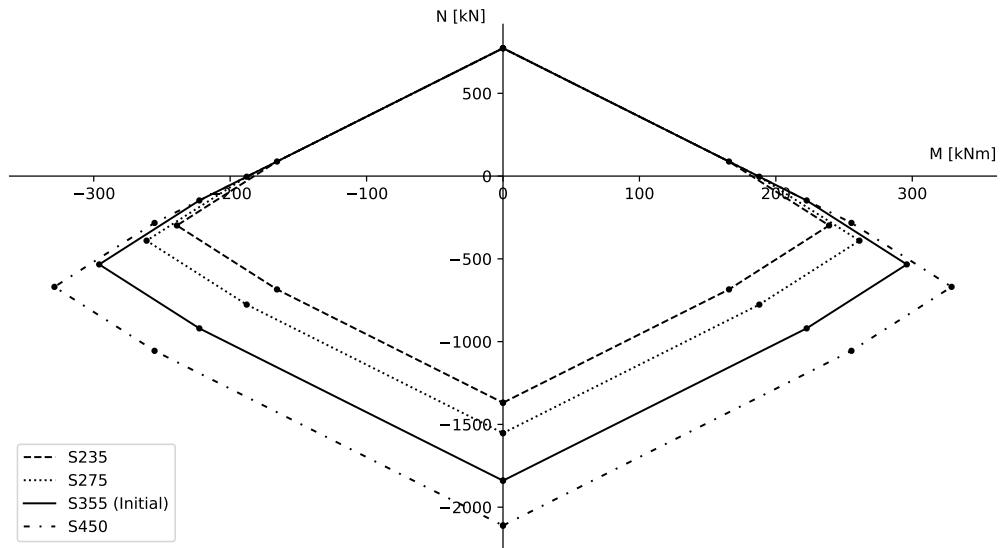


Ensaio	a	b	c	d	e	f	g
nominal	61.00	74.00	61.00	61.00	74.00	61.00	61.00
EE1	61.62	73.65	61.12	61.34	74.00	60.93	61.62
EE5	62.20	73.93	60.93	62.46	73.60	60.90	62.75
EE3	62.38	73.36	61.82	61.32	74.15	61.03	61.92
EE4	62.63	73.71	60.93	62.96	73.95	61.37	61.66
EE2	61.98	73.72	61.19	62.06	73.86	61.68	63.20
EE7	61.70	73.58	61.34	61.92	74.08	61.00	62.44
EE6	61.69	73.68	60.75	62.73	73.89	60.78	61.99
Ensaio	h	i	j	k	l	m	d1
nominal	74.00	61.00	5.00	52.00	134.00	134.00	22.00
EE1	73.79	61.48	51.85	51.44	134.34	133.57	22.12
EE5	73.94	60.48	52.01	51.94	133.80	134.14	22.20
EE3	73.64	61.46	51.78	52.43	133.77	134.04	22.07
EE4	73.84	60.90	51.98	51.89	133.94	133.85	22.20
EE2	73.70	61.19	51.98	52.06	133.69	134.38	22.00
EE7	74.40	61.33	51.68	52.27	134.24	133.85	22.07
EE6	73.68	60.50	52.07	52.02	134.20	134.02	22.00
Ensaio	d2	d3	d4	d5	d6	tfb1	tfb2
nominal	22.00	22.00	22.00	22.00	22.00	17.00	17.00
EE1	22.10	22.05	22.06	22.05	22.14	16.13	16.12
EE5	22.12	22.04	22.09	22.15	22.08	15.85	16.00
EE3	22.20	22.10	22.10	22.08	22.12	15.91	15.90
EE4	22.07	22.06	21.90	22.20	22.11	16.00	15.98
EE2	21.96	22.11	22.15	22.03	22.13	15.74	15.95
EE7	22.10	21.98	22.19	21.87	22.13	15.94	16.07
EE6	22.14	22.11	22.10	22.02	22.12	15.93	16.70
Ensaio	twc	wcf	dh				
nominal	10.00	240.00	240.00				
EE1	10.23	240.64	241.65				
EE5	9.90	241.83	240.00				
EE3	9.60	240.96	239.78				
EE4	9.70	240.89	239.53				
EE2	9.70	240.90	240.73				
EE7	9.80	240.82	239.28				
EE6	9.90	240.92	241.72				

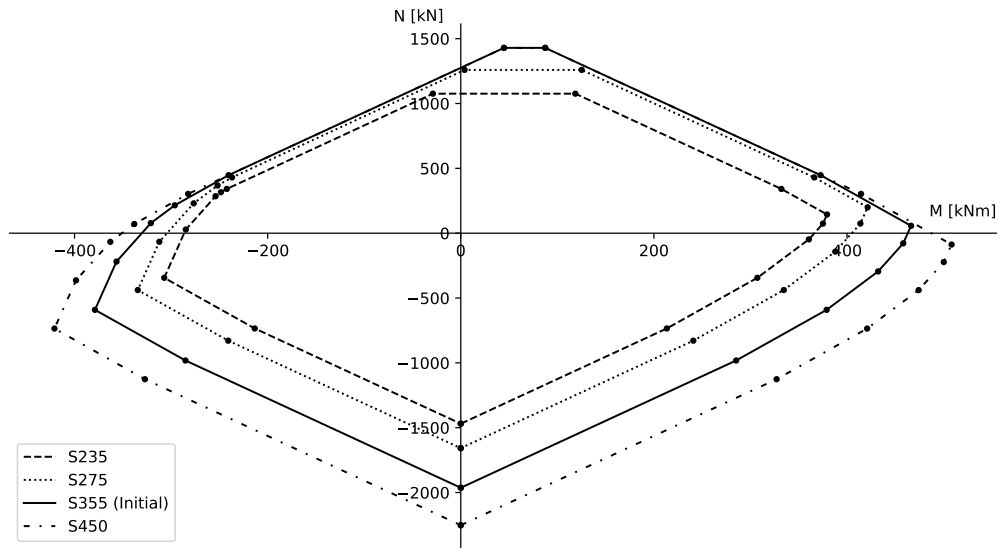
Figure B.10: Coimbra - EE tests - Actual column geometrical properties [15]

## **Appendix C**

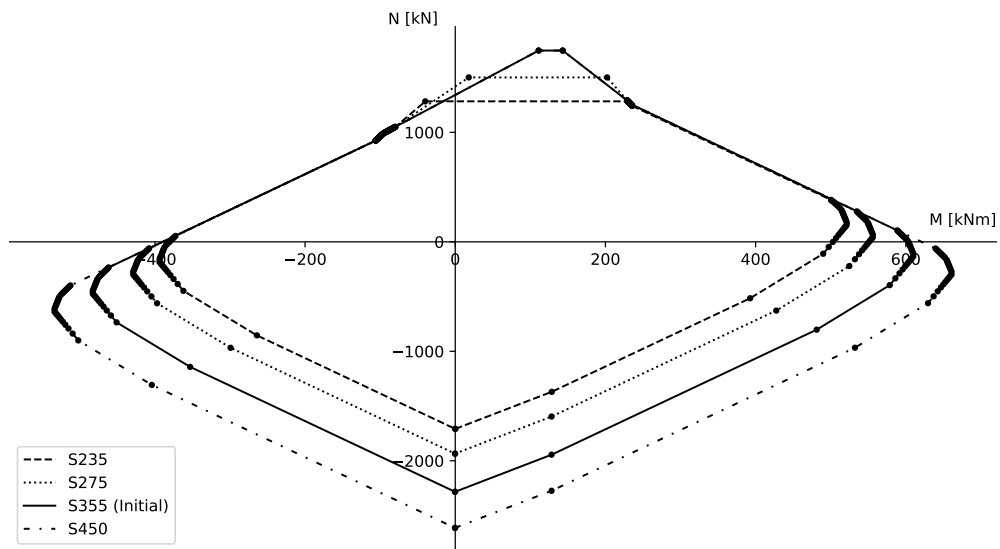
### **Parametric Analysis**



(a) Configuration A1

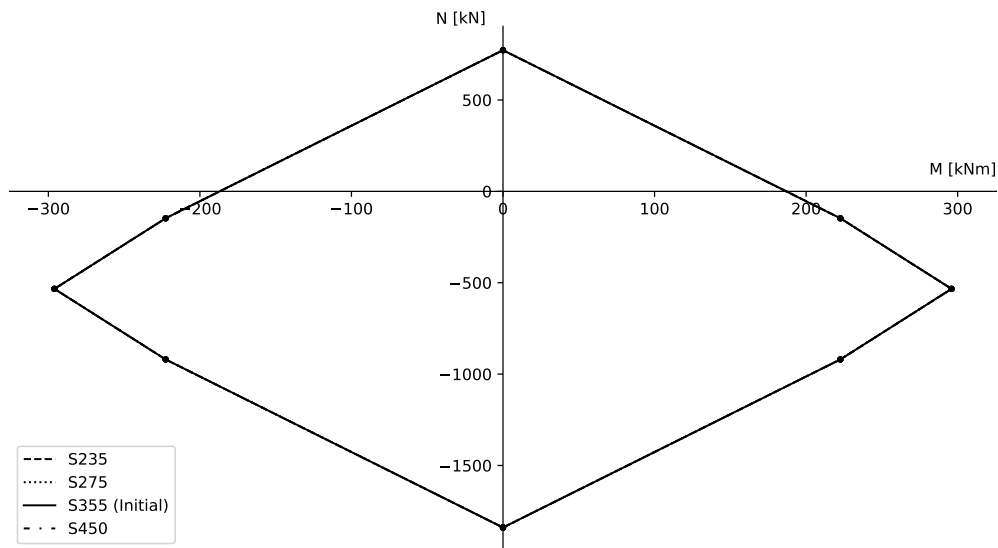


(b) Configuration C2

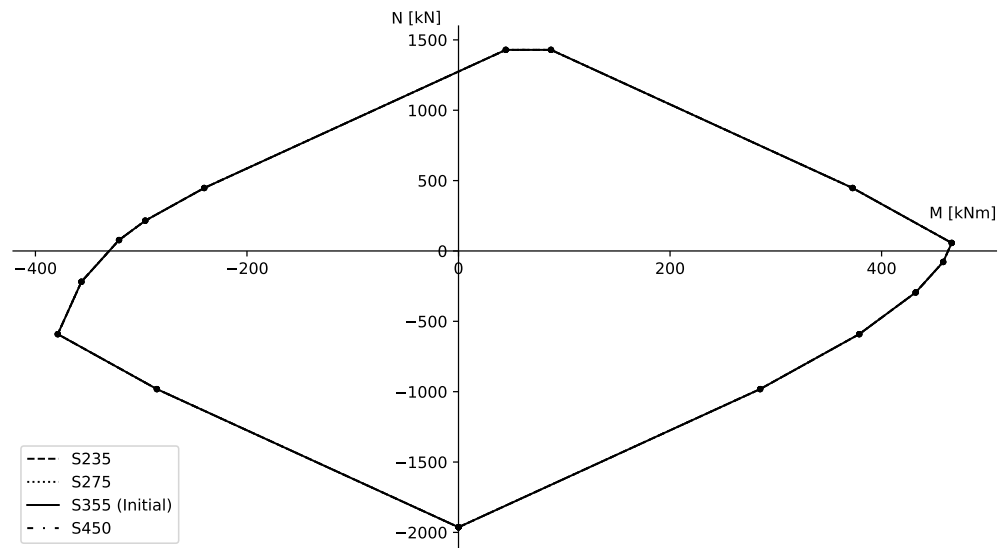


(c) Cerfontaine example

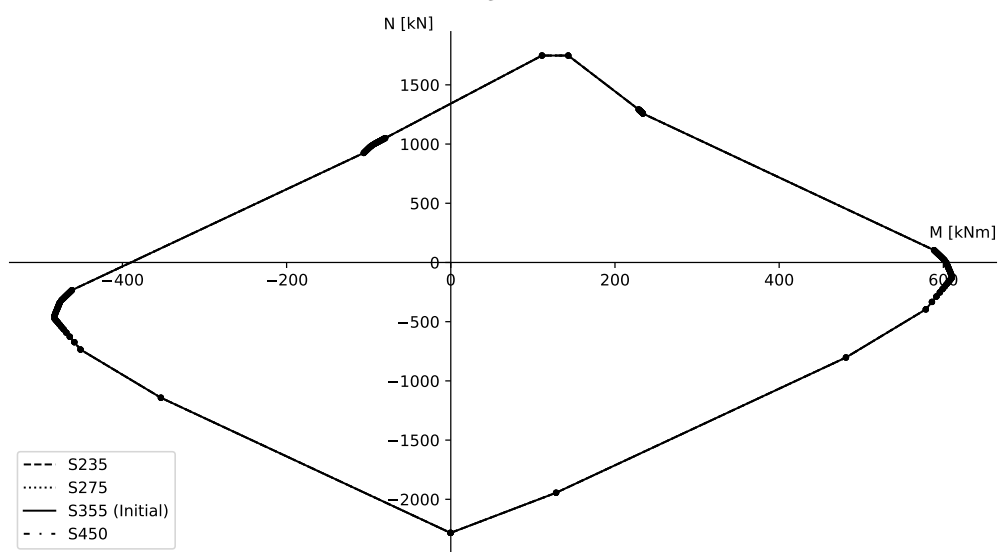
Figure C.1: Parametric analysis - Variation of the column steel grades



(a) Configuration A1

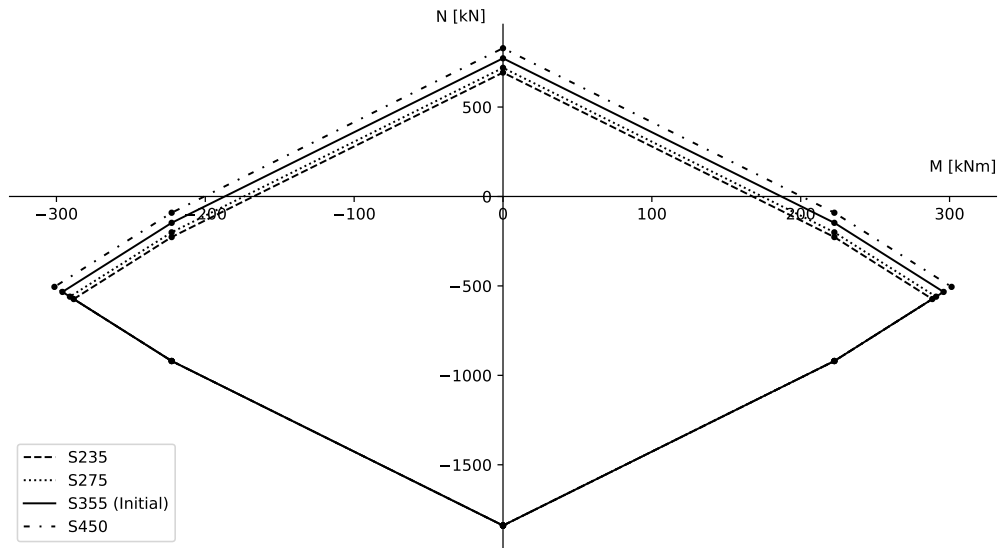


(b) Configuration C2

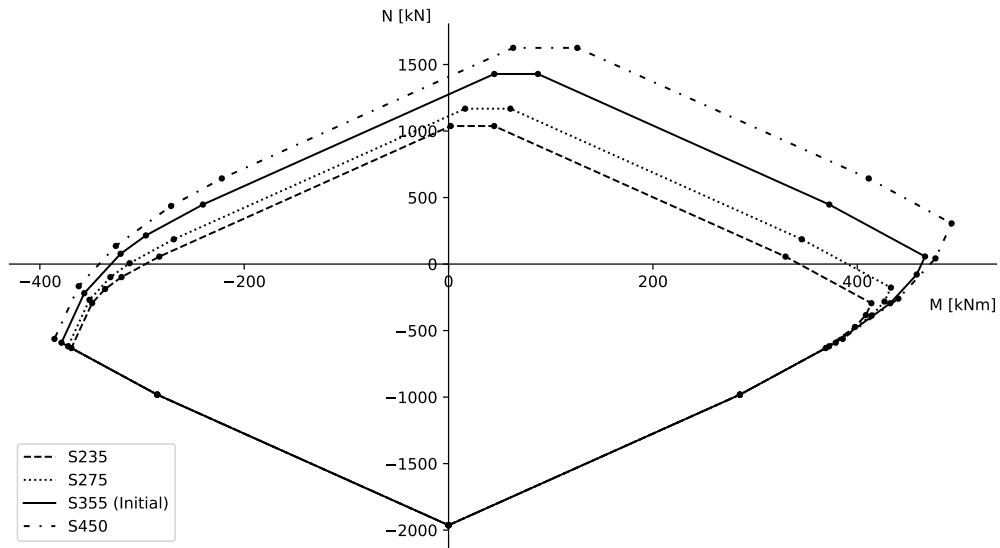


(c) Cerfontaine example

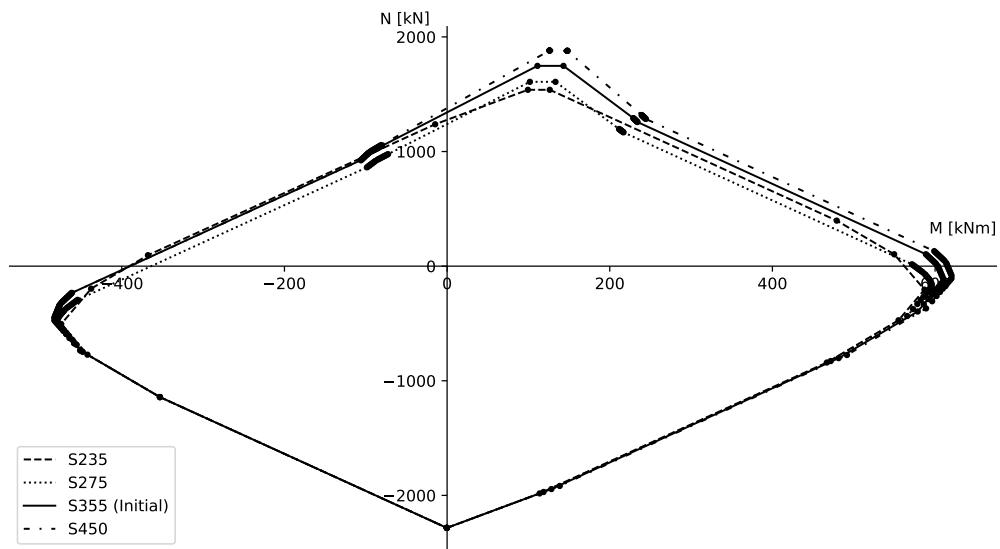
Figure C.2: Parametric analysis - Variation of the beam steel grades



(a) Configuration A1

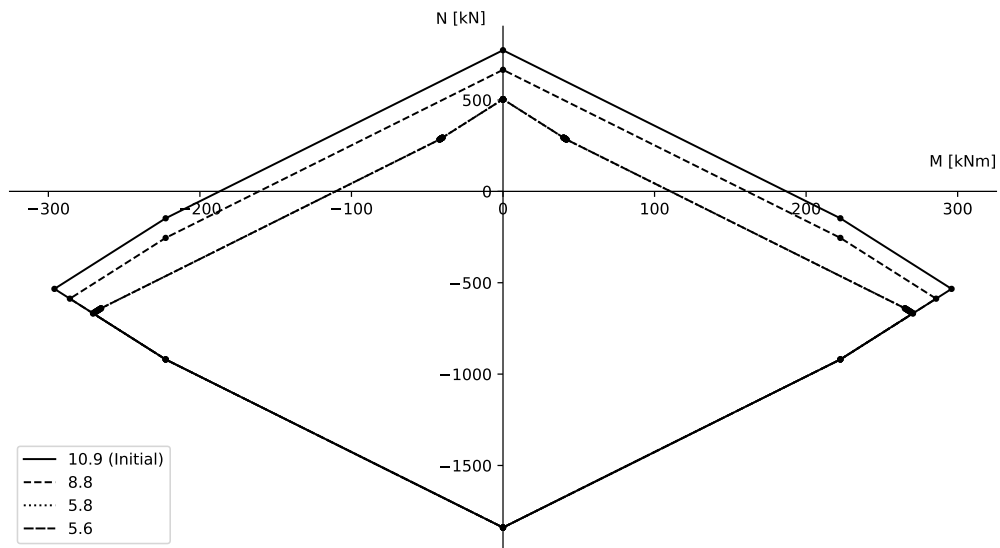


(b) Configuration C2

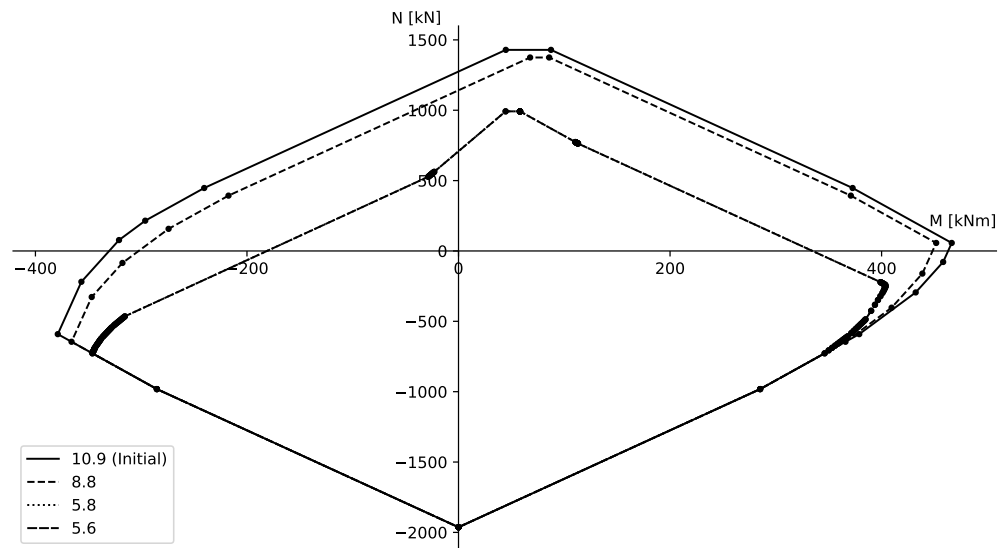


(c) Cerfontaine example

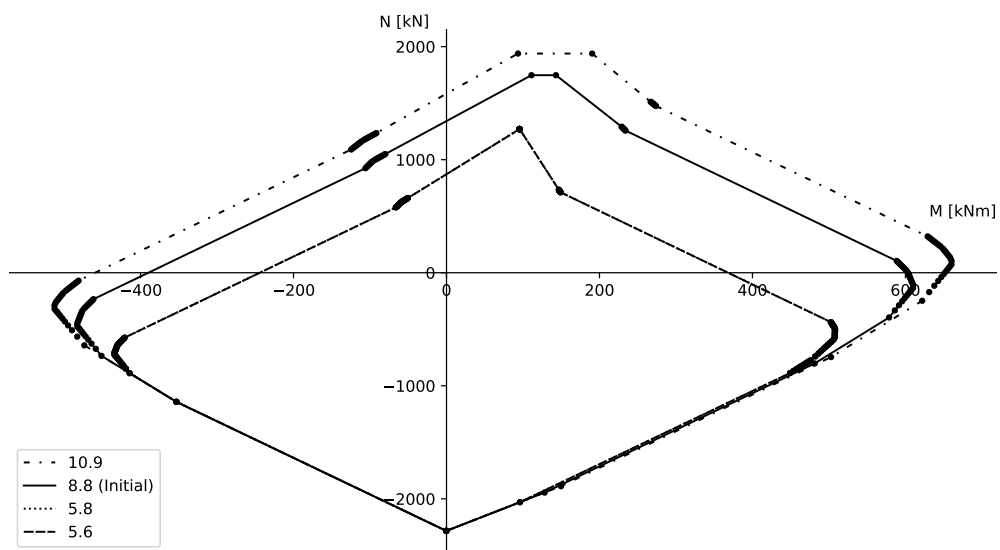
Figure C.3: Parametric analysis - Variation of the end-plate steel grades



(a) Configuration A1

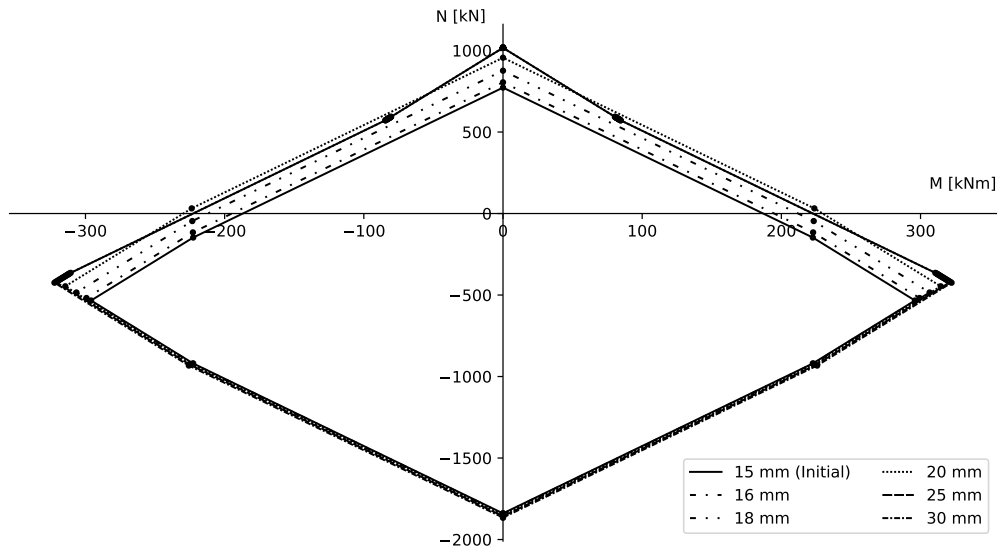


(b) Configuration C2

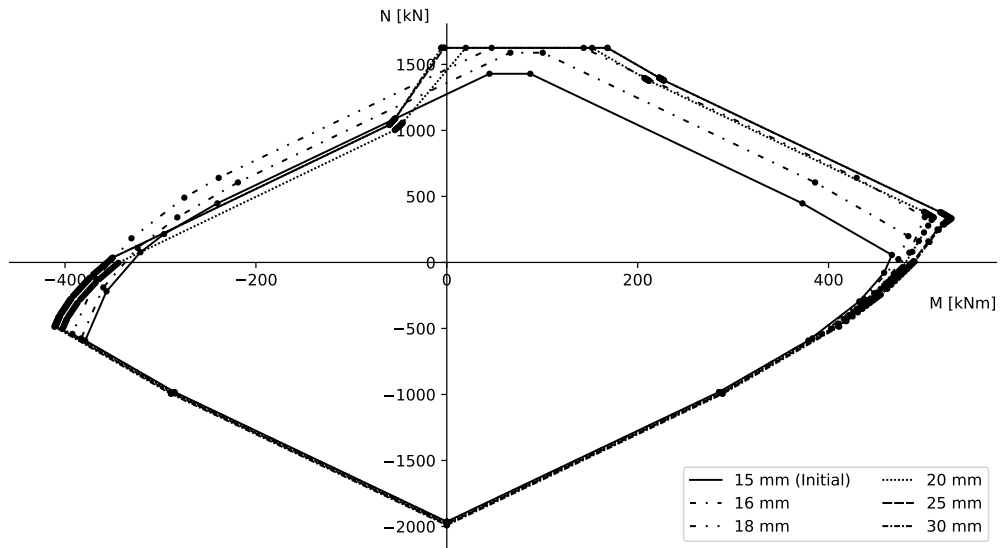


(c) Cerfontaine example

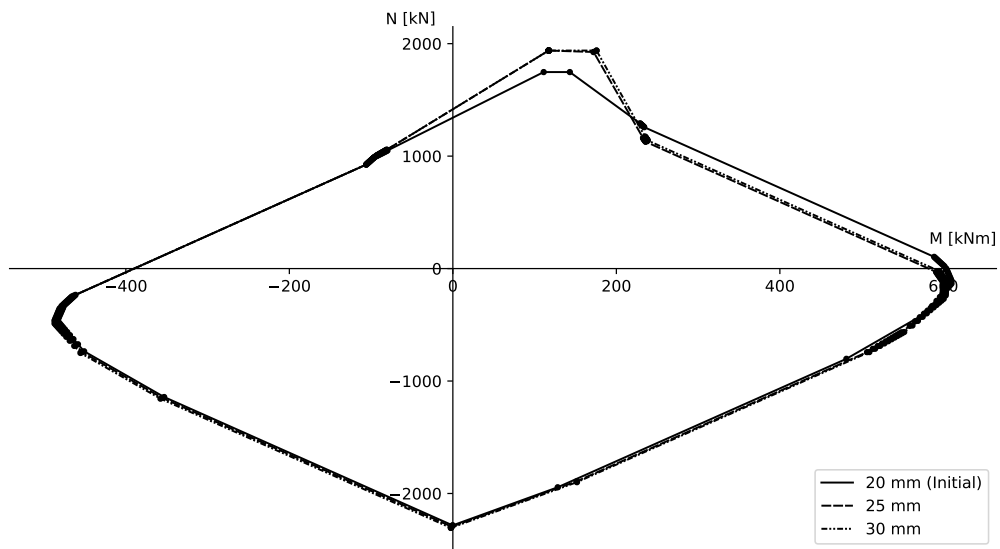
Figure C.4: Parametric analysis - Variation of the bolts steel grades



(a) Configuration A1

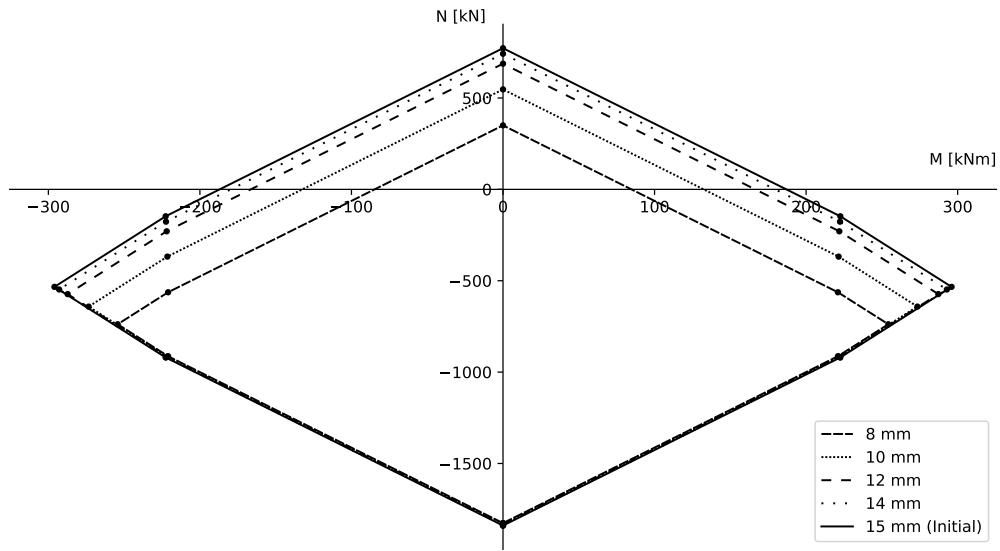


(b) Configuration C2

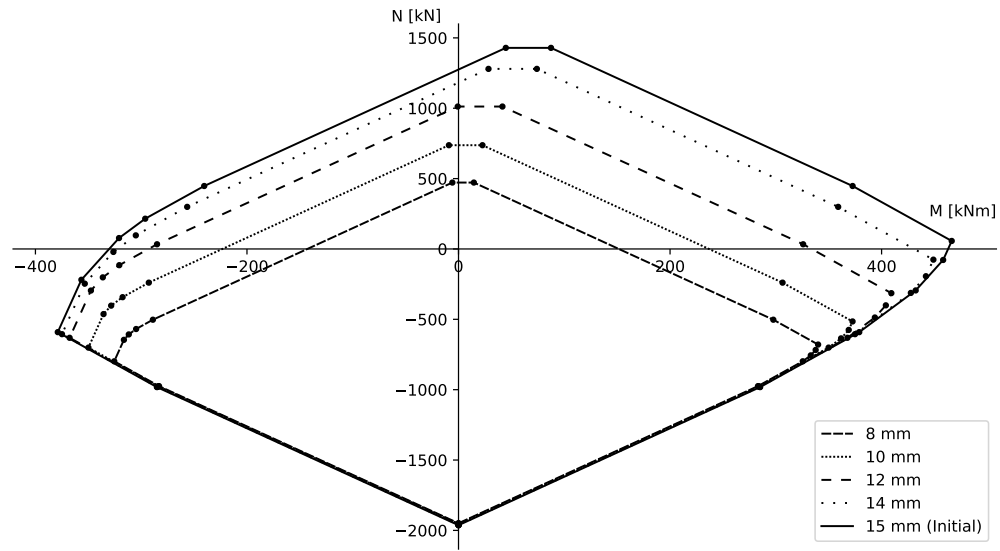


(c) Cerfontaine example

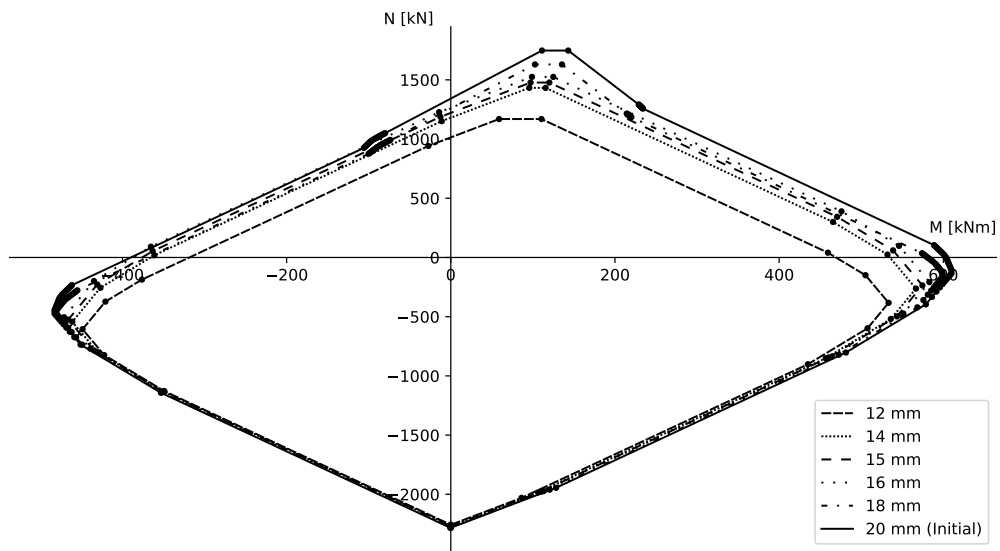
Figure C.5: Parametric analysis - Increase of the end-plate thickness



(a) Configuration A1



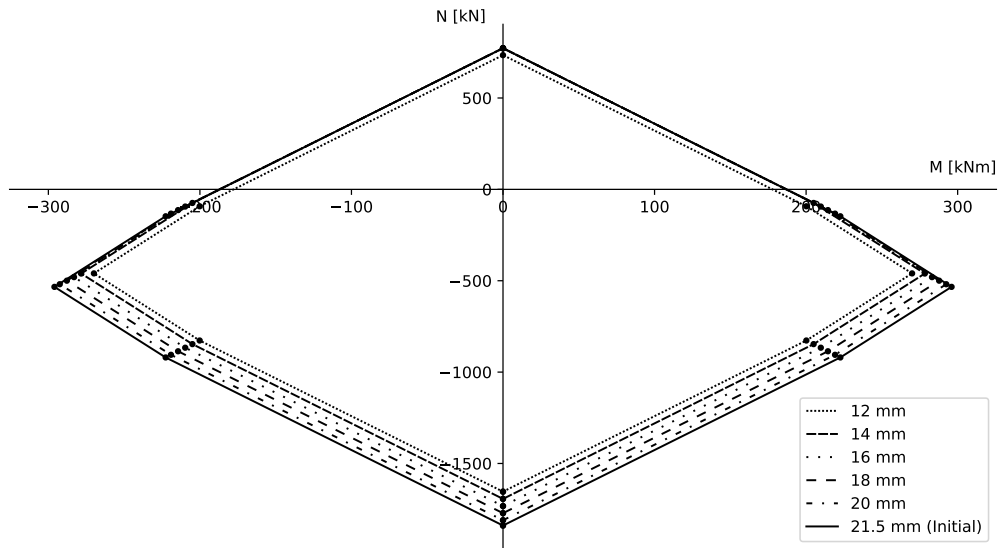
(b) Configuration C2



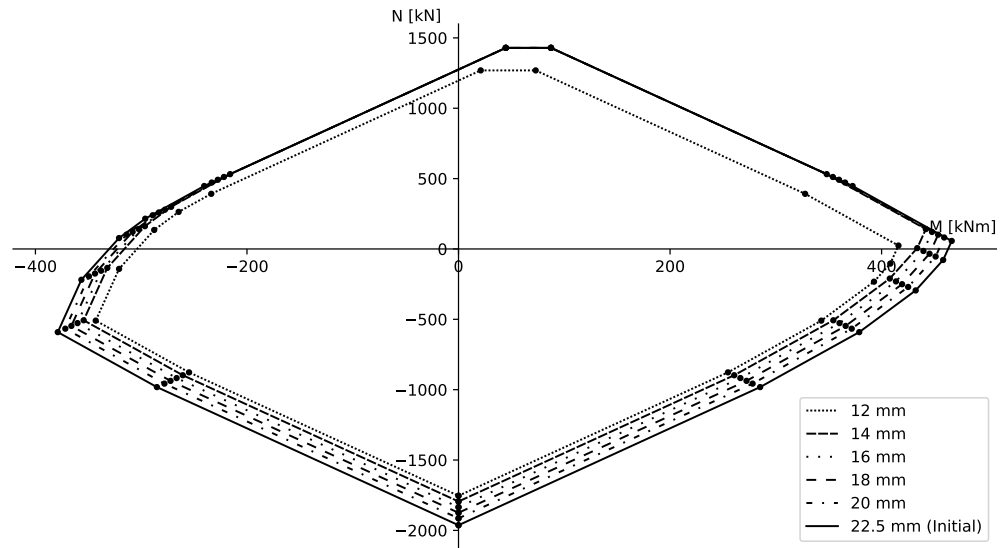
(c) Cerfontaine example

Figure C.6: Parametric analysis - Decrease of the end-plate thickness

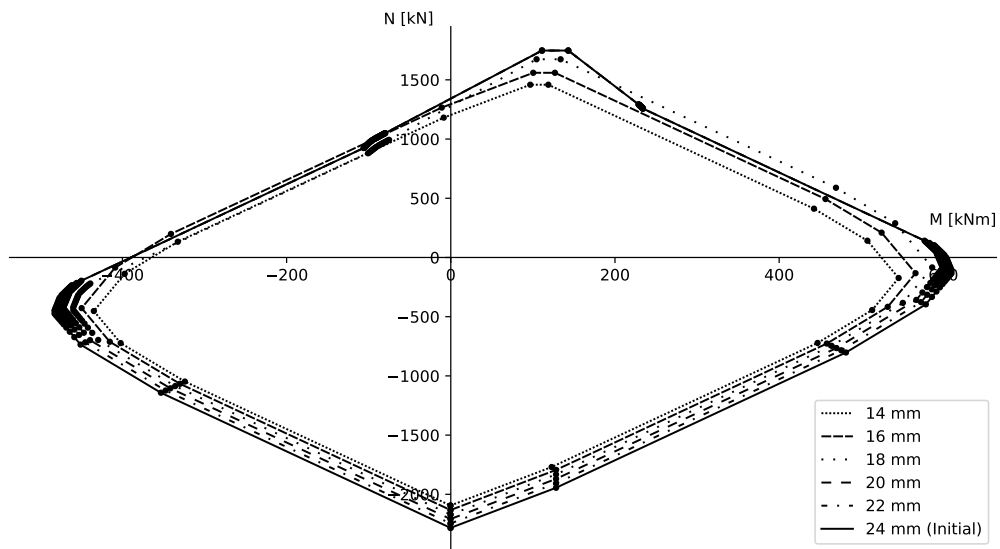




(a) Configuration A1

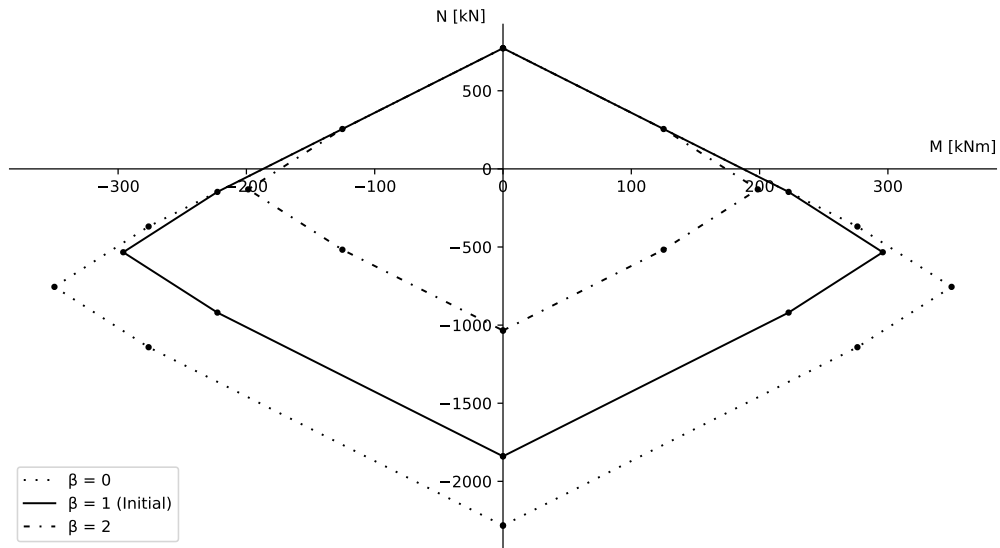


(b) Configuration C2

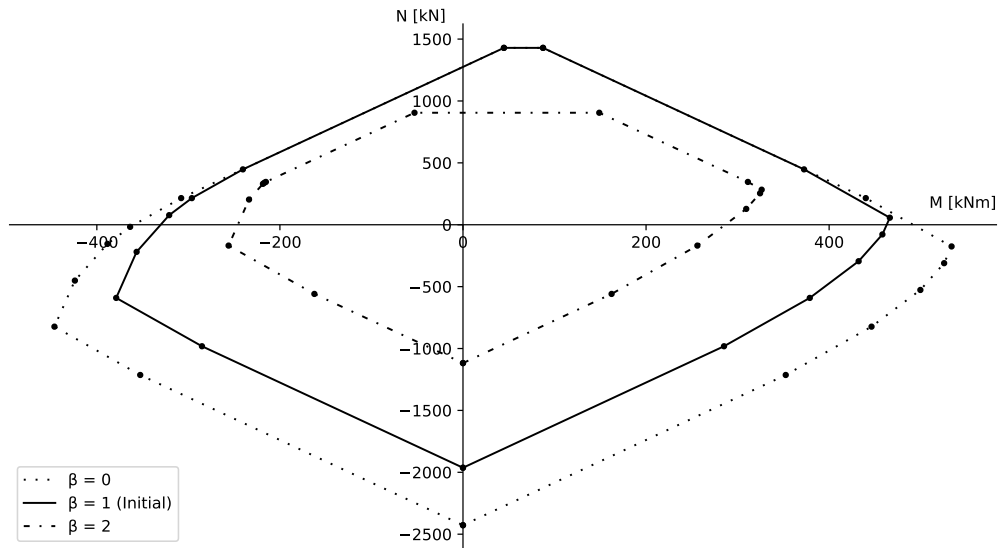


(c) Cerfontaine example

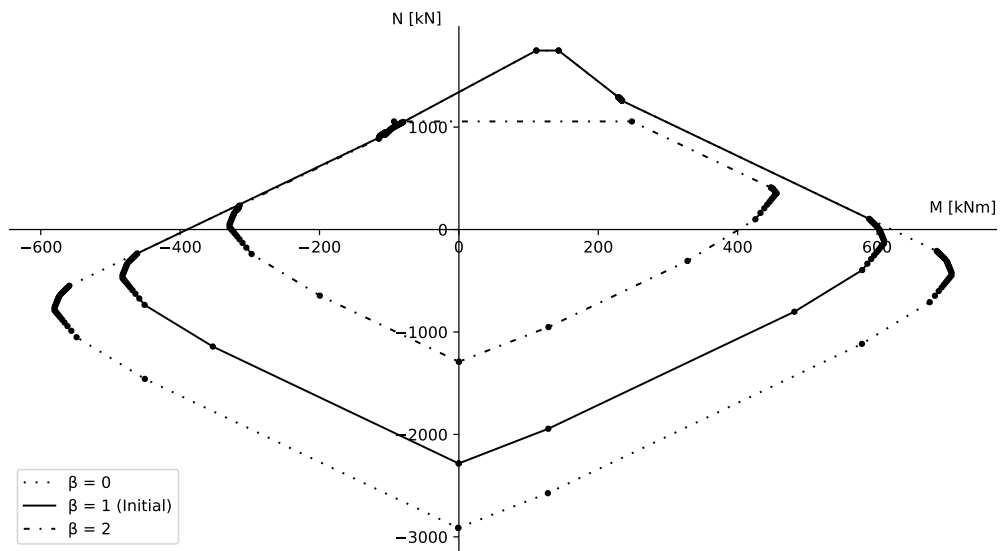
Figure C.7: Parametric analysis - Decrease of the column flange thickness



(a) Configuration A1



(b) Configuration C2



(c) Cerfontaine example

Figure C.8: Parametric analysis - Variation of the transformation parameter  $\beta$